



TECHNISCHE UNIVERSITÄT MÜNCHEN

FAKULTÄT WISSENSCHAFTSZENTRUM WEIHENSTEPHAN

FÜR ERNÄHRUNG, LANDNUTZUNG UND UMWELT

LEHRSTUHL FÜR ENTWICKLUNGSGENETIK

**From Novel Disease Genes to New Mouse Models - A Complementary
Approach**

Caroline Alexandra Biagosch

Vollständiger Abdruck der von der Fakultät Wissenschaftszentrum Weihenstephan für Ernährung, Landnutzung und Umwelt der Technischen Universität München zur Erlangung des akademischen Grades eines

Doktors der Naturwissenschaften

genehmigten Dissertation.

Vorsitzender: Prof. Dr. Martin Hrabě de Angelis

Prüfer der Dissertation: 1. Priv.-Doz. Dr. Thomas Floss

2. Prof. Angelika Schniecke, Ph.D.

Die Dissertation wurde am 10.10.2016 bei der Technischen Universität München eingereicht und durch die Fakultät Wissenschaftszentrum Weihenstephan für Ernährung, Landnutzung und Umwelt am 08.03.2017 angenommen.

To my family.

TABLE OF CONTENTS

| | |
|---|-----------|
| ABSTRACT | 9 |
| English | 9 |
| German | 11 |
| I. IDENTIFICATION OF A NEW DISEASE-ASSOCIATED GENE – <i>FBXL4</i> ... | 13 |
| I.1. INTRODUCTION | 13 |
| I.1.1. Genetic disease and mitochondriopathies | 13 |
| I.1.2. Development of genetic disorders | 13 |
| I.1.3. Mitochondria and oxidative phosphorylation | 14 |
| I.1.4. Mitochondriopathies | 15 |
| I.1.5. Gene discovery approaches | 15 |
| I.1.6. Functional validation of candidate genes | 16 |
| I.2. RESULTS | 18 |
| I.2.1. Identification of <i>FBXL4</i> as a candidate gene for early-onset mitochondrial encephalopathy | 18 |
| I.2.2. Molecular genetic analysis of <i>FBXL4</i> | 19 |
| I.2.3. Clinical and biochemical features | 20 |
| I.2.4. Validation of <i>FBXL4</i> via cellular rescue experiments | 21 |
| I.2.5. Mutations in <i>FBXL4</i> are related to a reduction of mitochondrial proteins | 23 |
| I.3. DISCUSSION | 24 |
| I.3.1. <i>FBXL4</i> dysfunction causes a clinically and biochemically distinct phenotype | 24 |
| I.3.2. <i>FBXL4</i> dysfunction causes a mitochondrial disorder | 25 |
| I.3.3. Outlook: Relevance for diagnosis and protein function | 27 |
| II. GENERATION OF A MOUSE MODEL (<i>WDR45</i> KO) RESEMBLING THE HUMAN DISEASE BPAN | 29 |
| II.1. INTRODUCTION | 29 |
| II.1.1. Generation of a knockout mouse model | 29 |
| II.1.1.1. The use of mouse models and genetic engineering | 29 |
| II.1.1.2. TALEN | 30 |
| II.1.1.3. CRISPR/Cas9 | 31 |

TABLE OF CONTENTS

| | | |
|-----------|--|----|
| II.1.1.4. | The German Mouse Clinic and the establishment of a mouse model..... | 33 |
| II.1.2. | The human disease BPAN and the corresponding <i>Wdr45</i> knockout | 34 |
| II.1.2.1. | Neurodegeneration with brain iron accumulation (NBIA) | 34 |
| II.1.2.2. | Beta-propeller protein-associated neurodegeneration (BPAN) | 35 |
| II.1.2.3. | Genetics of BPAN and the disease-associated gene <i>WDR45</i> | 36 |
| II.1.2.4. | The brain-specific <i>Wdr45</i> knockout mouse model | 36 |
| II.1.2.5. | WDR45 and its function in autophagy | 38 |
| II.2. | RESULTS | 41 |
| II.2.1. | Clinical presentation in human BPAN patients..... | 41 |
| II.2.2. | Generation of a <i>Wdr45</i> knockout mouse via TALENs | 43 |
| II.2.3. | Systemic <i>Wdr45</i> KO is viable in mice..... | 45 |
| II.2.4. | Analysis of preliminary <i>Wdr45</i> KO mice (F2) shows neurobehavioral deficits | 47 |
| II.2.5. | Screen of the disease progression <i>Wdr45</i> cohort (F3)..... | 50 |
| II.2.5.1. | Neurologic deterioration in <i>Wdr45</i> KO mice | 50 |
| II.2.5.2. | Pathologic brain abnormalities in <i>Wdr45</i> KO mice | 54 |
| II.2.6. | Secondary screen of aged <i>Wdr45</i> KO GMC cohort (F4) | 58 |
| II.3. | DISCUSSION | 59 |
| II.3.1. | Of mice and men: the <i>Wdr45</i> KO mouse as a model for BPAN | 59 |
| II.3.2. | The BPAN mouse model helps investigate disorders of autophagy | 62 |
| II.3.3. | From the BPAN mouse model to therapeutic strategies | 65 |
| III. | THERAPEUTIC STRATEGY FOR GLUTARIC ACIDURIA TYPE 1..... | 67 |
| III.1. | INTRODUCTION..... | 67 |
| III.1.1. | The lysine degradation pathway..... | 67 |
| III.1.2. | Glutaric aciduria type 1 - GCDH..... | 69 |
| III.1.3. | 2-aminoadipic 2-oxoadipic aciduria – DHTKD1 | 71 |
| III.1.4. | Glutaric aciduria type 3 – C7ORF10 | 72 |
| III.1.5. | DHTKD1 inhibition as a therapy for glutaric aciduria type 1 | 72 |
| III.2. | RESULTS..... | 73 |
| III.2.1. | Generation of a <i>Dhtkd1</i> KO mouse via TALENs..... | 73 |
| III.2.2. | Clinical and biochemical characterization of the <i>Dhtkd1</i> KO mouse | 75 |
| III.2.3. | Generation of a <i>Gcdh/Dhtkd1</i> -double KO mouse..... | 77 |
| III.2.4. | Biochemical characterization of the double KO mouse | 78 |

TABLE OF CONTENTS

| | |
|---|----|
| III.2.5. High-lysine diet challenges knockout lines..... | 79 |
| III.3. DISCUSSION..... | 82 |
| III.3.1. DHTKD1 inhibition is not a promising treatment strategy for GA-I..... | 82 |
| III.3.2. Murine double KO experiments question the current theory of lysine degradation | 82 |
| III.3.3. Future investigations of the lysine degradation pathway towards GA-I therapy | 83 |
| IV. CONCLUSION AND OUTLOOK..... | 85 |
| V. MATERIAL AND METHODS | 88 |
| V.1. Material | 88 |
| V.1.1. Chemicals and reagents | 88 |
| V.1.2. Enzymes and proteins | 89 |
| V.1.3. Antibodies..... | 89 |
| V.1.4. Kits..... | 89 |
| V.1.5. Other materials..... | 90 |
| V.1.6. Technical devices | 90 |
| V.1.7. Oligonucleotides..... | 91 |
| V.1.8. Vectors and plasmids | 92 |
| V.1.9. Bacteria..... | 92 |
| V.1.10. Cell lines | 92 |
| V.1.11. Mouse lines..... | 93 |
| V.2. Methods | 94 |
| V.2.1. Genetic and molecular biological methods..... | 94 |
| V.2.1.1. Preparation of plasmid DNA | 94 |
| V.2.1.2. Preparation of genomic DNA..... | 94 |
| V.2.1.3. Polymerase Chain Reaction (PCR) and subsequent purification | 94 |
| V.2.1.4. Sequencing of PCR fragments | 95 |
| V.2.1.5. Restriction digestion of DNA | 96 |
| V.2.1.6. Ligation of DNA..... | 96 |
| V.2.1.7. DNA gel electrophoresis and subsequent DNA extraction | 96 |
| V.2.1.8. <i>In vitro</i> transcription..... | 96 |
| V.2.1.9. RNA purification..... | 97 |
| V.2.1.10. RNA gel electrophoresis | 97 |

TABLE OF CONTENTS

| | | |
|-----------|--|-----|
| V.2.1.11. | Transformation of <i>E.coli</i> by electrophoresis | 98 |
| V.2.1.12. | <i>In silico</i> design and in vitro testing of TALENs | 98 |
| V.2.2. | Protein analytics | 99 |
| V.2.2.1. | Immunoblot analysis | 99 |
| V.2.2.2. | β -Galactosidase assay | 100 |
| V.2.2.3. | Luciferase assay | 101 |
| V.2.2.4. | Biochemical analysis of metabolites (GA and OA) | 101 |
| V.2.3. | Tissue culture | 102 |
| V.2.3.1. | Culturing, freezing and thawing of fibroblast cells..... | 102 |
| V.2.3.2. | Transfection of HEK cells | 102 |
| V.2.3.3. | Lentiviral transduction of fibroblasts | 103 |
| V.2.3.4. | Cellular respiration assay using Seahorse | 103 |
| V.2.4. | Mouse work | 104 |
| V.2.4.1. | Legal approvals | 104 |
| V.2.4.2. | Mouse housing, nutrition and handling | 105 |
| V.2.4.3. | Mouse embryo-injection..... | 105 |
| V.2.4.4. | Mouse genotyping based on PCR and sequencing | 105 |
| V.2.4.5. | Neurobehavioral experiments..... | 106 |
| V.2.4.6. | GMC examinations | 108 |
| V.2.4.7. | High-lysine diet | 108 |
| V.2.4.8. | Organ withdrawal..... | 108 |
| V.2.5. | Statistical analysis..... | 108 |
| V.2.6. | Authors' contribution..... | 108 |
| VI. | TABLE OF FIGURES..... | 110 |
| VII. | TABLE OF TABLES | 112 |
| VIII. | SUPPLEMENTARY MATERIAL | 113 |
| IX. | ABBREVIATIONS..... | 118 |
| X. | REFERENCES..... | 122 |
| XI. | ACKNOWLEDGEMENTS | 133 |
| XII. | CURRICULUM VITAE | 134 |

ABSTRACT

English

Genetic research is evolving rapidly, with technologies like Next Generation Sequencing (NGS) generating vast amounts of genetic data. Bringing this research “from bench to bedside” requires intensive effort in translational research. This work contributes to three different neurological disorders, each at a specific stage of scientific research, and is separated into three parts:

- I.) Disease-associated gene discovery (*FBXL4*)
- II.) Development of a disease relevant mouse model (BPAN)
- III.) Evaluation of a therapeutic strategy (Glutaric aciduria type 1)

Part I focusses on genetic diagnosis in a rare form of mitochondriopathy, early-onset mitochondrial encephalopathy. The identification of the novel disease gene, *FBXL4*, associated with early-onset mitochondrial encephalopathy was more than routine and required a collaborative effort of geneticists and genome scientists. *FBXL4* was previously not known as a mitochondrial protein, and biochemical measurements of respiratory chain complex activities normalised to citrate synthase (CS) levels were normal in patients. Reduced CS was found in all patients analysed (n=4). Therefore, normal biochemical measurements of patients were explained by the normalisation to reduced CS levels. Additionally, reduced maximal respiration measured via microoxygraphy in patient fibroblasts was shown, which was rescued upon lentiviral delivery of wild-type *FBXL4*. These results indicate a deficiency in mitochondrial biogenesis or maintenance. The knowledge of the causal gene has led to the diagnosis of at least 28 cases since the first publication in 2013.

In part II, a *Wdr45* knockout (KO) mouse model for the neurodegenerative disease beta-propeller protein-associated neurodegeneration (BPAN) was generated. BPAN belongs to a group of diseases known as neurodegeneration with brain iron accumulation (NBIA). The disease-associated gene, *WDR45*, is located on the X-chromosome, and *de novo* mutations had been shown to lead to BPAN in a dominant pattern of inheritance. A systemic KO of *WDR45* is believed to be embryonic lethal due to the gender imbalance of 44 to 4 female to male patients and the analysis of male patients indicating mosaicism. In order to generate the *Wdr45* KO mouse, the targeted genome editing approach was used based on transcription activator-like effector nucleases (TALENs). It was found that systemic *Wdr45* KO mice are viable. They developed signs of neuropathology at four months of age with 100% penetrance making this model suitable for therapeutic studies. Intensive characterization of the BPAN mouse model found resemblance to the human phenotype in several facets, with neurobehavioral decline in the ageing organism during an observation period of 22 months. The mouse model will be beneficial to the elucidation of the disease pathomechanism. Overlaps of

ABSTRACT

the phenotype and disease mechanism of BPAN with common disorders like Alzheimer's and Parkinson's disease increases the potential impact of therapeutic studies with this model. The TALEN genome editing tool enabled the generation of a KO mouse line within four months, and proved fast and efficient. It was recently largely replaced by the more advanced CRISPR/Cas9 system. The CRISPR/Cas9 system made it to the general media due to its efficiency, ease of application and ground breaking universal applicability. This scientific milestone in targeted genome editing and its rapid advances are currently leading to the generation of many disease models facilitating therapeutic studies.

As described in part III, in the case of glutaric aciduria type 1 (GA-I), appropriate mouse models are necessary for the evaluation of treatment approaches. GA-I is a neurodegenerative metabolic disorder, characterized by the accumulation of the putative toxic metabolite glutaryl-CoA and its derivatives. It results from mutations in *GCDH* (coding for glutaryl-CoA dehydrogenase). This enzyme is key to the lysine degradation pathway, in which DHTKD1 (dehydrogenase E1 and transketolase domain-containing protein 1) is thought to act directly upstream of GCDH. In theory, the inhibition of DHTKD1 should prevent glutaryl-CoA accumulation and rescue the GA-I phenotype. Human DHTKD1 deficiency causes no or only a mild phenotype. A *Dhtkd1* KO mouse was generated, and it showed clinical and biochemical resemblance to the human situation with 2-oxoadipate (OA) accumulation and no obvious clinical abnormalities. Using an established *Gcdh* KO mouse with toxic accumulations of glutaryl-CoA, a *Dhtkd1*/*Gcdh*- double KO mouse line was generated. This was supposed to mirror the situation of DHTKD1 inhibition in a GA-I patient. The double KO mouse proved to be both clinically and biochemically abnormal. These results suggest that DHTKD1 inhibition is not sufficient to rescue GA-I phenotypes, neither clinically nor biochemically. This disapproves the efficiency of the proposed therapeutic approach of DHTKD1 inhibition and suggests a better defined combined approach inhibiting two targets simultaneously, DHTKD1 and C7ORF10. It is proposed that novel branches in the lysine degradation pathway exist, highlighting its complexity and raising new questions. This unexpected finding underlines the necessity of animal models to validate new therapeutic approaches.

German

Genetische Forschung durchläuft eine rasante Entwicklung. Mit Technologien wie dem *Next Generation Sequencing* (NGS) werden große Mengen genetischer Daten generiert. Es bedarf jedoch einen immensen Aufwand in der translationalen Forschung um dieses Wissen „vom Labortisch zum Krankenbett“ zu bringen. Diese Arbeit trägt zum Kenntnisstand von drei unterschiedlichen neurologischen Erkrankungen und ihrem jeweiligen Stand der Forschung bei, und gliedert sich daher in drei Teile:

- I.) Identifizierung eines krankheitsrelevanten Gens (*FBXL4*)
- II.) Entwicklung eines krankheitsrelevanten Mausmodells (BPAN)
- III.) Evaluierung eines therapeutischen Ansatzes (Glutarazidurie Typ I)

Teil I konzentriert sich auf die genetische Diagnostik einer seltenen Form der Mitochondriopathie. Die Identifizierung des neuen krankheitsrelevanten Gens, *FBXL4*, das mit einer frühen mitochondrialen Enzephalopathie assoziiert ist, war mehr als Routine und erforderte die Zusammenarbeit von Genetikern und Genomforschern. *FBXL4* war bisher nicht als mitochondriales Protein beschrieben und biochemische Messungen der Atmungskettenkomplexe normalisiert auf Citrat-Synthase (CS) zeigten sich als unauffällig in Patienten. Allerdings wurde eine Erniedrigung der CS aller analysierten Patienten (n=4) gefunden. Die unauffälligen biochemischen Messwerte der Atmungskettenkomplexe bei den Patienten können auf die Normalisierung auf reduzierte CS Werte zurückgeführt werden. Zudem konnte eine Reduktion der maximalen Atmung in Fibroblasten von Patienten mittels Microoxygraphy identifiziert werden, die durch lentiviralen Transfer des nicht-mutierten *FBXL4*-Allels aufgehoben wurde. Dies sind Hinweise auf einen Defekt der mitochondrialen Biogenese. Das Wissen über das krankheitsrelevante Gen hat bereits zur Diagnosestellung bei mindestens 28 Patienten seit der ersten Veröffentlichung im Jahre 2013 geführt.

In Teil II wurde ein *Wdr45* Knockout-Mausmodell für die neurodegenerative Erkrankung BPAN (β -propeller protein-associated neurodegeneration) generiert. BPAN gehört zu einer Gruppe von Erkrankungen namens NBIA (neurodegeneration with brain iron accumulation). *WDR45* ist auf dem X-Chromosom lokalisiert und es wurde gezeigt, dass *de novo* Mutationen mit dominantem Erbgang zu BPAN führen. Der systemische Knockout (KO) von *WDR45* ist als höchstwahrscheinlich embryolethal beschrieben. Dies liegt an dem auffälligen Geschlechterverhältnis von 44 zu 4 weiblichen zu männlichen Patienten, und daran, dass die Analyse der männlichen Patienten sie als Mosaik beschrieben hat. Um die *Wdr45* KO-Maus zu generieren wurde das Genome Editing System TALEN benutzt. Das murine Modell zeigte sich trotz systemischem KO als lebensfähig. KO-Mäuse entwickelten Neuropathologien im Alter von vier Monaten mit einer Penetranz von 100%. Diese Eigenschaften machen die *Wdr45* KO-Maus zu einem geeigneten Krankheitsmodell für präklinische Studien. Eine intensive Charakterisierung des Mausmodells zeigte einige Ähnlichkeiten mit dem humanen Phänotyp auf, wie zum Beispiel neurologische

ABSTRACT

Verhaltensauffälligkeiten im alternden Organismus innerhalb eines Beobachtungszeitraumes von 22 Monaten. Überschneidungen beim Phänotyp und Pathomechanismus von BPAN mit häufigen Erkrankungen wie Alzheimer oder Parkinson steigern den potentiellen Nutzen therapeutischer Studien an diesem Mausmodell. Des Weiteren wird dieses Modell zur Aufklärung des Pathomechanismus von Vorteil sein. Das Genome Editing System TALEN ermöglichte die Generierung von KO-Mauslinien innerhalb von vier Monaten und bewies sich als schnell und effizient. Allerdings wird es seit kurzem größtenteils abgelöst von dem noch fortschrittlicheren System, CRISPR/Cas9. Dieses System erlangte breite Publizität aufgrund seiner Effizienz, der leichten Anwendung und der bahnbrechenden und universellen Einsetzbarkeit. Dieser wissenschaftliche Meilenstein beim zielgerichteten Genome Editing und die schnellen Fortschritte führen derzeit zur Generierung vieler neuer Mausmodelle und vereinfachen somit die Durchführung präklinischer Studien.

Wie in Teil III anhand der Glutarazidurie Typ I (GA-I) beschrieben ist, sind die entwickelten Mausmodelle von großem Nutzen wenn es darum geht Behandlungsansätze zu evaluieren. GA-I ist eine neurodegenerative metabolische Erkrankung, die durch die Akkumulation des mutmaßlich toxischen Metaboliten, Glutaryl-CoA und seinen Derivaten, charakterisiert ist. Die Erkrankung ist eine Folge von Mutationen in *GCDH*, das für das Enzym Glutaryl-CoA Dehydrogenase kodiert. Dieses Enzym hat eine Schlüsselrolle beim Abbauweg von Lysin bei dem DHTKD1 (Dehydrogenase E1 und transketolase domain-containing protein 1) vermutlich GCDH direkt vorgeschaltet agiert. In der Theorie sollte die Hemmung von DHTKD1 die Akkumulation von Glutaryl-CoA verhindern und den GA-I Phänotyp aufheben. Humane DHTKD1-Defizienz führt jedoch zu keinem oder lediglich einem milden Phänotyp. Eine *Dhtkd1* KO-Maus wurde generiert und spiegelte sowohl klinisch als auch biochemisch die humanen Auswirkungen wider. Ohne klinische Auffälligkeiten zu entwickeln akkumuliert die *Dhtkd1* KO-Maus, 2-Oxoadipat. Mittels der etablierten *Gcdh* KO-Maus, die toxisches Glutaryl-CoA akkumuliert, wurde eine *Gcdh/Dhtkd1*-Doppel-KO-Mauslinie generiert. Diese imitiert die Hemmung von DHTKD1 in GA-I Patienten. Es konnte gezeigt werden, dass diese Hemmung nicht ausreichend ist, um den GA-I Phänotyp zu verhindern und zwar weder klinisch noch biochemisch. Die Effizienz des vorgeschlagenen Therapieansatzes der Hemmung von DHTKD1 wird widerlegt und es werden neue Ansätze für eine zielgerichtete kombinierte Therapie vorgeschlagen, zum Beispiel durch die parallele Hemmung der zwei Enzyme, DHTKD1 und C7ORF10. Die Existenz neuer bislang unbekannter Wege des Lysin-Abbaus wird dadurch nahegelegt und die vielen ungelösten Fragen innerhalb des Lysin-Abbauweges und seine Komplexität verdeutlicht. Dieses unerwartete Ergebnis unterstreicht die Notwendigkeit von Mausmodellen, um Therapieansätze validieren zu können.

I. Identification of a new disease-associated gene – *FBXL4*

I.1. INTRODUCTION

I.1.1. Genetic disease and mitochondriopathies

Genetic disorders are conditions caused by abnormalities in the genetic material, the genome, which is composed of deoxyribonucleic acid (DNA). The human body consists of more than 37 trillion cells (Bianconi et al., 2013) with each one carrying its own genome (except for erythrocytes). The DNA of each cell is tightly packed into two types of organelles. One of them, the nucleus contains 22 autosomes in duplicate and two sex chromosomes, XX or XY, harbouring the vast majority of genes. The other, mitochondria, contain hundreds of copies of circular DNA (mtDNA). Alterations of the DNA sequence can lead to genetic diseases depending on type, locus, tissue and time of a mutation.

Mitochondriopathies are caused by defective mitochondria. Mitochondria are commonly referred to as the powerhouse of the cell as they generate the majority of the energy transporter adenosine triphosphate (ATP) through oxidative phosphorylation (OXPHOS, see I.1.3.). Mitochondrial proteins are encoded by either mitochondrial or nuclear DNA. The latter gene products are transported to the mitochondria. Mutations in either nuclear or mitochondrial DNA can cause mitochondriopathies. Most disease-causing mutations affect nuclear encoded proteins, including all three disorders covered in this work.

I.1.2. Development of genetic disorders

There are several types of DNA mutations, such as synonymous and non-synonymous (missense), the latter results in substitution of one amino acid. Also insertions and deletions (indels), often leading to frame-shift (fs) mutations can cause genetic disorders. Depending on the locus, that is the chromosome of the mutation, one can distinguish between mitochondrial, X-linked or autosomal inheritance. In general, the mode of inheritance can be recessive or dominant, which describes the number of mutant copies necessary for disease outbreak. An autosomal dominant inheritance will lead to 50% affected offspring. With X-linked dominant inheritance, the disease will be passed from mothers to half of their daughters and all their sons, but from fathers to all daughters and none of the sons. This special case of inheritance is also influenced by other mechanisms such as inactivation of genes on one X-chromosome. Mitochondrial inheritance is caused by disease-associated variants located on the mitochondrial DNA. The high number of mtDNA copies per cell can cause heteroplasmy, which describes the parallel existence of genetically different mtDNA copies per cell. Furthermore, the tissue where the mutation occurs during development of an organism is of importance. If it happens in germ-line cells, the mutation will be passed onto the next generation and will affect every tissue of the offspring. Somatic mutations occur in somatic cells and are only passed onto progeny cells after cell division leading to mosaicism. Mosaic humans or animals consist

of somatic cells of more than one genotype. This has to be taken into account when generating knockout mouse lines via genome editing tools.

I.1.3. Mitochondria and oxidative phosphorylation

As the powerhouse of cells mitochondria produce the intracellular energy transporter ATP through several redox reactions. Electrons are transferred from electron donors (e.g. NADH) to electron acceptors such as oxygen in an exergonic reaction. The energy is used to transport protons across the inner mitochondrial membrane. This leads to a pH gradient forming an electrical potential across this membrane. Protein complexes involved in this process are called respiratory chain complexes (RCCs) I-V, which work with coenzymes and cofactors as well as the electron transfer flavoprotein-Q oxidoreductase (figure 1). The proton gradient is used by the ATP synthase to phosphorylate ADP to ATP, the latter being known as the molecular energy currency.

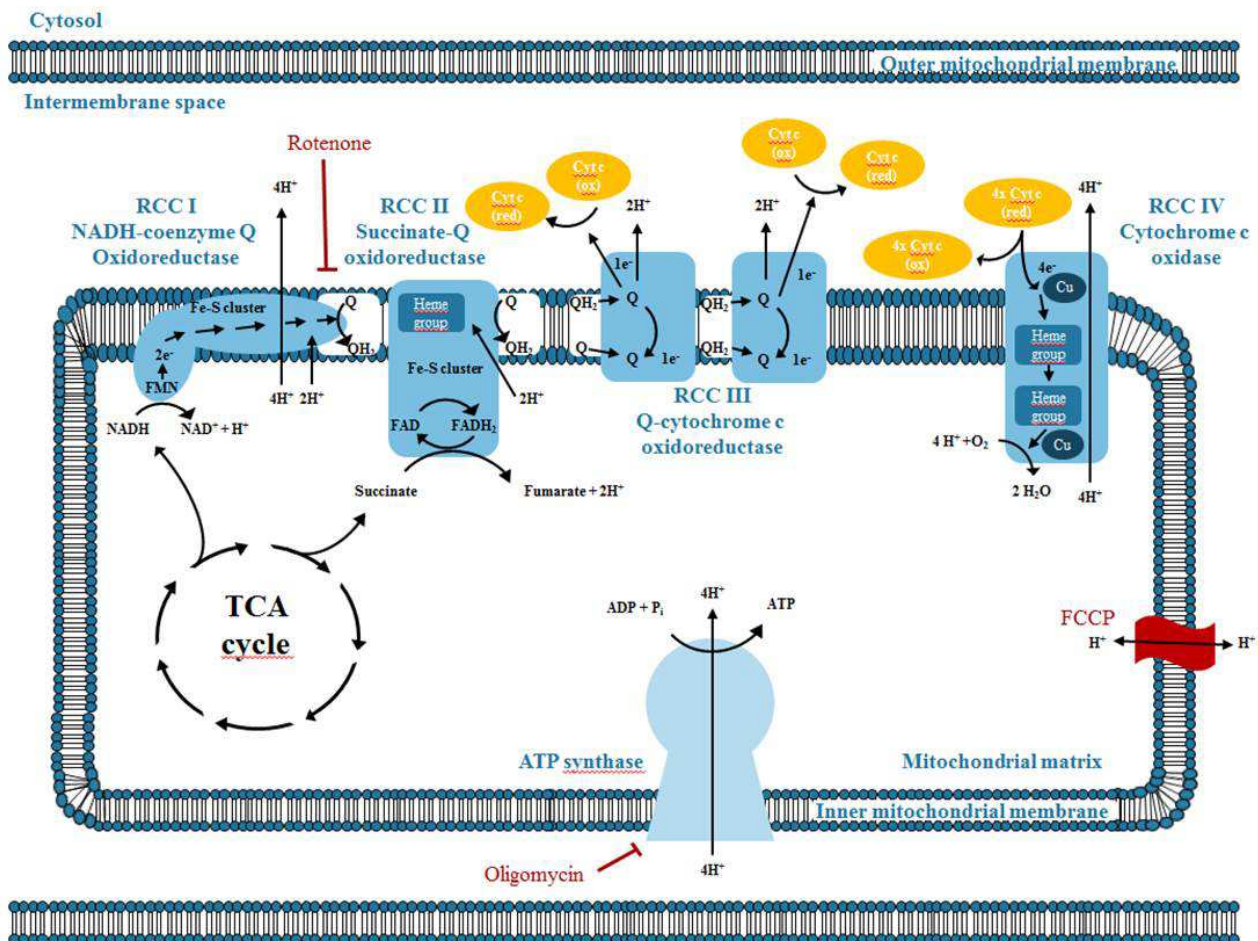


Figure 1: Mitochondria and oxidative phosphorylation: the electron transport chain. Simplified presentation about the electron transport and the ATP gradient at the inner mitochondrial membrane with inhibitors and an uncoupling agent used in this work depicted in red. RCC I to IV = respiratory chain complexes I to IV; Q = coenzyme Q₁₀/ubiquinone (mobile electron carrier); Cyt c = cytochrome c (mobile electron carrier); ADP/ATP = adenosine diphosphate/ triphosphate; FCCP = uncoupling ionophore (carbonylcyanide p-trifluoromethoxyphenylhydrazine); FMN = flavin mononucleotide; Cu = copper; Fe-S = iron-sulfur; TCA = tricarboxylic acid.

I. INTRODUCTION

In order to depict OXPHOS deficiencies in patient samples one can measure the biochemical activities of specific RCCs in different tissues. To evaluate the whole oxidative phosphorylation machinery and the interplay between complexes and subunits, microoxygraphy is a valuable tool. It measures energy utilization via oxygen consumption in living cells and quantifies mitochondrial respiration in a robust and multiplex mode. There are several known inhibitors of RCCs. For example, rotenone inhibits RCC I by blocking the ubiquinone-binding site and preventing the transfer of electrons from RCC I to ubiquinone. Oligomycin is known to block RCC V. Uncoupling agents such as the ionophore FCCP disrupt the proton gradient across the membrane, thereby uncoupling proton pumping from ATP synthesis. These compounds are used as the gold-standard for measuring maximal mitochondrial respiration in cellular assays (see I.1.6. and I.2.4.).

I.1.4. Mitochondriopathies

Mitochondriopathies are a genetically and phenotypically heterogeneous group of disorders that share some major clinical presentations (Mayr et al., 2015). With the onset varying between birth and early adulthood, patients typically present with a progressive course of symptoms and multi-organ involvement. The most often affected organs are those with the highest energy demand such as brain and muscles. Symptoms include neurological deterioration, mental retardation and dementia with developmental disorder, movement disorders and dystonia. In general, all of these are accompanied by a variety of other phenotypes. Despite recent advances in understanding disease mechanisms, treatment options are still limited and focus on supportive intervention (Viscomi et al., 2015). There are numerous trials currently in progress or recruiting (see clinicaltrials.gov), but statistically significant results remain scarce (Rai et al., 2015). This is primarily due to the small patient groups available and comparable within this heterogeneous group of disorders. This underlines the necessity to use animal models in this research field.

I.1.5. Gene discovery approaches

In the past, the genetic basis of Mendelian disorders was commonly revealed using linkage studies and homozygosity/autozygosity mapping. These techniques depend on high penetrance as well as large multigenerational pedigrees. Due to the limited number of recombination events within one family, investigation often ends up with a large genomic region containing many candidate genes co-segregating with the disease. In rare disorders, which are genetically and phenotypically heterogeneous, such as mitochondrial disorders, this presents a major burden. Moreover, sporadic cases due to *de novo* mutations are nearly undetectable. Currently, especially in mitochondrial research the most promising and robust method to unravel novel disease genes are whole exome sequencing (WES) and whole genome sequencing (WGS) (Wortmann et al., 2015, Stranneheim and Wedell, 2016). Massively parallel sequencing obtained through NGS of exonic regions generates a list of candidate genes. Applications of different filters such as a maximal minor allele frequency (MAF) of 0.01 to 0.001 in reference exomes and assumptions of specific

I. INTRODUCTION

inheritance models narrow this list down to ideally one candidate gene. In order to verify this candidate it needs a substantial number of patients and/or functional validation experiments. The recent advances in patient registries and recruitment, as well as in NGS technology together contribute to the continuing discoveries of novel disease genes. A publicly available online database of all known Mendelian disorders called OMIM (Online Mendelian Inheritance in Man; <http://www.ncbi.nlm.nih.gov/omim>) catalogued 4,636 disease-associated cytogenic locations or genes as at January 2016.

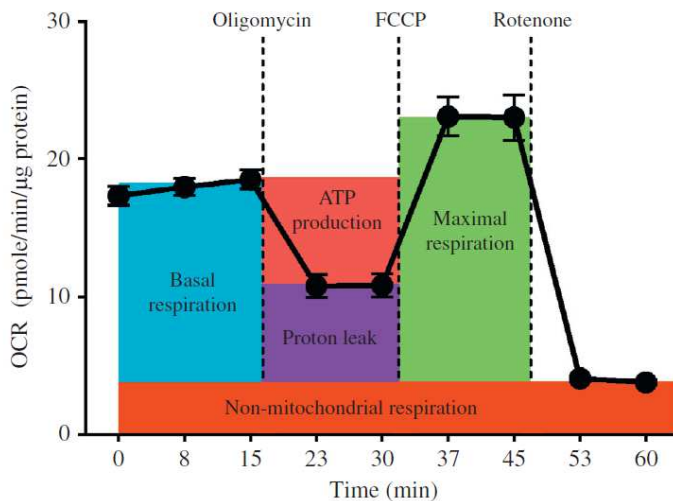


Figure 2: Exemplified mitochondrial stress experiment. (Bugge et al., 2014) Measurement of the oxygen consumption rate (OCR) upon administration of several compounds; visualized and with a detailed description on <http://www.seahorsebio.com/products/xfpconsumables/aboutcellmitostresstest.php>. Oligomycin blocks ATP synthase; FCCP permeabilizes the inner mitochondrial membrane and uncouples mitochondrial OXPHOS and rotenone inhibits RCC I interrupting the mitochondrial electron transport chain.

I.1.6. Functional validation of candidate genes

In mitochondriopathies, the gold-standard for functional validation of candidate genes are rescue experiments. Cultured fibroblast cell lines from patients' skin biopsy often present with impaired OXPHOS activity, which can be measured via oxygen consumption. In order to prove pathogenicity of a candidate gene an expression cassette of its wild-type cDNA is introduced into the patient cell line via lentiviral transduction. Subsequent rescue of deficient OXPHOS activity validates the candidate gene as the location of the disease-associated variant for the patient at hand. Microoxygraphy measures the oxygen consumption rate (OCR).

Microoxygraphy analysis of the oxygen consumption rate (OCR) is measured over time and after sequential injection of up to four different compounds through injection ports. We used three of such ports, hereafter termed Port A, B and C. A standardized procedure measures basal respiration first. Injection of oligomycin using port A to block ATP synthase activity validates functionality of mitochondrial membranes and determines proton leak. Complex I dependent maximal (= rotenone-sensitive uncoupled) OCR is analysed by injecting FCCP and rotenone via Port B and C, respectively (see figure 2). The ionophore FCCP abolishes the proton gradient across the inner mitochondrial membrane, thereby uncoupling mitochondrial oxidative phosphorylation. Rotenone interrupts mitochondrial electron transport chain by inhibiting RCC I (see figure 1). It is also possible to add antimycin A via port C or D to halt

I. INTRODUCTION

mitochondrial respiration by inhibiting RCC III. In this work, it was found that rotenone entirely inhibited mitochondrial respiration and a simultaneous or subsequent addition of antimycin A did not cause any further reduction in OCR.

In order to calculate rotenone-sensitive uncoupled OCR, mean values for non-mitochondrial respiration are subtracted from mean measurements after FCCP and before rotenone administration. This value is significantly decreased in many mitochondriopathy patients as compared to control samples and will be named maximal respiration rate from this point forward. If lentiviral expression of the wild-type candidate gene in the patient cell line rescues maximal respiration, the candidate is highly likely to be the underlying disease-associated gene. This is standard practice for functional validation of candidate genes in the field of mitochondriopathies (Gai et al., 2013, Holzerova et al., 2015, Powell et al., 2015).

I.2. RESULTS

I.2.1. Identification of *FBXL4* as a candidate gene for early-onset mitochondrial encephalopathy

The database of patients with a clinical mitochondriopathy and no genetic diagnosis at the Helmholtz Zentrum Muenchen (Institute of Human Genetics) contained roughly 110 samples in 2013. WES of these samples revealed three samples with lists of seven, eleven and 82 candidate genes harbouring two rare variants per individual. Rare variants in one gene, *FBXL4*, were present in all patient chromosomes and absent in 4,500 in-house European control chromosomes or over 8,000 alleles from the Exome Variant Server. The three paediatric individuals (subject 6, 7 and 8 in figure 3) were born to unrelated families and collected from different clinical centres. Single nucleotide variants (SNVs) identified via WES were confirmed by Sanger sequencing (supplementary figure 1), and striking resemblance in the biochemical analysis was found. All patients showed decreased activity of all RCCs as well as reduced citrate synthase (CS) levels. This very rare condition was recognized in one further patients' clinical report (subject 9 in figure 3) who was subsequently molecularly diagnosed via Sanger sequencing of *FBXL4*. All subjects share several phenotypes including decreased birth weight, developmental delay, distinct dysmorphic features, lactic acidemia, white matter lesions, hypotonia, seizures and swallowing dysfunction. Three other groups simultaneously identified *FBXL4* as a candidate gene in one single kindred each. Since *FBXL4* has not been annotated as a mitochondrial protein before, single affected families were equivocal proof for this new disease-associated gene. Hence, in collaboration four groups identified *FBXL4* as the causal gene for nine patients with early-onset mitochondrial encephalomyopathy (Gai et al., 2013) from seven unrelated disease families (figure 3).

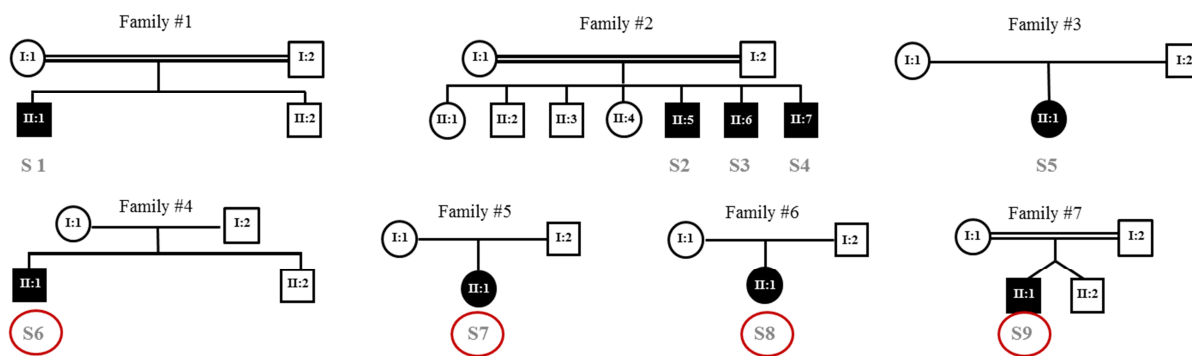


Figure 3: Pedigrees of paediatric individuals carrying mutations in *FBXL4*. Black symbols represent affected individuals; subject numbers are given in bold grey; red circled subjects were analysed in this thesis at the Institute of Human Genetics of the Helmholtz Zentrum Muenchen (figure was adapted from Gai et al., 2013).

I.2.2. Molecular genetic analysis of *FBXL4*

FBXL4 is located on the long arm of chromosome 6 on 6q16.1-6q16.3, and encodes the F-box and leucine-rich repeat protein 4. Its putative functional domains are one F-Box and nine leucine-rich repeat domains. After initial identification of *FBXL4* as a novel disease gene (Bonnen et al., 2013, Gai et al., 2013), a total of 28 individuals have been diagnosed as at January 2015 (Huemer et al., 2015). All together 23 known variants are spread across the gene, but affect mainly the N-terminus or one of the leucine-rich repeat domains (see figure 4A). All affect highly conserved regions (see figure 4B) and are predicted to be pathogenic by the prediction software Mutation Taster (Schwarz et al., 2010). There were no significant differences in the clinical presentation between patients with biallelic missense or loss-of-function mutations. No genotype-phenotype correlations within this group of patients were found.

Taken together these results confirm *FBXL4* as the underlying disease gene.

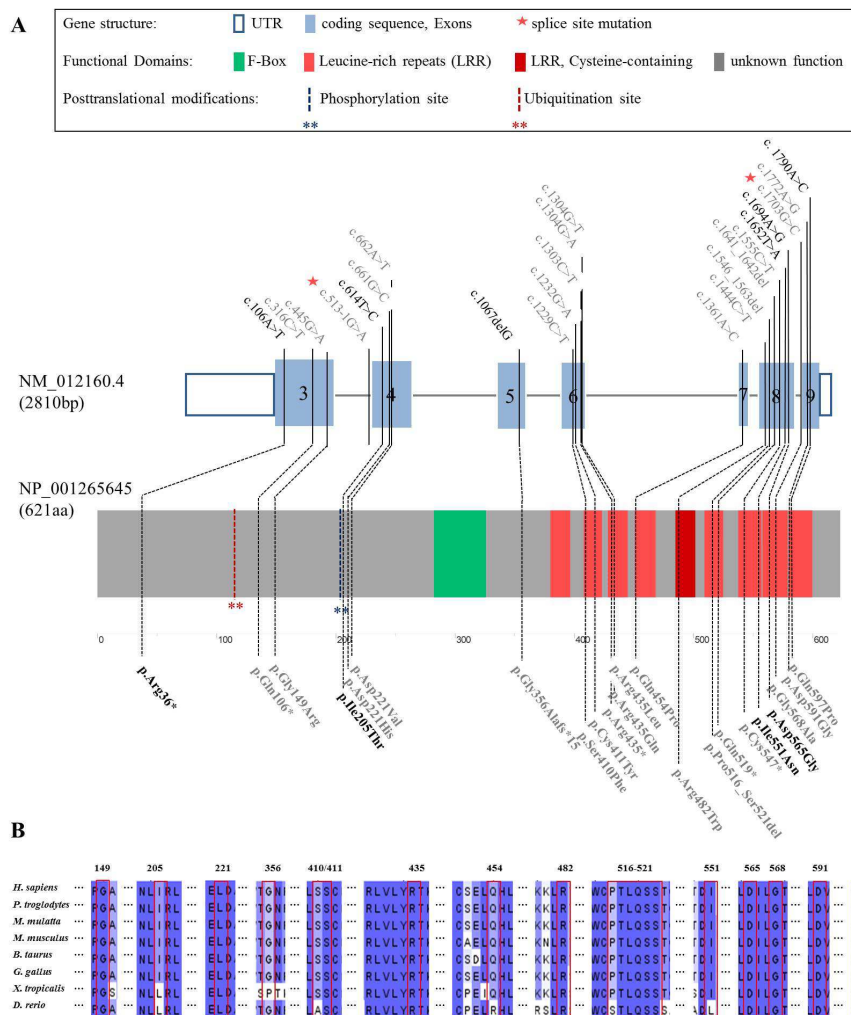


Figure 4: *FBXL4* mutation status and gene structure. (Huemer et al., 2015) **A)** *FBXL4* gene structure with mutations of 28 known cases. Putative functional domains are coloured in green and red, regions of unknown function in grey. Red and blue asterisks indicate post-translational modification sites. Mutations depicted in black bold are from patients analysed at the Institute of Human Genetics of the Helmholtz Zentrum Muenchen. NM_012160.4 describes the gene sequence used and NP_001265645 the respective protein sequence. **B)** Conservation of amino acid residues affected by mutations. Human (*H. sapiens*), chimpanzee (*P. troglodytes*), rhesus monkey (*M. mulatta*), mouse (*M. musculus*), cattle (*B. taurus*), chicken (*G. gallus*), frog (*X. tropicalis*), zebrafish (*D. rerio*).

I.2.3. Clinical and biochemical features

In collaboration, the clinical presentation of 21 patients with *FBXL4*-associated early-onset mitochondrial encephalomyopathy was summarized (Huemer et al., 2015). Biochemical analysis of three patient fibroblast cell lines showed reduced maximal respiration, which was restored after lentiviral transduction of wild-type *FBXL4*.

The disease is also known as mitochondrial DNA depletion syndrome 13, the encephalomyopathic type (OMIM #615471). Surprisingly, according to laboratory standards at the Institute of Human Genetics (Technische Universitaet Muenchen) mtDNA amounts from patient muscle cells revealed no clear, but only borderline or no mtDNA depletion. The term depletion syndrome should therefore not be used for *FBXL4*-associated early-onset mitochondrial encephalopathy anymore. Patients were examined by 14 different physicians and derived from 19 families. Eleven patients were born to consanguineous parents. Ethnicity was diverse within the group, ranging from Arabian, European and Mexican, to Palestinian, Pakistani, Portuguese and African American. Being a mitochondriopathy *FBXL4*-associated early-onset mitochondrial encephalomyopathy is likely to result in phenotypic heterogeneity. Nevertheless, all patients suffered from similar disease development albeit at different ages of onset and with different additional symptoms. The age of onset varied between one day and two years (mean = 115 days) and typically presented with high urinary lactate, acidosis, acute metabolic crisis, failure to thrive (i.e. feeding problems), impaired speech, muscular hypotonia and neurodevelopmental delay with cognitive impairment. These symptoms were frequently accompanied by vomiting, growth impairment, seizures, impaired hearing, microcephaly, eye problems, cardiac- liver- or renal-disease and neutropenia (figure 5). Neutropenia was associated with a deficit in the unspecific immune system leading to recurrent infections and dysfunctional wound healing. Furthermore, 67% showed dysmorphic features such as a prominent forehead and abnormal shapes of the eyes, nose and ears. During disease progression almost all patients experienced further worsening of symptoms mainly in developmental retardation, speech-, hearing- and cognitive impairment, as well as seizure and eye problems. Only one child was described with improved symptoms by his physician. With movement disorders occurring in most patients during disease course, 14 out of 15 patients were completely unable to walk at follow-up investigation and had no functional speech or severe speech impairment. At a mean age of 37 months seven children died from multi-organ failure accompanied with a dramatic metabolic acidosis (Huemer et al., 2015). The oldest living patient reported to date is more than 13 years old and suffers from left sided spastic hemiparesis following a stroke at ten years of age (Ebrahimi-Fakhari et al., 2015). She further developed ptosis, optic nerve atrophy with severe visual impairment and hearing loss by the age of eleven years and seven months. A list of symptoms is summarized in figure 5 and more detailed in supplementary table 1.

I. RESULTS

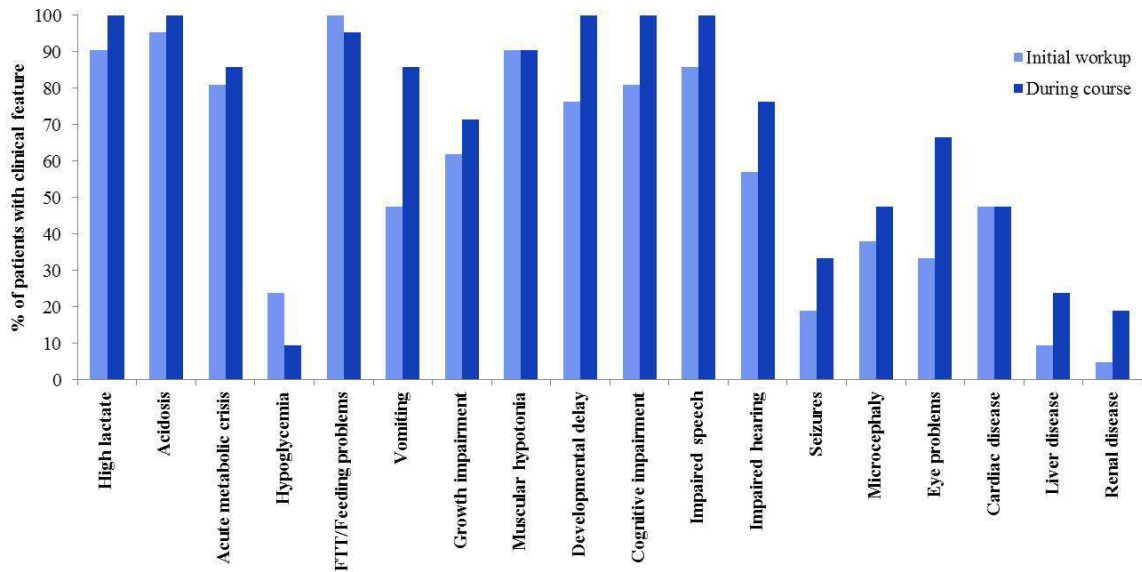


Figure 5: Summary of main clinical features of 21 FBXL4 patients at initial disease presentation and during course. (Huemer et al., 2015) The initial workup phase was generally within the first two years of life. Numbers for the analysis of features during course of disease are derived from eleven patients alive and approachable at the time of the study (ranging from two to 139 months of age with a mean of 46 months). FTT = failure to thrive.

Biochemical analysis was performed of subject 7 (Gai et al., 2013) and subjects 8 and 9 (see table 1 and figure 7) using the microoxygraph technology (Seahorse Bioscience, USA). Measurement of maximal respiration in patient fibroblasts showed significant reductions to 37% (subject 7), 45% (subject 8) and 13% (subject 9) of controls as summarized in table 1.

| Patients' fibroblasts | Max. Resp. [% of control] |
|-----------------------|---------------------------|
| S7 | 37% |
| S8 | 45% |
| S9 | 13% |

Table 1: Biochemical respiration deficiency in patients' fibroblast cell lines. Fibroblasts from subject 7, 8 and 9 were analysed as described in I.1.6. and figure 2. Max. Resp. = maximal respiration = uncoupled rotenone-sensitive respiration.

I.2.4. Validation of FBXL4 via cellular rescue experiments

In order to prove pathogenicity, functional studies are essential. As described in the methods section (see V.2.3.4.) a cellular rescue experiment was used for functional validation of the candidate gene *FBXL4*. Fibroblast cell lines derived from skin biopsies of subjects 7, 8 and 9 were cultured. They were transduced with the wild-type *FBXL4* allele via lentiviral transduction. Maximal respiration was measured via microoxygraphy on the Seahorse instrument in a multiplex manner ($n > 7$ per time point and cell line). Ports A, B and C contained oligomycin, FCCP and rotenone, respectively as shown on the example of subject 7 (figure 6). A detailed explanation was given in figures 1 and 2 (I.1.3. and I.1.6.).

I. RESULTS

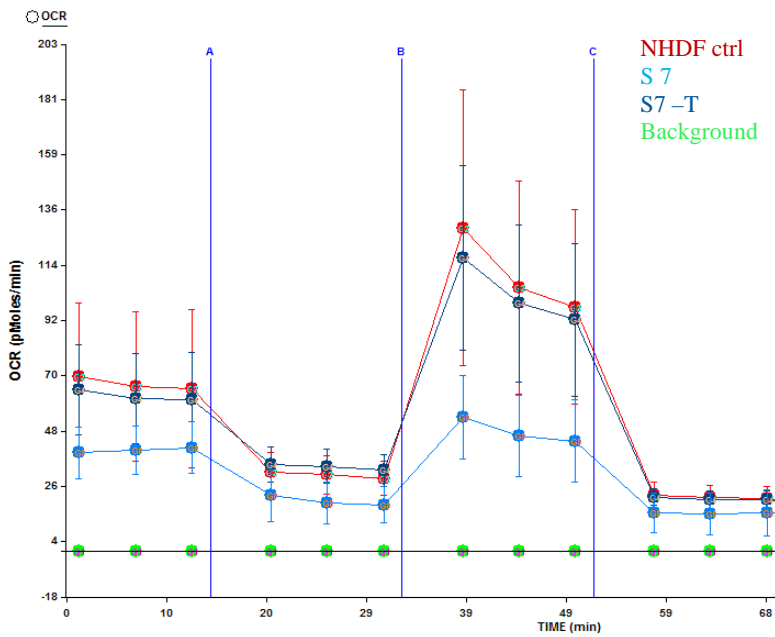


Figure 6: Oxygen consumption rate of *FBXL4* subject 7. Each data point represents the mean value of at least 8 measurements. Through ports A, B and C, the compounds oligomycin, FCCP and rotenone were added. Background correction was applied to all measurements. NHDF was the control fibroblast cell line, S7 describes the fibroblast cell line of subject 7 and S7-T the *FBXL4*wt transduced patient cell line. Three measurements were performed between additions of each port with mixing in between. Standard deviation is indicated as error bars.

With regard to basal respiration and the maximal respiration rate as explained in I.1.6., all three patient cell lines showed a reduction as compared to control cell lines measured on the same plate (see figure 7 and table 1). Each patient fibroblast cell line generated, was transduced with wild-type *FBXL4* via lentiviral transduction. Lentiviral mediated expression of the wild-type *FBXL4* cDNA resulted in significant rescue of the reduced maximal respiration in all three transduced patient cell lines (figure 6 and 7).

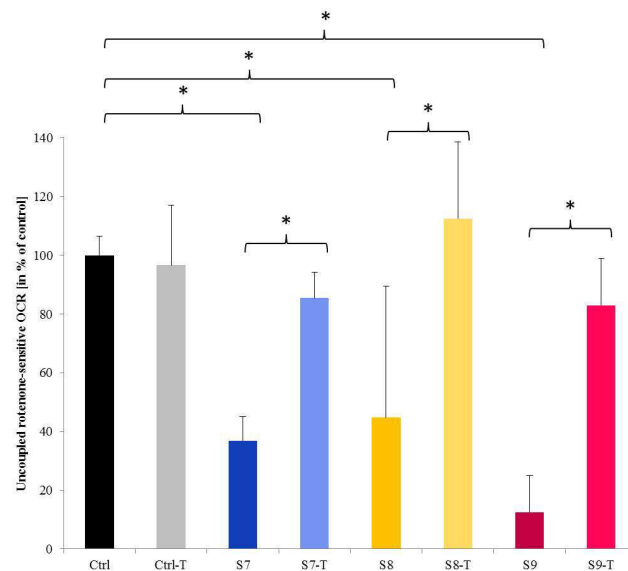


Figure 7: Maximal respiration of non-transduced and transduced *FBXL4* patient fibroblast cell lines. All patient fibroblasts show significantly reduced maximal respiration, whereas transduction with the wild-type *FBXL4* allele rescues this phenotype. Ctrl = control; -T = cell line transduced with wild-type *FBXL4* allele; S7-S9 = cell lines derived from subjects 7-9; n > 7 measurements for each cell line; * t-test $p < 0.05$. Parts of data presented in this figure have been published (Gai et al., 2013).

I. RESULTS

I.2.5. Mutations in *FBXL4* are related to a reduction of mitochondrial proteins

Immunoblot analysis of total cell lysate derived from *FBXL4* patient's (subject 7) fibroblasts and NHDF control cells was performed with two different protein concentrations for each cell line as technical replicates. Immunological detection (figure 8A) and its quantification (figure 8B) showed a clear reduction in all mitochondrial proteins analysed. All RCCs and pyruvate dehydrogenase (PDH) were analysed, as well as the mitochondrial mass through TOMM20, which is a translocase located in the outer mitochondrial membrane. The mean reduction of all mitochondrial proteins analysed was 27% (low concentration) and 28% (high concentration) as compared to NHDF control cells (see figure 8).

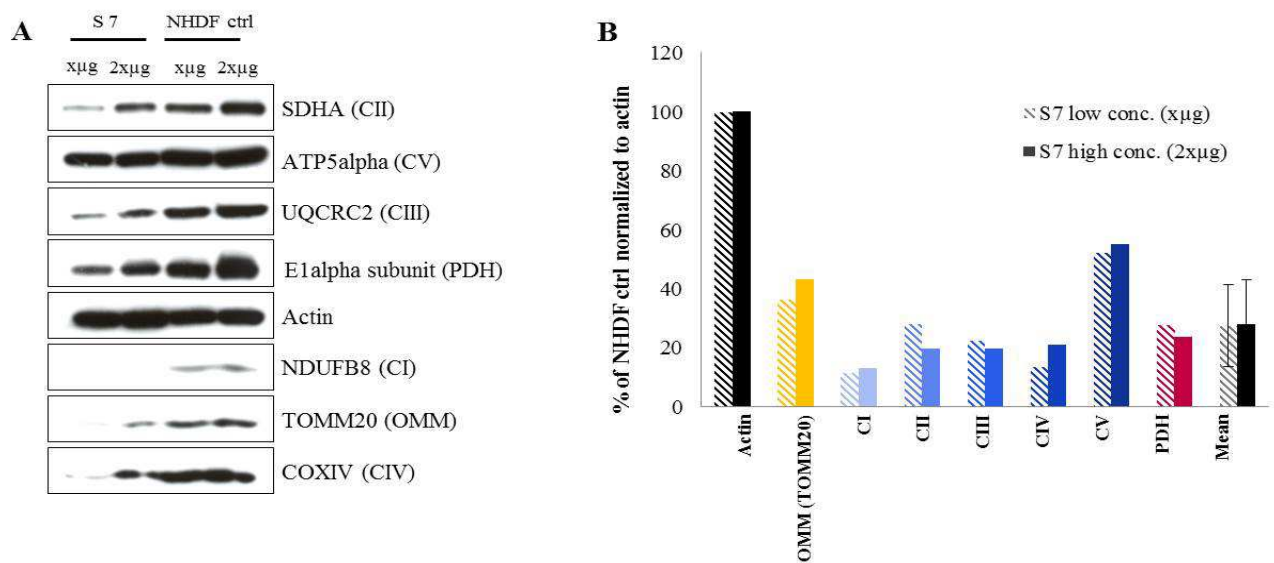


Figure 8: Immunoblot analysis of a *FBXL4* patient showed reduction of mitochondrial proteins. **A**) Immunoblotting of total cell lysate derived from subject 7's fibroblast cell line and NHDF control cells. Two different quantities were applied per cell line onto a total of 4 membranes. Quantities were varied according to the antibody used in order to stay within the dynamic range of antibody sensitivity: x[SDHA]=2; x[ATP5alpha]=5; x[E1alpha subunit]=10; x[Actin]= 2; x[UQCRC2]=15; x[NDUFB8]=10; x[TOM20]=5; x[COXIV]=15. CI-CV = RCC I-RCC V; PDH = pyruvate dehydrogenase; OMM = outer mitochondrial membrane. In brackets are the structures detected by the corresponding antibodies. **B**) Quantification of immunoblot analysis from S7 were normalised to actin and shown as percentage of NHDF ctrl for both concentrations. Ctrl = control; conc. = concentration.

I.3. DISCUSSION

I.3.1. FBXL4 dysfunction causes a clinically and biochemically distinct phenotype

This study revealed *FBXL4* missense and loss-of-function mutations in an either compound heterozygous or homozygous state in four patients. WES data was analysed and confirmed by Sanger sequencing. These results were in accordance with sequencing results obtained from available parents or healthy siblings. With *FBXL4* previously not annotated as a mitochondrial protein, acquisition of further patients was necessary. At present more than 20 patients who share several features of the clinical and biochemical spectrum of *FBXL4*-associated early-onset mitochondrial encephalomyopathy have been diagnosed (Gai et al., 2013, Huemer et al., 2015). The clinical and biochemical picture was confirmed by another research group (Bonnen et al., 2013).

All publications report frequent albeit variable abnormalities in the clinical presentation. Brain imaging showed irregularities such as brain atrophy, swollen white matter or periventricular cysts. This was recently confirmed in another neonatal case (Antoun et al., 2015). In general, the reported non-specific features such as growth retardation, microcephaly and muscular hypotonia with multi-organ involvement are common findings in mitochondriopathies. However, distinct craniofacial abnormalities with eye problems often in form of cataract and severe early-onset developmental delay are no classic mitochondriopathy features (Chinnery, 2010, Mayr et al., 2015), but seem to be associated with *FBXL4* patients. The biochemical pattern of patients with reduction of all RCCs as well as reduced CS levels is unique. This combination suggests direct sequencing of *FBXL4*. But, the retrospective design and hence, the variable age at initial and follow-up examinations impede comparability between patients. Most subjects were very young at follow-up analysis and might not yet display their complete phenotype. For example, the oldest survivor to date (over 13 years of age) has recently been reported to show stroke-like episodes (Ebrahimi-Fakhari et al., 2015). Hence, the clinical spectrum might be broader than currently known. Moreover, with more than 14 physicians writing clinical reports and referring biomaterial to a list of specialised laboratories performing non-standardised biochemical analysis, this retrospective study design carries a high risk of bias.

The following biochemical experiments confirmed *FBXL4* as the underlying disease-associated gene. Expression of the wild-type *FBXL4* allele in three patient fibroblast cell lines rescued OXPHOS deficiency, i.e. maximal respiration rate (Gai et al., 2013). For this analysis microoxygraphy (Seahorse XF) was used, which measures the oxygen consumption rate of fibroblasts in 96well plates by adding inhibitors to each well through up to four ports sequentially. This way, several replicates can be measured at the same time. In order to reduce surrounding influences and variance between different plates, controls and samples were

always measured on the same plate. This resulted in at least seven replicates per measured cell line at each time point. Maximal respiration rates from the three patients analysed were significantly reduced as compared to same-plate-controls and were rescued in all three patients. Bonnen and colleagues successfully rescued mtDNA depletion and reduced membrane potential (Bonnen et al., 2013). OXPHOS deficiency was confirmed via RCC enzyme activities using standard spectrophotometric techniques in muscles and fibroblasts (Gai et al., 2013).

Taken together these results strongly support *FBXL4* as the underlying mitochondrial disease-associated gene for *FBXL4*-associated early-onset mitochondrial encephalomyopathy formerly known in OMIM as mtDNA depletion syndrome 13, the encephalomyopathic type.

I.3.2. FBXL4 dysfunction causes a mitochondrial disorder

There is convincing evidence for *FBXL4* carrying causal variants in the suspected patient group, but further challenging questions remain as to whether *FBXL4* is a mitochondrial protein and what its functions are.

FBXL4 is located on chromosome 6 and therefore part of the nuclear genome. Different software packages identified a mitochondrial targeting sequence at the N-terminal end but did not discover any transmembrane domain (Calvo et al., 2016). Subcellular fractionation assays in mouse liver cells, as well as from intact mitochondria isolated from digitonin-treated *FBXL4*-transfected HEK293T cells came to the same conclusion. *FBXL4* is mainly located in mitochondria, more precisely in the intermembrane space (Bonnen et al., 2013, Gai et al., 2013). With an estimated size of 70kDa, involved in a 400kDa complex shown via Blue Native Gel Electrophoresis (BNGE) (Gai et al., 2013), its exclusive localisation to the intermembrane space seems challenging concerning its large size. With its localisation detected neither in the cytosol nor the nucleus via fluorescence experiments, it is still possible that *FBXL4* attaches to the outer mitochondrial membrane. Disruption of the suggested mitochondrial targeting sequence lead to a localisation signal in mitochondria and the cytosol, however, no signal was detected in the nucleus (Gai et al., 2013). This finding is somewhat contradictory to an earlier publication (Van Rechem et al., 2011). Van Rechem and colleagues showed direct interaction between *FBXL4* and *JMJD2A*, a histone demethylase acting exclusively inside the nucleus. However, this interaction was shown using immunopurified *JMJD2A* with a lysate of *FBXL4*-overexpressing cells, and not within the cellular context. Both proteins are potentially spatially separated *in vivo*. Additionally, Van Rechem and colleagues also showed that siRNA-mediated downregulation of *FBXL4* inhibited proteasomal degradation of *JMJD2A*. F-Box proteins, being essential components of the ubiquitin-proteasome system (UPS) are generally involved in a variety of cellular processes, such as cell cycle progression and cell proliferation as previously reviewed (Uddin et al., 2015). Involved in ubiquitination, they target proteins to ubiquitination and subsequent proteasomal degradation. *FBXL* proteins are a group of F-Box proteins containing leucine-rich repeat domains generally involved in protein-protein interactions also located in the cytosol. Van Rechem and colleagues

I. DISCUSSION

did not show direct interaction of FBXL4 with JMJD2A, but suggest FBXL4-involvement in the proteasomal degradation of JMJD2A. The underlying mechanism for indirect participation or the functional cascade is still unclear. Since results from Gai and colleagues, in line with Bonnen and colleagues, suggest a mainly mitochondrial localisation, and the experiments from Van Rechem do not directly contradict this, FBXL4 is suggested as a mitochondrial protein with potentially diverse localization.

Further evidence of FBXL4 being a mitochondrial protein is its association to global mitochondrial dysfunction. Fewer in number and dysmorphic mitochondria were detected in patient samples, via cell staining with a commonly used mitochondrial marker, TOMM20 (Antoun et al., 2015), as well as altered mitochondrial network and nucleoid morphology via Mitotracker Red and PicoGreen staining (Bonnen et al., 2013).

Mitochondrial membrane potential was clearly reduced in mutant cell lines (Antoun et al., 2015, Bonnen et al., 2013, Gai et al., 2013). In general, reduced membrane potential has previously been shown to stabilize serine/threonine-protein kinase PINK1, which in turn activates the E3 ligase parkin (Narendra et al., 2010). Parkin is a component of the UPS. Furthermore parkin promotes disposal of mitochondria (Narendra et al., 2008). This macro-autophagic process is called mitophagy. Hence, FBXL4 deficiency could potentially lead to an induction of mitophagy.

Decreased OXPHOS-related ATP production was identified together with a reduction of patients' fibroblasts viability upon obligate respiration on galactose (Bonnen et al., 2013). Under glucose availability patient fibroblasts showed OXPHOS deficiency via reduced maximal respiration. This was confirmed by others via reduced activities of all RCCs in nearly all available muscle and fibroblast patient cells (Gai et al., 2013). Since all RCCs, including the only nuclear encoded one, RCC II, showed reduced activities, this suggests a reduced number of mitochondria or of mitochondrial mass. In case of mtDNA depletion, one would expect RCC II to show normal activity in biochemical measurements. In fact, Bonnen and colleagues detected normal RCC II activity in three patients' fibroblast cells, but a reduction in their muscle cells. This finding is somewhat contradictory to all other patients' biochemical data showing a reduction in all RCCs.

Two groups independently published significant mtDNA depletion in all analysed patient derived fibroblasts and muscle cells (Bonnen et al., 2013, Gai et al., 2013), but the extent of depletion is questionable. In the laboratory setting of the Institute of Human Genetics (Technische Universitaet Muenchen), mtDNA depletion is diagnosed at less than 15% mtDNA as compared to healthy controls. FBXL4 patients show levels of 15-30%, which is classified as borderline mtDNA depletion and can occasionally be found in healthy controls. This thesis shows a reduction in TOMM20, a translocase in the outer mitochondrial membrane, as well as in all other mitochondrial proteins analysed (n=6), to roughly 30% in patient fibroblasts. The similar extent of reduction in mtDNA and mitochondrial proteins supports

the theory of a reduced number of mitochondria. This reduction could be due to deficient mitochondrial biogenesis or impaired autophagy or mitophagy.

Analysis of patients' enzymatic data found remarkably reduced CS in all available patient muscle cells and fibroblasts. Being a nuclear encoded mitochondrial matrix protein, CS is expected to be associated with a decrease in mitochondrial mass. With TOMM20 and CS reduced in *FBXL4* patient samples, *FBXL4* deficiency likely results in a reduction of mitochondria.

In many laboratories RCCs activity is normalised to CS for diagnosis. In the case of *FBXL4* patients, this may lead to a false negative result, as CS levels are also decreased and might lead to normal values after normalisation. It is suggested to analyse total CS levels before normalising RCC measurements.

In summary, *FBXL4* has repeatedly been shown to be localised to mitochondria, however, the entire localisation pattern still contains contradictions. The protein appears to play a central role in energy metabolism due to its severe pleiotropic effects on mitochondrial function (figure 9). *FBXL4* is supposedly involved in mtDNA maintenance, mitochondrial homeostasis and possibly mitophagy. However, the exact mechanism remains unclear.

I.3.3. Outlook: Relevance for diagnosis and protein function

The discovery of the disease-associated gene and the detailed clinical and biochemical description of the *FBXL4*-associated early-onset mitochondrial encephalomyopathy contributed to the diagnosis of this disorder. There is no treatment known to date that improves or halts symptoms and disease progression. Typical substances such as riboflavin, biotin, thiamine, pyridoxine, coenzyme Q and carnitine have been tried in a severely affected patient, but showed no signs of improvement (Antoun et al., 2015). In general, early diagnosis saves patients and their families from unnecessary sometimes painful treatments without any benefit for their quality of life. *FBXL4* is a rare disease-associated gene of increasing relevance, with at least 20 patients diagnosed since 2013. *FBXL4* should be analysed upon identification of mitochondrial dysfunction accompanied with reduced CS levels. Children showing these symptoms in combination with others such as early-onset muscular hypotonia, failure to thrive, facial abnormalities and developmental delay in combination with mtDNA depletion and reduced RCC II activity should immediately be tested for *FBXL4* mutations. WES is the preferred method, but in case no WES facility is available panel-diagnostics are routinely applied. With roughly 30 patients known to be diagnosed since the first publication in 2013, *FBXL4* can be considered a suitable gene to be put onto the list of genes detected on a Mito-NGS diagnostic panel. In collaboration, the Institute of Human Genetics from the Technische Universität München (Dr. Prokisch) and the Center for Genomics and Transcriptomics CeGaT (Tübingen, Germany) developed a Mito Panel, currently composed of 37 mitochondrial encoded and 265 nuclear encoded proteins (by January 2016). This list should be extended by *FBXL4* in the near future.

I. DISCUSSION

The biochemical experiments performed in this work contribute to the knowledge of FBXL4s' function. The identified reductions of maximal respiration in patient fibroblasts, as well as the reduction in mitochondrial RCCs and mitochondrial mass add to the suggested role in mitochondrial maintenance and mitophagy. The role of FBXL4 in mitophagy and its functional relevance for ubiquitin-related proteasomal degradation as depicted in figure 9 remain to be investigated. It is unclear whether global respiratory dysfunction is mainly due to a reduction in mitochondrial mass or respiration deficiency of mitochondria. Both hypotheses are schematically summarized in figure 9.

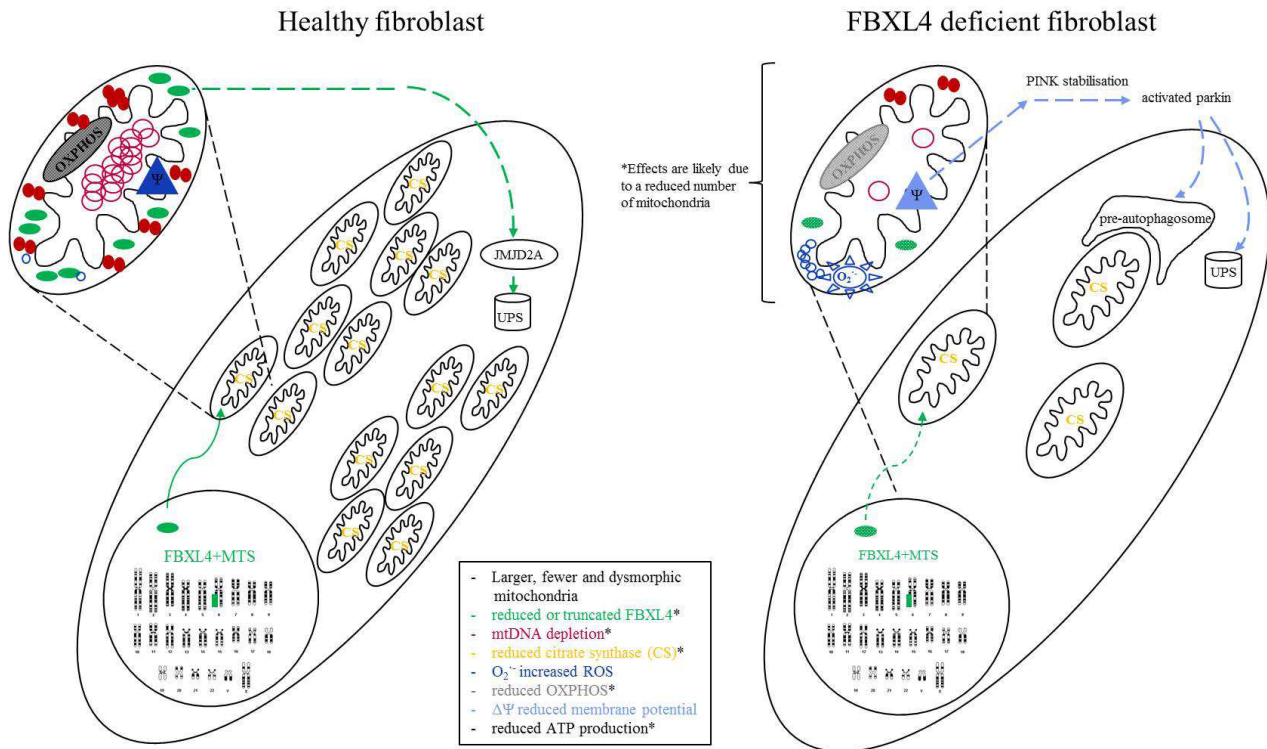


Figure 9: Schematic comparison of a healthy versus FBXL4-deficient fibroblast. The figure shows experimental results schematically presented in the figure legend. MTS = mitochondrial target sequence; $\Delta\Psi$ = membrane potential; ROS = reactive oxygen species; O₂⁻ superoxide radical anion; CS = citrate synthase; UPS = ubiquitin-proteasome system; ATP = adenosine triphosphate.

Elucidation of FBXL4s' function constitutes a step towards disease treatment. A few treatment approaches seem promising such as inhibition of autophagy (or mitophagy) or mitochondrial biogenesis induction (e.g. via fibrates). In combination with the obtained functional data on FBXL4, these treatments seem promising and should be tested on the available patient cell lines. In order to properly investigate treatment efficiency, controlled preclinical studies are needed. Due to the small patient numbers in mitochondrialopathies, as well as unknown side effects of some treatment approaches, the establishment of mouse models is important. This will be addressed in the second part of this thesis.

II. Generation of a mouse model (*Wdr45* KO) resembling the human disease BPAN

II.1. INTRODUCTION

II.1.1. Generation of a knockout mouse model

II.1.1.1. The use of mouse models and genetic engineering

As one of the most popular model organisms the mouse remains of great use to a variety of research fields. It often is the first choice model species for modelling human diseases and for subsequent development and validation of treatment strategies. However, criticism on the use of laboratory animals is still present for various ethical and practical reasons. The public is asking for replacement, reduction and refinement via strict laboratory animal regulations, which were further tightened in August 2013. Even though complete replacement is still out of reach, there are ways to inform more focused animal experiments to reduce animal numbers by using cell culture and tissue experiments. On the other hand, refinement can be achieved by several approaches one of them being more efficient genetic engineering.

Recently, in terms of reducing numbers of laboratory animals there is significant enthusiasm about miniature organs-on-a-chip. They provide a surplus for high-throughput drug screening and investigation of toxic reactions and drug efficacy. The technology of the Dutch company Mimetas (Reardon, 2015) enables the 3D-culturing of tissue cells to form different organs-on-a-chip. Currently, several companies are developing chips with single organ-like structures resembling liver (Ebrahimkhani et al., 2014) and bone-marrow (Kim et al., 2015). Consideration has been paid to the idea of a body-on-a-chip. However, this will most probably never capture the complexity of organ function and especially the complex interplay between different organs in an entire organism. Such discoveries can complement animal studies, and they have the potential to decrease the number of laboratory animals, but they will most likely never replace it completely.

A method of mimicking genetic disorders used since decades is the generation of genetically engineered mouse lines. The history of genetic engineering shows rapid advances with dramatic increases in specificity and efficacy reducing not only excess animal numbers, but also time and cost. Even before the completion of the human genome project in 2003, numerous leading scientists emphasized the need for mutant model organisms to elucidate the function of genes (Hrabe de Angelis and Balling, 1998). They developed a systematic approach to generating mutant mice via ethylnitrosourea (ENU), which as a strong mutagen introduces random point mutations in spermatogonial stem cells (Hrabe de Angelis et al., 2000). Another widely used method is gene trapping. This lead to numerous mouse models (Becker et al., 2014,

II. INTRODUCTION

Nechiporuk et al., 2016) and can be used to generate conditional loss-of-function alleles (Floss and Schnutgen, 2008). A systematic approach to introducing mutations across the genome in mouse embryonic stem cells via gene trapping resulted in the International Gene Trap Consortium (IGTC) with a database of 120,814 cell lines as at February 2016. A different approach to generate mutant cell lines was to introduce double-strand breaks into the target DNA. First attempts were based on a zinc-finger DNA-binding domain fused to a DNA-cleavage domain building the zinc-finger nuclease (ZFN) (Bibikova et al., 2001, Bibikova et al., 2003, Porteus and Carroll, 2005). Lacking efficiency and rewarding advances ZFNs were largely replaced by transcription activator-like effector nucleases (TALENs) (Boch et al., 2009, Moscou and Bogdanove, 2009), which revolutionized the field of genetic engineering until recently. This technique was used to generate the two knockout mouse lines established within this work and will be described in the following section. Very recently an even more efficient and easy-to-use approach has largely replaced the use of TALENs. The current method of choice is called CRISPR/Cas9 and will be described in II.1.1.3. It has reached global media at exceptional speed demonstrating once again its scientific and revolutionary potential.

II.1.1.2. TALEN

Targeted genetic engineering using TALENs is based on the discovery of transcription activator-like effector proteins (TALEs), which were found in the bacterial plant pathogen *Xanthomonas* (Boch et al., 2009, Moscou and Bogdanove, 2009). These proteins form loops of repetitive sequence with a repeat variable domain (RVD), where two amino acid residues at position 12 and 13 recognize a specific nucleotide in the DNA (see figure 10, supplementary figure 2 and V.2.1.12 for detailed procedure). The only limitation to the targeted sequence is that it has to start with a thymine residue. The combination of the following loops can be designed to target the desired DNA sequence specifically, which should be around 15 bp in length (Christian et al., 2010, Zhang et al., 2011). If attached to a FokI nuclease, TALENs function in dimers to introduce a double-strand break into the DNA. For proper DNA cutting, both TALENs need to target the DNA in close proximity, which is achieved by a spacer of 15 bp as shown in figure 10. The fact that TALENs are only functional in the dimeric state further increases specificity. The double-strand break is repaired via non-homologous end joining (NHEJ) leading to the loss of a variable number of nucleotides. This often generates a frameshift mutation resulting in a loss-of-function allele. If a targeting vector is present, a specific sequence can be inserted at the target site via homologous recombination (HR). For the purpose of generating a knockout mouse line as in this work, NHEJ was sufficient, and there was no need for a targeting vector.

II. INTRODUCTION

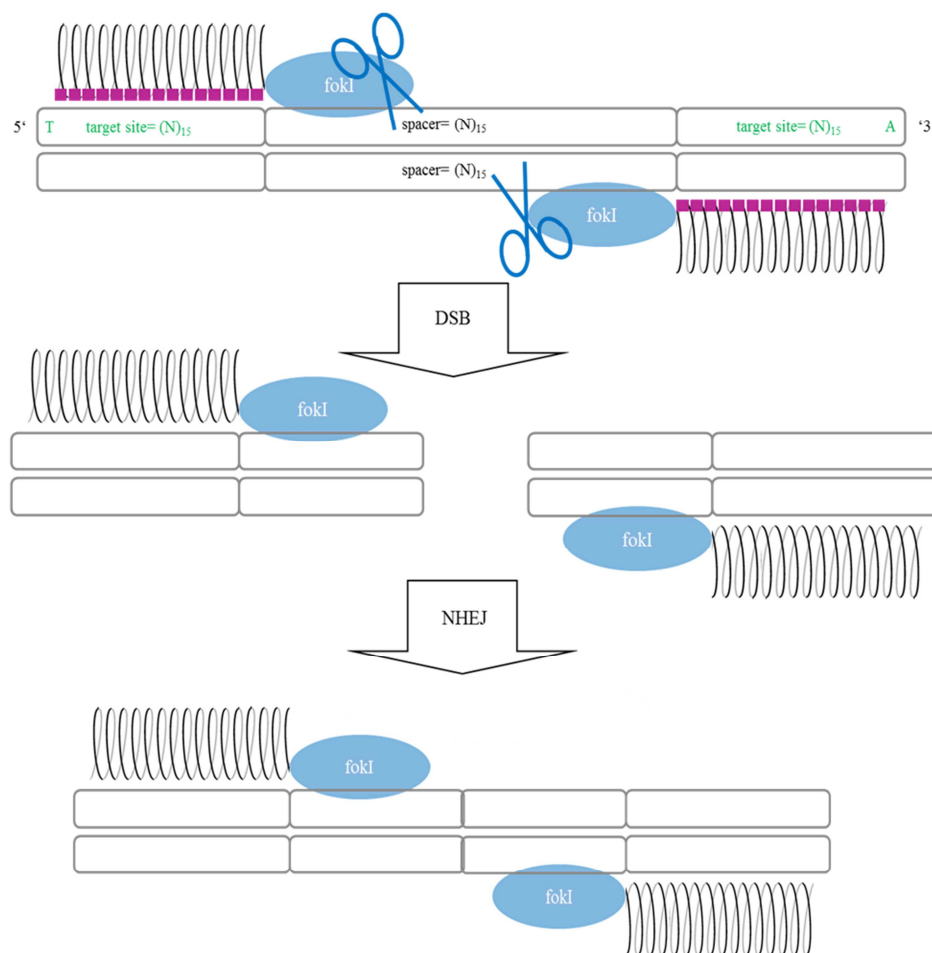


Figure 10: Schematic of TALEN genome editing. 5' denotes the 5-prime-end of the target DNA-sequences starting with a T (thymine). Two TALENs with a FokI domain (FokI nuclease) each act in defined proximity due to a 15bp spacer to induce a double-strand break (DSB). Due to non-homologous end-joining (NHEJ) small deletions or insertions are edited in the genome.

It is well-established to generate mutant mouse lines by embryo microinjection of TALENs (Panda et al., 2013, Wefers et al., 2013a, Wefers et al., 2013b, Wefers et al., 2014). Panda and colleagues optimized the TALEN system to an efficiency of more than 40% mutant offspring. Overall, for the generation of knockout mouse lines, TALEN is still a useful tool that can be readily established. Ordering this kind of repetitive custom designed sequences is costly with up to \$ 1,000 per TALEN-pair. The alternative of cloning the sequences yourself is time consuming. In summary, two huge proteins are needed for each new target implying a major burden in terms of applicability. This was largely improved by the most recent discovery in the field of genome editing, CRISPR/Cas9.

II.1.1.3. CRISPR/Cas9

The clustered regularly interspaced short palindromic repeats (CRISPR) system with CRISPR-associated protein 9 (Cas9) for genetic engineering, has recently gained public interest. It has been reported about in the worldwide press including the *Economist* (Aug. 2015) and the *New York Times* (Nov. 2015). It was initially discovered as an obscure microbial repeat sequence and later identified as a microbial immune system. Microbes use CRISPR/Cas9 as a defence system against viruses. They insert DNA fragments of invading viruses into their CRISPR array, in order to instruct a nuclease (Cas9 nuclease) to target that specific viral DNA (figure 11). Insertion of almost any specific DNA region of interest into the CRISPR

II. INTRODUCTION

array leads to the nuclease targeting that specific sequence. This enables targeted mutation at the desired site in the genome. This genetic editing tool is widely used nowadays, but its discovery took approximately 20 years. It required extensive efforts from numerous institutes throughout the world. Eric Lander described the development of CRISPR/Cas9 and highlighted the importance of pioneer studies in his review (Lander, 2016). The last and essential steps to use CRISPR/Cas9 for genetic engineering were published by Emmanuelle Charpentier and Jennifer Doudna and their colleagues (Jinek et al., 2012).

There are different CRISPR systems with slightly different operating modes. The system described here is type II, which is the system of choice for genome editing. As visualized in figure 11 (Lander, 2016) the system contains a CRISPR array, which contains the sequences the system is programmed to target (coloured rectangles). In nature these sequences are of viral origin as they contain sequences of invading viruses, which the microbe aims to destroy. A complex interplay with the so called tracrRNA and RNase III leads to the generation of single-guide RNA (sgRNA) and recruitment of Cas9 with subsequent nuclease activity at the target site. For targeted genome editing, for example in a mouse zygote to generate a knock-out mouse, sgRNA can be generated directly via molecular cloning. It recruits the Cas9 nuclease and guides it to the target site, where it cuts the double strand DNA to form blunt ends. As described before, these are generally repaired via NHEJ and normally leave a small deletion behind. Hence, the generation of a targeted knock-out mouse line requires the administration of Cas9 and a specifically designed sgRNA. In order to generate KO mouse lines the CRISPR/Cas9 system can be microinjected into zygotes the same way as TALENs.

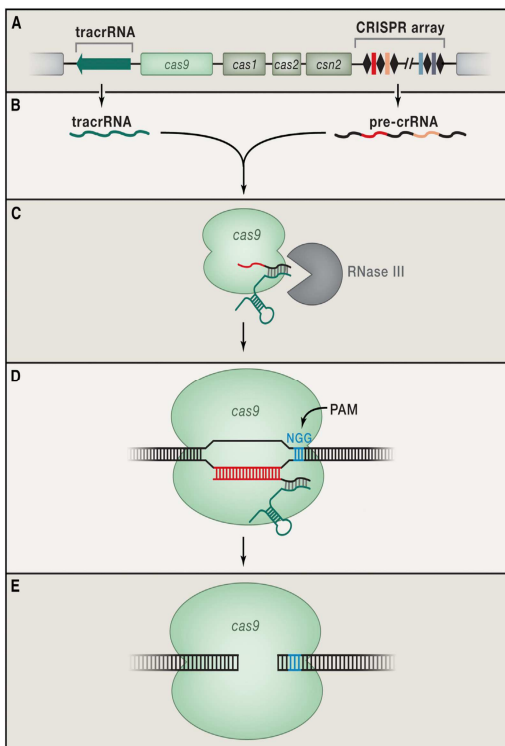


Figure 11: Schematic of CRISPR/Cas9 genome editing. (Lander, 2016)

The type II system from *Streptococcus thermophilus* is the basis for genome editing. **A)** The system contains tracrRNA, four protein coding genes (*cas9*, *cas1*, *cas2* and *csn2*) and a CRISPR array. The latter is composed of repeat regions (black diamonds), which are separated by spacer regions (coloured rectangles) derived from the DNA of invading infectious pathogens. Trans-activating CRISPR RNA (tracrRNA) is complementary to the repeat regions. The *cas9* gene encodes the nuclease, which cuts double-strand DNA that matches the sequence of spacer regions. *Cas1*, *cas2* and *csn2* are necessary for the acquisition of new spacers acting as an immune response. **B)** TracrRNA and CRISPR array are transcribed into tracrRNA and pre-crRNA. **C)** Via the complementary regions within tracrRNA and repeat regions of pre-crRNA the two strands hybridise and are processed by RNase III to form single-guide RNA (sgRNA), which is approached by Cas9. **D)** A complex between sgRNA and Cas9 binds to a DNA sequence, complementary to the spacer region. For proper binding, the protospacer adjacent motif (PAM) is needed (NGG). **E)** Upon proper binding DNA is cleaved three nucleotides upstream of the PAM site to form blunt ends.

II. INTRODUCTION

A huge advantage of the CRISPR/Cas9 system is that it is RNA-guided. This results in a substantially smaller protein complex than it is the case for TALENs. It is cheaper and easier to generate the sgRNA needed to guide the Cas9 nuclease. sgRNAs can easily be exchanged to target different DNA loci. It is also possible to use sgRNA libraries within one system in a high-throughput screen as reviewed by Peng and colleagues (Peng et al., 2015).

The applicability of the CRISPR system reaches beyond research centres. CRISPR has a high potential for the use in therapy such as infectious disease caused by various viruses (for example, human immunodeficiency virus, hepatitis B virus, human papillomavirus and Epstein-Barr virus) and related cancer development or via gene therapy for monogenic disorders as reviewed by Saayman and colleagues (Saayman et al., 2015). Overall, it is likely that the potential of CRISPR is not yet fully exploited. However, studies aiming for human therapy have to be tested in laboratory animals like mice beforehand for safety reasons. There is still the risk for off-target effects due to limitations in the systems specificity. On the other hand, many diseases are caused by germline mutations and involve several organs, clarifying the need for studies on an organismal level. In order to be able to investigate a specific disease in several organs or to reveal potential phenotype rescue through a specific therapy or its side effects, the generated animal model has to be characterized extensively as described in the following.

II.1.1.4. The German Mouse Clinic and the establishment of a mouse model

The German Mouse Clinic (GMC) located at the Helmholtz Zentrum Muenchen was founded in 2001 as an institution to comprehensively phenotype mouse models for human diseases. In the framework of the Nationales Genomforschungsnetz (NGFN) the GMC was established with the aim of mutant mouse phenotyping in a standardised and systematic manner. By looking at the whole organism instead of cells or tissues, multi-system disorders can be analysed, as well as treatment options validated and potential side effects evaluated. The GMC is split into several screening areas according to medical disciplines. A classic screen involves behaviour, bone and cartilage development, neurology, clinical chemistry, eye development, immunology, allergy, steroid metabolism, energy metabolism, lung function, vision and pain perception, molecular phenotyping, cardiovascular analyses and pathology (Fuchs et al., 2012). This screen takes approximately five months and results in more than 550 parameters. Each screen is analysed by scientists who specialise in the corresponding field in order to evaluate the significance of each finding. Experiences of more than 300 mouse lines analysed by February 2016 are supplied in GMCs phenomap, publicly available online (<http://tools.mouseclinic.de/phenomap/jsp/annotation/public/phenomap.jsf>). The GMC also aims to investigate environmental influences such as nutrition, exercise, infections, stress and air composition. Currently, the speed by which new mouse lines are generated necessitates proper characterization of the new lines, clarifying the GMCs contribution to medical research.

II.1.2. The human disease BPAN and the corresponding *Wdr45* knockout

II.1.2.1. Neurodegeneration with brain iron accumulation (NBIA)

Neurodegeneration with brain iron accumulation (NBIA) was first described in 1922 by Julius Hallervorden and Hugo Spatz. It was formerly described as a rare disorder of progressive extrapyramidal dysfunction and dementia. Today, NBIA is diagnosed mainly by its most prominent feature iron deposition in the basal ganglia often occurring in combination with progressive movement disorder. The prevalence is 1-3 in 1,000,000, and there are ten disease-causing genes identified to date each responsible for a specific subtype of NBIA as described in figure 12.

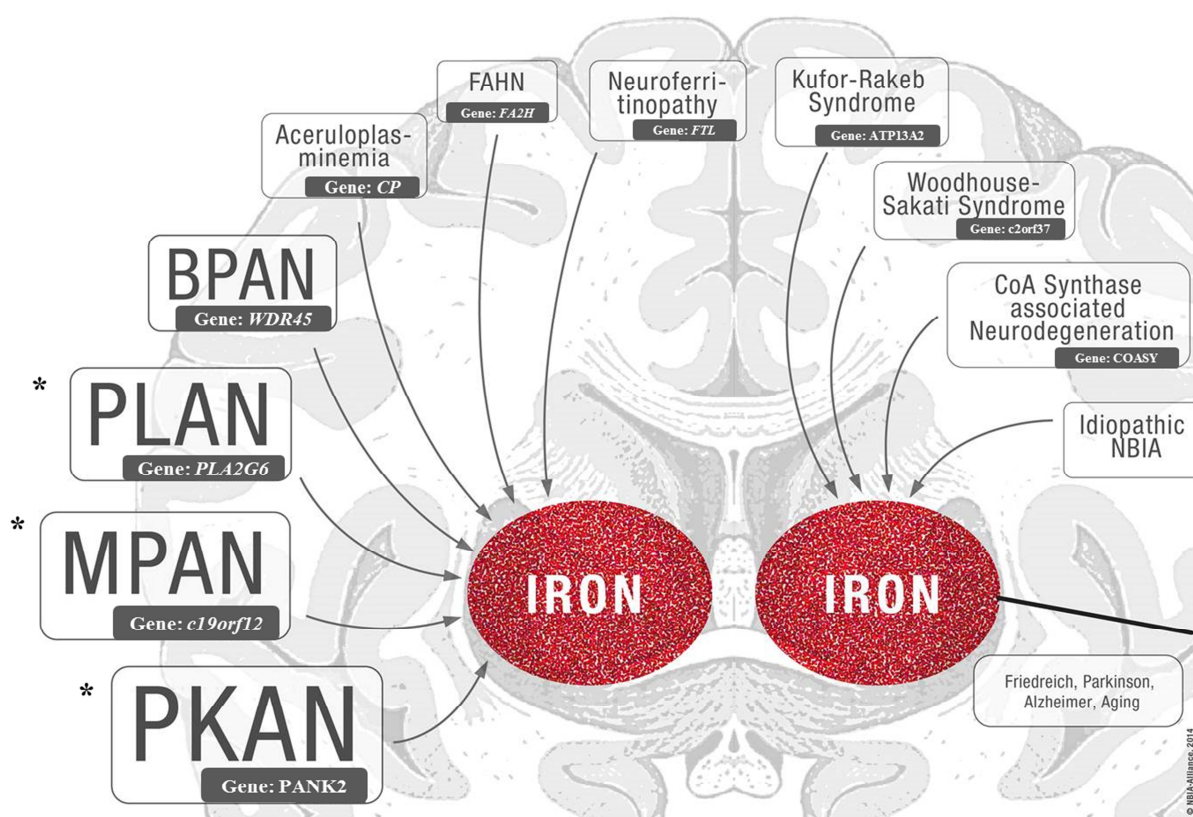


Figure 12: Subgroups of NBIA. (Figure was adapted from and kindly provided by the seventh framework EU-project, TIRCON). Disease abbreviations are depicted in large boxes and their underlying disease-associated gene is named in small grey boxes underneath; *indicates mitochondrial pathologies. Friedreich’s ataxia, Parkinson’s disease, Alzheimer’s disease and Aging also lead to increased iron in the brain. PKAN = Pantothenate kinase-associated neurodegeneration; MPAN = Mitochondrial-membrane protein-associated neurodegeneration; PLAN = PLA2G6-associated neurodegeneration; BPAN = Beta-propeller protein-associated neurodegeneration; FAHN = Fatty acid hydroxylase-associated neurodegeneration.

The disease-genes mentioned in figure 12 are often associated with typical accompanying features such as “eye of the tiger” in T2-weighted imaging (in pantothenate kinase-associated neurodegeneration and

II. INTRODUCTION

mitochondrial-membrane protein-associated neurodegeneration) or diabetes and iron accumulation in the liver (in late onset aceruloplasminemia). At least three subgroups of NBIA are mitochondriopathies (as indicated by asterisks in figure 12). Detailed clinical characterisation of genetically diagnosed patients guides diagnostic testing for idiopathic patients (Kruer and Boddaert, 2012). Approximately 30% of NBIA cases are currently idiopathic with no genetic diagnosis. It is likely that further disease-causing genes will be identified. Despite rapid advances in genetic research in this field, treatment options are currently aimed at palliation of symptoms only. There is no curative treatment available. However, single cases treated with the iron chelator deferiprone have been reported with clinical improvement and reduced iron content in the brain (Cossu et al., 2014, Kwiatkowski et al., 2012). Randomised, controlled and sufficiently powered studies are needed to confirm this finding. Low prevalence and low patient numbers imply the necessity to build a platform for future investigations in the form of a patient registry and biobank. In 2012 an international consortium started the TIRCON (treat iron-related childhood-onset neurodegeneration) project, which was supported by the European commission's seventh framework programme. It currently conducts a randomised, placebo controlled and double-blind deferiprone study with PKAN patients based on promising case reports (Kalman et al., 2012). Since curative treatment is missing and controlled studies in this field of research are rare, animal studies are another way to push forward on the way to successful treatment. A PKAN mouse model was already established showing growth reduction, retinal degeneration and male infertility (Kuo et al., 2005) as well as mitochondrial dysfunction (Brunetti et al., 2012). Only when stressed via ketogenic diet did it show neurological and motor impairment (Brunetti et al., 2014). The mouse model for PLAN also partly recapitulates the neurologic deterioration (Sumi-Akamaru et al., 2015). For most other NBIA subtypes there was no suitable mouse model established since the discovery of *WDR45* mutations as disease-associated (Haack et al., 2012). Also, due to an increasing number of patients diagnosed with beta-propeller protein-associated neurodegeneration (BPAN) especially in the Japanese population (Nishioka et al., 2015), it was reasonable to generate a mouse model for this disease.

II.1.2.2. Beta-propeller protein-associated neurodegeneration (BPAN)

BPAN is a subtype of NBIA and was formerly known as static encephalopathy of childhood with neurodegeneration in adulthood (SENDA). Its old name describes the main clinical features of this disorder. Since the underlying disease gene *WDR45* was discovered (Haack et al., 2012, Saito et al., 2013) an increasing number of patients were diagnosed with 48 cases published to date. Within the group of NBIA disorders, BPAN shows a unique clinical presentation (Hayflick et al., 2013). Global developmental delay normally starts early in childhood with impaired speech, motor impairment and intellectual disability, albeit to a variable extent. Features remain essentially static until early adulthood. Between 25 and 35 years of age, most patients rapidly progress to severe disability with progressive Parkinsonism, dystonia, spasticity and intellectual deterioration. Neurodegeneration is often diagnosed with cerebral atrophy as well as a so called 'Halo' in T1-weighted MRI. Hypointense globus pallidus and substantia

nigra in T2-weighted MRI are in concordance with iron depositions in both cerebral regions (figure 14). The detailed clinical spectrum will be described in II.2.1.

II.1.2.3. Genetics of BPAN and the disease-associated gene *WDR45*

BPAN is caused by X-linked, dominant *de novo* mutations in the gene *WDR45*, which is composed of 10 coding exons with known mutations scattered throughout. It encodes for the WD repeat domain 45 (*WDR45*) also known as *WIPI4*. *De novo* mutations were proven for all investigated patients (n = 20). The majority of mutations were predicted to cause loss-of-function (> 24 different alleles). In general, an X-linked dominant pattern should lead to a balanced sex ratio in patients. Surprisingly, of 48 patients diagnosed to date, there are only 4 male patients (f/m = 44/4). Systemic *WDR45* loss of function is assumed to be lethal in order to explain the striking sex ratio. In that case, one would expect male survivors to be somatic mosaics meaning they consist of cells with different *WDR45* genotypes due to postzygotic *de novo* mutations. This has indeed been shown in one male patient along with skewed X-inactivation in 10 female patients (Haack et al., 2012). The functional relevance of *WDR45* has not yet been revealed completely, but relevant findings are summarized in II.1.2.5. They indicate an association between impaired autophagy and the development of this neurodegenerative disorder. Further evidence was generated in a CNS-specific *Wdr45* knockout mouse model as described in the following (Zhao et al., 2015).

II.1.2.4. The brain-specific *Wdr45* knockout mouse model

Zhao and colleagues recently characterized and published all data described in this section (Zhao et al., 2015). They used a central nervous system (CNS)-specific *Wdr45* knockout mouse line. A number of experiments revealed neurobehavioral and neurological abnormalities. The CNS-specific *Wdr45* knockout mouse at the age of 11-13 months resembled the human phenotype in motor impairment, intellectual disability and cognitive dysfunction. Neuropathological findings suggested severe neurodegeneration with eosinophilic spheroids indicating axon swellings. Axon degeneration, swollen mitochondria and vacuolated structures in different brain regions as well as lower autophagic activity were discovered (table 2).

II. INTRODUCTION

| | Human BPAN phenotype | CNS-spec. <i>Wdr45</i> KO mouse phenotype | Experiment | Tissue/ Brain region |
|------------------------------|--|--|-------------------------------------|--|
| B | Motor impairment | Impaired motor coordination | Rotarod | |
| | Intellectual disability | Impaired immediate learning | Y-maze | |
| | Cognitive dysfunction | Impaired spatial memory | Morris water maze | |
| | Hippocampal dysfunction | Impaired fear recall | Contextual fear conditioning test | |
| No difference in fear recall | | Cued fear conditioning test | | |
| N | Neurodegeneration | Decreased fEPSP amplitude in hippocampal slides | LTP via Θ -burst stimulation | Hippocampal Schaffer Collateral (SC)-CA1 synapses |
| | | Eosinophilic spheroids/ axonal swellings | I: H&E | Cortex, thalamus, hypothalamus, white matter: DCN |
| | Neurodegeneration | Vacuolated structures | I: H&E | Thalamus, inferior colliculus, medulla |
| | | Axon degeneration | EM | DCN and medulla |
| | | Swollen mitochondria | EM | DCN |
| | Cerebellar atrophy | Eosinophilic spheroids/ axonal swellings in Purkinje cells | I: H&E | Cerebellar white matter: DCN |
| | | Purkinje cells axon swelling surrounded by myelin | I: CALB | In swollen axons of DCN |
| | Neuronal damage | Mild reactive astrogliosis | I: GFAP | Cortex, hippocampus, thalamus, hypothalamus, caudate nucleus, DCN, pons |
| | Mitochondriopathy | Swollen axons containing swollen mitochondria | EM | |
| | Myelination delay | Demyelinated axons | EM | |
| | Lower autophagic activity | Impaired autophagic flux | I: SQSTM1 + ubiquitin | Co-accumulation: thalamus, DCN + medulla; SQSTM1 in caudate nucleus and dentate gyrus of hippocampus |
| | | | I: SQSTM1 + NeuN | Pyramidal neural cells of hippocampus and cortex contained SQSTM1 aggregates, none in Oligodendrites |
| | | | I: CALB + ubiquitin | Ubiquitin aggregates in DCN only in small axon spheroids but absent from large ones |
| | | Accumulation of aberrant autophagic structures * | B: LC3-I + LC3-II + SQSTM1 | Cultured primary neurons |
| Impaired autophagic flux * | | I: SQSTM1 + ubiquitin | DCN | |
| Neurodegeneration | Eosinophilic spheroids/ axonal swellings * | I: CALB + MBP | Dilated axons | |

Table 2: Summary of findings in CNS-specific *Wdr45* knockout mouse model (content taken from Zhao et al., 2015).

Behavioural and neurological analysis of *Wdr45* knockout mice performed separately in male and female cohorts as indicated of maximal eleven animals per group. Behaviour screening was performed only in males at the age of 11-13 months; *denotes female neuropathology, which is listed for homozygous mutants. Heterozygous animals showed intermediary effect size. fEPSP = field excitatory post-synaptic potential; LTP = long-term potentiation; I = immunostaining; B = immunoblotting; EM = electron microscopy; DCN = dorsal cochlear nucleus; H&E = hematoxylin and eosin stain; medulla = medulla oblongata; CALB = calbindin; GFAP = glial fibrillary acid protein; SQSTM1 = p62 = autophagic marker; NeuN = neuronal marker; LC3-I/-II = microtubule-associated protein 1A/1B-light chain 3; MBP = myelin basic protein as myelin marker.

II.1.2.5. WDR45 and its function in autophagy

In NBIA most genes affect mitochondria. The precise function of WDR45 also known as WIPI4 (WD repeat domain phosphoinositide-interacting protein 4) is largely unknown. It belongs to the WD repeat protein family, which contains a conserved structural motif of more than 40 amino acids that terminate in tryptophan-aspartic acid (WD) residues. WDR45 consists of seven repeat units, which form a circularized seven bladed beta-propeller. This secondary structure is responsible for its associated disease name beta-propeller protein-associated neurodegeneration (BPAN).

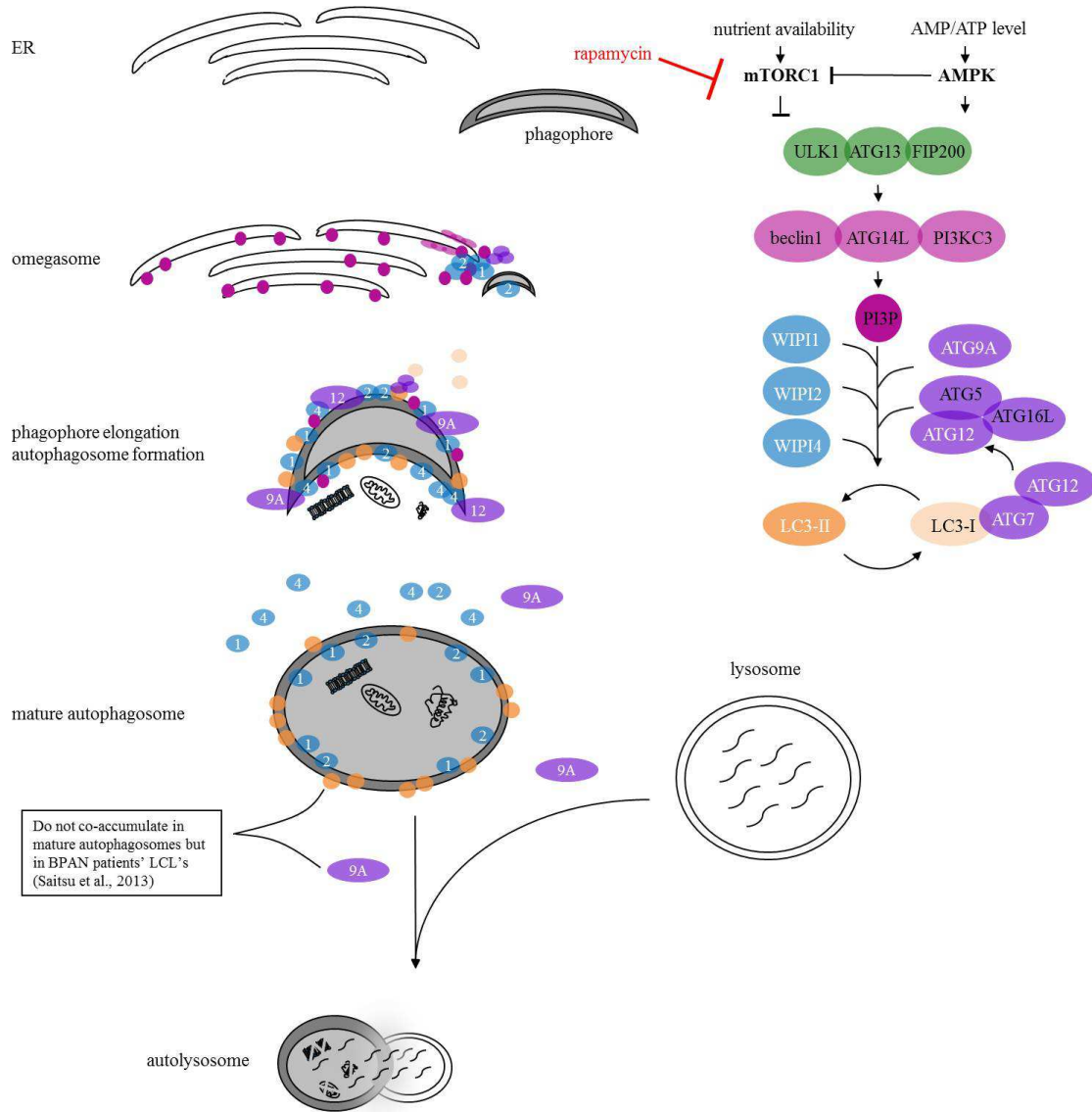


Figure 13: WIPI proteins in autophagy. Schematic model of autophagy and the involvement of WIPI proteins. ER = endoplasmic reticulum; mTORC1 = mammalian target of rapamycin complex 1; AMPK = adenosine monophosphate-activated protein kinase; ULK = unc-51-like kinase; ATG = autophagy related protein; PI3KC3 = phosphatidylinositol 3-kinase class III; PI3P = phosphoinositol 3-phosphate; WIPI = WD repeat protein interacting with phosphoinositides; LC3-I = microtubule-associated protein-light chain 3, cytosolic form; LC3-II = microtubule-associated protein-light chain 3, membrane-bound form; LCL = lymphoblastoid cell line.

II. INTRODUCTION

In humans and mice, there are four WIPI proteins 1-4. WIPI proteins are involved in cell cycle control, apoptosis and autophagy (Behrends et al., 2010). They are known to play a central role in detecting the PI3P (phosphatidylinositol 3-phosphate) pool within cells, which is a critical step in the process of autophagy (Proikas-Cezanne et al., 2015).

Autophagy is a cytoprotective process of partial self-degradation within cells, which has been comprehensively reviewed by Klionsky and colleagues (Klionsky et al., 2016). In all eukaryotic organisms this pivotal process secures cellular homeostasis and survival via lysosomal degradation of cytoplasmic compartments such as proteins, membranes or organelles. For instance, rapamycin treatment or nutrient shortage during starvation leads to induction of autophagy by inhibition of mTORC1. In order to initiate autophagy, a complex interplay of factors including several autophagy-related proteins (ATGs) leads to the assembly of PI3P at the endoplasmic reticulum. This PI3P-enriched structure is called the omegasome. The assembly of complexes beclin1/ATG14L/PI3KC3, and subsequently ATG12/ATG5/ATG16L at the autophagosome initiation site interacting with WIPI proteins, recruits phagophores. With the help of WIPI1 and WIPI2, LC3-I is lipidated to its membrane-bound form LC3-II, which accumulates at the nascent and mature autophagosome. ATG9A as well as WIPI4 are released and therefore absent from the mature autophagosome, which is subsequently fused with the lysosome. Acidic hydrolases degrade the enclosed cargo, which results in recycled compounds. As visualized in figure 13, WIPI proteins are PI3P effectors crucial for autophagosome formation. Nevertheless, distinction between the functions in autophagy of the four different WIPI proteins remains a challenge. WIPI4 was shown to act downstream of ATG5 involved in proper omegasome maturation and autophagosome formation (Lu et al., 2011). Impaired autophagic flux was consistently shown in genetically confirmed BPAN patients' lymphoblastoid cell lines (Saito et al., 2013). They showed accumulation of abnormal early autophagic structures by co-localization of LC3-II with ATG9A with the latter normally being absent from mature autophagosomes in contrast to LC3-II. Involvement of WIPI4 in normal autophagic flux is also suggested by studies in homologues from other species. Atg18 is the yeast homologue of the four WIPI proteins and binds the membrane of the endoplasmic reticulum via its PI3P-binding motif. This enables recruitment of further factors necessary for proper autophagy (Polson et al., 2010). EPG-6 is the *C. elegans* homologue of human WIPI3 and WIPI4 involved in interactions with several ATG's and the regulation of nascent autophagic size. It is critical for the progression from omegasome structure to autophagosome formation (Lu et al., 2011).

Taken together, the function of WDR45 (WIPI4) seems necessary for functional autophagy. Its dysfunction leads to impaired autophagic flux with the accumulation of aberrant early autophagic structures. It might play a role in autophagosome maturation and size determination. WIPI proteins have been reported to be aberrantly expressed in cancer (Proikas-Cezanne et al., 2004). Moreover, WIPI homologues in several model organisms have been shown to be involved in lifespan, longevity, ageing and age-related diseases (Rubinsztein et al., 2011). Accordingly, dysfunctional WIPI4 (WDR45) was shown to impair autophagy in

II. INTRODUCTION

patients with BPAN, a neurodegeneration with progression in ageing patients (Saito et al., 2013). Saito and colleagues showed accumulation of abnormal autophagic structures in lymphoblastoid cell lines of BPAN patients.

Patient material is scarce and only a limited number of organs or tissues are accessible. Therefore, the generation of a BPAN mouse model enables further elucidation of the role of WDR45 in the complex mechanism of autophagy. Furthermore, the comprehensive characterization of the mouse model helps to generate a complete spectrum of the clinical presentation, which might resemble BPAN patients. A more detailed description of the clinical presentation of BPAN patients could help physicians to get a faster molecular diagnosis. A well-characterized mouse model can be used as a basis for treatment strategies.

II.2. RESULTS

II.2.1. Clinical presentation in human BPAN patients

A detailed clinical picture of the human phenotype is useful in order to establish a suitable mouse model. To date there are 48 BPAN patients published with a confirmed deleterious mutation in *WDR45* (Abidi et al., 2015, Haack et al., 2013, Hamdan et al., 2014, Hayflick et al., 2013, Ichinose et al., 2014, Nishioka et al., 2015, Ohba et al., 2014, Okamoto et al., 2014, Ozawa et al., 2014, Rathore et al., 2014, Ryu et al., 2015, Saitsu et al., 2013, Takano et al., 2015, Tschentscher et al., 2015, Verhoeven et al., 2014).

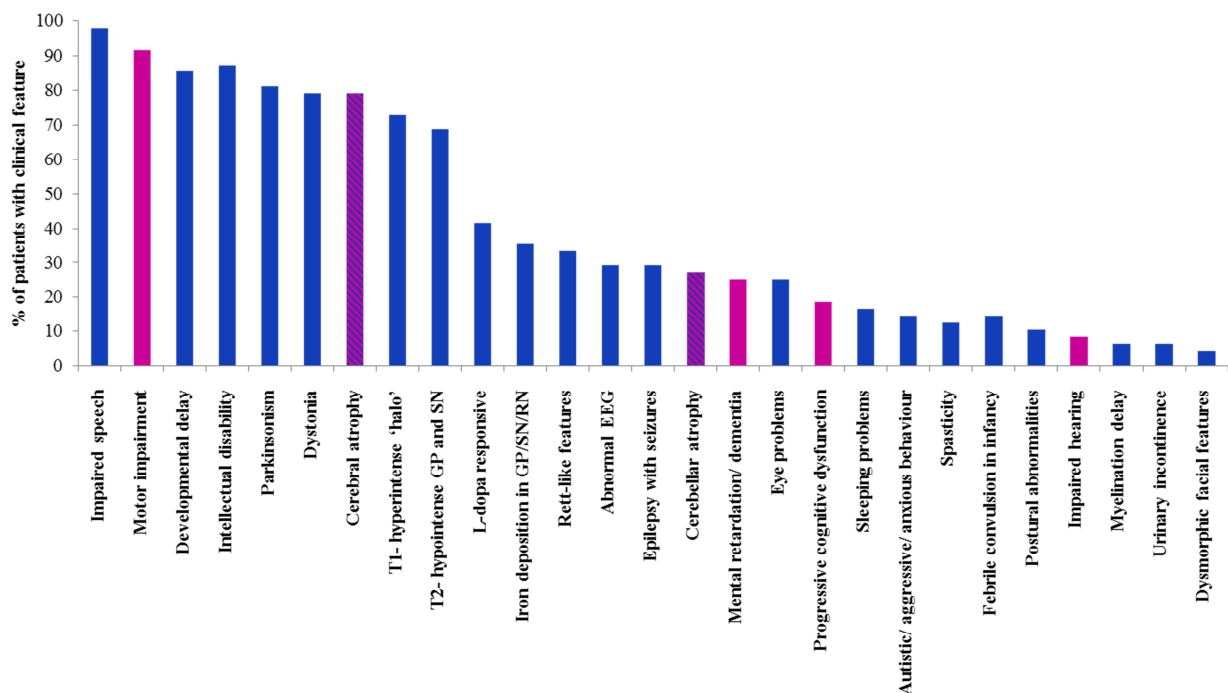


Figure 14: Clinical summary of BPAN patients. Clinical reports of 48 published patients have been summarized. If a feature was not reported by the clinician, it might not have been investigated but could still be present. Pink bars indicate features also found in the here established *Wdr45* mouse model (II.2.2.); bicoloured bars indicate that cerebellar and cerebral signs of degeneration were found in the murine disease model, but in a different form. Several human symptoms like dystonia are hard to translate to the murine system. L-Dopa = L-3,4 dihydroxyphenylalanin; GP = globus pallidus; SN = substantia nigra; RN = red nucleus; EEG = electroencephalography.

Most patients show impaired speech with none or only a few words or at best severely limited expressive language. The majority are wheelchair bound with no ability to walk unassisted. This symptom often develops with motor impairment and psychomotor retardation. Almost all patients are developmentally delayed as well as intellectually disabled. In early adulthood all patients experience a dramatic clinical decline. This is mainly due to the onset of Parkinsonism and dystonia. By that time clinicians normally discover cerebral atrophy via MRI, and the typical 'halo' of hyperintensity in T1-weighted MRI and hypointensity in T2-weighted MRI. They classically also find iron depositions in the globus pallidus and

II. RESULTS

substantia nigra and occasionally in the nucleus ruber. All patients treated with the dopamine precursor L-Dopa initially responded well to this therapy with less prominent Parkinsonism and dystonia. Unfortunately this effect was largely short-lived in BPAN patients (Hayflick et al., 2013). Many patients show Rett-like features with involuntary and abnormal hand movements. One BPAN patient was identified by sequencing the probe of a suspected Rett syndrome patient without the typical MECP2 mutation (Ohba et al., 2014). Less frequent findings in patients are abnormal EEGs, epilepsy often accompanied with seizures, cerebellar atrophy, mental retardation and dementia with disease progression and ocular problems. The latter are of various nature, and include optic atrophy, cortical blindness, myopia, abnormal pupil shape, astigmatism, retinal detachment or coloboma and increased latency in visual evoked potential (VEP). Progressive cognitive dysfunction in adulthood was mentioned in several clinical reports. Other features published in association with BPAN are sleeping problems, spasticity, and febrile convulsion in infancy, postural abnormalities and behavioural changes. The latter is mainly expressed as autistic, aggressive or anxious attitude. Impaired hearing was reported rarely. Of note, hearing is examined at birth and during early development in a standardized manner. But with late progression of neurodegeneration, intellectual disability, cognitive dysfunction and impaired speech, dysfunctional hearing might not be the focus during medical examinations of those patients. Stated in the minority of patients were features such as myelination delay, urinary incontinence and dysmorphic facial features (figure 14).

In summary, onset of first symptoms was normally during the first decade of life, but disease manifestation and diagnosis predominantly during the second or third decade. All patients were described to have experienced a period of rapid, severe and so far relentless disease progression before the age of 35 (figure 15).

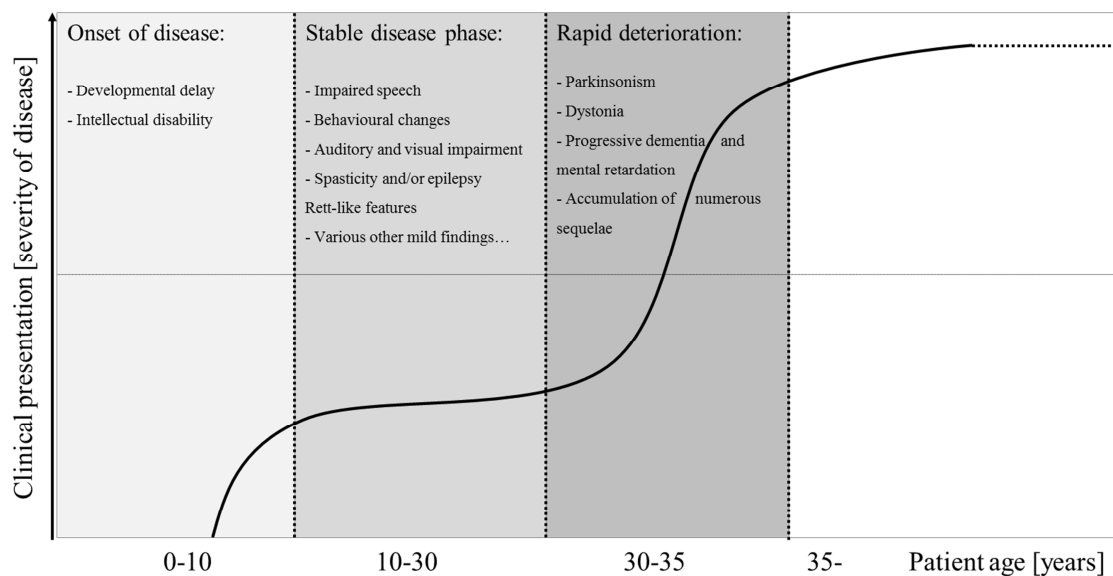


Figure 15: Clinical presentation of BPAN patients over time. The three stages of disease progression are depicted by different shades of grey with the main or most common clinical symptoms summarized.

II. RESULTS

II.2.2. Generation of a *Wdr45* knockout mouse via TALENs

In order to generate a mouse model for BPAN, two *Wdr45*-TALEN pairs were designed *in silico* according to established standards described in V.2.1.12. for murine genome editing. The human *WDR45* and murine *Wdr45* sequence are highly homologous with only 7 out of 360 non-identical amino acids. TALEN pairs for exon 2 and exon 5 were created. Both were tested *in vitro* and the better one used for *in vivo* oocyte injection. Exon 2 is the first coding exon in both humans and mice. Accordingly, choosing exon 2 aimed at generating an early frameshift mutation leading to a premature stop-codon. Exon 5 is known to be the location of several human causal mutations. Hence, four customer-designed oligonucleotides were ordered as described in V.2.1.12, which were codon optimized for murine usage. They were built to address *Wdr45* exon 2 and exon 5 in pairs (figure 16) and predicted to create a double-strand break in close proximity of the target region.

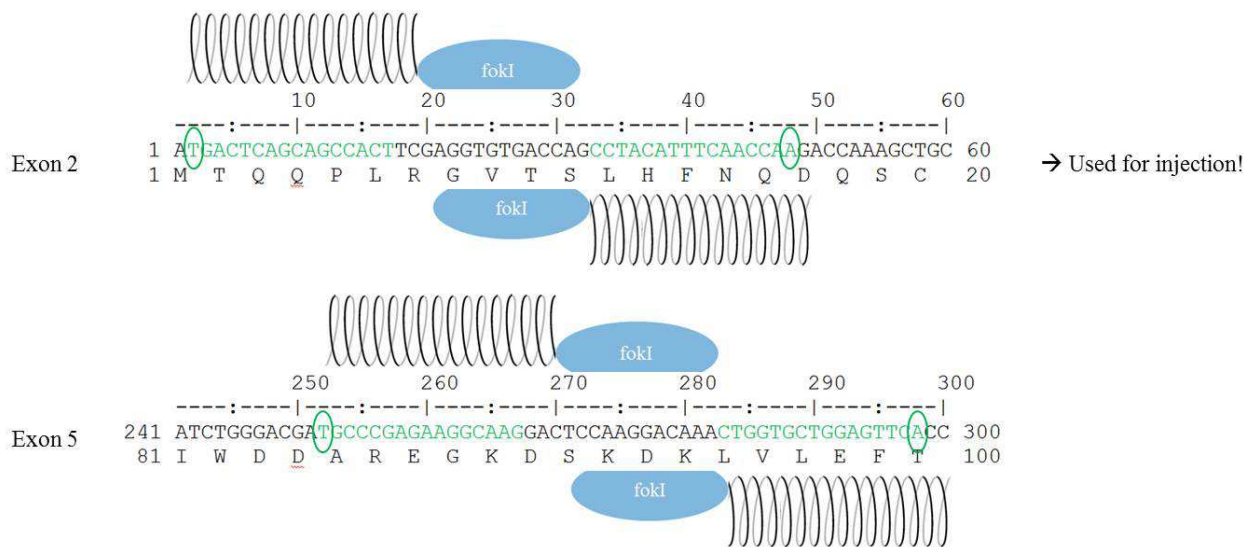


Figure 16: TALEN target sequences in *Wdr45* exon 2 and exon 5. Sequences were provided by the Genome Browser (NCBI37/mm9) and transcript uc009smd.1 was used. Depicted in green are 15 bp regions targeted by the designed TALENs with one of the pair starting with an additional thymine as well as the other one, where the complementary adenine is highlighted with green circles. TALENs are shown as loop-like structures attached to a fokI domain (blue). Working in dimers they introduce a double-strand break around the target site.

All four TALENs were separately cloned into expression vectors (figure 17A) containing a fokI nuclease sequence, which is attached to the c-terminus of each TALEN as described previously (Wefers et al., 2013b, Wefers et al., 2014). In order to test TALEN efficiency *in vitro* the two target sequences of exons 2 and 5 were separately cloned into a reporter vector flanked by a broken β -galactosidase cassette. A plasmid containing a luciferase cassette enables analysis of the transfection efficiency. For each TALEN pair, four plasmids were used to transiently co-transfect HEK293 cells. Figure 17A describes the four plasmids on the example of the TALEN pair targeting exon 2 of *Wdr45*. Only a double-strand break in the target

II. RESULTS

sequence of pREP-*Wdr45ex2* enables recombination of β -galactosidase and its subsequent expression. To control that the double-strand break was induced via the TALEN pair, and to control for spontaneous β -galactosidase recombination, co-transfections were performed either with or without expression plasmids (e.g. pCAG-*Wdr45ex2*-Tal1 and pCAG-*Wdr45ex2*-Tal2). All β -galactosidase measurements were normalised to luciferase in order to control for transfection efficiency. As a control we used a TALEN pair, which was known to result in 40% efficiency *in vivo* (established by the Institute of Developmental Genetics, Helmholtz Zentrum Muenchen). Hence, injection of this control TALEN-pair (Ctrl TALEN) into the oocytes of foster mice should result in mutations within the target region in approximately 40% of the living offspring (figure 17).

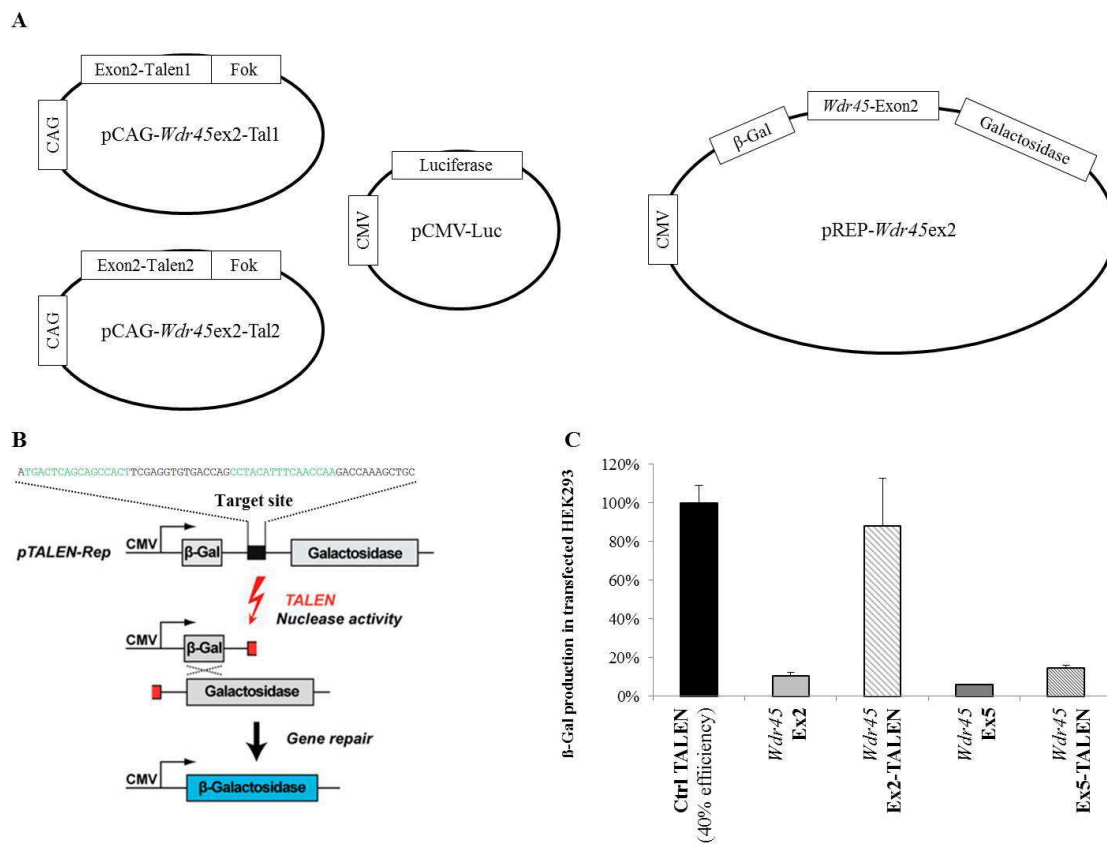


Figure 17: *In vitro* testing of TALENs. **A)** Plasmids used for the cell culture test of TALENs on the example of *Wdr45* exon 2. CAG and CMV are promoters, Fok describes the fok nuclease domain and β -Gal and Galactosidase describe the broken β -Galactosidase cassette. **B)** Schematic of *in vitro* TALEN testing vector system adapted and taken from Wefers et al., 2013b. **C)** TALEN efficiency assay; measurements were normalized to luciferase measurements. *Wdr45* Ex2 was transfected with the reporter plasmid only as well as *Wdr45* Ex5 respectively. Samples *Wdr45* Ex2-TALEN and *Wdr45* Ex5-TALEN were co-transfected with the reporter plasmid and both expression plasmids to express the corresponding TALEN-pair; β -Gal = β -galactosidase; Ctrl TALEN = control TALEN-pair known to result in 40% mutated offspring.

As visualised in figure 17C via the β -galactosidase assay, the TALEN dimer designed to target exon 2 seems as efficient as the control TALEN-pair, whereas the second TALEN-set (Ex5-TALEN) was less

II. RESULTS

efficient in cell culture. Based on this assay, mRNA of Ex2-TALENs was generated and chosen to be injected into the pronucleus of mouse zygotes according to established protocols (Meyer et al., 2010, Meyer et al., 2012). The mRNA injection probe was prepared as described in V.2.4.3. and injected by an experienced injection team from the Institute of Developmental Genetics at the Helmholtz Zentrum Muenchen. Zygotes (i.e. one-cell embryos) were obtained from superovulated FVB females mated with C57Bl6/N males. On one injection day, 30 zygotes were used to inject the TALEN-probe into each pronucleus. Injected zygotes were transferred into 3 pseudo-pregnant CD1 foster females, which gave birth to a total of 26 pups (table 3). All pups were genetically analysed by Sanger sequencing of the target region in order to identify offspring harbouring a deleterious heterozygous or hemizygous mutation in *Wdr45*. The procedure took approximately four months from TALEN design until genotyping of the first founder animals (figure 18).

| | |
|---|-----------|
| TALEN design and ordering | 0.2 |
| TALEN generation at GenScript | 4-6 |
| Proofreading of TALEN sequence | 0.1 |
| Shipping of TALENs | 1 |
| Cloning of expression and reporter vectors | 1 |
| Activity assay <i>in vitro</i> | 1 |
| mRNA production | 0.1 |
| Preparation of animals for embryo injection | 2 |
| Embryo injection | 0.1 |
| Pregnancy of foster females | 3 |
| Ear clipping for genotyping at age 3weeks | 3 |
| Total time | 15.5-17.5 |

Figure 18: Timeline to generate a knockout mouse line via TALEN embryo microinjection.

The TALEN design and ordering takes 1-2 days. TALEN custom design ordering at GenScript (New Jersey, USA) including codon optimization for mice takes 4-6 months due to the repetitive sequences of the loops. Before shipping sequences suggested by GenScript should be proofread for correct endings and loop sequences. The preparation of the desired mRNA for injection takes more than 2 weeks. Preparation of animals for microinjection takes 2 weeks followed by another 3 weeks of pregnancy. 3 weeks after birth, the founder generation can be used for genotyping.

II.2.3. Systemic *Wdr45* KO is viable in mice

As described in V.2.4.4. a PCR- and Sanger sequencing-based strategy was used to genotype the *Wdr45*-TALEN-injected offspring. The F0 generation consisted of 26 pups with five of them (19%) carrying a deleterious *Wdr45*-KO allele as visualised in figure 19A.

Mutant mice #1 and #2 carrying an identical 20 bp deletion were used for further mating and generation of all following cohorts (table 3). This small deletion causes a frame-shift and is predicted to result in a premature stop-codon 35 amino acids after the initial methionine. Since founder mice #1 and #2 were female and male it was possible to set up three matings with one male and two female mice with the C57Bl/6 background, resulting in ten out of 16 mutant animals (62.5%) in the F1 generation (six heterozygote females and four hemizygous males). As expected only a fraction of F1 carried the mutation, which is dependent on the time of the genome editing event in F0. Only when the event occurs in the

II. RESULTS

germline the mutation is transmitted to the offspring. Due to the *Wdr45* genes' location on the X-chromosome there are five genetically distinguishable groups, wild-type, heterozygous and homozygous females, and wild-type and hemizygous males. Sequencing of ear clip-derived DNA of *Wdr45* exon 2 distinguishes all different genotypes as visualised in figure 19B.

A systemic *Wdr45* KO was thought to be lethal since all human patients known today are either heterozygous or hemizygous mosaics carrying *de novo* mutations. To date, this is the first viable systemic *Wdr45*-knockout transmitted via germline mutations. Inbreeding of the mutant F1 generation resulted in hemizygous, heterozygous and homozygous *Wdr45* KO mice in the F2 generation proving both, viability and fertility in male and female mutants lacking a wild-type *Wdr45* allele.

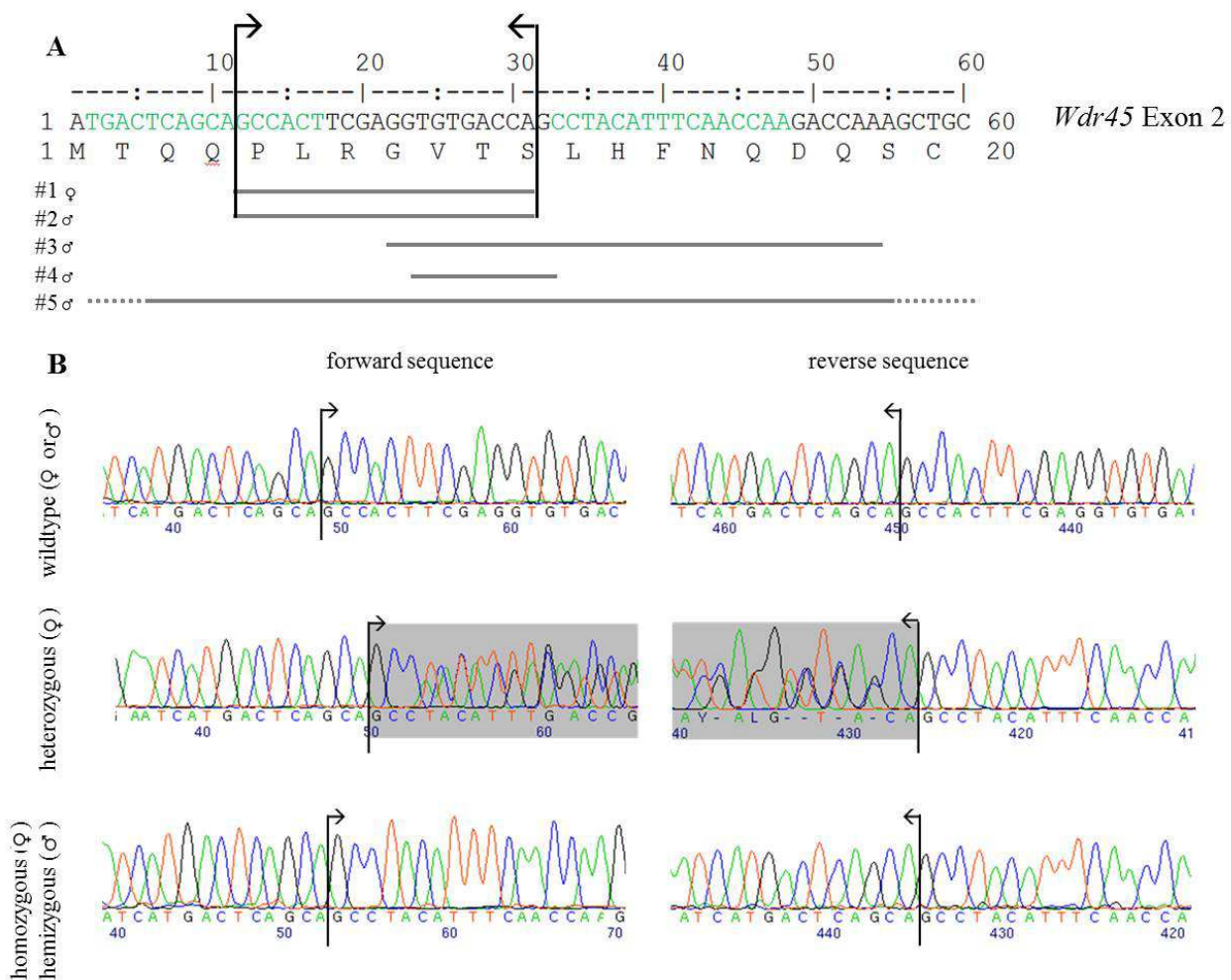


Figure 19: Genetic analysis of founder mice (*Wdr45*-Ex2-TALEN injected) and their offspring. **A**) Indicates the target sequence within exon 2 of *Wdr45* with TALEN-binding sites depicted in green. Lines underneath the exonic sequence indicate the regions deleted in each of the five mutated founder mice (#1-#5). Black arrows point towards the region deleted in individuals #1 and #2, which is sequenced in B. #1: del20; #2: del20; #3: del33; #4: del10; #5: del>60. **B**) Sanger sequencing example of ear clip-derived DNA from all three genotypically different animal groups.

II. RESULTS





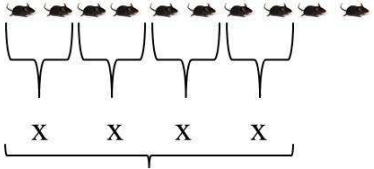
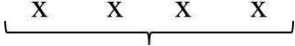
| Procedure | Description | Generation | |
|--------------------------------------|--|------------|---|
| TALEN mRNA injection into zygotes | 30 zygotes* used | |  |
| Transfer into pseudopregnant females | 3 females used | |  |
| Birth and genotyping of 26 pups | 5 mosaic mutant animals | F0 |  |
| Matings of F0 with C57Bl/6N | 3 matings of #1 and #2 | |  |
| Birth and genotyping of 16 pups | 10 germline mutants 6x female het 4x male hemi | F1 |  |
| Mating of female het with male hemi | 4 matings | |  |
| Birth and genotyping | 21 of 4 genotypes | F2 | female: het, homo and male: wt, hemi |
| | viability and fertility | ← | preliminary cohort |
| Inbreeding | 52 animals of 5 genotypes | F3 | disease-progression cohort |
| Inbreeding | 127 animals of 5 genotypes | F4 | GMC cohort (> 1 year of age) |

Table 3: *Wdr45* KO mouse generation scheme and breeding strategies for different cohorts. *Zygotes were derived from superovulated females with FVB background mated with C57Bl/6N males. Wt = wild-type; het = heterozygous; homo = homozygous; hemi = hemizygous, GMC = German Mouse Clinic.

II.2.4. Analysis of preliminary *Wdr45* KO mice (F2) shows neurobehavioral deficits

In humans the mode of inheritance was shown to be X-chromosomal dominant (Haack et al., 2013). The female to male ratio is 44/4 with suspected male lethality when *WDR45* was depleted in the germline. In contrast, we found the murine *Wdr45* knockout to be viable both in homozygous KO females as well as in hemizygous KO males. Hence, it remained an open question whether the *Wdr45*-KO mouse line developed a phenotype at all. And if so, whether heterozygous female animals showed pathologic features. In humans the disease onset is generally during the first ten years of life with dramatic disease progression during early adulthood. The preliminary cohort was aimed at addressing the murine onset and development of pathologic features in *Wdr45* KO mice.

A first cohort of 21 animals of the F2 generation (table 3) was intensively characterised. The cohort was composed of six hemizygous and six wild-type males as well as four homozygous and five heterozygous females. Due to the inbreeding strategy where hemizygous males were mated with heterozygous females, there were no wild-type females in this generation. The characterisation included weight development, performance on a balance beam, grip strength and inverted grid, as well as a modified SHIRPA protocol

II. RESULTS

(see V.2.4.5.) on a weekly to monthly basis in order to screen for neurologic deterioration (figure 20). Due to the small cohort size, significant results were not expected, but a trend on which to base future more detailed screens on larger cohorts.

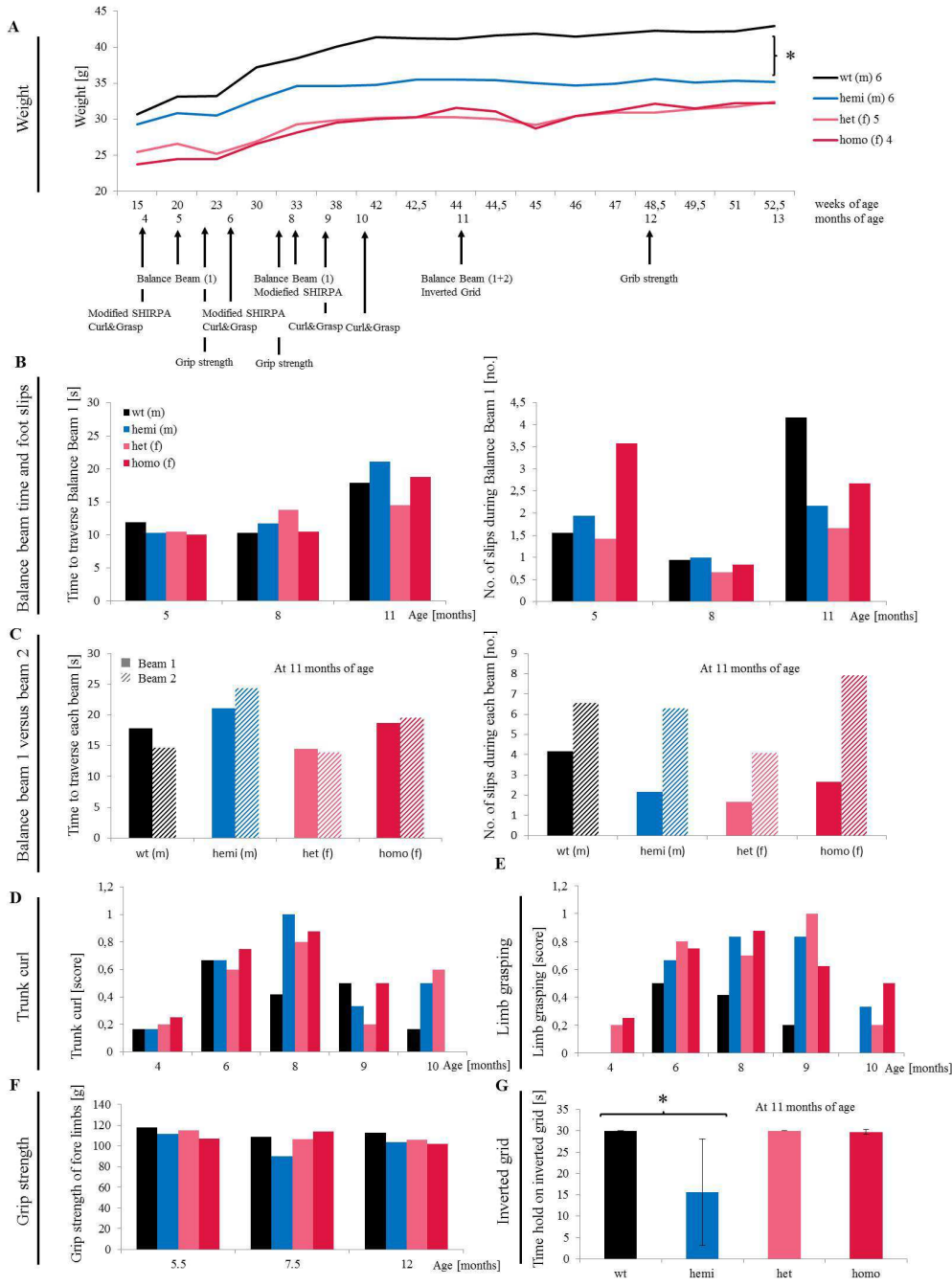


Figure 20:
Preliminary analysis of the *Wdr45* KO cohort.

The cohort consists of 21 animals with six male wild-type, six male hemizygous, four female homozygous and five female heterozygous animals with mutations in *Wdr45*. **A**) Weight development with summary of tests performed at corresponding ages of the cohort. **B**) and **C**) balance beam using beam 1 (round; 22 mm) at five, eight and eleven months of age. At eleven months of age a second beam was used; beam 2 (rectangular; 7 mm). For each balance beam experiment, the time to traverse the beam was measured as well as the number of foot slips counted. **D+E**) Modified SHIRPA was measured including positional activity, trunk curl, limb grasping (only hind limbs), biting, vocalisation, body position, tremor, palpebral closure, coat appearance, whiskers, lacrimation, defecation, transfer arousal, locomotor activity, gait, tail elevation and touch escape. **D**) Trunk curl was assessed as absent = 0 or present = 1 **E**) Limb grasping was assessed as absent = 0 or present = 1 **F**) Grip strength of fore limbs was measured at 5.5, 7.5 and 12 months of age. **G**) Inverted grid was performed at the age of eleven months and the time measured until loss of grid with a maximum observation of 30 s. Bars indicate standard deviation; *t-test: $p < 0.05$.

Trunk curl, limb grasping (only hind limbs), biting, vocalisation, body position, tremor, palpebral closure, coat appearance, whiskers, lacrimation, defecation, transfer arousal, locomotor activity, gait, tail elevation and touch escape. **D**) Trunk curl was assessed as absent = 0 or present = 1 **E**) Limb grasping was assessed as absent = 0 or present = 1 **F**) Grip strength of fore limbs was measured at 5.5, 7.5 and 12 months of age. **G**) Inverted grid was performed at the age of eleven months and the time measured until loss of grid with a maximum observation of 30 s. Bars indicate standard deviation; *t-test: $p < 0.05$.

II. RESULTS

In summary, the preliminary analysis of this small *Wdr45* cohort revealed a decrease in weight gain in hemizygous males as compared to wild-type males, which was nominally statistically significant at 13 months of age ($p = 0.037$; figure 20A). Balance beam analysis showed no significant effects on neither beam 1 (round, 22 mm) nor beam 2 (rectangular, 7 mm). However, there was a trend towards mutants taking more time to traverse the beam (figure 20B and C). All tests performed within the modified SHIRPA protocol did not show any trend between genotypes (data not shown). Only trunk curl and even more pronounced limb grasping was increased in mutants (figure 20D and E). Grip strength showed a slight reduction in mutant animals (figure 20F). And inverted grid analysis at the age of eleven months revealed, that only hemizygous males are struggling to hold on to the grid for up to 30 sec (figure 20G). This resulted in a significant difference between genotypes in males ($p = 0.018$). At the age of 13 months this preliminary cohort was delivered to the German Mouse Clinic.

The GMC analysis revealed nominally significant results for startle response ($p = 0.023$), balance beam ($p = 0.004$) and open-field ($p = 0.014$) in 13 months old mutant animals (data not shown).

Based on the combined results, a cohort was generated to be analysed for its disease progression. It will be referred to as the disease progression cohort in the following. Another large cohort was generated for GMC screening at the age of one year or more – hereafter referred to as the GMC cohort.

II.2.5. Screen of the disease progression *Wdr45* cohort (F3)

A cohort of 56 animals (15 hemizygous, 12 male wild-type, eleven homozygous, ten heterozygous and eight wild-type female) was generated in F3 (table 3) to be monitored and characterized regularly during ageing until the age of 22 months. As described in figure 21 all animals were weighted every two weeks. In order to monitor neurologic deterioration, the cohort was analysed using the modified SHIRPA protocol as well as the balance beam analysis on two different beams. Every two months an inverted grid analysis was performed. For brain pathology more than 20 mice (not taken from the disease progression cohort but also from F3) of different ages and genotypes underwent necropsy in order to examine several brain regions and the spinal cord.

II.2.5.1. Neurologic deterioration in *Wdr45* KO mice

The disease progression cohort was screened for neurologic deterioration as indicated in figure 21. Frequent weight measurement over 22 months of age showed higher body weight in mutant animals for both genders as opposed to earlier weight analysis of the preliminary cohort.

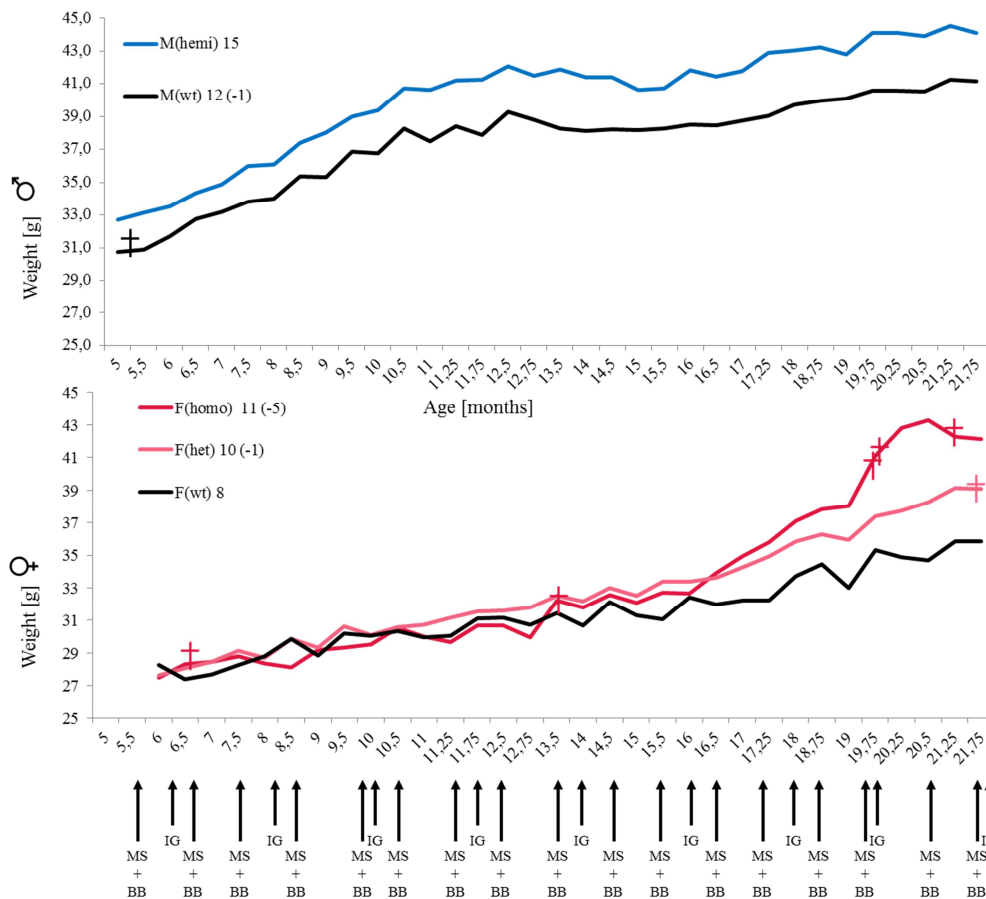


Figure 21: Neurology screen of the *Wdr45* disease progression cohort. 52 animals were characterized at different ages as indicated in months on the x-axis. Blue and red lines depict male and female mutants with black indicating their wild-type gender matched littermates. Weight measurement from five to 22 months of age with neurologic investigations as indicated underneath with inverted grid (figure 22), balance beam (see figure 23) and modified SHIRPA (figure 24). Crosses indicate deceased animals.

Wt = wild-type; hemi = hemizygous; het = heterozygous; homo = homozygous; MS = modified SHIRPA; BB = balance beam; IG = inverted grid.

II. RESULTS

As visualized in figure 22, inverted grid analysis indicated that young male mutants perform better at holding onto the inverted grid, which is even though they are heavier in weight. As of the age of 20 months, their performance is significantly weaker when compared to wild-type males. Heterozygous females performed similar as wild-type females, whereas homozygous females performed worse throughout the one year screening period.

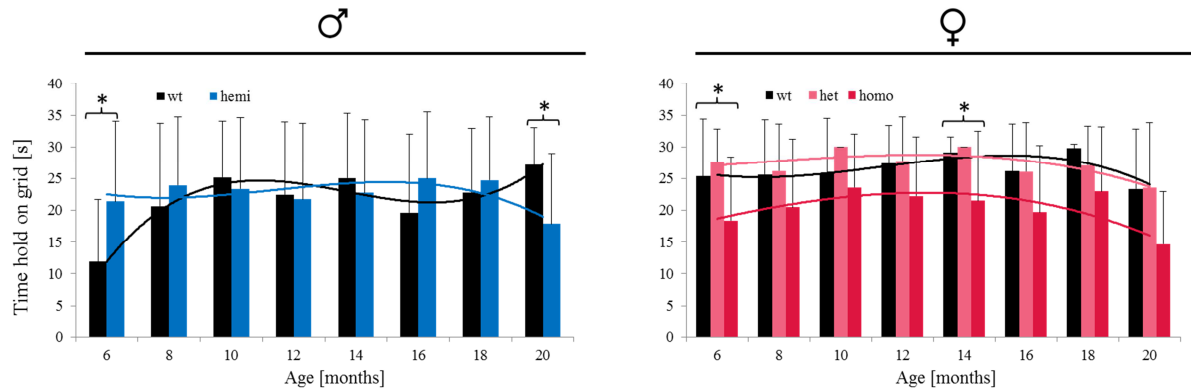


Figure 22: Inverted grid of the disease progression *Wdr45* cohort. Inverted grid analysis was performed until a maximum of 30 seconds, with mean and standard deviation indicated with black bars. Wt = wild-type; hemi = hemizygous; het = heterozygous; homo = homozygous; * t-test: $p < 0.05$ (in females, wt+heterozygous versus homo). Polynomic trend lines were added.

On the balance beam the time to traverse each beam was not significantly different between genotypes in both genders (supplementary figure 3A). Male fall downs (figure 23A) occurred mainly in mutant animals with 55 out of 66 total falls during the 22 months period on beam 1 ($> 83\%$) and 69 out of 75 falls on beam 2 ($= 92\%$). In females mainly heterozygous and homozygous animals experienced a fall from the beam with less than 17% of falls experienced by wild-type animals on beam 1 and less than 4% on beam 2, respectively. Foot slips tended to be increased in both male and female mutants with significant differences at several ages (figure 23B). There was no difference in the number of stops between genotypes (supplementary figure 3B).

II. RESULTS

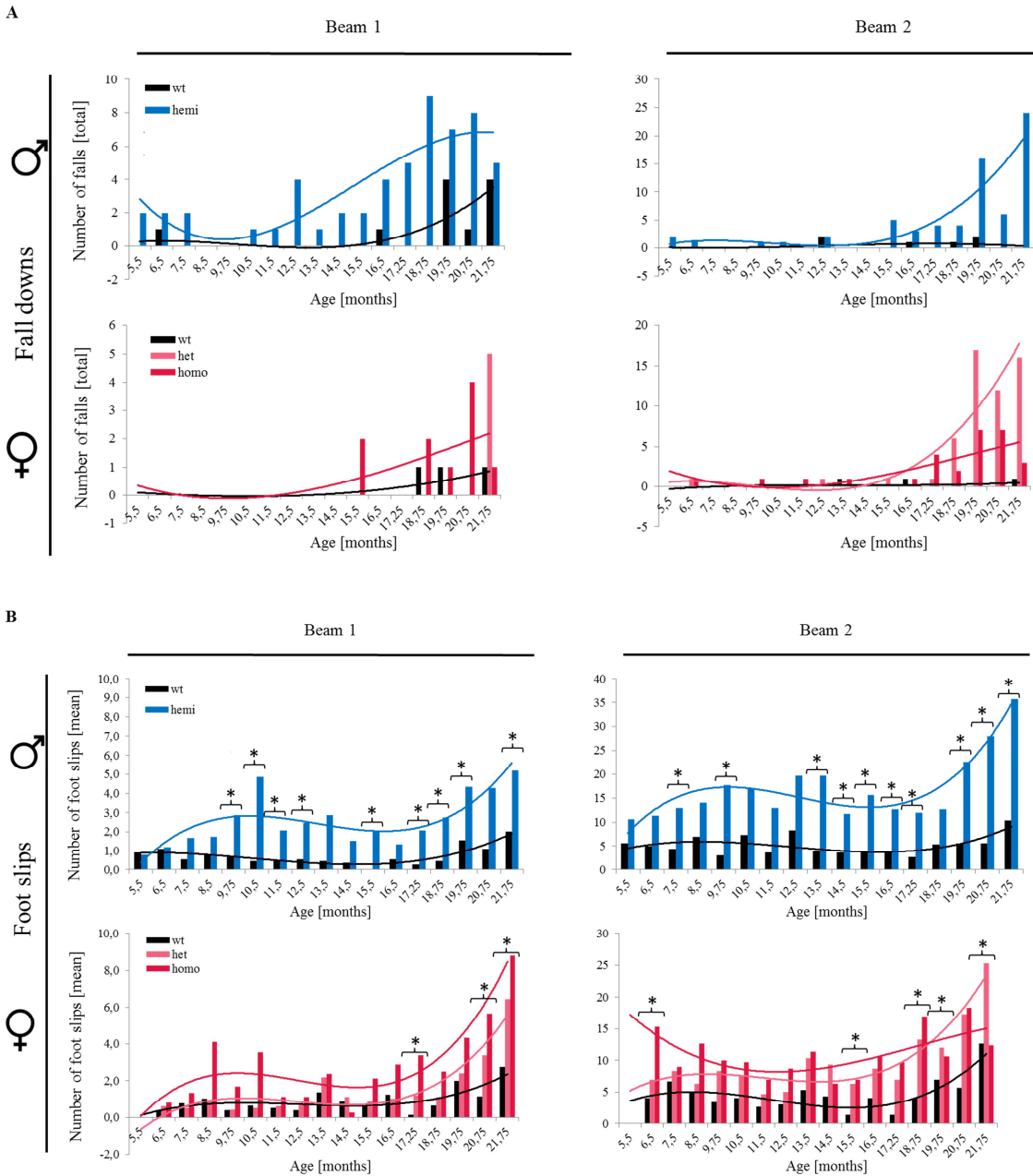


Figure 23: Balance beam of the disease progression *Wdr45* cohort. Balance beam was performed in triplicate with each mouse, with one prior practicing the day before. Two different beams were used with beam 1 (left column, round and 22 mm in diameter) and beam 2 (right column, rectangular and 7 mm in diameter). **A)** Cumulative number of fall downs per genotype on each beam. **B)** Mean number of foot slips with either paw on each beam. Wt = wild-type; hemi = hemizygous; het = heterozygous; homo = homozygous; * t-test: $p < 0.05$ (in females, wt+het versus homo). Polynomic trend lines were added.

A modified SHIRPA analysis revealed that mutants were more likely to show tremor (figure 24A) with significant differences at 20 months of age. The most consistent phenotype starting at the age of around eleven months in both genders was the loss of hearing ability assessed by the clickbox test (figure 24B). Trunk curl and even more prominent limb grasping occurred in mutants more often than in wild-type animals (figure 24C and D), as exemplified in figure 25.

II. RESULTS

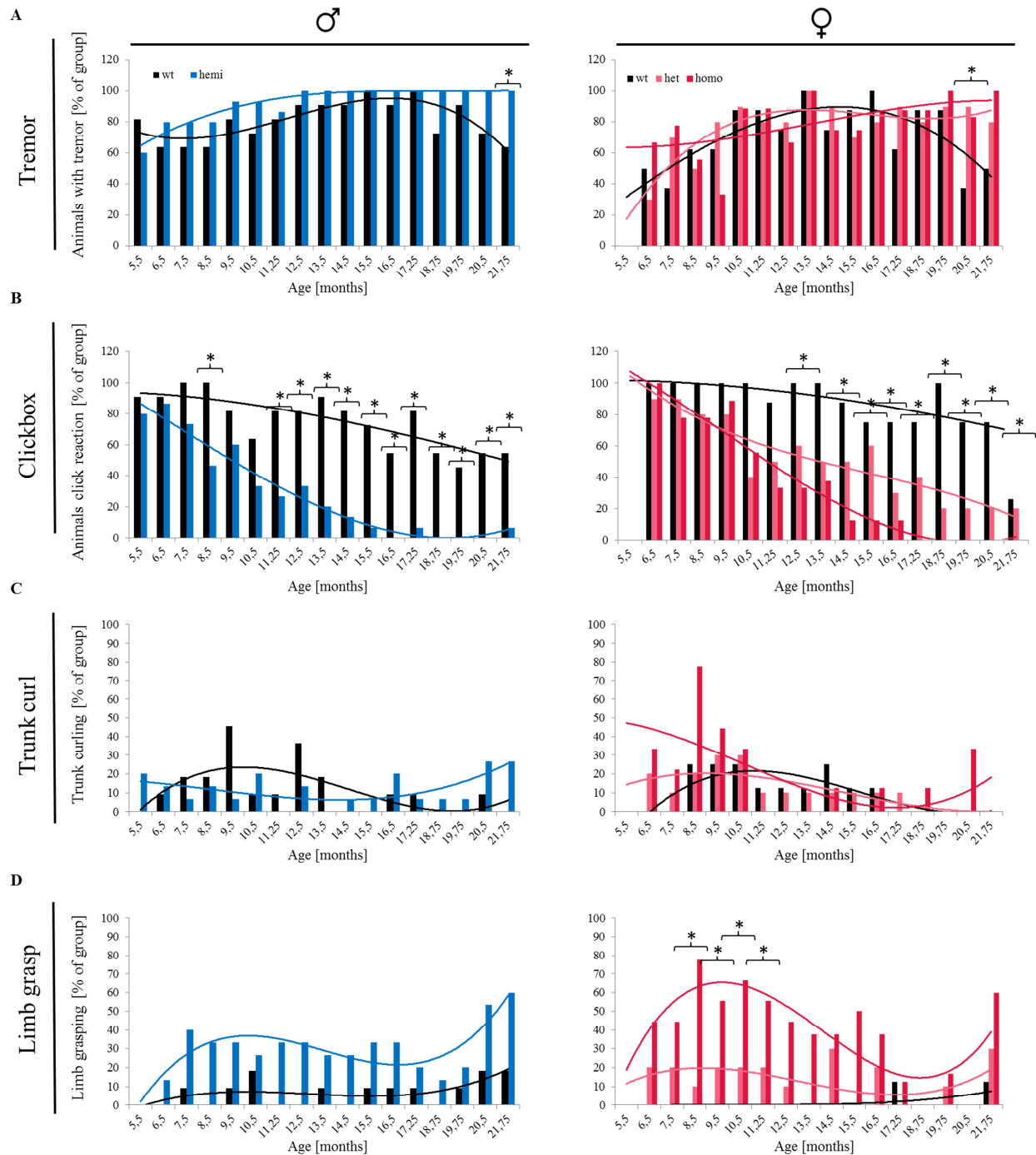


Figure 24: Modified SHIRPA analysis of the disease progression *Wdr45* cohort. The analysis included also locomotor activity, transfer arousal, body position, gait abnormality, tail elevation, touch escape and urination, but results were not significant and showed no interesting trends (supplementary figure 4). **A)** Tremor was analysed by observation of forepaws while lifting the mouse by the tail. **B)** Reaction to a click sound was analysed. **C)** Trunk curl was assessed as whole body curl when elevated by the tail, see figure 25D. **D)** Limbs were observed and checked for grasping (see also figure 25C). All variables were binary (scored as absent = 0; present = 1) and therefore analysed by Fisher's Exact test * Fisher's exact: $p < 0.05$ (in females, wt+heterozygous versus homo). Polynomic trend lines were added.

II. RESULTS

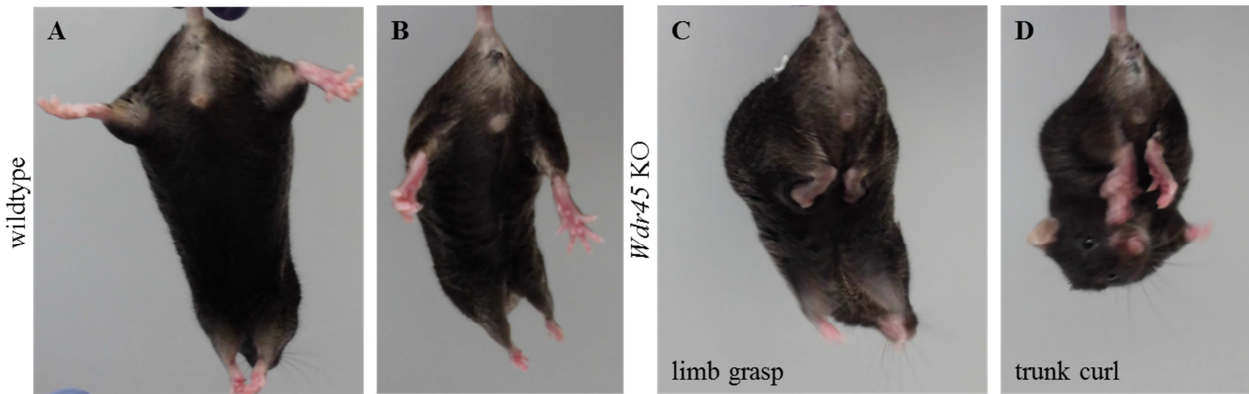


Figure 25: Limb grasping and trunk curl assessment in wild-type versus *Wdr45*-KO mice at the age of 18 months. This analysis is part of the modified SHIRPA protocol. Male mice are elevated by their tail for up to 5 seconds with a grid in roughly 10 cm proximity. **A+B)** Wild-type animals when lifted by the tail. **C)** Limb grasping is assessed as grasping of hind limbs as observable in the *Wdr45* KO. **D)** Trunk curl is assessed via curling of the entire mouse trunk with fore paw to hind paw touching as observed in the *Wdr45* KO.

In summary, with a cohort size of eight to 15 per group we identified a few genotype specific differences. Mutants showed increased weight gain and slight motor coordination deficits via inverted grid and balance beam. Increased limb grasping and trunk curl hint towards neurologic deterioration in mutant animals. Prominent hearing loss in mutants started at the age of eleven months followed by a stage of stable disease progression. At the age of about 20 months mutants show a more rapid deterioration than wild-types as shown in more falls and foot slips from the beam (figure 23A and B) as well as increased tendency to show tremor and limb grasping (figure 24A and D).

II.2.5.2. Pathologic brain abnormalities in *Wdr45* KO mice

Necropsy and brain sections were performed at the Institute of Pathology at the Helmholtz Zentrum Muenchen in collaboration with Dr. F. Neff and Dr. D. Janik. They were given 35 animals with different genotypes at varying ages from four to 18 months. All mutant animals hemizygous males ($n = 13$) as well as homozygous ($n = 8$) and heterozygous ($n = 7$) females revealed pathologic neurology. Importantly, none of the wild-type brain sections ($n = 7$) did even at the age of 18 months. As described in figure 26, *Wdr45*-KO animals showed axonal spheroids and swollen structures, which most likely present degenerated neurons. This pathology was found in mutant cerebral cortex (figure 26B) and thalamus (figure 26C) resembling the human BPAN pathology of axonal spheroids and macrophages in the substantia nigra (figure 26D). None of these phenotypes was observed in wild-type littermates (figure 26E and F).

II. RESULTS

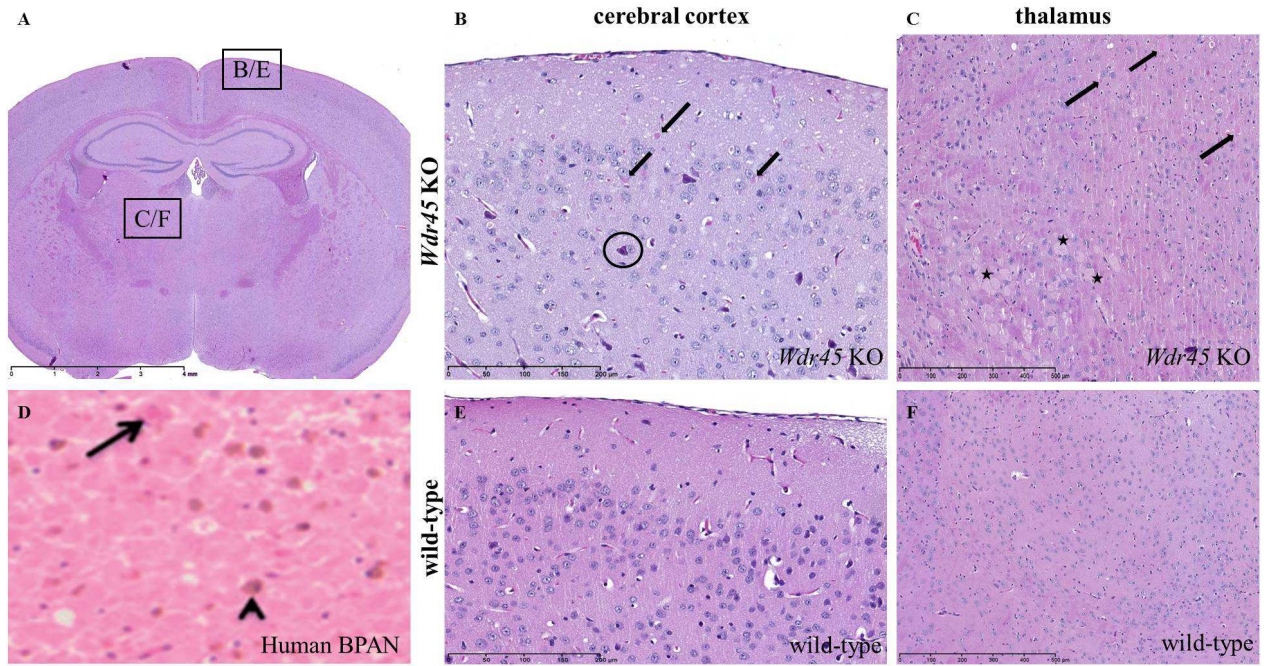


Figure 26: Neurodegeneration in *Wdr45* KO cerebral cortex and thalamus resembling BPAN patient's substantia nigra. H&E staining of brain sections. **A)** Murine diencephalon and telencephalon with indicated brain regions analysed in B/E) and C/F). **B)** Cerebral cortex of a *Wdr45* KO mouse (at 18 months of age); arrows indicate eosinophil spheroids. An exemplary dark neuron is indicated by the circle, but denotes a preparatory artefact. **C)** Thalamus of a *Wdr45* KO mouse with arrows indicating eosinophil spheroids and asterisks showing swollen structures possibly due to degenerating neurons. **D)** Picture taken from Hayflick and colleagues, showing substantia nigra from a BPAN patient with numerous large dystrophic axonal spheroids (arrow) and macrophages (arrowhead) full of haemosiderin (Hayflick et al., 2013). **E)** Cerebral cortex of wild-type littermate of *Wdr45* KO mouse. **F)** Thalamus of wild-type littermate of *Wdr45* KO mouse.

Neuropathologic findings with abnormal structures visible via H&E staining were also present in four months old mutants (figure 27A). This indicates that even with behavioural symptoms manifesting at the age of one year, neurologic deterioration starts early in life of murine *Wdr45* KO animals.

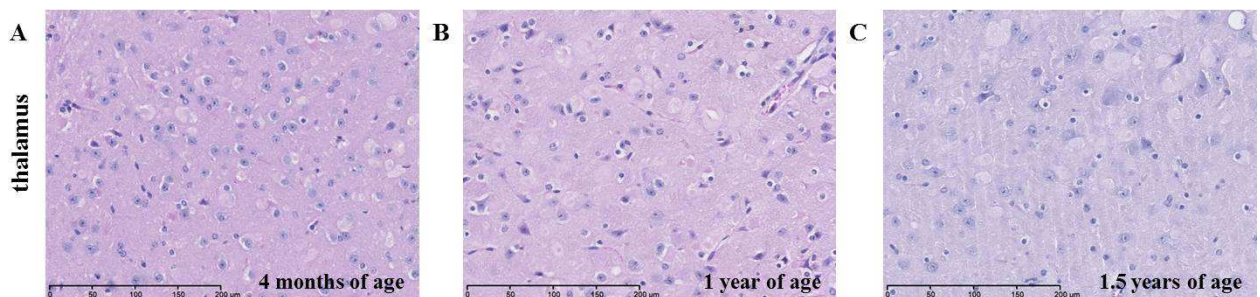


Figure 27: Timeline of neurodegeneration in *Wdr45* KO thalamus. H&E staining of thalamus from three homozygous *Wdr45* knockout animals at A) four months of age; B) one year of age and C) 1.5 years of age showing numerous eosinophil spheroids and swollen structures in all three.

II. RESULTS

Sectioning of more brain regions revealed the described signs of neurodegeneration also in medulla oblongata (figure 28B and C), ascending and descending fibres of the spinal cord (figure 28D) and deep cerebellar nuclei (figure 28G). Via GFAP-staining medulla oblongata showed remarked astrocytosis and astrogliosis (figure 28I).

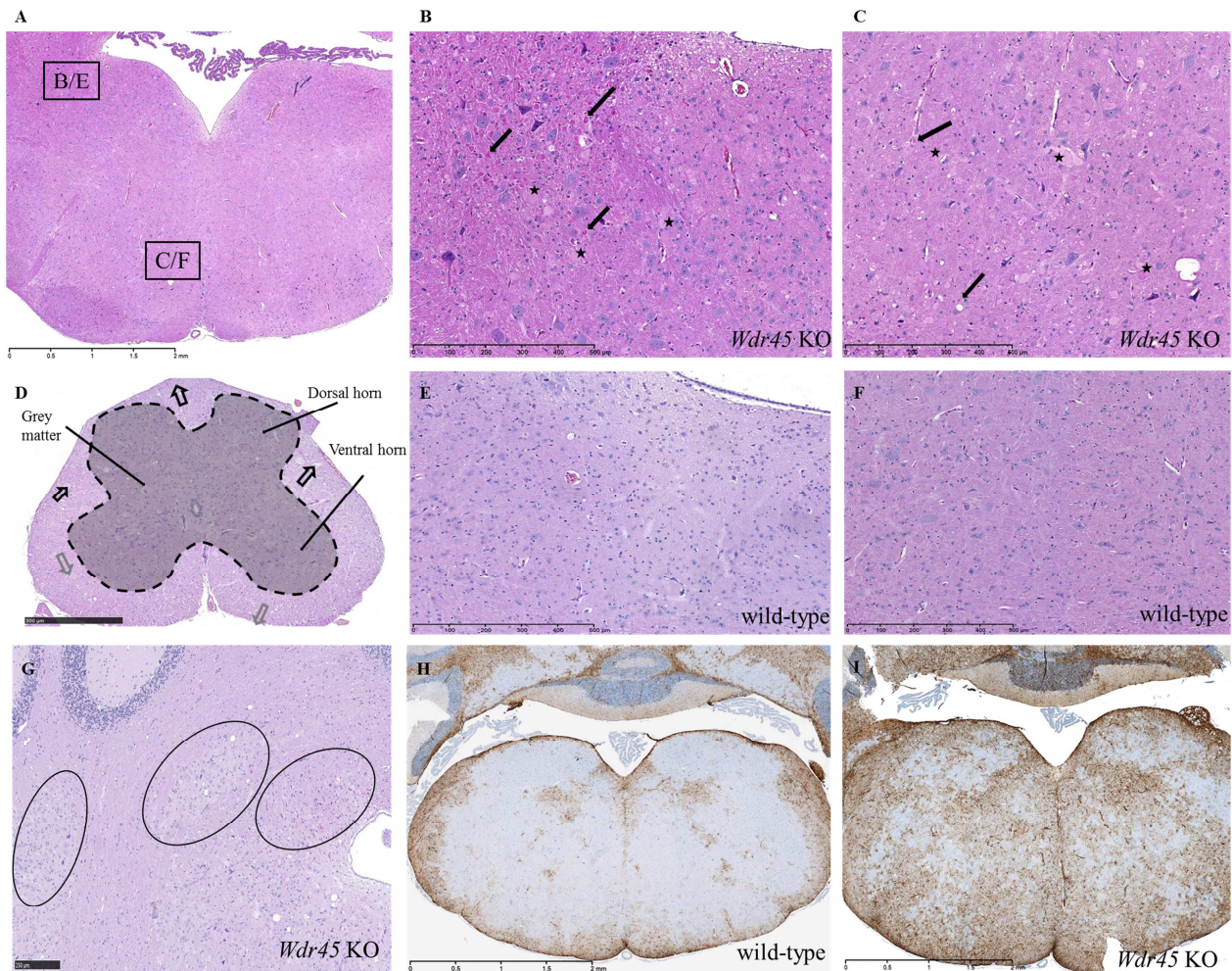


Figure 28: Neurodegeneration in *Wdr45* KO medulla oblongata, cerebellum and spinal cord with astrocytosis in medulla. H&E staining (A-G) and GFAP immunostaining (H-I). **A)** Medulla oblongata with indicated brain regions for B/E and C/F. **B+C)** Medulla oblongata of a *Wdr45* KO mouse, arrows indicate eosinophil spheroids; asterisks indicate swollen structures potentially showing degenerated neurons. **D)** Spinal cord of a *Wdr45* KO brain with indicated grey matter. Axonal spheroids were identified in ascending fibers (black arrows) at the dorsal horn, as well as in descending fibers (grey arrows) at the ventral site. **E+F)** Medulla oblongata of wild-type littermates of *Wdr45* KO mice with no signs of eosinophil spheroids or swollen and degenerated neurons. **G)** Altered deep cerebellar nuclei with signs of eosinophil spheroids and potentially swollen or degenerated neurons circled. **H)** Wild-type medulla oblongata. **I)** *Wdr45* KO medulla oblongata showing marked astrocytosis and astrogliosis.

II. RESULTS

In order to investigate potentially accumulating substances within swollen or degenerating structures, immunostainings were performed as visualized in figure 29 and 30. These mouse specimen showed no iron accumulation (figure 29A and B) as opposed to BPAN patients. Immunostainings showed that neither lipofuscin nor polysaccharides such as glycogen, glycoprotein or glycolipids were accumulating in *Wdr45* KO tissue (figure 29C and D).

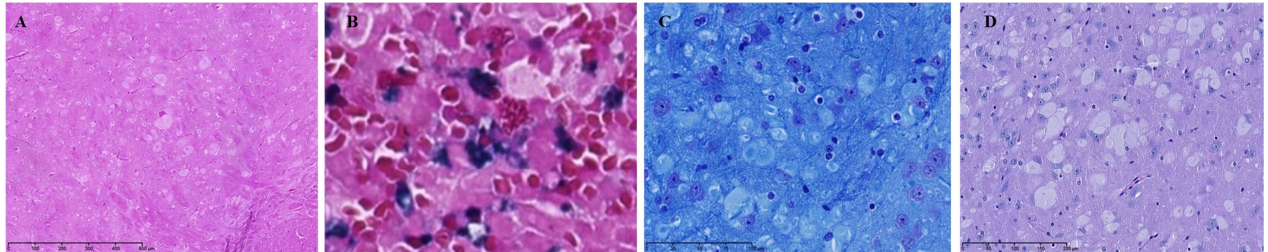


Figure 29: No accumulation of iron, lipofuscin or polysaccharides in degenerating *Wdr45* KO brain sections. A) Turnbull's Blue revealed no iron deposition in medulla oblongata with the positive control in B). C) Kluver-Barrera staining revealed no lipofuscin accumulation. D) Periodic acid-Schiff staining revealed no glycogen, glycoprotein or glycolipids.

Also LC3II- and SDHA-stainings revealed normal cytoplasmic localization in neurons of medulla oblongata (figure 30A and B). Figure 30C shows numerous ubiquitin-positive aggregates in mutant medulla oblongata. Via calbindin-staining an impaired purkinje cell layer of mutant cerebellar cortex was visualized (figure 30D).

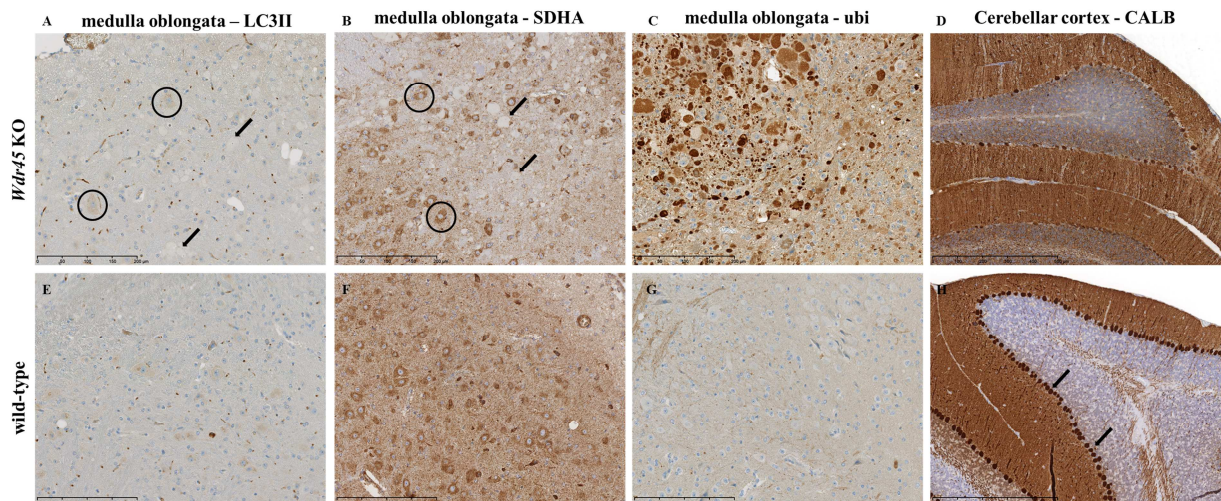


Figure 30: Immunostaining revealed ubiquitin accumulation in medulla oblongata, no SDHA-accumulation in abnormal swollen structures and impaired purkinje cell layer in the cerebellar cortex of *Wdr45* KO mice. Arrows in A and B point towards abnormal neurons in H towards normal purkinje cells, circles denote unaltered normal neurons. A-D) Tissue from a homozygous *Wdr45* KO mouse at the age of 1.5 years. E-H) Corresponding tissue of a wild-type littermate. A+E) Medulla oblongata LC3-immunostained. B+F) Medulla oblongata SDHA-stained. C+G) Medulla oblongata ubiquitin-stained. D+H) Cerebral cortex calbindin-stained.

II.2.6. Secondary screen of aged *Wdr45* KO GMC cohort (F4)

In accordance to GMC guidelines, a cohort of 127 animals was generated in the F4 generation. These animals were not characterized or tested in any way, except for weight measurement until their entry into the secondary screen. It was composed of 38 male wild-type and 26 hemizygous animals, as well as 21 wild-type females, 25 heterozygous and 17 homozygous female animals. This cohort was weighted every two weeks as shown in figure 31 and further left naïve for future observational tests. This was in accordance to regulations from the GMC. At the age of 11 months the cohort was delivered to the GMC for a detailed whole body screen in order to get a complete phenotypic spectrum of the *Wdr45* KO in mice.

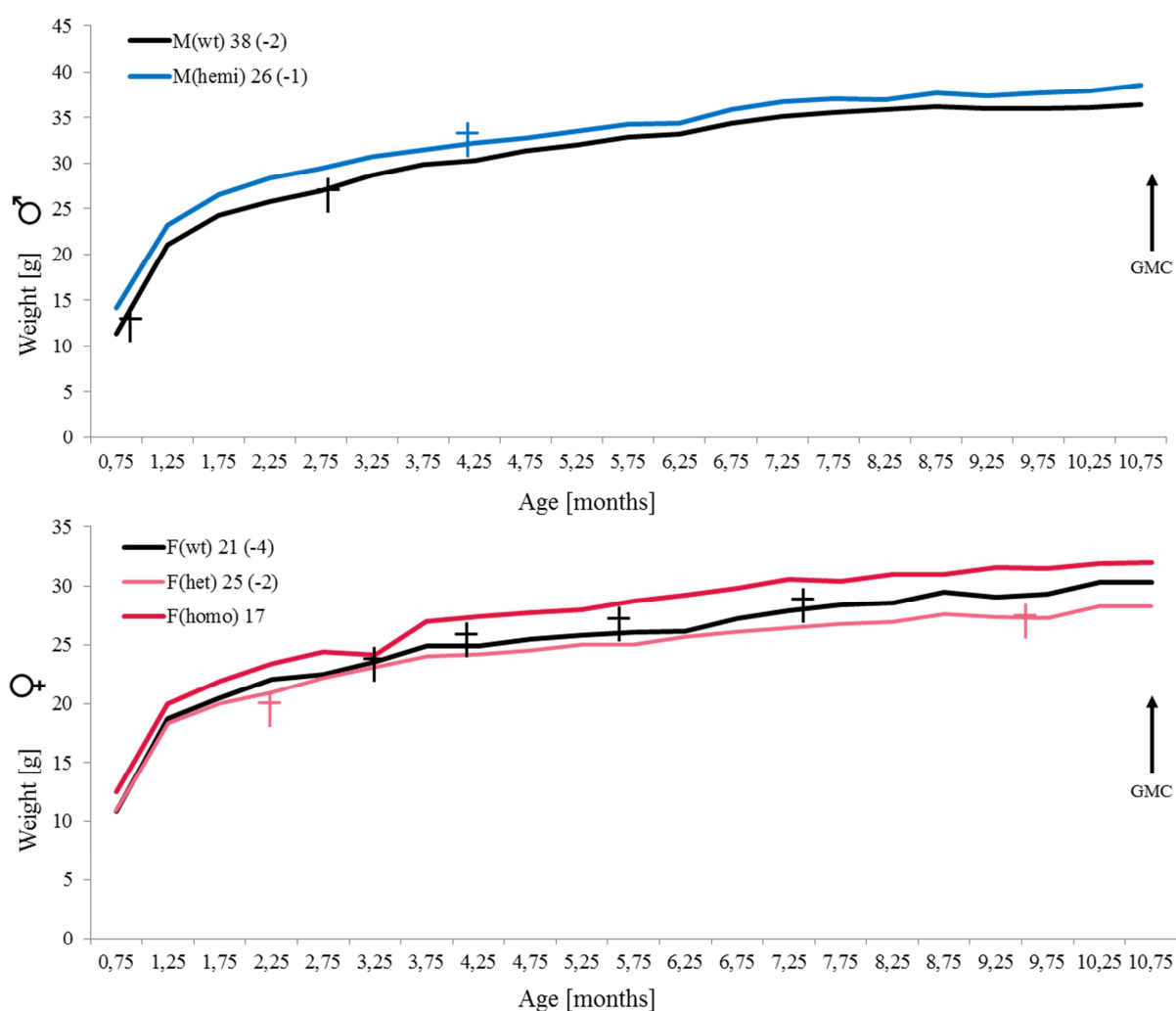


Figure 31: Weight development of the *Wdr45* KO GMC cohort. The upper graph shows the mean male weight development of 38 wild-type and 26 hemizygous animals. The lower graph shows female weight increase of 21 wild-type, 25 heterozygous and 17 homozygous animals. Crosses indicate deceased animals. At eleven months of age the cohort was delivered to the GMC. GMC = German Mouse Clinic.

II.3. DISCUSSION

II.3.1. Of mice and men: the *Wdr45* KO mouse as a model for BPAN

The here established mouse model for BPAN presented the first systemic *Wdr45* knockout mouse. It recapitulated several features of the CNS-specific WDR45-deficient mouse recently published (Zhao et al., 2015). But as a systemic knockout it showed for the first time viability as well as fertility of mice lacking a wild-type *Wdr45* allele. The follow-up analysis of an ageing cohort monitored the disease onset and progression. This data complements the data from the large cohort screen (n = 127) within the GMC in order to elucidate the complete phenotypic spectrum. The GMC cohort was analysed at over one year of age, after the most significant deterioration in mutants should have occurred according to prior characterizations of the preliminary cohort (n = 21) and the disease progression cohort (n = 52). In order to narrow down the screening spectrum within the GMC, our data helps to focus on relevant phenotypes (figure 32).

| Phenotype of <i>Wdr45</i> KO | Preliminary cohort | Disease progression cohort | GMC cohort |
|------------------------------------|--------------------|----------------------------|-------------------------------|
| Weight gain | ↘ | ↗ | ↗ |
| Neurobehavioral abnormality | | | |
| Balance Beam | time ↘ | fall downs↓* foot slips↓* | ↓* |
| Trunk curl | ↘ | ↘ | nya |
| Limb grasp | ↘ | ↓* | nya |
| Grip strength | ↘ | na | nya |
| Inverted grid | ↓* only males | ↓* | nya |
| Impaired hearing (clickbox/ABR) | na | ↓* | ↓* |
| Tremor | nd | ↘ | ↓* |
| Startle response | na | na | ↓* |
| Neuropathology | | | |
| | ↓* | ↓* | nya |
| Evidence | Figure 20A-G | Figures 21-25 | data not shown ^{GMC} |

Figure 32: Overview of identified *Wdr45* KO phenotypes. Overview of phenotypes identified irrespective of the age of onset. Inclining and declining arrows describe trends identified; arrows up and down with asterisks indicate a statistically significant increase or decrease in clinical appearance; nya = not yet analysed; na = not analysed; nd = no difference detected between wild-type and mutant animals. ^{GMC} analysis was performed within the neurology screen of the GMC in cooperation with Dr. L. Becker and Prof. Dr. med. T. Klopstock.

First signs of disease in mice via brain pathology were already visible at four months of age presenting a potential clinical endpoint for therapeutic approaches (figure 33). We found severe neuropathy with axonal spheroids and swollen structures in medulla oblongata of four months old mutants. However, clinically at

II. DISCUSSION

this early state we could not detect any abnormalities in mutants except for slightly increased limb grasping in female mutants. Before one year of age mutant animals showed a trend for motor impairment and neurodegeneration in several investigations (inverted grid, balance beam, locomotor activity, tremor, clickbox, trunk curl and limb grasp). The most prominent signs were an increased number of deaf animals in mutants of both genders as examined by the clickbox and increased limb grasping among mutants. Brain pathology of eleven months old animals revealed substantial neurodegeneration in cerebral cortex, thalamus, cerebellum, medulla oblongata and spinal cord. Neurodegeneration manifested in axonal spheroids and swollen structures with prominent ubiquitin accumulation found in medulla oblongata and severe Purkinje cell depletion in cerebellum.

By the age of one year as analysed within the GMC, WDR45-deficient mice had accumulated a number of phenotypes. Neurobehavioral analysis showed significantly increased tremor and startle response for male and female mutants. Hearing impairment via auditory brainstem response (ABR) analysis was identified in all WDR45-deficient animals with heterozygous females showing intermediate results when compared to knockout and wild-type animals hearing abilities (data not shown). This confirms our findings from the disease progression cohort. Further results from the GMC are in preparation.

A rapid deterioration in mutants as compared to age-matched wild-type animals was observed at 20 months of age within the disease progression cohort. Clinical decline was identified via hearing loss, poor performance on the balance beam, increased tendency for tremor as well as limb grasping. This correlates to the dramatic clinical decline experienced by human patients before the age of 35 years (figure 33).

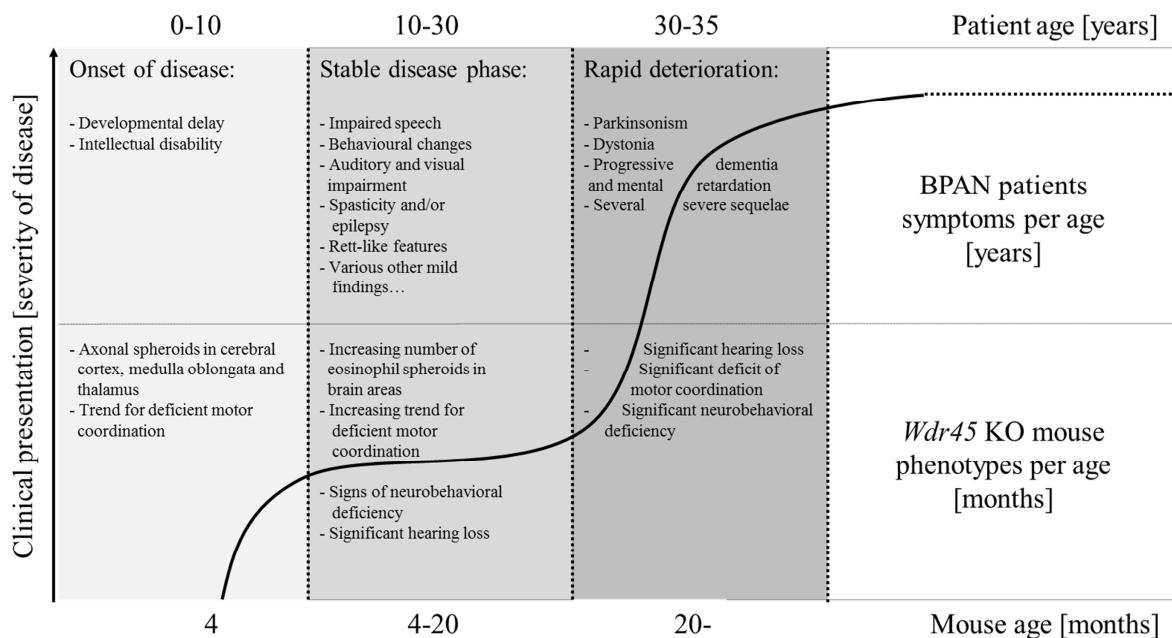


Figure 33: Systematic comparison of BPAN patients' symptoms and *Wdr45* KO mouse phenotypes. The upper half of the graph summarizes human disease progression and the lower half shows phenotypic and pathologic observations in *Wdr45* knockout mice.

II. DISCUSSION

Investigations based on a broad phenotype screening as the one offered by the GMC always involve a multiple testing problem. The p-values reported in this work are nominally significant and were not corrected for multiple testing such as Bonferroni correction. The more reliable genotype specific differences are those consistently significant over time such as neuropathology, clickbox and limb grasp. Also balance beam started to be significant after a certain age. If one would aim for significant results after correction for multiple testing when performing a screen of several hundred parameters the cohort size to reach an acceptable power would increase to impossible numbers. Therefore, it is important to consider these findings as a basis to investigate more targeted questions in the future.

The detailed phenotypic screen of this large cohort aimed to elucidate a comprehensive picture of the clinical spectrum of *Wdr45* KO mice. This spectrum resembled the human phenotype in several characteristics. In both species prominent neurodegeneration occurred in hand with neurobehavioral deficits. After mild onset human and murine mutants seem to experience a stable phase, which in humans is followed by a rapid disease progression. Mice also seem to experience a decline around the age of one year with a rapid clinical deterioration after 20 months of age as compared to age-matched wild-type animals. However, the exact severity is difficult to estimate. A clear difference worth noting is that heterozygous females showed a near-wild-type or intermediate phenotype in almost all examinations. In human patients, BPAN is reported to be caused by one *de novo* loss-of-function allele (Haack et al., 2013). This shows a major difference between mice and may imply that mice can compensate one loss-of-function allele better than humans. This is concordant with the finding that mice are viable without a *Wdr45* wild-type allele, whereas humans do not seem to be.

Overall, it is challenging to generate a suitable disease model and there will always be substantial differences between mice and men. Nevertheless, the knockout of *Wdr45* seems to evoke a severe and comparable defect. Unfortunately, when comparing the preliminary screen, the disease progression cohort, and the GMC cohort, there are a few differences (figure 32). They differ in genotype-related findings such as weight development, motor impairment via inverted grid in females and total deafness, which was either complete in mutant groups by the age of one year or one and a half years. This variance might be due to the genetic background of this mouse line. Since our mouse line has a mixed background of C57BL/6 with FVB and has been inbred for four generations, the genetic background may differ to some extent with every generation. Moreover, the X-linked location of *Wdr45* requires mating between non-litter-mates in order to get all five genotypes. Therefore, genetic drift may influence the phenotype, which could be an increasing problem with later generations. Nevertheless, all cohorts are comparable in the most significant findings of neuropathology and neurobehavioral deficiency, which is in concordance with the CNS-specific *Wdr45* KO mouse from Japan, reported to have a clear C57BL/6N background (Zhao et al., 2015). However, the mixed background of our BPAN model also had an advantage. Mixing the commonly used and well established C57BL/6 background with FVB was beneficial, because wild-type C57BL/6 mice

II. DISCUSSION

generally suffer from hearing impairment at the age of approximately half a year. The great majority of wild-type animals with mixed background used in this work were able to react to the acoustic clickbox test even after one and a half years of age (15/19). This enabled investigation of hearing impairment in age-matched mutant animals. Hearing ability of only 4% of hemi- and homozygous males and females (1/23) and intermediate ability in heterozygous females (4/10) was shown.

Several brain regions with proposed functions were shown to be affected in the CNS-specific *Wdr45* KO as well as in the here established systemic knockout mouse line. For example caudate nucleus, cortex and cerebellum are involved in learning and memory. Thalamus and cerebellum are also associated with motor coordination and pons with sleeping behaviour. It is to note that many brain areas deteriorated in both mouse models affect the auditory system, such as dorsal cochlear nucleus, pons and inferior colliculus. This may connect to impaired hearing found in the here established systemic *Wdr45* KO mouse line. Affected cell types range from glial cells, astrocytes to neurons and include Purkinje cells with the most characteristic finding being axonal swellings.

In general, BPAN is a neurodegenerative disorder, but it might involve deleterious effects on multiple organs. Surprisingly, even in our systemic knockout mouse, major symptoms seem to be mainly of neurologic decent. Nevertheless, the systemic *Wdr45* KO model provides means to study other organs, which might develop an earlier phenotype than the ones identified so far. Also identification of affected tissues, which are accessible in living animals, would be beneficial to the use of the BPAN model for treatment approaches. Elucidation of the pathomechanism can benefit from the model established in this work. *Wdr45* is known to be involved in autophagy as described in II.1.2.5., which is an essential cellular process. Dysfunctional autophagy has been shown to lead various consequences involving multiple organs, once again underlining the importance of a systemic *Wdr45* KO.

II.3.2. The BPAN mouse model helps investigate disorders of autophagy

The cytoprotective metabolic pathway of autophagy and lysosomal degradation is essential for cellular homeostasis. Genetic or environmental disruption leads to multisystem disorders. Most dramatically affected organs are those with high energy consumption. Neurons and muscle cells show high energy demand, and accordingly brain and skeletal as well as cardiac muscle develop severe symptoms upon impaired autophagy. Associated phenotypes include neurodegeneration (Saito et al., 2013), muscle diseases (Ravenscroft et al., 2015) and cardiovascular diseases (Lavandro et al., 2013). Other pathologies like infectious disease (Huang and Brumell, 2014), cancer (Galluzzi et al., 2015) and metabolic disorders (Behrends et al., 2010) have been reported in association with impaired autophagy. Congenital disorders of autophagy often result from germline transmitted, hence systemic knockout mutations in autophagy-related genes. In the following it will be discussed how different organs are affected by autophagy impairment.

II. DISCUSSION

This highlights the importance of the here established systemic *Wdr45* KO mouse, which can be used in the future for elucidation of the autophagy pathway and its impact on different organs.

Neurodegeneration is a major consequence of inefficient autophagy. When large proteins or organelles are not properly degraded via autophagy in neurons, protein aggregates accumulate. In this respect three well-known neurodegenerative disorders have been reported in the context of autophagy, Huntington's disease (HD) (Ravikumar et al., 2002), Alzheimer's disease (AD) (Berger et al., 2006) and Parkinson's disease (PD) (Webb et al., 2003). In the case of HD, resulting aggregates seem to be toxic. The polyglutamine expansion disease builds mutant huntingtin with increased propensity to form aggregates. This toxic accumulation first leads to damaged basal ganglia and substantia nigra, which is the same affected region as in BPAN patients. With disease progression cerebral cortex, hippocampus, Purkinje cells and cerebellum are affected, which is similar to our results in the *Wdr45* mouse model. This may hint towards these brain regions and cell types being more vulnerable towards impaired autophagy. AD has been linked to autophagy, as it accumulates hyperphosphorylated tau protein in neurofibrillary tangles. Also amyloid-beta plaques accumulate mainly in mitochondria, decreasing the affected neurons capability to utilize glucose. Accumulation of autophagosomes and autolysosomes in a mouse model for AD as well as in patient brains hint towards impaired autophagic flux. PD is an α -synucleinopathy accumulating α -synuclein within Lewy bodies in neurons. It is characterized by a loss of dopaminergic cells primarily in the substantia nigra accompanied with iron accumulation. This is also the most prominent feature of BPAN and may connect the two disease patho-mechanisms possibly via autophagy impairment. For all these common pathological disorders as well as BPAN, autophagy upregulation may be a way to approach treatment strategies. This could increase degradation of the respective aggregate and potentially improve the clinical presentation.

Murine impairment of autophagy, for example in a CNS-specific *Atg7* KO mouse leads to neurodegeneration with neuronal loss in cerebral and cerebellar cortices and poly-ubiquitination in degenerating neurons. Animals present with limb grasping and impaired motor coordination with mortality at around seven months of age (Komatsu et al., 2006). Except for premature mortality all phenotypes overlap with observations found in the *Wdr45* deficient mouse. This indicates that decreased autophagic flux may result in similar phenotypes albeit caused by abrogation at various pathway stages. In terms of the here established BPAN mouse model, iron accumulation in basal ganglia and substantia nigra was not detected, however we did identify severe neurologic deterioration. Therefore, this model can be used to further investigate possible autophagy inducing agents and their effect on affected brain areas. Findings in this model may then be translatable to more common disorders like PD, HD or AD disease. Conversely, BPAN research can translate findings from PD, HD and AD. All show increased neuronal apoptosis, which can be tested via TUNEL. This marker of endonucleolytic chromatin cleavage should be tested in *Wdr45* brain tissue in order to investigate whether increased apoptosis follows impaired autophagy. This would be

II. DISCUSSION

a sign that swollen structures found in several brain regions in our *Wdr45* mouse line are indeed degenerating neurons.

Myopathy classically presents with hypotonia and muscle weakness and has also been reported in connection with impaired autophagy (Ravenscroft et al., 2015). mTORC1 as one of the key regulators of autophagy when deficient in mice results in skeletal muscle atrophy, and when constantly activated it leads to late-onset myopathy (Castets et al., 2013). This demonstrates the highly sensible regulation of the autophagy pathway. Muscle-specific *Atg5* KO mice on the other hand, show muscle fibre atrophy with p62-accumulation and ubiquitin-positive fibres. Similarly muscle-specific *Atg7* KO mice present with skeletal muscle atrophy and force deficits (Masiero et al., 2009, Masiero and Sandri, 2010). Systemic *Atg5* KO mice die postnatally with energy depletion in the heart (Kuma et al., 2004). Heart-specific KO of *Atg5* in mice causes cardiac hypertrophy, contractile dysfunction and ubiquitin-positive aggregates as well as aggregated mitochondria (Nakai et al., 2007). Cardiomyocyte-specific depletion of mTORC1 leads to dilated cardiomyopathy in mice along with premature death (Zhang et al., 2010). Together, these reports suggest the heart to be an organ highly vulnerable to autophagy impairment (Lavandro et al., 2013).

Since *WDR45* is highly expressed in brain and muscle tissue both skeletal and cardiac (Proikas-Cezanne et al., 2004) it is likely a key player in autophagy within these organs. But it remains an open question whether its protein family members WIPI1, WIPI2 and WIPI3 can substitute its function in distinct organs leading to a less significant organ-specific phenotype in our BPAN mouse model.

The process of autophagy does not only differ between tissues, but it also handles various types of cargo. There is a subtype of autophagy that degrades mitochondria, called mitophagy. This specific subtype might be subject to *Wdr45*-deficiency, as swollen mitochondria have been shown to accumulate in brains of CNS-specific *Wdr45* KO mice (Zhao et al., 2015) via electron microscopy. Impaired mitochondrial respiration leads to increased reactive-oxygen species (ROS), which normally induces autophagy (Lemasters, 2005). Therefore, if mitophagy is deficient, defective mitochondria cannot be cleared by the increased autophagy induction and in turn lead to accumulation of early autophagic structures. It would be interesting to test whether *WDR45* is particularly involved in mitophagy. Another subtype involved in metabolic diseases is lipophagy (Christian et al., 2013). Lipophagy regulates storage of lipids such as Apolipoprotein B, and therefore maintains lipid homeostasis. Mainly affected organs via impaired lipophagy should be liver and adipose tissue. Functional autophagy leads to the conversion of white to brown adipose tissue, hence impairment of lipophagy would lead to increased white adipose tissue in affected animals.

In conclusion, autophagy is essential for all tissues and impairment leads to a variety of phenotypes involving multiple organs. As autophagy serves to degrade non-functional proteins and organelles it becomes increasingly important in the ageing organism. As mentioned above, it is involved in the

II. DISCUSSION

development of typically late-onset disorders such as PD and AD. This can also be an explanation for the characteristic rapid disease progression in BPAN. With lower activity of autophagy due to mutant enzymes of the pathway at onset and early adulthood, first symptoms arise in patients. But, with ageing-induced additional decrease of the remaining autophagic activity the cells cannot keep up with minimum cellular needs. Therefore, not reaching a required threshold of autophagic activity would lead to the observed rapid clinical decline. If this theory is true, autophagy induction should delay the rapid disease progression in patients. Furthermore, the here established *Wdr45* KO model should improve or delay its clinical abnormalities upon autophagy induction. This therapeutic approach is discussed in the following along with other treatment strategies.

II.3.3. From the BPAN mouse model to therapeutic strategies

In terms of development of a therapy for BPAN there are several approaches. A general approach for severe single gene disorders is gene transfer therapy. Using a vector such as lentivirus or adeno-associated virus (AAV) a wild-type copy of the respective gene is transferred into the affected tissue.

Also enzyme replacement therapy can be an option, where the functional enzyme is injected intrathecally into the affected patients' brain. Clinical trials for this enzyme replacement therapy have been completed for other disorders such as mucopolysaccharidose type I (Trial ID: NCT00786968) or are currently recruiting for example for metachromatic leukodystrophy (Trial ID: NCT01510028).

These approaches can be used even when the pathomechanism of the monogenetic disease is not known. *Wdr45* dysfunction has been shown to be at least partly due to impaired autophagy. Therefore, pathway-specific drug development should be the focus of translational research. A direct approach would be to administer autophagy inducing drugs to an appropriate animal model and investigate a suitable primary outcome. In this respect, the here established BPAN mouse model could be used with a primary outcome of neurodegeneration at four months of age, which has been shown to be 100% penetrant. Also a non-lethal way to investigate brain pathology such as brain MRI would be beneficial for future use of the model, facilitating the assessment of long-term therapy effects. Identification of a non-invasive outcome would greatly improve the use of this disease model. Several autophagy-inducing drugs have been tested, such as resveratrol in rats (Shu et al., 2015). Rapamycin as an mTORC1 inhibitor, induced autophagy and rescued age-related ocular muscle dysfunction in mice (McMullen et al., 2009). An FDA (U.S. Food and Drug Administration) and EMA (European Medicines Agency) approved analog of rapamycin, temsirolimus has been tested *in vitro* and *in vivo* in animal models. It induced autophagic clearance of pathologic tau protein aggregates and is suggested as a treatment in HD, PD and AD (Jiang et al., 2014). Resveratrol, rapamycin, temsirolimus or other autophagy inducing drugs, should therefore be part of future therapy related research on BPAN.

II. DISCUSSION

As discussed earlier, WDR45 might be involved in proper mitophagy. Since mitophagy has been suggested to be induced by non-functional mitochondria or generally reduced mitochondrial respiration via increased ROS production, increased respiration might halt mitophagy. In this respect nicotinamide riboside has been tested as a vitamin and precursor of NAD⁺, which in turn regulates mitochondrial function via sirtuins and mitochondrial gene expression (Cerutti et al., 2014). In an AD mouse model long-term dietary nicotinamide riboside-supplementation lead to an increased life span as well as increased CS activity and prevention of mitochondrial membrane depolarization during oxidative stress. Nicotinamide riboside treatment further rescued cognitive dysfunction in murine AD amyloid neuropathology (Gong et al., 2013). But before investigation of mitochondrial activity influencing agents it needs to be tested whether the *Wdr45* mouse shows decreased mitochondrial respiration.

Currently, there is a trial within the framework of TIRCON recruiting PKAN patients, which like BPAN is a subtype of NBIA with iron accumulation in the substantia nigra. The multicenter, unblinded, single-arm pilot study administers deferiprone in a twice daily oral dose to patients for one year (TIRCON NCT00907283). Deferiprone is an iron chelator, which can cross the blood-brain barrier as well as mitochondrial membranes. Iron chelation is a promising approach as iron overload might lead to neuronal death via its interaction with ROS in oxidative stress. Nevertheless, iron accumulation in substantia nigra could as well be harmless, since substantia nigra is even in healthy patients high in iron content. But promising results in single case-studies of deferiprone on PKAN patients (Forni et al., 2008) lead to a trial on PD patients (Trial ID: NCT00943748), who also abnormally accumulate iron in substantia nigra.

Conclusively, there are several treatment approaches based on current genetic engineering and gene transfer techniques as well as pathway-specific modifier drugs. These should be tested *in vitro* in neurons differentiated from patient-derived iPS cells (induced pluripotent stem cells). Promising treatments can then be tested on organismal level in the here established *Wdr45* KO mouse line and provide a basis for BPAN patient treatment.

III. Therapeutic strategy for glutaric aciduria type 1

III.1. INTRODUCTION

III.1.1. The lysine degradation pathway

The lysine degradation pathway is the central pathway involved in glutaric aciduria type 1 (GA-I). The essential amino acid, lysine is degraded in a pathway involving the amino acids L-tryptophan and L-hydroxylysine. As described in figure 34A, there are two distinct degradation routes, the peroxisomal pipercolate- and the mitochondrial saccharopine pathway. They are thought to constitute the major cerebral and hepatic route, respectively. Both pathways converge at the synthesis of mitochondrial 2-aminoadipate-6-semialdehyde. This product is exported to the cytosol, where it is oxidised to 2-aminoadipate and degraded to 2-oxoadipate via the AADAT transaminase (2-aminoadipate transaminase). If further degradation of 2-oxoadipate within mitochondria is impaired, for example via non-functional 2-oxoglutarate-dehydrogenase-like-complex (OGDHL) or dysfunctional DHTKD1 (probable 2-oxoglutarate dehydrogenase E1 component), the two metabolites 2-aminoadipate (AA) and 2-oxoadipate (OA) accumulate. In individuals with 2-aminoadipic 2-oxoadipic aciduria (see III.1.3.), liver and brain are the mainly affected tissues. However, most individuals with 2-aminoadipic 2-oxoadipic aciduria are asymptomatic. In case DHTKD1 is functional, OA is decarboxylated to glutaryl-CoA. Glutaryl-CoA is further degraded to glutaconyl-CoA, crotonyl-CoA and finally to acetyl-CoA, which is a key player in the tricarboxylic acid cycle. GA-I is characterised by non-functional GCDH (see III.1.2.), where glutaryl-CoA cannot be properly degraded. This leads to the accumulation of glutaric acid (GA), 3-hydroxyglutaric acid (3-OHGA) and glutaryl-carnitine (C5DC). GA as well as OA can be released via urine. However, abnormally high levels of GA lead to an accumulation of glutaryl-CoA. Like 3-OHGA, glutaryl-CoA is putatively toxic. C7ORF10 transfers CoA from succinyl-CoA to GA generating glutaryl-CoA. This way C7ORF10 acts as a metabolic repair mechanism. Non-functional C7ORF10 is described as glutaric aciduria type III (GA-III) with mainly asymptomatic patients. Glutaric aciduria type II (GA-II) results from an imbalance of FAD/FADH caused by mutations in genes involved in the electron transfer of the mitochondrial respiratory chain. It is therefore indirectly involved in the lysine degradation pathway and will not be addressed further.

Overall, the lysine degradation pathway is not well understood to date and figure 34A summarizes the current understanding. In order to evaluate the essentiality of enzymes involved in this pathway, the ExAC Browser was used (figure 34B). It calculates the expected number of mutations within genes and compares this to the observed number of mutations in a database of more than 60,000 exomes. This results in a z-score, which is positive when the number of expected exceeds the number of observed mutations per gene. A positive z-score as in the case of *GCDH* describes this gene as less tolerable to mutations than expected

III. INTRODUCTON

(figure 34B). This is also the case for *ETFA* and *AADAT*. The genes associated to conditions with asymptomatic patients such as *C7ORF10* and *DHTKD1* are shown to tolerate mutations better.

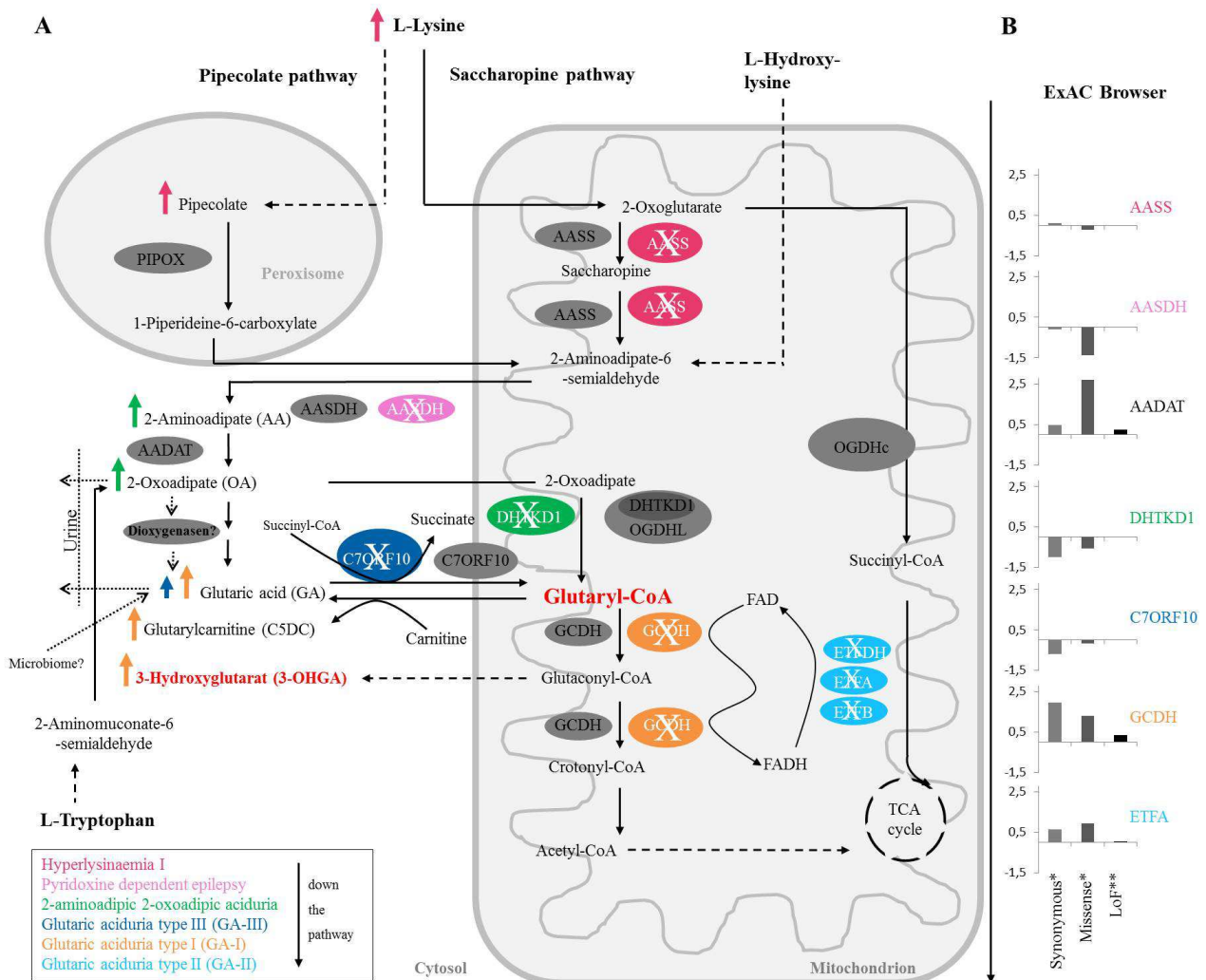


Figure 34: Schematic of the lysine degradation. **A)** L-lysine, L-tryptophan and L-hydroxylysine degradation pathway. All enzymes are shown in round grey shapes. Crossed, coloured enzymes describe their state of deficiency. Consequences of deficiencies, such as GA-I due to GCDH deficiency, are depicted in orange; DHTKD1 deficiency in green and AASS and AASDH deficiency and its consequences in red and pink. C7ORF10 deficiency (GA-II) is visualised in dark blue and enzymes leading to GA-II in light blue. The legend names associated diseases in order of appearance within the pathway. Coloured arrows describe accumulating metabolites during colour coded deficiencies. PIPOX = pipecolate oxidase; AASS = 2-aminoadipate-6-semialdehyde synthetase; AASDH = 2-aminoadipate-6-semialdehyde dehydrogenase; AADAT = 2-aminoadipate transaminase; OGDHc = 2-oxoglutarate-dehydrogenase-complex; OGDHL = OGDHc-like complex; DHTKD1 = probable 2-oxoglutarate dehydrogenase E1 component, mitochondrial; GCDH = glutaryl-CoA dehydrogenase, mitochondrial; C7ORF10 = succinate-hydroxymethylglutarate CoA-transferase; FAD = flavin adenine dinucleotide; ETF = electron transfer flavoprotein; TCA = tricarboxylic acid. Red bold metabolites are potentially toxic. **B)** ExAC Browser data describes discrepancies between expected and observed variant counts for synonymous, missense and loss-of-function (LoF) variants (Exome Aggregation Consortium, Cambridge, MA (URL: <http://exac.broadinstitute.org>) [20th May, 2016]). * z-score, if positive it describes fewer variants, if negative more variants than expected. ** constraint metric is a measure of tolerance to LoF variants, with 0 denoting complete tolerance.

III. INTRODUCTON

The complex lysine degradation pathway is known to be disturbed in several disorders sometimes leading to toxic accumulations of metabolites. Importantly, there are asymptomatic individuals known, which harbour blocks in the degradation pathway upstream of the toxic accumulation. In theory, inhibition of this specific step in the degradation pathway prevents the toxic accumulation without development of a disease. The most direct target to block, in order to prevent the development of GA-I with its glutaryl-CoA and 3-OHGA accumulation, is DHTKD1. If this theory stands an inhibitor of DHTKD1 could be used as a therapy for GA-I patients.

III.1.2. Glutaric aciduria type 1 - GCDH

Glutaric aciduria type 1 (GA-I, OMIM #231670) is a disorder of autosomal recessive inheritance, with impaired mitochondrial metabolism of L-lysine, L-hydroxylysine and L-tryptophan. This specific impairment of the lysine degradation pathway leads to an accumulation of GA, C5DC and putatively toxic 3-OHGA in tissues and body fluids of patients. Its estimated prevalence is 1 in 100,000 newborns (Lindner et al., 2004) with increased incidence among some ethnic groups such as the Amish populations. The disease onset is typically between 3 months and 3 years of age. It presents with acute encephalopathy with leukoencephalopathy and macrocephaly as well as injury of the basal ganglia with striatal lesions. Movement disorders and various other symptoms such as spasticity are often present. A trigger for disease manifestation is an early encephalopathic crisis evoked by routine vaccination or more frequently intercurrent febrile illnesses. The current standard of care includes mainly lysine-restricted diet, L-carnitine supplementation and intensified emergency treatment aimed at prevention of a catabolic state during infectious disease. Other prescribed therapeutics are limited to standard symptom-specific substances such as baclofen, benzodiazepines and botulinum toxins for the treatment of dystonia and spasticity (Kolker et al., 2007). Riboflavin is often used to enhance mitochondrial activity and improve neurological outcome in several mitochondriopathies (Bugiani et al., 2006), but its effect on GA-I patients is questionable (Kolker et al., 2006). If treated by the gold-standard guidelines (Kolker et al., 2007), encephalopathic crisis can often be prevented during the most vulnerable first three years of life. This circumvents most irreversible long-term symptoms, but some patients are not respondent to this treatment (Strauss and Morton, 2003). Early diagnosis of this disease is essential for effective treatment. Consequently, GA-I is part of the nationwide newborn screening since 2005 (Heringer et al., 2010). Probands are tested for increased glutaryl-carnitine in dried blood spots. In case of a positive result, levels of glutaric-acid (GA), as well as 3-hydroxyglutaric acid (3-OHGA) should be measured in urine via GC-MS (gas chromatography - mass spectrometry). The final confirmation of GA-I as a diagnosis can be achieved via sequencing of the disease-associated gene *GCDH* or enzyme analysis of GCDH. Depending on the biochemical urinary GA level one can distinguish between low (<100 mmol/mol carnitine) and high excretors (>100 mmol/mol carnitine), harbouring 30% and no GCDH activity, respectively. The excretor group does not predict the clinical phenotype (Muhlhausen et al., 2003, Christensen et al., 2004). Of note, in the group of low

III. INTRODUCTON

excretors, there are more false-negative screening results hindering early diagnosis for affected individuals. But, even if treatment is started early before onset of the disease, there are several patients, roughly one third, who still develop severe symptoms (Strauss and Morton, 2003), highlighting the need for improved therapeutic approaches.

Genetic and biochemical analysis of GA-I patients revealed more than 60 different deleterious mutations within *GCDH* (Zschocke et al., 2000). The gene is located on 19p13.2 and is composed of 11 coding exons. The resulting protein GCDH is composed of 438 amino acids with an N-terminal mitochondrial targeting sequence. It is located in the mitochondrial matrix and forms a homotetramer of 45 kDa subunits. GCDH is flavin-dependent and catalyses the oxidative decarboxylation of glutaryl-CoA to glutaconyl-CoA and further to crotonyl-CoA within the lysine degradation pathway (figure 34). Impairment of GCDH function leads to brain accumulation of GA (500-5000 $\mu\text{mol/l}$), 3-OHGA (40-200 $\mu\text{mol/l}$) and C5DC sometimes along with secondary glutaconic acid accumulation. Upon lysine-reduced diet, patients' metabolite levels normalise to GA of 5-39 $\mu\text{mol/l}$ and 3-OHGA of 7 $\mu\text{mol/l}$ in brain. GA accumulation was long believed to be toxic, and it is up to 1000-fold higher in brain than in plasma. However, nowadays glutaryl-CoA or 3-OHGA are considered the most likely causal toxic metabolites. This was confirmed by the condition GA-III, where most affected individuals are asymptomatic, and GA, but neither glutaryl-CoA nor 3-OHGA, are accumulating.

There are established mouse models for GA-I recapitulating various disease symptoms. The well characterised mouse model *Gcdh*^{-/-} has been generated via homologous insertion of a targeting vector carrying a β -galactosidase reporter gene, thereby lacking the first seven exons of *Gcdh* (Koeller et al., 2002). The mouse recapitulates major neurologic deteriorations such as brain vacuolisation in the striatum, which has also been shown in human frontal white matter. Human patients show severe striatal lesions leading to dystonia often accompanied with spasticity. *Gcdh*^{-/-} mice show no neuronal loss or gliosis in striatum, but impaired reactivity to the pre-pulse inhibition test, which is an indicator of deficient striatal development. Neurobehavioral deficiency was assessed via deteriorated performance on a rotarod and balance beam test. Strikingly, the biochemical analysis of this GA-I mouse model reveals putative neurotoxic accumulations of organic acids, consistent with the human biochemistry. *Gcdh*^{-/-} mice excrete 19 ± 3 mg GA/mg creatinine versus normal mice's excretion of less than 0.187 mg GA/mg creatinine, describing a 100-fold GA increase in *Gcdh* deficient animals. 3-OHGA is not detectable in normal human and mouse urine but does accumulate in both diseased probes to roughly 0.7 mg/mg creatinine. Brain levels in *Gcdh* KO mice are 0.52 mM for GA and 0.038 mM for 3-OHGA (Koeller et al., 2002). Overall, there is a striking biochemical resemblance between mice and men, both in urinary excretion and brain levels. Some neurobehavioral abnormalities and brain pathology in mice show neurodeterioration, which is present in human patients. Hence, if the putatively toxic accumulation of organic acids in patients indeed

leads to the observed neurodeterioration, the biochemically highly similar GA-I mouse model is considered to be of great use for treatment approaches.

III.1.3. 2-aminoadipic 2-oxoadipic aciduria – DHTKD1

2-aminoadipic 2-oxoadipic aciduria (OMIM #204750) is a biochemical condition with high levels of 2-aminoadipate and 2-oxoadipate. Affected individuals show urinary 2-oxoadipate levels of 10-120 mmol/mol creatinine and blood plasma 2-aminoadipate levels of 120 $\mu\text{mol/l}$, where the normal reference range is below five for both measurements. Its clinical manifestation is heterogeneous with more than half of all known patients being asymptomatic (Danhauser et al., 2012). Therefore, it should not be described as a disease, but as a biochemical condition. The other patients develop a variety of symptoms with mild to severe intellectual disability, muscular hypotonia, ataxia, epilepsy or developmental delay (Duran et al., 1984, Hagen et al., 2015, Stiles et al., 2015). As an autosomal recessive condition, patients harbour compound heterozygous or homozygous deleterious mutations in the disease-associated gene *DHTKD1*. Mutations in *DHTKD1* have even been associated to the neurological disorder Charcot-Marie-Tooth Type 2 (CMT2) with a dominant pattern of inheritance within a single Chinese family (Xu et al., 2012). Since heterozygous mutations have not been associated to disease in any of the families studied in context of 2-aminoadipic 2-oxoadipic aciduria, its causality for CMT2 is uncertain and to our knowledge has not been confirmed by any other group since the first publication.

The condition-associated gene *DHTKD1* encodes the probable 2-oxoglutarate dehydrogenase E1 component DHTKD1 with mitochondrial localisation (Bunik and Degtyarev, 2008), which is also known as dehydrogenase E1 and transketolase domain containing 1. With high homology to the OGDHc (oxoglutarate dehydrogenase complex), DHTKD1 supposedly serves as an E1 enzymatic component of an OGDHL (OGDHc-like complex) with dihydrolipoamide succinyltransferase as E2 and lipoamide dehydrogenase as E3. OGDHc catalyzes the conversion of 2-oxoglutarate to succinyl-CoA as visualised in figure 34A. DHTKD1 is likely involved in the decarboxylation of OA to glutaryl-CoA and if deficient leads to the accumulation of its substrate OA, as well as AA. Xu and colleagues have investigated functional relevance of DHTKD1 via suppression studies in tumour cell lines and found altered energy metabolism in hand with decreased ATP production, increased ROS, increased apoptosis and a reduced number of mitochondria indicating impaired mitochondrial homeostasis. Moreover, silencing of DHTKD1 also reduced the activity of OGDHc, strengthening the hypothesis of their tight interaction (Xu et al., 2013).

Detailed structure-function analysis of OGDH as well as DHTKD1 was performed by Bunik and Degtyarev (Bunik and Degtyarev, 2008), which revealed several functional domains and active sites within DHTKD1. A co-factor of DHTKD1 is thymidine diphosphonate (ThDP) describing DHTKD1 as well as OGDHc as ThPD-dependent enzymes. They harbour a domain PP (E1_dh domain in PFAM), which binds

the pyrophosphate part of ThDP and a domain PYR (Transket_pyr domain in PFAM) for the pyrimidine part. There are three active site loops with the first one interacting with thiamine diphosphate (ThDP) and the second and third loop leading to the high affinity binding of the 2-oxoglutarate substrate and a proper decarboxylation reaction. Since DHTKD1 and OGDHc are sensitively regulated by ThDP, this co-factor has been suggested as a possible drug target. ThDP is a universal systemic regulator of central metabolism, but its derivatives can be used to specifically manipulate metabolism (Trofimova et al., 2010, Bunik et al., 2013). This opens new perspectives for novel therapeutic approaches.

III.1.4. Glutaric aciduria type 3 – C7ORF10

Glutaric aciduria type 3 (GA-III) is a condition (OMIM #231690) characterized by high glutaric acid in urine and blood of patients. It was first described in 1991 (Bennett et al., 1991), and the underlying disease-associated open reading frame *C7ORF10* was identified in 2008 at first in the Old Order Amish children. *C7ORF10* carries a putative mitochondrial targeting sequence as well as a coenzyme A (CoA) transferase domain, which is thought to transfer CoA to glutaric acid to form glutaryl-CoA (Sherman et al., 2008). Single cases of GA-III have been reported with clinical features such as failure to thrive, dysmorphic features and postprandial vomiting. The majority of cases are free of symptoms leading to GA-III being better described as a biochemical condition than disease (Knerr et al., 2002). This condition is not detected in the newborn screening, because the screen measures levels of C5DC to detect GA-I. But the clinical relevance of a GA-III diagnosis is negligible. Its investigation helps understanding the lysine-degradation pathway in general and the pathomechanism of GA-I in particular. Knowledge of the condition GA-III, resulting in high GA but no accumulation of glutaryl-CoA and its downstream derivatives 3-OHGA and C5DC (see figure 34), questions GA as the primary neurotoxin in GA-I. This leaves glutaryl-CoA or its derivative 3-OHGA as the putative neurotoxins. Furthermore, in theory, inhibition of *C7ORF10* could lead to a decrease of glutaryl-CoA in GA-I patients, when GA cannot be converted.

III.1.5. DHTKD1 inhibition as a therapy for glutaric aciduria type 1

As first suggested in 2012 by the Institute of Human Genetics at the Technische Universitaet Muenchen (Danhauser et al., 2012), inhibition of DHTKD1 in human GA-I patients could prevent accumulations of toxic metabolites and improve clinical presentation. First it needs to be shown that DHTKD1 inhibition or in the extreme scenario *DHTKDI* knockout is harmless. Generation and characterization of a *Dhtkd1* KO mouse would help answering this question. However, to date there is only one mouse model available with a knockout in an enzyme directly involved in the lysine degradation pathway. This is the GA-I mouse model (*Gcdh* KO), which could be crossed with a *Dhtkd1* KO mouse line if asymptomatic, to investigate whether a double knockout of *Dhtkd1* and *Gcdh* can rescue the GA-I phenotype.

III. RESULTS

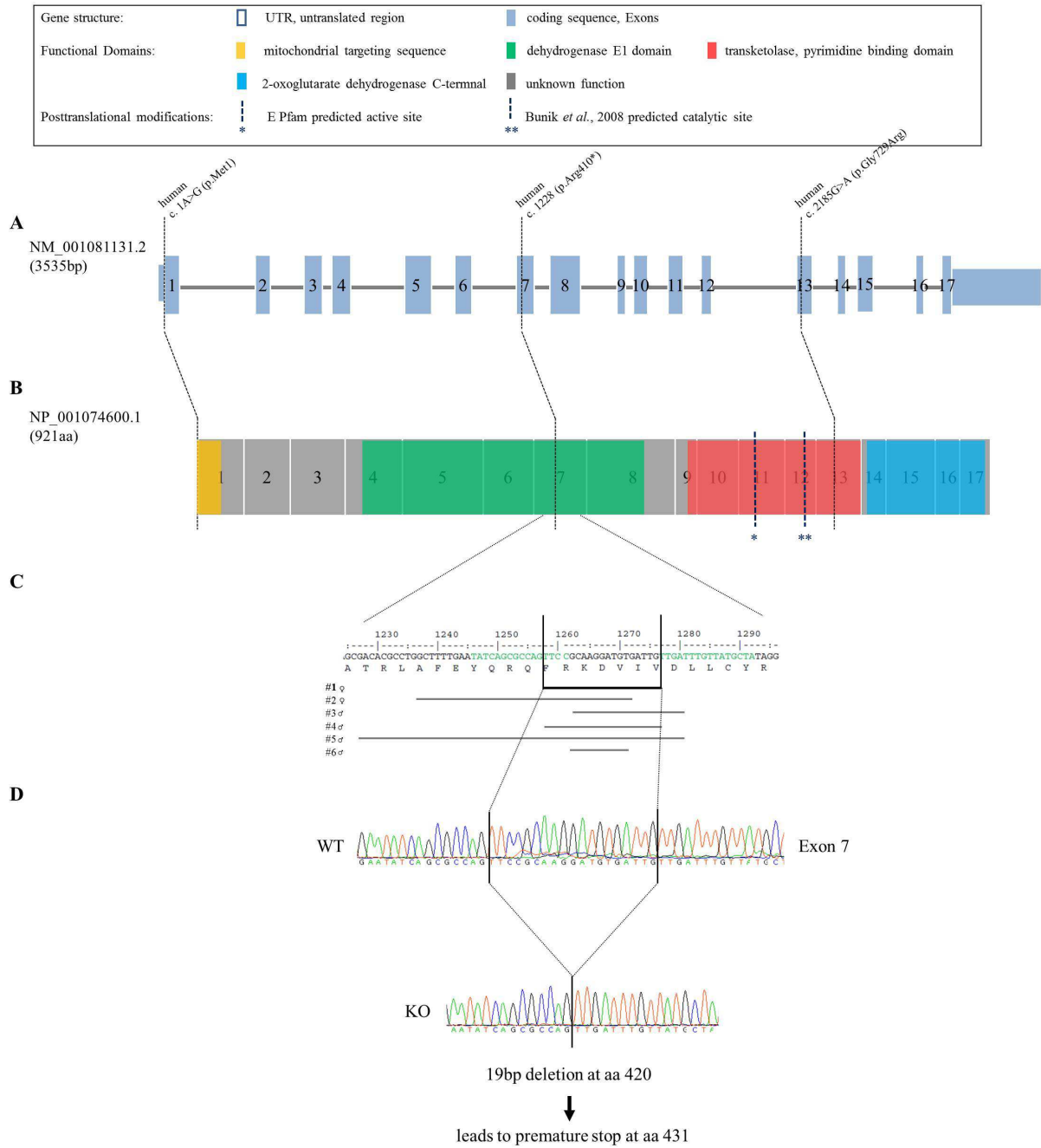


Figure 36: Murine *Dhtkd1* gene structure in wild-type and knockout *Dhtkd1* mice. **A)** Genomic structure of murine *Dhtkd1* based on Genome Browser (GRCm38/mm10) with coding exons and UTR's. Known mutations in humans (Danhauser *et al.*, 2007) are added at corresponding murine amino acid (aa) positions. **B)** Protein structure of murine *Dhtkd1* with functional domains and posttranslational modifications as predicted by Pfam and Bunik *et al.*, 2008. **C)** Target sequence within exon 7 of *Dhtkd1* with Ex7-TALEN-binding sites depicted in green. Lines underneath the exonic sequence indicate the region deleted in each of the six mutated founder mice (#1-#6). Black arrows point towards the region deleted in individual #1, which was used for further mating; #1: del19; #2: del35; #3: del17; #4: del19; #5: del52; #6: del10. **D)** Sanger sequencing results from a wild-type and a homozygous knockout offspring from #1 indicating the 19bp deletion. ExPASy software predicts a premature stop codon at aa 431.

III. RESULTS

Cell culture testing was performed as described (V.2.1.12.). B-galactosidase levels suggested the TALEN-pair targeting exon 7 to be more efficient (figure 37B). When compared to the control TALEN-pair established by the Institute of Developmental Genetics at the Helmholtz Zentrum Muenchen, it was expected that approximately 20% of the offspring harbour a small deletion or insertion. The exon 1 TALEN-pair was measured to be less efficient in introducing double-strand breaks. Therefore, mRNA of the exon 7 TALEN-pair was generated to be injected into mouse oocytes. The oocytes were derived from FVB mice and fertilised with C57Bl/6 sperm resulting in a mixed background.

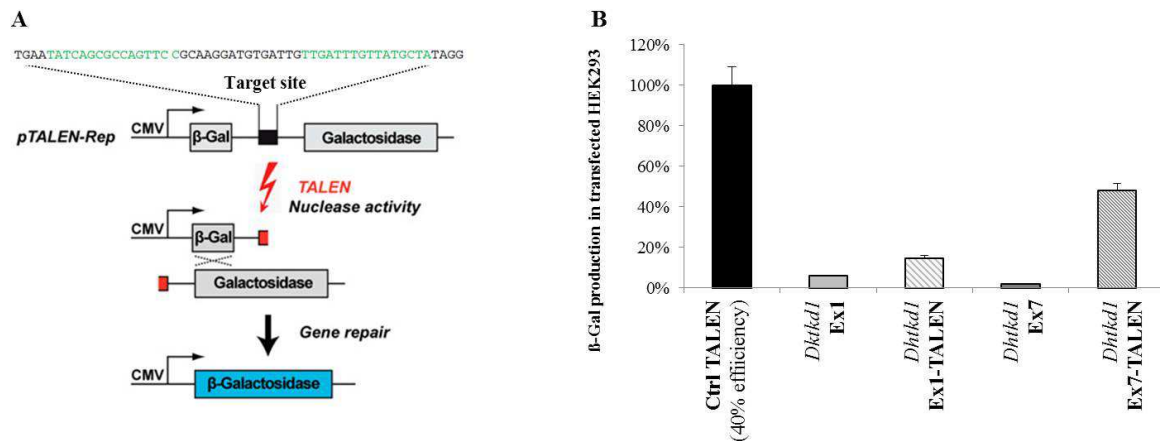


Figure 37: *In vitro* testing of TALENs. A) Schematic of *in vitro* TALEN testing adapted from Wefers et al., 2013b. B) TALEN efficiency assay; measurements were normalized to luciferase measurements; β-Gal = β-galactosidase; Ctrl TALEN = control TALEN-pair known to result in 40% mutated offspring; both *Dhtkd1* Ex1 and *Dhtkd1* Ex7 were transfected with the reporter plasmid only; *Dhtkd1* Ex1-TALEN and *Dhtkd1* Ex7-TALEN were co-transfected with the reporter plasmid and both expression plasmids to express the corresponding TALEN-pair.

From TALEN design to genotyping of the founder generation it took approximately four months (figure 18). A genotyping approach based on Sanger sequencing of murine exon 7 revealed 6 mutants out of 59 pups (approx. 10%) born to seven foster animals. All deletions lead to a frameshift and we chose to use mouse #1 carrying a 19bp deletion for further mating (figure 36C). As described in figure 36D the deletion of 19bp leads to a premature stop codon at aa 431 resulting in a truncated protein lacking most functional domains. The *Dhtkd1* knockout mouse was first mated with C57Bl/6 to generate germline mutated offspring in F1. Via inbreeding of F1, homozygous knockout animals of both genders were generated in F2.

III.2.2. Clinical and biochemical characterization of the *Dhtkd1* KO mouse

In order to characterize a *Dhtkd1* KO cohort, eight heterozygous KO males were measured against eight homozygous KO males at the age of 3 months. Due to the breeding strategy, there were no age-matched

III. RESULTS

wild-type animals available. A modified SHIRPA protocol was performed as well as grip strength analysis, inverted grid and balance beam (figure 38). No differences were found between genotypes in these neurobehavioral examinations except in touch escape analysis. This test measures behaviour upon approaching the animal frontally and can be interpreted as fear behaviour or visual impairment examination. The Students t-test for touch escape revealed a p-value of 0.02, which was not significant when corrected for multiple testing. Moreover, due to the other tests showing no abnormalities at all, this finding was considered negligible.

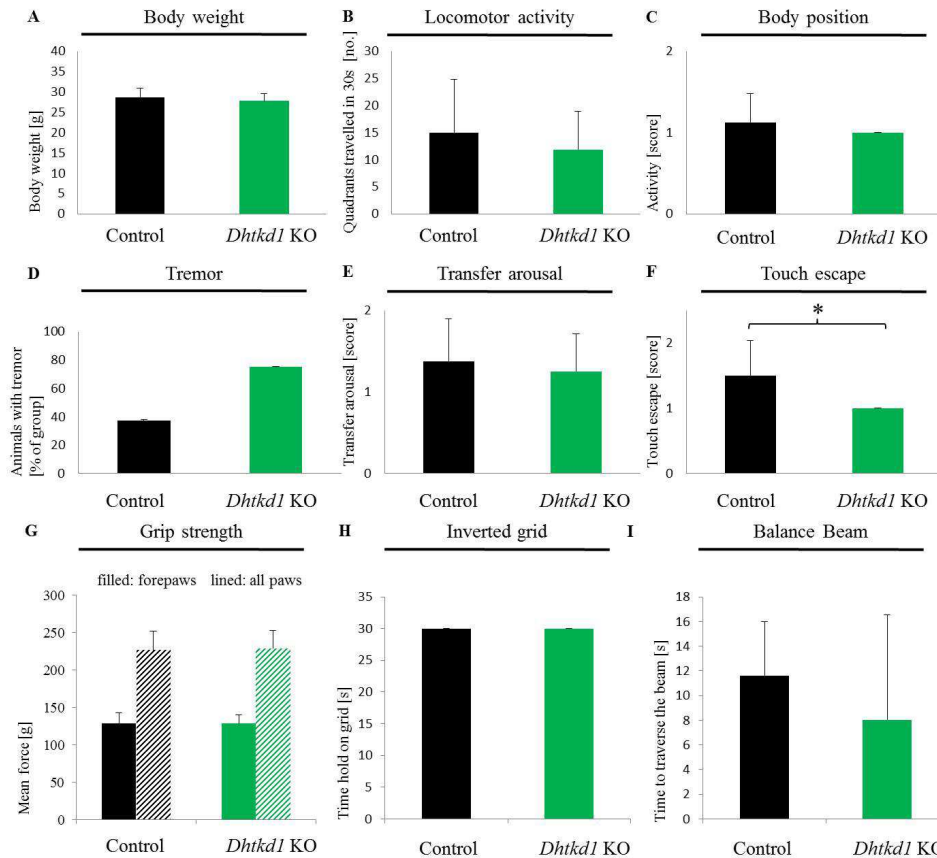


Figure 38: Clinical characterization of *Dhtkd1* KO mice. (Biagosch et al., 2016; in preparation) Modified SHIRPA analysis was performed at three months of age with eight heterozygous control animals and eight homozygous *Dhtkd1* KO animals; n=16 (all male at the age of 3 months). **A)** Body weight was measured **B)** Locomotor activity was assessed by counting quadrants within an arena travelled by an animal within 30 seconds. **C)** Body position was scored when placed into a viewing jar; inactive = 0, active = 1, excessively active = 2. **D)** Tremor was analysed by observation of forepaws while lifting the mouse by the tail. **E)** Transfer arousal was scored after placing the mouse into the middle of an arena and observing its activity during the first five seconds; prolonged freeze = 0, brief freeze = 1, immediate movement = 2. **F)** Touch escape was scored while a finger approached the mouse frontally; no response = 0, response to touch = 1, fleeing prior to touch = 2; p = 0.02. **G)** Grip strength was measured in triplicate with either forepaws only, or all paws holding onto the grid. **H)** Inverted grid analysis was performed until a maximum of 30 seconds. **I)** Balance Beam was measured in triplicate on beam 1 (no genotype-specific differences on beam 2; data not shown). There were no differences in foot slips, number of falls and stops on neither beam (data not shown). Other observations such as gait, tail elevation, clickbox, trunk curl, limb grasping and urination were without any genotype-specific differences (data not shown). Bars indicate standard deviation; * t-test: p < 0.05.

III. RESULTS

For the biochemical characterization of *Dhtkd1* KO animals, OA and GA were measured in brain and liver homogenate. These two tissues are mainly affected in human patients and accumulate characteristic metabolites. Both tissues were measured from four wild-type and three mutant animals (figure 39). As expected and schematically recalled in figure 39, *Dhtkd1* KO leads to OA accumulation as compared to wild-type animals. Surprisingly, GA seems to be accumulating in liver. Of note, this level is still 10-fold lower than in *Gcdh* KO mice.

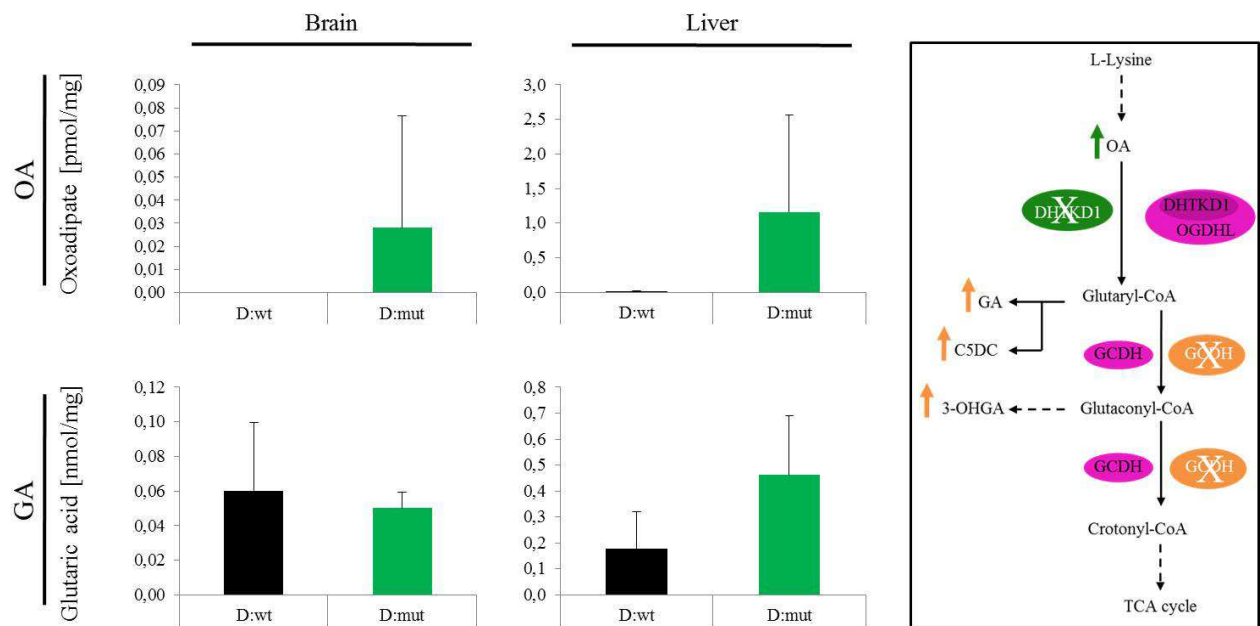


Figure 39: Biochemical characterization of *Dhtkd1* KO mice. Cerebral (brain) and hepatic (liver) measurements of 2-oxoadipate (OA) and glutaric acid (GA) via GC/MS and MS/MS. “D:” describes the genetic status of *Dhtkd1* as either wild-type (wt) or homozygous knockout (mut). D:wt n = 4; D:mut n = 3. Schematic on the right is a segment from figure 34 (see figure 34 legend for further explanations).

Overall, *Dhtkd1* KO does not result in obvious clinical abnormalities in mice. This strengthens the argument of the human condition 2-aminoadipic 2-oxoadipic aciduria being a condition with numerous asymptomatic patients. Furthermore, increased OA levels indicate successful inhibition of *Dhtkd1* in the generated *Dhtkd1* KO mouse line.

III.2.3. Generation of a *Gcdh/Dhtkd1*-double KO mouse

In order to validate whether inhibition of DHTKD1 can rescue the *Gcdh* KO phenotype, the two KO lines were crossed. It took several inbreeding generations to obtain double KO lines homozygous for both *Dhtkd1* and *Gcdh*. The *Gcdh* KO line was kindly provided by the Stoffwechselzentrum at the University of Heidelberg. It was based on the Sv129 strain adding the third background to the *Gcdh/Dhtkd1*-double KO line. The resulting mixture of mouse backgrounds in the double-KO line was 50% Sv129, 37.5% C57Bl/6 and 12.5% FVB as visualised in figure 40.

III. RESULTS

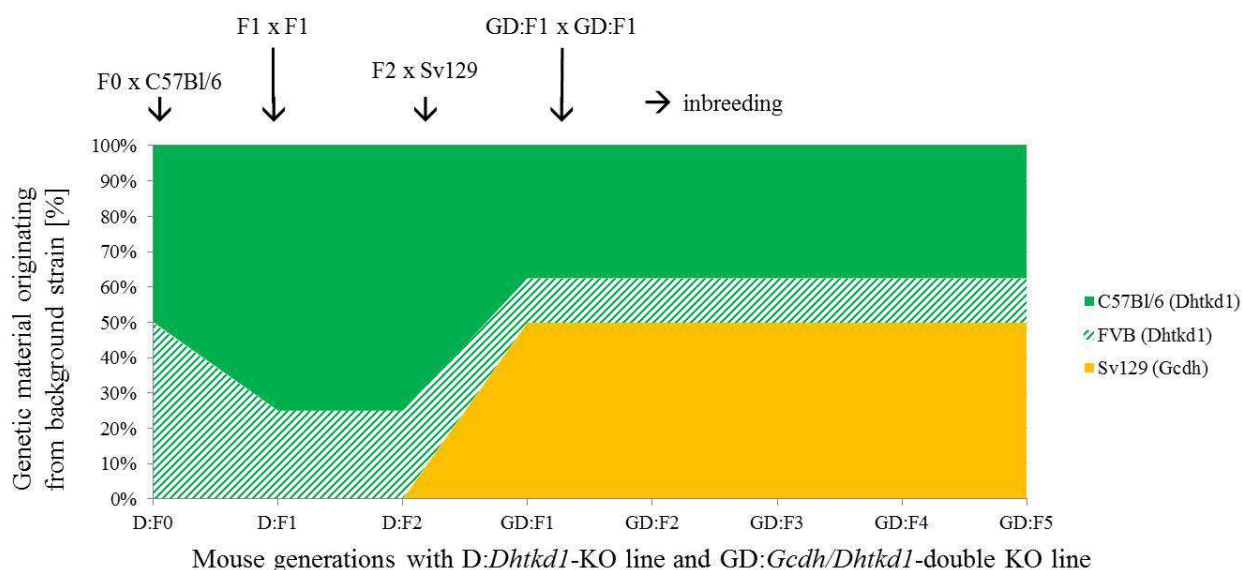


Figure 40: Mouse backgrounds involved in *Gcdh/Dhtkd1*- double KO line. Percentages of different mouse backgrounds per mouse generation. The breeding strategy leading to the indicated proportions are listed above the graph. The *Dhtkd1* KO mouse was generated as 50% C57Bl/6 and 50% FVB and subsequently backcrossed to C57Bl/6. The resulting F1 generation was inbred to generate homozygous KO mice in F2. These were crossed with *Gcdh* KO mice on the Sv129 background with subsequent inbreeding leading to a distinct mixture of backgrounds as of GD generation F1.

The mouse background can influence clinical and biochemical characteristics of a mouse line. This may change from one generation to the other. It is therefore important to keep track of the mouse background composition.

III.2.4. Biochemical characterization of the double KO mouse

The established double KO line was used to measure brain and liver metabolites in double KO mice as compared to *Dhtkd1* KO, *Gcdh* KO and wild-type age-matched animals (approximately 5 weeks of age). Using littermates was not always possible due to the complex breeding strategy necessary to obtain double KO animals. Based on the lysine-degradation pathway theory summarized in figure 41, a *Gcdh/Dhtkd1*-double KO should lead to increased OA levels with a corresponding decrease in GA, ideally back to a normal level as seen in wild-type animals. This should prevent the toxic glutaryl-CoA and 3-OHGA accumulation. Figure 41 shows liver OA levels of the double KO cohort comparable to the *Dhtkd1* KO as expected. Brain OA levels below 0.1 pmol/mg are negligible. However, GA levels show no significant decrease and instead are similar to *Gcdh* KO mice. Of note, the standard error bars indicated are high with only a small number of animals from each genotype (n = 3-5). In order to challenge the model and evoke a distinct metabolic signature in each genotype, a high lysine diet strategy was implemented (III.2.5.).

III. RESULTS

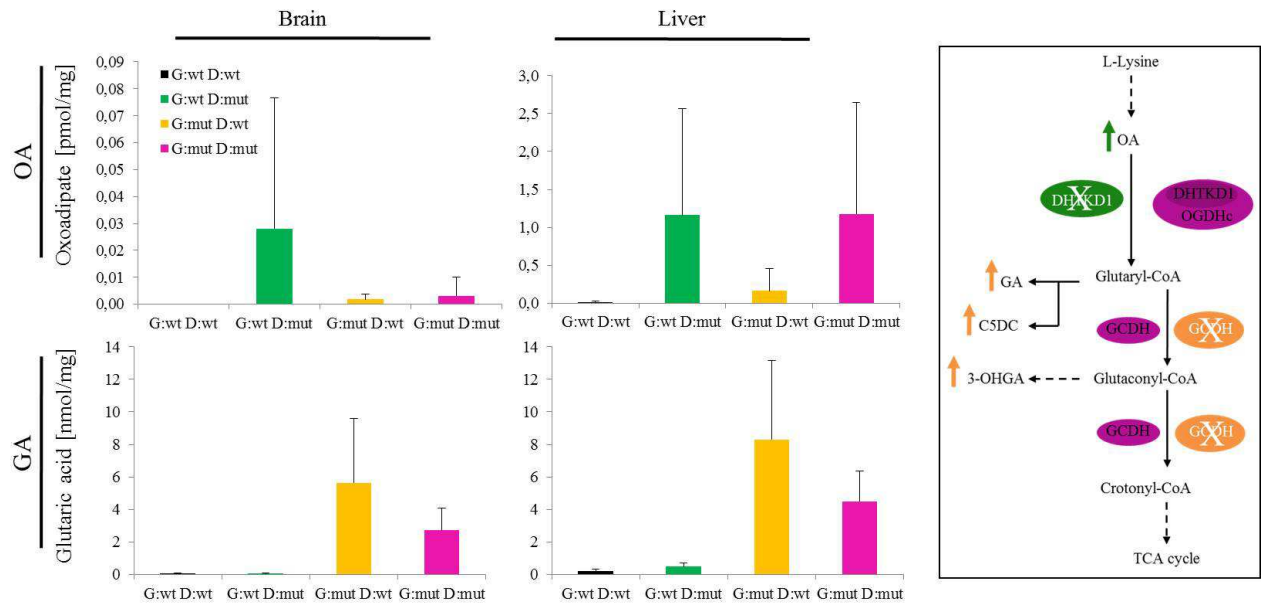


Figure 41: Biochemical characterization of the *Gcdh/Dhtkd1*-double KO line. Cerebral (brain) and hepatic (liver) measurements of 2-oxoadipate (OA) and glutaric acid (GA) in different genotypes of the *Gcdh/Dhtkd1*-double KO line via GS/MS and MS/MS. G:wt D:wt = wild-type (n = 4); G:wt D:mut = *Gcdh*:wt *Dhtkd1*:homozygous KO (n = 3); G:mut D:wt = *Gcdh*:homozygous KO *Dhtkd1*:wild-type (n = 5); G:mut D:mut = *Gcdh/Dhtkd1*-double KO (n = 5). Schematic on the right is a segment from figure 34 (see figure 34 legend for further explanations).

III.2.5. High-lysine diet challenges knockout lines

High-lysine diet is known to result in high GA levels accompanied with clinical decline in *Gcdh* KO mice (Sauer et al., 2015). The aim was to verify the hypothesis that *Dhtkd1* KO can rescue the *Gcdh* KO specific phenotype in a double KO mouse. The primary clinical outcome was weight change upon diet or experiment start. The clinical endpoint of the study was at a critical weight loss of more than 15% since start of the high-lysine diet (4.7% in chow and water). Figure 42A shows that 24 hrs after diet start none of the wild-types and only one *Dhtkd1* KO had reached the endpoint. As expected, 80% (4/5) from the *Gcdh* KO group reached the endpoint (Sauer et al., 2015). Surprisingly, all double KO mice (7/7) lost the critical amount of weight within 24 hrs indicating clinical decline similar to *Gcdh* KO mice. The secondary outcome was behavioural abnormality, which presented as extreme passivity. As depicted in figure 42B almost all *Gcdh* KO as well as double KO animals showed lethargic behaviour 24 hrs on high-lysine (approx. 376 mg daily lysine-load) diet. This was found only in a single wild-type case and twice in *Dhtkd1* KO animals. Surprisingly, double KO animals seemed to be clinically as affected as *Gcdh* KO mice. This was in contrast to our hypothesis of the pathway, where the double KO should have coped better on high-lysine load. In reality, double KO animals lost weight, as well as ability for active movement, rapidly with all animals on high-lysine having reached the endpoint before 24 hrs of the diet.

III. RESULTS

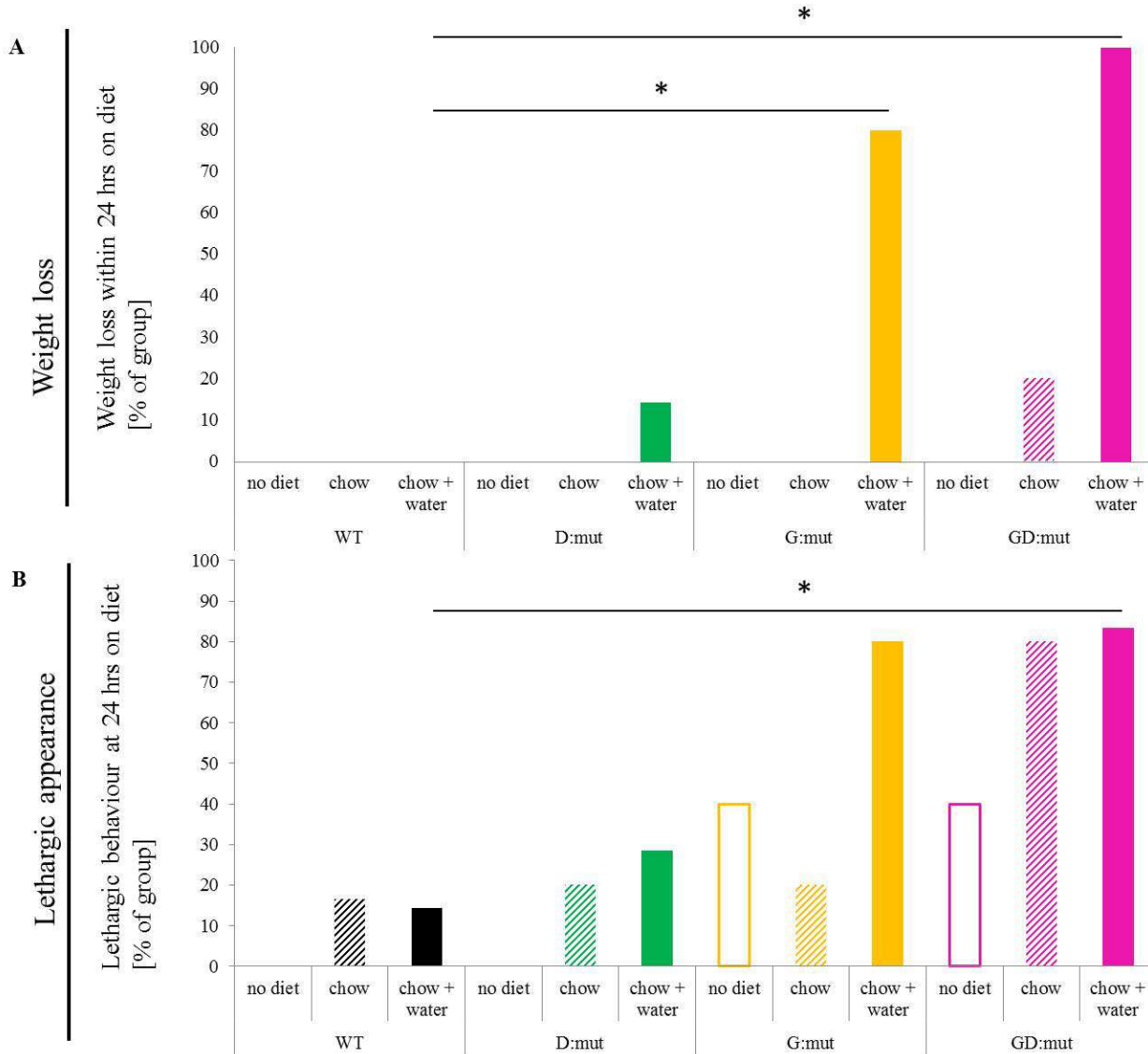
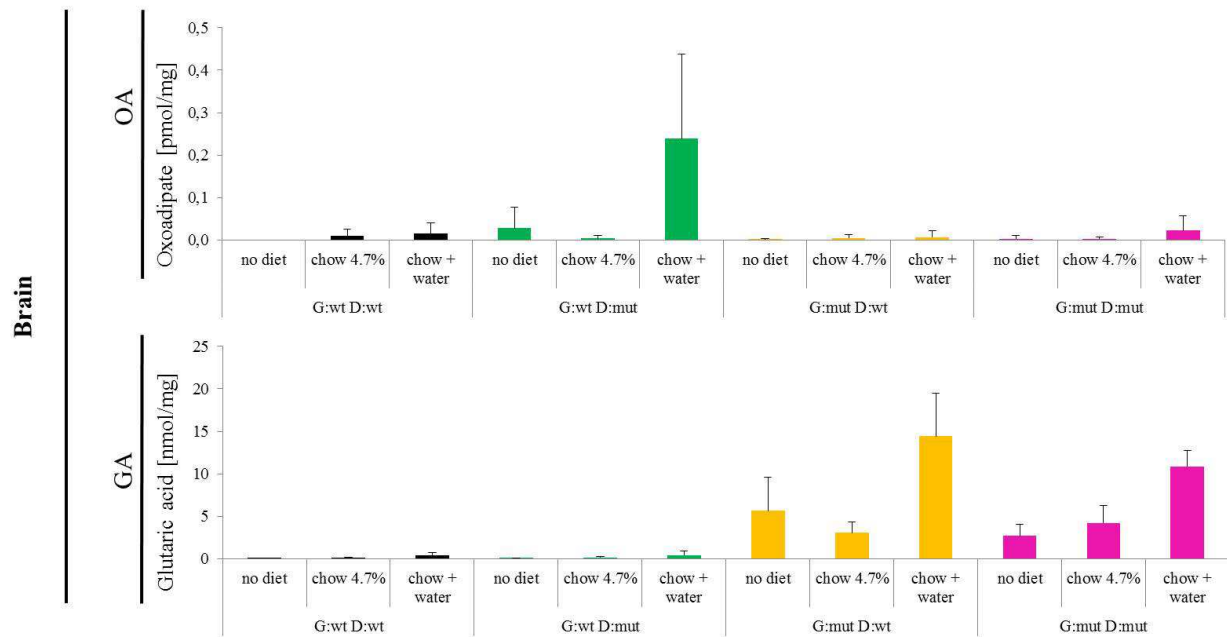


Figure 42: *Gcdh*-*Dhtkd1* double knockout does not rescue weight loss or behavioural decline on high-lysine diet. (Biagosch et al., 2016; in preparation) Clinical analysis 24 hrs after start of the diet with normal lysine, high-lysine in chow, or in chow and water from four different genotypes; **A**) Critical weight loss within 24 hrs was reached at > 15% loss as compared to diet start. **B**) Behavioural abnormality was assigned when animals, put into an arena, moved 2 or less quadrants within 30 s. (n = animal numbers: no diet/chow/chow + water) G:wt D:wt = wt (8/6/7); G:wt D:mut = *Gcdh*:wt *Dhtkd1*:homozygous KO (n = 5/5/7); G:mut D:wt = *Gcdh*:homozygous KO *Dhtkd1*:wt (n = 5/5/5); G:mut D:mut = *Gcdh*/*Dhtkd1*-double KO (n = 5/5/6). *Fisher's Exact test: p < 0.05.

The clinical data disproves *Dhtkd1* KO as a strategy to rescue *Gcdh* KO phenotypes or at least as a strategy on its own. To elucidate the biochemical signature of the double KO upon lysine-load, brain and liver homogenate were used to measure OA and GA from all genotypes at different lysine-loads (figure 43). OA levels were increased in liver but not in brain of double KO mice. GA levels were elevated in both brain and liver tissue to an extent similar to the *Gcdh* KO mouse but significantly increased as compared to wild-type or *Dhtkd1* mice.

III. RESULTS

A



B

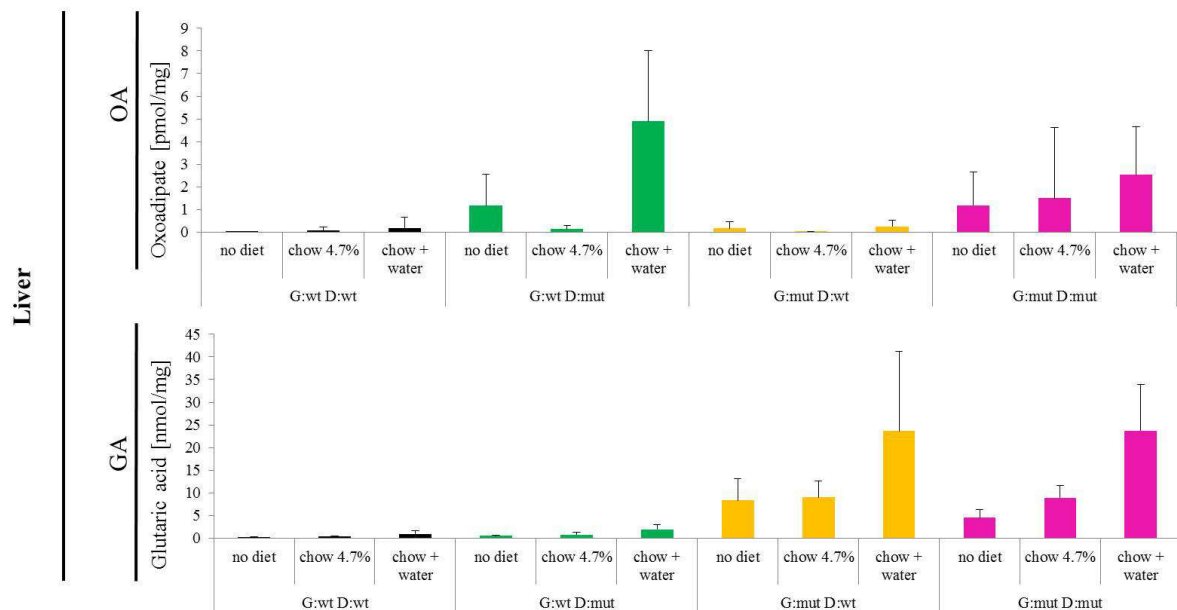


Figure 43: Biochemical analysis of the *Gcdh*-*Dhtkd1* double knockout mouse line on normal versus high-lysine diet. (Biagosch et al., 2016; in preparation) Oxoalipate (OA) and glutamic acid (GA) levels were measured via CG/MS and MS/MS in **A**) brain tissue and **B**) liver tissue from four different genotypes on three different dietary treatments; (no diet/ high-lysine in chow/ high-lysine in chow and water); G:wt D:wt = wild-type (n = 4/6/7); G:wt D:mut = *Gcdh*:wt *Dhtkd1*:homozygous KO (n = 3/5/7); G:mut D:wt = *Gcdh*:homozygous KO *Dhtkd1*:wild-type (n = 5/5/6); G:mut D:mut = *Gcdh*/*Dhtkd1*-double KO (n = 5/5/4). Bars indicate the standard deviation.

Conclusively, *Dhtkd1* KO in a *Gcdh* KO mouse model does not rescue the GA-I phenotype, neither clinically nor biochemically. Therefore, simple DHTKD1 inhibition is not sufficient to convert symptoms of GA-I to 2-aminoadipic 2-oxoadipic aciduria.

III.3. DISCUSSION

III.3.1. DHTKD1 inhibition is not a promising treatment strategy for GA-I

The institute of Human Genetics at the Technische Universitaet Muenchen identified *DHTKD1* as the associated gene for the condition 2-aminoadipic 2-oxoadipic aciduria (Danhauser et al., 2012). Numerous DHTKD1-patients are asymptomatic. Hence, Danhauser and colleagues suggested DHTKD1 inhibition as a therapeutic strategy to treat GA-I patients. This assumption was based on a simplified theory of the lysine degradation pathway at that time. The characterization of *Dhtkd1* KO mice showed that this KO does not lead to an obvious clinical phenotype, but as in human patients, results in higher OA levels. This increase seems to be clinically tolerable in both mice and men.

According to the former theory of the lysine degradation pathway, the main source of glutaryl-CoA is OA. Hence, inhibition of DHTKD1 should prevent the generation of glutaryl-CoA and its derivatives, rescuing the GA-I phenotypes. Results from the murine *Gcdh/Dhtkd1*-double KO, which mimics DHTKD1 inhibition in a GA-I patient, showed no rescue of the GA-I phenotypes. Our data is based on small animal numbers and experiments were not possible to be performed on the same day and between littermates. However, metabolic analysis via GC/MS and MS/MS are robust ways of measuring OA and GA. Furthermore, results are consistent for the different genotypes throughout all experiments, and clinical results match the biochemical analysis. Metabolic parameters, as well as the clinical outcomes like weight and extremely passive behaviour, are not likely influenced by environmental factors existing in animal housing facilities. One also has to take the mixed background into account, which could explain the high variance within genotypic groups. Still, neither clinical nor biochemical symptoms are rescued in the double KO as compared to *Gcdh* KO mice. This highlights the complexity of the lysine degradation pathway and suggests the presence of so far unknown branches.

III.3.2. Murine double KO experiments question the current theory of lysine degradation

The lysine-degradation pathway is one of the worst elaborated amino acid degradation pathways. Many research groups developed simplified schematic models to understand specific branches of this pathway. But the reality seems to be much more complex. It has been shown that there are tissue specific discrepancies in the pathway. The saccharopine pathway seems to be more abundant in liver, whereas the pipecolate pathway is thought to be more active in brain (Sauer et al., 2011). Within the pipecolate pathway, pipecolate is oxidised to 1-piperideine-6-carboxylate by a still unknown enzyme. This demonstrates one of the many open questions related to the lysine degradation pathway.

III. DISCUSSION

According to theory to date, OA is degraded via a linear pathway to glutaryl-CoA by one single enzyme, DHTKD1. Inhibition of DHTKD1 to prevent glutaryl-CoA accumulation was investigated via a *Gcdh/Dhtkd1*-double KO mouse. Results showed high GA levels, which imply glutaryl-CoA accumulation. This would require the existence of another source of glutaryl-CoA. It has been suggested that OGDHc is a multi-substrate specific enzyme (Shim da et al., 2011). Its substrate is normally 2-oxoglutarate but it seems to have low substrate affinity to OA. It is possible that during DHTKD1 inhibition OGDHc can compensate and decarboxylate OA to glutaryl-CoA.

Another source of glutaryl-CoA is GA. C7ORF10 transfers CoA from succinyl-CoA to GA generating glutaryl-CoA. Generally, GA can be excreted via urine, but in case of metabolic imbalance, C7ORF10 seems to act as a metabolic repair mechanism. However, if this is the main source of glutaryl-CoA in double KO mice, it remains an open question where GA comes from. In theory, an enzyme converting OA directly to GA could be an explanation. OGDH-dependent dioxygenases are potential candidates for this conversion, but there is no evidence to date.

Some research groups suggest GA can also be generated via the microbiome in the intestines. This could explain high GA in several tissues, but not in the brain. The blood brain barrier seems to prevent GA flux into cerebral tissue as shown via a hepatic *Gcdh* KO mouse (Sauer et al., 2006). Nevertheless, it cannot be excluded that the microbiome generates a precursor of GA that can pass the blood brain barrier and is degraded to GA and glutaryl-CoA in cerebral tissue.

Taken together recent findings disapprove the idea of a simple DHTKD1 inhibition to treat GA-I patients. They further demonstrate that some pathways thought to be linear, really include parallel reactions. We showed that DHTKD1 cannot be the only path within the lysine degradation pathway to generate glutaryl-CoA. It remains an open question whether unknown parallel reactions are involved, or whether the actual source of glutaryl-CoA is GA. And if the latter theory holds the source of GA is still unknown.

III.3.3. Future investigations of the lysine degradation pathway towards GA-I therapy

The lysine degradation pathway, as complex as it is, offers more targets to prevent glutaryl-CoA accumulation. DHTKD1 is the target acting directly upstream of the toxic metabolite. There are several enzymes further upstream, which when non-functional also lead to conditions with asymptomatic patients or to unknown consequences.

2-Amino adipate-6-semialdehyde synthetase (AASS) is a bifunctional enzyme catalysing the first two reactions of the saccharopine pathway. Loss-of-function results in hyperlysinaemia type 1, which is mainly asymptomatic. This is confirmed by the high tolerability to mutations detected by the ExAC database (figure 34B). Inhibition of this enzyme has the potential to lower glutaryl-CoA accumulation in GA-I

III. DISCUSSION

patients. However, it is unclear whether the pipercolate pathway could compensate this loss-of-function within the sacchropine pathway. Of note, patients with hyperlysinaemia type 1 show high serum pipercolate levels. This suggests no efficient compensation via the pipercolate pathway or at least not in all tissues.

Another putative target downstream of AASS is 2-aminoadipate-6-semialdehyde dehydrogenase (AASDH). It looks like a condition without clinical consequences when comparing ExAC database scores, but it is known to result in pyridoxine-dependent epilepsy. Inhibition of AASDH is therefore no promising target to treat GA-I.

The 2-aminoadipate transaminase (AADAT) converts 2-aminoadipate to OA. To date there are no patients known with loss-of-function of AADAT. This could either be due to no clinical effect upon loss-of-function or a dramatic possibly lethal effect. Data from ExAC suggests the latter to be likely. In more than 60,000 healthy control samples they found only 4 loss-of-function variants with 16 expected if the gene were not essential for health. Only 64 missense variants were observed with 126 expected, leading to scores comparable to *GCDH* as visualised in figure 34B. Overall, AADAT would not be the first choice target to treat GA-I.

A promising target is the succinate-hydroxymethylglutarate CoA-transferase (*C7ORF10*) associated to GA-III. It transfers CoA from succinate-CoA to GA generating glutaryl-CoA. It serves as a metabolic repair, in parallel to urinary excretion if GA levels are high. The ExAC database assigns minimal scores to *C7ORF10* suggesting GA-III as a condition with none or minor clinical consequences. This is confirmed by patients being mainly asymptomatic.

The most promising strategy towards GA-I treatment seems to be *C7ORF10* inhibition. Since this branch in the lysine degradation pathway works in parallel to the *DHTKD1* pathway, a dual treatment inhibiting both enzymes should be tested. The generation of a *c7orf10* KO mouse line is required to test this new treatment strategy. If a *Dhtkd/c7orf10*-double KO does rescue the GA-I phenotype in a *Dhtkd1/c7orf10/Gcdh*-triple KO mouse these two branches would likely be the major sources of glutaryl-CoA. In case there is no rescue it seems like OGDHc can compensate *DHTKD1* inhibition and generate glutaryl-CoA. With our current knowledge, the existence of another completely unknown pathway leading to glutaryl-CoA cannot be excluded.

IV. CONCLUSION AND OUTLOOK

This complementary approach addresses three different steps of a classic research cycle (figure 44) from identification of the disease-associated gene (section I) to the development of a mouse model for a human disorder (section II). An already established mouse model (for GA-I) enabled us to validate a therapeutic approach (section III). Each part is based on a different human neuropathological disease either proven or expected to be a mitochondriopathy.

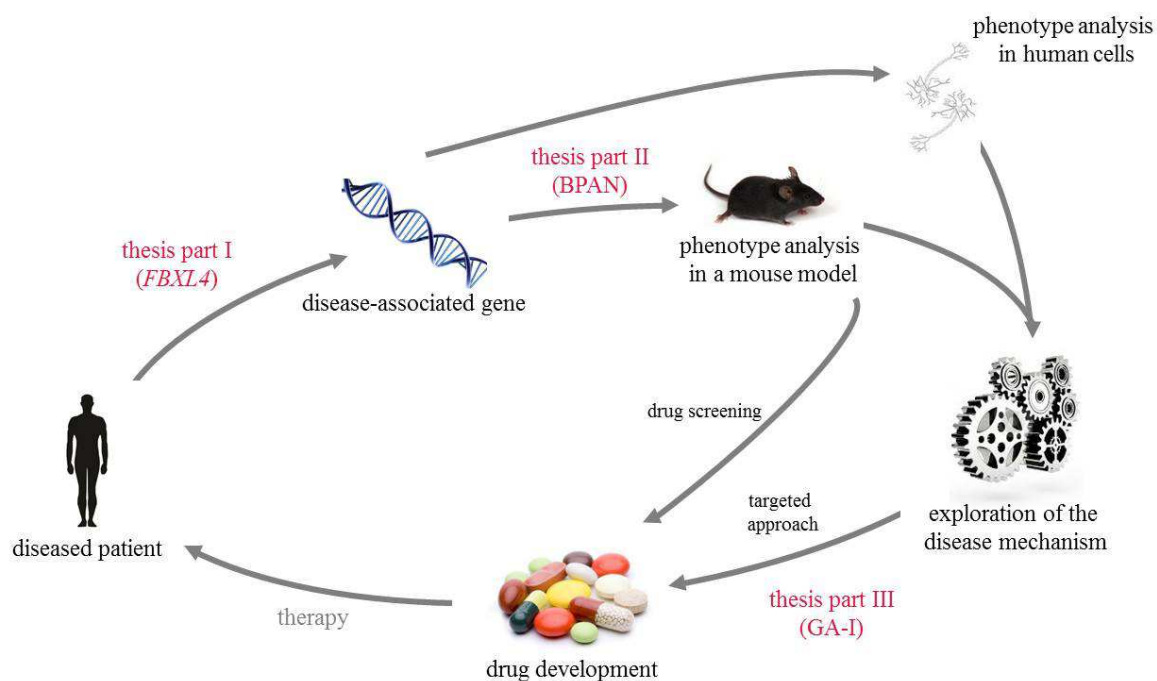


Figure 44: Scheme of a classic research cycle for genetic human diseases. Investigations addressed within this thesis are indicated in red with the corresponding disease-gene (for section I) and disease type (for sections II and III) named in brackets.

In section I of this thesis a disease-associated gene was identified. *FBXL4* mutations were found to cause early-onset mitochondrial encephalopathy. This is the first mitochondriopathy known to date where patients show reduced levels of CS indicating a reduction in mitochondrial mass. Since biochemical analysis to diagnose mitochondriopathies involves measurements of RCCs normalised to CS, these patients misleadingly showed normal levels. Without normalisation to CS total activity of all RCCs was decreased and microoxygraphy showed reduced maximal respiration. As the underlying disease mechanism, impaired mitochondrial biogenesis or mitophagy are suggested. Since the identification of the disease-associated gene *FBXL4*, more than 20 patients have been published. With this frequency *FBXL4* is among the more common disease-associated genes for mitochondriopathies. Accordingly, it has attracted the attention of several research groups around the globe. Diagnostics of further patients was facilitated by the detailed clinical description of all patients concluding a characteristic clinical pattern. The most distinctive clinical feature is the dysmorphic facial appearance. In some cases this has already led to direct sequencing of

IV. CONCLUSION AND OUTLOOK

FBXL4 and positive *FBXL4* diagnosis, before other painful, timely and costly diagnostic procedures were performed.

In sections II and III, two KO mouse lines were generated within approximately four months each using the TALEN approach. This was a revolution in mouse model generation, established a few years ago, which has recently been further facilitated and accelerated by the discovery of the CRISPR/Cas9 system. It offers new perspectives for disease-associated gene investigations and therapeutic studies.

In section II, a *Wdr45* KO mouse was generated and characterized in order to establish a model for the human disease BPAN. A biallelic KO was suggested to be lethal in humans but proved to be viable in mice. The model resembled the human disorder in several facets with mainly neurobehavioral and neuropathological abnormalities. Neuropathological findings occurred with 100% penetrance in mutants as of the age of four months. As a clinically relevant endpoint this can be used for therapeutic studies. *WDR45* is known to be involved in autophagy, and BPAN shares features with common disorders such as Alzheimer's disease and Parkinson's disease. Therefore, studies on the *Wdr45* KO model can be implemented in other research areas and potentially inform therapeutic strategies of more patients. This model will also be beneficial to investigations of the pathomechanism of BPAN and may enhance current knowledge of the cellular process of autophagy.

In section III, a *Dhtkd1*-KO mouse line was generated. Clinical and biochemical characterization found no abnormalities and identified elevated OA levels comparable to the human condition. This suggested 2-aminoadipic 2-oxoadipic aciduria a condition with no or minor clinical consequences in mice and men. A *Gcdh/Dhtkd1*-double KO mouse using the well-established *Gcdh*-KO mouse was generated. It imitated a situation of DHTKD1 inhibition in GA-I patients. DHTKD1 inhibition was shown to be not sufficient to rescue the phenotype associated to GA-I in mice. The double KO was clinically abnormal. Biochemically it accumulated GA in liver and brain, indicating a toxic glutaryl-CoA accumulation. This disproved the theory of DHTKD1 being the major source of glutaryl-CoA, and suggested unresolved branches within the lysine degradation pathway. *C7ORF10* is another potentially major source of glutaryl-CoA and is suggested as the next logic target to be inhibited as a therapy for GA-I. Supposedly a dual treatment consisting of both DHTKD1 and *C7ORF10* inhibitors would reduce glutaryl-CoA accumulation and would improve the clinical picture of GA-I patients. A *C7orf10/Dhtkd1/Gcdh*-triple KO could help elucidating this question.

Nonetheless, until a drug can be delivered to patient's bedside there is still a long way to go. Overall, this work highlights that simplified schematic pathways generated to understand the rough mechanism are not always reflecting reality. Therapeutic ideas based on biochemical findings and cell culture experiments should be confirmed on organismal level. Therapeutic interventions can have different consequences for different tissues as well as the complex interplay between organs. This demonstrates the need for well-

IV. CONCLUSION AND OUTLOOK

established model organisms. The generation of disease models has greatly benefited from recent technologies such as TALEN and CRISPR/Cas. But in terms of generating a KO mouse for a specific disorder it is essential to know the underlying disease-associated gene to be targeted. Hence, the research cycle is necessary on the way towards therapy for diseased patients. This work aims to bring research from bench one step closer to patient's bedside.

V. MATERIAL AND METHODS

V.1. Material

V.1.1. Chemicals and reagents

| | |
|--------------------------------------|---|
| 1 kb DNA Ladder | Thermo Fisher Scientific, Waltham, USA |
| 100 bp Plus DNA Ladder | Thermo Fisher Scientific, Waltham, USA |
| 6-carboxyfluorescein-labeled primers | Metabion international AG, Martinsried, GER |
| Agarose | Biozym Scientific, Oldendorf, GER |
| Big Dye Buffer | Applied Biosystems, Foster City, USA |
| Big Dye Terminator | Applied Biosystems, Foster City, USA |
| DMEM | Life Technologies, Carlsbad, USA |
| DMSO | Sigma-Aldrich, Taufkirchen, GER |
| DNA Agarose | Biozym Scientific, Hessisch Oldendorf, GER |
| DNA Stain G | Serva, Electrophoresis, Heidelberg, GER |
| dNTP Set (dATP+dCTP+dGTP+dTTP) | Thermo Fisher Scientific, Waltham, USA |
| DPBS | Life Technologies, Carlsbad, USA |
| EDTA | Sigma-Aldrich, St. Louis, USA |
| Ethanol absolute | Merck, Readington, USA |
| Fetal bovine serum (FBS) | Life Technologies, Carlsbad, USA |
| HPLC water | VWR International, Radnor, USA |
| L-Lysine $\geq 98\%$ TLC | Sigma-Aldrich, St. Louis, USA |
| Loading Dye | Thermo Fisher Scientific, Waltham, USA |
| Magnesium chloride | Qiagen, Hilden, GER |
| NEB Buffer1 (1x) | New England Biolabs, Ipswich, USA |

V. MATERIAL AND METHODS

| | |
|--|--|
| PenStrep | Life Technologies, Carlsbad, USA |
| Q-Solution (5x) | Qiagen, Hilden, GER |
| Serva DNA Stain Clear G | Serva Electrophoresis, Heidelberg, GER |
| T ₁₀ E _{0.1} microinjection buffer | Self-prepared accordingly (Wefers et al., 2013b) |
| Taq-DNA-Polymerase (5 U/ μ l) | Qiagen, Hilden, GER |
| Taq PCR buffer (10x) | Qiagen, Hilden, GER |
| Tris | Merck, Readington, USA |
| Trypsin | GE Healthcare, Giles, USA |

V.1.2. Enzymes and proteins

| | |
|-------------------------|-----------------------------------|
| All restriction enzymes | New England Biolabs, Ipswich, USA |
|-------------------------|-----------------------------------|

V.1.3. Antibodies

| | |
|-----------------------------------|---------------------------------|
| A5441 (Beta-actin) | Sigma-Aldrich, Taufkirchen, GER |
| ab110242 (NDUFB8 – CI) | Abcam, Cambridge, UK |
| ab110330 (E1 alpha subunit – PDH) | Abcam, Cambridge, UK |
| ab14715 (SDHA – CII) | Abcam, Cambridge, UK |
| ab14745 (UQCRC2 – CIII) | Abcam, Cambridge, UK |
| ab14748 (ATP5alpha – CV) | Abcam, Cambridge, UK |
| ab16056 (COXIV – CIV) | Abcam, Cambridge, UK |
| sc11415 (TOM20 - mitochondria) | Santa Cruz, Heidelberg, GER |

V.1.4. Kits

| | |
|---|--|
| AllPrep DNA/RNA Mini Kit | Qiagen, Hilden, GER |
| Amersham Western Blotting Detection | GE Healthcare Life Sciences, Freiburg, GER |
| β -Gal Reporter Gene Assay, chemiluminescent | Roche Applied Science, Penzberg, GER |

V. MATERIAL AND METHODS

| | |
|---|--|
| Luciferase reporter Gene Assay | Roche Applied Science, Penzberg, GER |
| MinElute Gel Extraction Kit | Qiagen, Hilden, GER |
| mMESSAGE mMACHINE [®] T7 ULTRA, Transcription Kit | Thermo Fisher Scientific, Waltham, USA |
| Mouse Direct PCR Kit | Bioutil, Houston, USA |
| NorthernMax [®] -Gly Kit | Thermo Fisher Scientific, Waltham, USA |
| pLenti6.3/V5-TOPO [®] TA Cloning [®] Kit | Fisher Scientific, Waltham, USA |
| PureLink HiPure Plasmid Filter DNA | Thermo Fisher Scientific, Waltham, USA |
| Qiagen Taq-Polymerase kit | Qiagen, Hilden, GER |
| QIAprep Spin Miniprep Kit | Qiagen, Hilden, GER |
| RNA Millennium [™] marker | Thermo Fisher Scientific, Waltham, USA |

V.1.5. Other materials

| | |
|---|--|
| Altromin 1314 standard mouse diet | Altromin, Rosenberg, GER |
| HEK 293 cells | Lonza, Basel, CH |
| Lignocel [®] 3-4S mouse bedding | Altromin, Rosenberg, GER |
| LumiNunc [™] 96-well plates | Thermo Fisher Scientific, Waltham, USA |
| NHDF neo | Lonza, Basel, CH |
| Nunc [™] Cell-Culture Treated 12-well dish | Thermo Fisher Scientific, Waltham, USA |
| PAGEr [™] EX Gels 4-12% | Lonza, Basel, CH |
| PCR Purification Plate Nucleofast | Macherey-Nagel, Düren, GER |
| TD 04412 high-lysine diet for rodents | Harlan, Indianapolis, Indiana, USA |

V.1.6. Technical devices

| | |
|-------------------------|-------------------------------------|
| Camera E.A.S.Y 440K | Herolab, Wiesloch, GER |
| Electrophoresis chamber | Bio-Rad Laboratories, Hercules, USA |

V. MATERIAL AND METHODS

| | |
|--|--|
| Gene Pulser Xcell™, Electroporation Systems | Bio-Rad Laboratories, Hercules, USA |
| Gene Pulser/MicroPulser, Electroporation Cuvettes | Bio-Rad Laboratories, Hercules, USA |
| NanoDrop 1000 Spectrophotometer | Thermo Fisher Scientific, Waltham, USA |
| Grip strength meter, BIO-GS3 | Bioseb, Virtrolles, FR |
| PTC-225 thermal cycler | Bio-Rad Laboratories, Hercules, USA |
| Sequencer ABI 3730 DNA Analyzer | Applied Biosystems, Foster City, USA |
| UVT-40 M Transilluminator | Herolab, Wiesloch, GER |
| Vacuum pump | Merck Millipore, Billerica, USA |
| XF69 Extracellular Flux Analyser | Seahorse Bioscience, Copenhagen, DK |

V.1.7. Oligonucleotides

| | |
|-------------|---|
| cDNA clones | Genecopoeia, Rockville, USA |
| Primers | Metabion International AG, Martinsried, GER |

| Assay | Gene symbol | Forward primer | Reverse primer | Amplification purpose |
|------------------|---------------|----------------------------|-----------------------------|-----------------------|
| human sequencing | <i>FBXL4</i> | CATCCTTCAAAGAGTTCATGC | ATCCCACCATGTCCCATAAG | sequencing exon 3 |
| human sequencing | <i>FBXL4</i> | TGCCAAAGAAGTAGTGGATTTC | TCTCCAATATTAACAACCAAAACC | sequencing exon 3 |
| human sequencing | <i>FBXL4</i> | CACACTGTGACATATTGGGC | TGCCAAACCAAAACAAAAGC | sequencing exon 4 |
| human sequencing | <i>FBXL4</i> | TGTTTCATAGAATGATACTGCTTTTC | CTACATAATAAGTATAACCTGCTGCTG | sequencing exon 5 |
| human sequencing | <i>FBXL4</i> | TGCTAAAATTCCAAAGTTCTTGC | GAAAACCAAATCTTCAGTTGGC | sequencing exon 6 |
| human sequencing | <i>FBXL4</i> | TTCTCTTGTTCACATTCATTCAC | GGATACATTCACCCATAGGAAG | sequencing exon 7 |
| human sequencing | <i>FBXL4</i> | CTCTAAACAGTTTGCATGCTGAG | TGAGATTGGCTTTCTGTCAAG | sequencing exon 8 |
| human sequencing | <i>FBXL4</i> | CATGGATGGATTCATTGTTAGC | TCCCAAAATTAACCCCAAC | sequencing exon 9 |
| mouse genotyping | <i>Wdr45</i> | CTTCAGAGAGGACACTGGGG | TCAGGGTATACGTGGGAAGG | sequencing exon 2-4 |
| mouse genotyping | <i>Dhtkd1</i> | ATGATAGCCCATGGCAACTG | GTGGAGAGAGAGGAGGAGGG | sequencing exon 7 |
| mouse genotyping | <i>Gcdh</i> | CTTCCGTAACACTGGCAGGAGCGG | CCCAGAACTCAGGAGGAAGAGGCAG | F13 and R17 * |
| mouse genotyping | <i>Gcdh</i> | GCGGTGGGCTCTATGGCTTCTGAGG | AGCTCTCGGGTCAGAAGCCCATAGG | Neo25 and R21 * |

Table 4: Primer table used for *FBXL4* sequencing in humans and for mouse genotyping of *Wdr45*, *Dhtkd1* and *Gcdh*.

*Primer pairs are taken from an orally delivered protocol, set up from Dr. Sven Sauer at University of Heidelberg, who delivered the *Gcdh*^{-/-} knockout mouse.

V.1.8. Vectors and plasmids

| <u>Type</u> | <u>Purpose</u> |
|---------------------------------------|---|
| pLenti6.3/V5-TOPO® | TOPO® cloning for lentiviral transduction |
| pCAG-“exon of interest”-Tal1 | Expression plasmid of TALEN 1* |
| pCAG-“exon of interest”-Tal2 | Expression plasmid of TALEN 2* |
| pCMV-Rep-“wild-type exon of interest” | β-Gal reporter plasmid* |
| pCMV-Luc | Luciferase reporter plasmid* |

*plasmids are identical to Wefers et al., 2013b and Wefers et al., 2014.

V.1.9. Bacteria

| <u>Type</u> | <u>Purpose</u> |
|---|--------------------------|
| One Shot® Stbl3™ Chemically Competent E. coli | Lentiviral TOPO® cloning |

V.1.10. Cell lines

| <u>Type</u> | <u>Purpose</u> |
|---------------------|---|
| HEK 293 | cell line for eukaryotic <i>in vitro</i> testing of TALENs |
| NHDF neo | normal human dermal fibroblasts as control cell line cultured from neonatal foreskin |
| Patient fibroblasts | taken from a patient biobank for suspected mitochondriopathy patients at the Institute of Human Genetics, Helmholtz Zentrum Muenchen and Technische Universitaet Muenchen |

V.1.11. Mouse lines

| <u>Helmholtz Zentrum Muenchen, internal name</u> | <u>Breeding</u> | <u>Background</u> |
|--|-----------------|-------------------------|
| WDR45 | inbreeding | C57Bl/6 N x FVB |
| GCDH* | inbreeding | Sv129 |
| DHTKD1 | inbreeding | C57Bl/6 N x FVB |
| GD (GCDH x DHTKD1) | inbreeding | C57Bl/6 N x FVB x Sv129 |

*mice were delivered from Dr. Sven Sauer, University of Heidelberg. They are descendants of a published and well characterized mouse line (Koeller et al., 2002).

V.2. Methods

V.2.1. Genetic and molecular biological methods

V.2.1.1. Preparation of plasmid DNA

For Miniprep plasmid isolation, a single *E.coli* colony was used to inoculate 5 ml LBamp and then incubated overnight. The preparation of high-copy plasmid DNA using the QIAprep Spin Miniprep Kit was performed according to manufacturer's protocol.

For Midiprep plasmid isolation, 50-100 ml overnight bacterial cultures were used, and preparation was performed using the Invitrogen PureLink HiPure Plasmid Filter DNA Purification Kit according to manufacturer's protocol.

V.2.1.2. Preparation of genomic DNA

Fibroblast cell lines were harvested and DNA isolated using the AllPrep DNA/RNA Mini Kit from Qiagen.

V.2.1.3. Polymerase Chain Reaction (PCR) and subsequent purification

DNA sequences with up to several kilobases were amplified with this technique, either from genomic or plasmid DNA. The Qiagen Taq-Polymerase kit was used with the following protocol:

| Component | Volume |
|--|--------------|
| 10x PCR Buffer | 2.5 μ l |
| dNTP mix (2 mM each) | 2.5 μ l |
| F-Primer (10 pmol/ μ l) | 0.5 μ l |
| R-Primer (10 pmol/ μ l) | 0.5 μ l |
| Taq-Polymerase | 0.1 μ l |
| DNA template genomic(10-300 ng/ μ l) | 1 μ l |
| or | |
| DNA template plasmid (10-15 ng/ μ l) | 1 μ l |
| H ₂ O | 16.9 μ l |
| Total | 25 μ l |

In case of subsequent cloning, e.g. TOPO[®] cloning for lentiviral transduction, the volumes were scaled up to 100 μ l in total. Thermal cycler settings were as follows: initially 95 °C for 5 min; 25 cycles of 95 °C for

30 s; temperature dependent on primer constitution 30 s; 72 °C time dependent of fragment length; finally 72 °C for 5 min.

Purification of the PCR product was done via MultiScreen® PCR 96 Filter Plate in a total volume of 100 µl (if needed volume added with HPLC water). Vacuum was applied using a vacuum pump (Merck Millipore, USA) for about 8 min until all liquid vanished. The corresponding well was mixed and pipetted up and down with 25 µl HPLC water to elute the DNA fragment from the bottom.

V.2.1.4. Sequencing of PCR fragments

The fragment obtained through PCR, purified on a filter plate, was used for sequencing. If applicable, a DNA gel electrophoresis was run before sequencing to check DNA quality, amount and fragment size. The sequencing reaction using BigDye Terminator (Applied Biosystems) and the corresponding BigDye buffer was set up as follows in duplicate with forward and reverse primer for each sample:

| Component | Volume |
|--|--------|
| 10x BigDye Buffer | 1.5 µl |
| Forward or Reverse Primer (10 pmol/µl) | 1 µl |
| BigDye | 0.5 µl |
| PCR-product | 1 µl |
| HPLC-H ₂ O | 1 µl |
| Total | 5 µl |

PCR program: initial 96 °C for 1 min, cycle start: 96 °C for 10 s, 50 °C for 5 s, 60 °C for 1 min 30 s, with 25 cycles.

Before sequencing the sample, DNA was precipitated. The sequencing reaction volume was mixed with 25 µl 100% ethanol and incubated in the dark for 1 h (minimum 15 min). Samples were then centrifuged at 3000 RZB for 30 min at room temperature. Subsequently, samples were centrifuged upside down at 100 RZB for 10 s. Then 125 µl of 70% ethanol was added and upside centrifugation at 2000 RZB for 10 min followed. Afterwards the plate was shaken empty upside down and centrifuged in the same orientation at 600 RZB for 1 min at room temperature. Ethanol was left to evaporate for 5 min in the dark. For sequencing the pellet was eluted in 25 µl HPLC water. The probe was transferred into a microtiter plate, which was placed into an automated ABI 3730 sequencer. Resulting sequences were analysed using the Staden Package (<http://staden.sourceforge.net>).

V.2.1.5. Restriction digestion of DNA

In order to digest DNA, restriction digestion reactions were set up with NEB restriction enzymes and corresponding buffers according to New England Biolabs' protocols. Depending on the purpose of the restriction digestion, different DNA amounts and incubation temperatures were used. Proper digestion was checked via DNA gel electrophoresis. In case of double digestion, manufacturer's advice was followed.

V.2.1.6. Ligation of DNA

Ligation of two fragments, i.e. a pre-cut vector and another DNA fragment, was set up using T4 DNA ligase (Thermo Fisher Scientific, USA) according to manufacturer's protocol.

V.2.1.7. DNA gel electrophoresis and subsequent DNA extraction

DNA gel electrophoresis was used to separate and detect DNA fragments of different sizes. Gels were prepared with 0.5-1% Agarose (Biozym Scientific, Germany) in 1x TBE buffer (840 mM Tris, 900 mM boric acid, 20 mM EDTA, add dH₂O up to 1 l, pH8) with 6 µl/100 ml Serva DNA Stain Clear G (Serva Electrophoresis, Germany). Serva stain binds to DNA and can be visualised under a 300 nm UV light transilluminator (Herolab, Germany). Before running the gel at 120 V in 1x TBE buffer, DNA (e.g. PCR product) was mixed with 6x DNA Gel Loading Dye (Thermo Fisher Scientific, USA) and added to one chamber per sample. One chamber per gel was loaded with either 1 kb DNA ladder or 100 bp Plus DNA ladder (Thermo Fisher Scientific, USA) according to manufacturer's instructions. If DNA extraction of a specific band on the agarose gel was desired, the MinElute Gel Extraction Kit (Qiagen, Germany) was used according to manufacturer's protocol.

V.2.1.8. *In vitro* transcription

The DNA was excised from an agarose gel and purified as described in V.2.1.7. Using NanoDrop (Thermo Fisher Scientific, USA) a minimum of 80 ng/µl DNA content was assured. For *in vitro* transcription the mMESSAGE mMACHINE[®] T7 ULTRA Transcription kit was used according to Wefers et al., 2013b. The following components were mixed and incubated for 2 hrs at 37 °C:

| Component | Volume |
|-------------------------------|--------|
| T7 2x NTP/ARCA reagent | 10 µl |
| 10x reaction buffer | 2 µl |
| DNA template (total 0.5-1 µg) | 6 µl |
| T7 enzyme mix | 2 µl |
| Total | 20 µl |

V. MATERIAL AND METHODS

After incubation the RNA sample was polyadenylated, according to the following reaction set up:

| Component | Volume |
|---------------------------------|------------|
| Transcription sample from above | 20 μ l |
| Nuclease-free water | 36 μ l |
| 5x E-PAP buffer | 20 μ l |
| 25 mM MnCl ₂ | 10 μ l |
| 10 mM ATP solution | 10 μ l |
| Total | 96 μ l |

5 μ l of the mixture were removed and stored as a control for later gel electrophoresis. The remaining 91 μ l were mixed with 4 μ l of E-PAP enzyme and incubated at 37 °C for 1 h.

V.2.1.9. RNA purification

For RNA purification the MEGAclean™ Transcription Clean-Up Kit (Thermo Fisher Scientific, USA) was used. Each 91 μ l sample was added up to 100 μ l with elution solution. 350 μ l binding solution were added as well as 250 μ l 100% ethanol. The sample was applied to a MEGAclean spin column, where RNA was bound to the filter and washed several times according to manufacturer's protocol. RNA was eluted in 100 μ l and subsequently precipitated via 5 M ammonium acetate and ethanol. The final RNA pellet was resuspended in 40 μ l T₁₀E_{0.1} microinjection buffer. 1 μ l was used for measurement of RNA content via nanodrop. The yield should exceed 30 μ g. 2 μ g of RNA were used for RNA gel electrophoresis to assure appropriate quality of the sample.

V.2.1.10. RNA gel electrophoresis

A 0.8% agarose gel of 60 ml was cast using the NorthernMax®-Gly Kit (Thermo Fisher Scientific, USA). Agarose was dissolved in 54 ml RNase-free water by the use of a microwave. After cooling 6 ml 10x NorthernMax-Gly buffer were added and the gel poured. The 2 μ g sample were diluted with nuclease-free water up to 10 μ l and mixed with 10 μ l of the supplied Glyoxal loading dye. The mixture was incubated for 30 min at 50 °C. The sample was loaded onto the gel along with 2 μ l of RNA Millennium™ marker (Thermo Fisher Scientific, USA). The gel was run in a chamber filled with 1x NorthernMax®-Gly buffer at 110 V for roughly 1.5 hrs until the blue marker reached the end of the gel. Visualisation under a 300 nm UV light transilluminator (Herolab, Wiesloch, Germany) revealed the expected band size of 3000 bp for TALEN-RNA.

V.2.1.11. Transformation of *E.coli* by electrophoresis

In order to transform *E.coli* with plasmid DNA, One Shot® Stbl3™ chemically competent *E. coli* (Thermo Fisher Scientific, USA) were used. The procedure was performed according to manufacturer's protocol, using 2-3 µl of the plasmid or ligation reaction. In the final step 100 µl of the reaction mix, and a 1/10 dilution of the reaction mix, were spread on a pre-warmed ampicillin plate each.

V.2.1.12. *In silico* design and *in vitro* testing of TALENs

Two mouse lines were generated using the well-established TALEN approach. Both were knockout lines generated by small deletions leading to a frame-shift in murine *Ddtkd1* and *Wdr45*. In order to be able to choose the more efficient TALEN-pair *in vitro*, two pairs for each gene were designed and generated to be tested in cell culture. Only the more efficient one was used to generate mRNA for embryo-injection. TALEN sequences were designed according to published protocols (Boch et al., 2009, Zhang et al., 2011) as described in supplementary figure 2A. Depending on the target sequence of each TALEN, as visualised in supplementary figure 2B, the corresponding TALEN protein sequence from supplementary figure 2A was attached, with variable amino acids at positions 12 and 13 targeting the specific bp within the target sequence as indicated. Protein sequences were ordered at GenScript (New Jersey, USA) as custom DNA synthesis with murine codon optimization offered by GenScript. The TALEN sequence was generated with fixed ends containing a target sequence for the restriction enzyme BbsI for later cloning, and containing the first two (LT) and last two (HG) amino acids from the corresponding TALEN repeats as indicated in supplementary figure 2C. GenScript shipped the construct packed in a pUC57 vector as listed in supplementary table 2. The first, as well as the last repeat sequence specific for the first T and the last nucleotide of the target sequence, are included in the expression vectors and do not need to be included in the synthetic custom nucleotide.

The following *in vitro* testing of TALENs was performed according to a previously established protocol (Wefers et al., 2013b). The four expression plasmids pCAG-TALEN-X-pA (X = A, C, G or T for the 16th protein repeat sequence contained inside the expression plasmid) as well as the ordered pUC57 containing the designed TALEN were BbsI digested. Probes were analysed on a DNA agarose gel and corresponding bands extracted and ligated via T4 ligase. In order to generate TALEN reporter plasmids containing the target sequence, two designed oligonucleotides were aligned to form the target region with compatible overhangs to later be cloned into an NruI and BstB1 digested reporter vector. HEK293 cells were transiently transfected via electroporation with each reporter plasmid as well as both expression plasmids per sample as described in V.2.3.2. Controls were used as suggested by Wefers and colleagues (Wefers et al., 2013b). Roughly one million HEK cells were transfected with each DNA (reporter and expression plasmid composition). Each sample was spread onto three wells after electroporation to enable

measurements in triplicates. Media was changed after 24 hrs. Further simultaneous β -galactosidase and luciferase assays were performed 48 hrs after transfection as described in V.2.2.2. and V.2.2.3.

V.2.2. Protein analytics

V.2.2.1. Immunoblot analysis

Immunoblot, also known as Western blot is a widely used technique to detect specific proteins in cell lysates. After determination of the protein concentration, sodium dodecyl sulphate polyacrylamide gel electrophoresis (SDS-PAGE), protein blotting and Ponceau S staining, Immunodetection enabled the desired analysis. Quantification of the luminescent signal was performed using the multi-imaging-instrument Fusion FX7 advance (Peqlab, Erlangen, Germany) in combination with the analysis software BIO-1D advanced.

Measurement of protein concentration in cell lysate was conducted after Bradford (Bradford, 1976). This dye-binding assay is based on Coomassie® Brilliant Blue G-250, a dye that changes its colour in response to different protein concentrations. When proteins bind the dye, it changes from a double protonated red form and stabilises as an unprotonated blue form. The maximal absorbance of the acidic Coomassie solution shifts from 465 nm (without protein binding) to 595 nm (with saturation protein binding). Coomassie® Brilliant Blue G250 (Sigma-Aldrich, USA) was used according to manufacturer's protocol. For accurate quantification of the results, a regression curve was done using protein standard BSA (0.1-2 mg/ml). Absorbance was measured at 595 nm.

Different protein amounts were used for SDS-PAGE. This separates proteins due to their size. SDS denatures the protein and proteins are separated via polyacrylamide gel electrophoresis. Precast 4-12% PAGEr™ EX Gels (Lonza, Switzerland) were used. Samples were diluted in 2x Laemmli sample buffer (Bio-Rad Laboratories, Hercules, USA) and heated for 3 min at 95 °C. Gels were run for approximately 2 hrs at 120 mA in SDS-running buffer (25 mM Tris, pH 8.3, 192 mM glycine, 0.1% (w/v) SDS). A prestained protein ladder (PageRuler Prestained Protein Ladder, Thermo Fisher Scientific, USA) was used in order to label the protein molecular weight on the gel.

To blot proteins on a PVDF membrane, the membrane was first incubated for 10 min in 100% ethanol for its activation. The gel, PVDF membrane and two Whatman blotting papers (GE Healthcare, Giles, UK) were gently shaken in blotting buffer (25 mM Tris, 190 mM Glycine, 20% MeOH) for 10 min. The gel was situated on top of the membrane surrounded by Whatman blotting paper in a semidry-blotting apparatus. Protein transfer was set to 90 min at 5 mA/cm². In order to check the efficiency of protein transfer, the membrane was shaken for 3 min in removable dye, shortly in Ponceau S (0.5 g Ponceau S, 1% (v/v) acetic acid in dH²O) and subsequently incubated for 5 min in fading solution (10% (v/v) acetic acid, 50% (v/v) methanol dH²O).

V. MATERIAL AND METHODS

For immunodetection, the membrane first had to be incubated in 5% skimmed milk powder for 1 h in order to block unspecific antibody binding. Following this, the membrane was decorated with a specific antibody at 4 °C overnight.

| Antigen | Antibody | Working dilution |
|-----------------------|----------|------------------|
| Beta-actin | a5441 | 1:15,000 |
| NDUFB8 – CI | ab110242 | 1:1,000 |
| E1alpha subunit – PDH | ab110330 | 1:1,000 |
| SDHA – CII | ab14715 | 1:1,000 |
| UQCRC2 – CIII | ab14745 | 1:1,000 |
| ATP5alpha – CV | ab14748 | 1:1,000 |
| COXIV – CIV | ab16056 | 1:500 |
| TOM20 - mitochondria | sc11415 | 1:1,000 |

Table 5: List of antibodies. Indicated is the identification number of each antibody with the working dilution used for the corresponding experiment.

Next day, the membrane was washed three times in 0.1% TBS-Tween for 10 min before incubation with the appropriate horseradish peroxidase (HRP)-coupled secondary antibody for 1 h at room temperature. After washing three times with TBS-Tween (0.1%) proteins were visualised on a photographic film. Amersham ECL Western Blotting detection agent (GE Healthcare Life Sciences, GER) was used according to manufacturer's protocol. Subsequent quantification was performed on the Fusion FX7 advance with the above mentioned analysis software.

For repeated immunodetection the membrane was stripped to remove bound antibodies. It was incubated gently shaking at 50 °C for 30 min in stripping buffer (62.5 mM Tris hydrochloride, pH 6.7, 2% (w/v) SDS, 100 mM β -mercaptoethanol) and subsequently washed three times in TBST for 10 min. The resulting membrane was then used for another immunodetection.

V.2.2.2. β -Galactosidase assay

β -Galactosidase activity was measured using the β -Gal Reporter Gene Assay, chemiluminescent (Roche Applied Science, Germany) according to Wefers et al., 2013b. 20 μ l lysate were added to 40 μ l substrate reagent in each well according to manufacturer's protocol. Every sample was prepared for measurement in triplicate on a white bottom 96-well LumiNunc plate (Thermo Fisher Scientific, USA). Before measurement the plate was incubated at room temperature in the dark for 30 min while shaking gently. With the use of the initiation reagent supplied in the kit, measurement was performed according to the table in V.2.2.3 using a luminometer.

V.2.2.3. Luciferase assay

In order to measure firefly luciferase activity, the luciferase reporter gene assay, high sensitivity (Roche Applied Science, Germany) was used according to Wefers and colleagues protocol (Wefers et al., 2013b). Each sample was measured in triplicate. 75 μ l of lysate were added into wells of 96-well LumiNunc plates (Thermo Fisher Scientific, USA). A luminometer added 150 μ l of luciferase reagent to each well according to the settings below.

| | | luciferase | β-gal |
|-------------|-----------------------|-------------------|-------------------------------|
| Dispense | Injector | 2 | 2 |
| | Volume | 150 | 20 |
| | Speed | middle | middle |
| | Measurement operation | by well | by well |
| | Repeated operation | yes | yes |
| | | | |
| Shake | Duration | 2.0 | 2.0 |
| | Speed | fast | fast |
| | Diameter | 0.1 | 0.1 |
| | Type | orbital | orbital |
| | Measurement operation | by well | by well |
| | Repeated operation | yes | yes |
| Measurement | Name | Firefly | betaGal |
| | Counting Time | 5.0 | 5.0 |
| | Measurement operation | by well | by well |

V.2.2.4. Biochemical analysis of metabolites (GA and OA)

Metabolites were measured from tissue homogenate using gas chromatography /mass spectrometry (GC /MS) and tandem mass spectrometry (MS /MS) to measure oxoadipate (OA) and glutaric acid (GA) levels. Measurements were performed at the Stoffwechselzentrum (Universitaet Heidelberg, GER) in cooperation with Dr. Sven Sauer and Dr. Stefan Koelker.

V.2.3. Tissue culture

V.2.3.1. Culturing, freezing and thawing of fibroblast cells

Patient skin biopsies were cultured in DMEM growth medium containing 4.5 g/l D-glucose, L-glutamine, pyruvate, 10% FBS (fetal bovine serum) and PenStrep (5,000 U/ml penicillin; 5,000 U/ml streptomycin). The fresh biopsy was cut into small pieces and incubated at 37 °C, 5% CO₂ and at 90% humidity in a 8.8 cm² tissue culture dish (Thermo Fisher Scientific, USA). Depending on cell division and the purpose of the cells, they were passaged every 2-5 days in cell culture flasks suitable for adherent cell culture with 25 cm² (10 ml), 75 cm² (25 ml) or 175 cm² (45 ml). When the desired confluency was reached, cells were washed with PBS (5-15 ml depending on flask size) and subsequently detached using Trypsin (0.5-2.5 ml). Cells were pelleted and resuspended in respective culture medium and spread onto several fresh culture flasks in order to passage them. In order to freeze a pellet, cells were resuspended in 1.8 ml DMEM containing 10% DMSO and applied to a 2 ml cryo vial. Packed in a Styrofoam box vials were stored at -80 °C to allow the sample to slowly cool down. In order to thaw a fibroblast cell line, the vial was thawed at 37 °C and subsequently resuspended in pre-warmed DMEM, containing all compounds described above necessary for growth.

V.2.3.2. Transfection of HEK cells

HEK293 cells were used for transfection with plasmid DNA. All DNA samples were sterilized in a 1/10 volume of 3 M sodium acetate and 2.5 volumes 100% ethanol at -20 °C overnight. After thawing and a 3 min centrifugation, the pellet was washed with 70% ethanol and centrifuged again for 3 min. After removal of the supernatant, another centrifugation step was used to discard any residual ethanol. Subsequently the pellet was dried under a sterile hood for another 5 minutes. The sterile DNA pellet was dissolved in sterile water up to a concentration of 1 µg/µl. For each sample, 5 µl (= 5 µg) per plasmid were added together (e.g. 5 µl pCAG-Wdr45ex2-Tal1 + 5 µl pCAG-Wdr45ex2-Tal2 + 5 µl pREP-Wdr45ex2 + 5 µl pCMV-Luc) and mixed with sterile PBS up to a total of 100 µl transfection-DNA. HEK cells were cultivated until a cell count of 1 million cells per transfection planned was available. Cells were washed carefully in PBS and trypsinised (4.5 ml) for 5 min at 37 °C. One million cells were pelleted and resuspended in 100 µl of the corresponding transfection-DNA sample in a 0.2 cm Gene Pulser/MicroPulser Electroporation Cuvette (BioRad, USA). Using the Gene Pulser Xcell™ Electroporation Systems (BioRad, USA) with settings: time constant, 225 V, 2 ms, 2 mm cuvette, electroporation was performed. Transfected cells were instantly resuspended in 9 ml pre-warmed media and 3 ml spread into three separate wells of a 12 well cell culture plate (Thermo Fisher Scientific, USA). 24 hrs after electroporation fresh media was supplied to the cells and measurement was performed another 24 hrs later.

V.2.3.3. Lentiviral transduction of fibroblasts

Lentiviral transduction was performed using the pLenti6.3/V5-TOPO[®] TA Cloning[®] Kit (Thermo Fisher Scientific, USA) according to manufacturer's protocols. TOPO cloning was done with desired full-length cDNA ordered at Genecopoeia (e.g. wild-type *FBXL4*). The HIV-based lentiviral transduction kit led to stable integration of the construct including the CMV promoter into the genome. Integration was assured via blasticidin selection of transduced cells for at least two weeks.

V.2.3.4. Cellular respiration assay using Seahorse

The Seahorse Bioscience[®] XF Extracellular Flux Analyser was used to measure cellular respiration on 96-well specifically applied cell plates. One day before the experiment, 20,000 cells of the corresponding cell line were seeded in each well. In general, a maximum of four different cell lines including controls were distributed per plate. The four corner wells were left empty as they were used for background corrections. Cells were grown in normal DMEM (V.2.3.1) for 24 hrs at 37 °C and 5% CO₂. A calibration plate (supplied by Seahorse Bioscience) was filled with 200 µl XF calibrant and left at 37 °C without CO₂ overnight. On the next day, using a multi-pipette, all wells were washed with PBS, carefully leaving 40 µl of liquid inside and finally leaving 180 µl unbuffered DMEM. The plate was incubated for 30 min at 37 °C without CO₂. In the meantime a loading cartridge (supplied by Seahorse Bioscience) containing four ports per well, was loaded with corresponding compounds. Oligomycin (final conc. 1 µM) was used to fill port A, FCCP (final conc. 0.4 µM) for port B and rotenone (final conc. 2 µM) for port C. The machine was set up to the instructions below.

Upon completion of the calibration cartridge after roughly 30 min, the cell culture plate was inserted into the Flux Analyser and the above mentioned measurement was started. The measurement took about 2 hrs. After measurement, the plate was washed with PBS once and incubated in a dry state at -20 °C overnight. In order to normalize results measured by the Seahorse instrument by cell number, the frozen plate was used the next day to analyse cell numbers via CyQuant Analysis. The CyQuant kit from Invitrogen was used. All compounds, as well as the cell plate, were left to equilibrate to room temperature. 200 µl CyQuant GR dye were added to 20 ml cell lysis buffer b. 200 µl of the resulting solution were added to each well of the cell plate and vigorously pipetted up and down. Subsequently, fluorescence was measured in a microplate reader with excitation of 485 nm and emission detection at 530 nm. Using a standard curve it was possible to calculate the exact number of cells for each well. These numbers were inserted to the Seahorse instrument, which delivered results normalised to each wells' cell number.

V. MATERIAL AND METHODS

Measurement instructions:

| Command | Time (min) | Port | #Repeats |
|---------------|------------|-----------------------|----------|
| Calibrate | 30 | | |
| Equilibrate | 15 | | |
| Mix | 2 | | } x 3 |
| Wait | 2 | | |
| Measure | 3 | | |
| Inject | | A (oligomycin) | |
| Mix | 2 | | } x 3 |
| Wait | 2 | | |
| Measure | 3 | | |
| Inject | | B (FCCP) | |
| Mix | 2 | | } x 3 |
| Wait | 2 | | |
| Measure | 3 | | |
| Inject | | C (rotenone) | |
| Mix | 2 | | } x 3 |
| Wait | 2 | | |
| Measure | 3 | | |

V.2.4. Mouse work

V.2.4.1. Legal approvals

The breeding, housing and characterisation of genetically modified mice with known or unknown handicap in order to research neuropathies and particularly mitochondriopathies (“Zucht, Haltung und Charakterisierung von genetisch veränderten Mäusen mit unbekannter oder bekannter Belastung für die Erforschung von Neuropathien und insbesondere Mitochondriopathien.”) was approved by the Regierung von Oberbayern with the Aktenzeichen: 55.2-1-54-2532-159-2015. The validation of DHTKD1 inhibition as a therapy for Glutaric Aciduria Type 1 in the *Dhtkd1/Gcdh* mouse model (“DHTKD1-Inhibitoren als Therapie gegen Glutarazidurie Typ 1 – Validierung am *Dhtkd1/Gcdh* Mausmodell.”) was approved with the Aktenzeichen: 55.2-1-54-2532-31-2014 at the same responsible german institution.

V.2.4.2. Mouse housing, nutrition and handling

Mice were kept at fully air conditioned experimental animal laboratories at the Helmholtz Zentrum Muenchen (mainly A-Streifen, some at the GMC). Housing rooms were kept at a 12/12 hrs light and dark cycle and in specific pathogen-free (SPF) condition. Humidity was set at 50-60%, temperature at 22 ± 2 °C. Mice were kept in filter top polycarbonate cages type II with 370 cm² surface area. In accordance to EU guidelines only up to 4 adult mice were joined in one cage. Mice were tried to be held with company whenever possible. In case of incompatibilities corresponding mice were separated. Cages were filled with Lignocel® 3-4S bedding (Rettenmaier & Söhne, GER), and standard nutrition was composed of sterile filtered water and standard diet for rodents (Altromin, GER) *ad libitum*. In order to enter the mouse housing facility, a wet shower gate had to be passed in order to keep the SPF condition. Monitoring of mouse hygiene was performed according to FELASA (Federation of European Laboratory Animal Science Associations) guidelines. Handling of mice was done with complete body coverage through sterile laboratory trousers, blouse, socks and mouth and hair masks as well as nitrile gloves. Universal mouse numbering based on ear punches was used, in order to uniquely mark each animal.

V.2.4.3. Mouse embryo-injection

Samples for microinjections were prepared as follows (Wefers et al., 2013b). Both TALEN mRNAs were diluted in T₁₀E_{0.1} to get a final volume of 30 µl containing 300 ng of RNA. This solution was cleaned using an Ultrafree centrifugal filter. Centrifugation for 1 min at room temperature and 12,000 g resulted in a 30 µl injection aliquot ready-to-use for one injection day. Until use it was stored at -80 °C for up to 2 months.

To set up one day of microinjections the specialised team of the Institute of Developmental Genetics (Helmholtz Zentrum Muenchen) started the procedure four days before, as previously described (Wefers et al., 2013b). As embryo donor females they used FVB for the generation of our *Wdr45* and *Dhtkd1* knockout lines. These hormone-treated animals were mated with C57Bl/6N males overnight. Resulting fertilized oocytes were collected and the TALEN injection-sample injected into the larger (male) pronucleus. Injected embryos were reimplanted into pseudopregnant CD-1 foster mothers. One injection day typically resulted in 4-5 foster females each carrying 10 embryos in each oviduct.

V.2.4.4. Mouse genotyping based on PCR and sequencing

Mouse genotyping was done with the resulting piece of skin after ear marking. Mouse Direct PCR Kit (Biotool, USA) was used to both isolate DNA from skin biopsy, as well as to amplify the gene of interest using designed primers. Standard PCR conditions with altered elongation temperatures and times were used (*Wdr45*: 1 min at 56 °C; *Dhtkd1*: 30 s at 56 °C and *Gcdh*: 2 min at 69 °C). In case of *Gcdh*, genotyping was based on a duplex-PCR, meaning the PCR setup consisted of two primer pairs (see table 4;

F13+R17 and Neo25+R21) with the same concentration each. For this mouse line, DNA gel electrophoresis was used for genotyping. A band at 570 bp only, indicated a wild-type mouse and one at 750 bp a homozygous mutant. If both bands were detected the analysed mouse was a heterozygote for *Gcdh*. The protocol was developed and kindly shared with us by S. Sauer (Universitaet Heidelberg, Germany). In the case of genotyping the *Wdr45* or the *Dhtkd1* KO mouse line, a sequencing approach was established in this work to obtain genotypes. This was performed using both the forward and reverse primers as described in V.2.1.4.

V.2.4.5. Neurobehavioral experiments

All neurobehavioral experiments were performed within the light cycle of the animals. The SHIRPA protocol (SmithKline Beecham, Harwell, Imperial College, Royal London Hospital, phenotype assessment (Rogers et al., 1997, Rogers et al., 2001)) was used in its modified scope, as suggested by Masuya and colleagues (Masuya et al., 2005). According to their suggestions, the preliminary analysis as well as the disease progression analysis included the following experiments:

- Locomotor activity: Animals were dropped in the middle of an arena (52 x 30 cm, divided in 28 optically distinguishable squares). 30 seconds upon dropping the mouse into a middle square, the number of squares, travelled by all four paws, was measured. This test enabled assessment of overall locomotor activity. For the statistical analysis of this quantitative variable the Student's t-test was used.
- Body position: The mouse was placed into a 5 l viewing jar and observed for a few seconds. Inactive behaviour scored 0, active behaviour 1 and excessive activity often including jumping scored 2. The statistical analysis of this categorical variable was performed using the Student's t-test.
- Tremor: Animals were lifted by the tail and their forepaws examined for tremor. Like in humans a tremor was described as rhythmic muscle contraction that seemed to be involuntary. This binary variable was statistically analysed using the Fisher's exact test.
- Transitional Activity: This observation is noted when the animal is dropped into the arena for locomotor activity. In case of an extended freeze for over 5 seconds, the animals scores 0 in this test. A shorter freeze results in a score of 1 and immediate movement in a score of 2. This categorical variable was analysed using the Student's t-test.
- Gait: Gait was judged while walking in the arena. Any abnormalities were scored with 1, otherwise a 0 was assigned. This binary variable was analysed using the Fisher's exact test.
- Tail elevation: The position of the tail while traveling the arena was rated as 0 when the tail was dragging, 1 when it was horizontally extended and 2 when it was elevated. This categorical variable was analysed using the Student's t-test.

V. MATERIAL AND METHODS

- Clickbox: A clicking sound was applied out of the animals' sight. Its reaction was measured as either absent or present in order to judge the hearing capability. This binary variable was analysed using the Fisher's exact test.
- Touch escape: In order to investigate the animals' reaction to touch, the mouse was frontally approached by an extended finger. In case of no response at all, the mouse scored 0. If the response occurred at touch it scored 1, and if the animal fled prior to touch it was assigned a score of 2.
- Trunk curl: This observation was assessed while lifting the animal by the tail. Trunk curl describes an instant and straight body curl towards the tail. This was often accompanied by the forepaws touching the hind paws. Since this observation is either absent or present, this binary variable was analysed using the Fisher's exact test.
- Limb grasp: This observation was analysed when the animal was lifted by the tail and described whether grasping of the limbs was present. As this is also a binary variable, the statistical analysis was performed using the Fisher's exact test.
- Urination: It was assessed whether urination occurred during the time of SHIRPA performance. Being a binary variable this was analysed using the Fisher's exact test.

The balance beam was performed in triplicates. All animals were trained to traverse the beam on the day before their first measurement. The set up was in a way that the final end of the beam was attached to the mouse's home cage, in order to encourage traversing. The height of the beam was 15 cm, the same as the height of the mouse cages. It was measured how long it took the animal to traverse 60 cm of the specific beam, and how many foot slips and falls were experienced in each trail.

Grip strength was measured via the grip strength meter (Bioseb, France) in triplicate. Forepaw measurements were used if not stated otherwise.

Inverted grid was performed using the standard cage cover grid. The mouse was placed on top and the cover was immediately turned upside-down. The time was measured until the mouse fell from the grid or left it on purpose. The experiment was terminated after 30 seconds.

V.2.4.6. GMC examinations

Examinations and characterizations performed within the German Mouse Clinic were conducted as published (Fuchs et al., 2012) and are based on experiences from over 250 mutant mouse lines that went through the phenotyping screen of the GMC. Unpublished data mentioned was performed in collaboration with Dr. L. Becker and Prof. Dr. T. Klopstock at the Institute of Neurology as part of a screen of the GMC with Prof. Dr. Hrabě de Angelis as head of the institute.

V.2.4.7. High-lysine diet

Animals were changed to high-lysine diet in either chow containing 4.7% L-lysine (Harlan, USA) or chow and water each containing 4.7% L-lysine (Sigma-Aldrich, USA). Based on the assumption of 3 ml drinking and 3.5 g eating a day per mouse, the daily intake of L-lysine was 235 mg (chow) and 376 mg (chow + H₂O) (Sauer et al., 2015). Weight was measured before start of the diet, and all following measurements were compared to the pre-diet weight. This was the main measure used to monitor the animals' condition. According to animal laws, and our approval by the Regierung von Oberbayern with the Aktenzeichen: 55.2-1-54-2532-159-2015, weight loss of more than 15% was not acceptable. All animals that lost more weight as compared to the start of the diet underwent immediate necropsy.

V.2.4.8. Organ withdrawal

In order to withdraw mouse organs, animals were transferred into a registered dissection room (Helmholtz Zentrum Muenchen) and euthanized via CO₂ according to German directives (TierschutzVersuchstierVerordnung, 1. August 2013). Pursept was used to keep clear off mouse hair during dissection of organs. The order of organ withdrawal was performed in a standardized manner from kidneys, liver, lung and heart to skeletal muscle and last the brain. Organs were shock-frozen in liquid nitrogen immediately after their dissection for 5-10 min and then stored on dry-ice for about 2 hrs. Long-term storage was at -80 °C, and samples for biochemical analysis were sent overnight on dry-ice to avoid thawing of samples.

V.2.5. Statistical analysis

The statistical tests used for each analysis, were mentioned directly in the corresponding results section. In general, the unpaired Students t-test was used for quantitative variables and the Fisher's exact test for binary variables. For quantitative variables describing small groups ($n < 5$) the Fisher's exact test was performed. Both tests resulted in a p-value, which is routinely judged significant with $p < 0.05$.

V.2.6. Authors' contribution

Section I: Identification of a new disease-associated gene – FBXL4. I contributed the genetic analysis and interpretation of clinical and biochemical reports of four patients. For all 28 cases, I evaluated the

V. MATERIAL AND METHODS

suspected deleterious mutations and genotype-phenotype correlations, and I summarized the findings in figure 4 as published in Huemer et al., 2015. I interpreted the clinical and biochemical reports (n=4) and measured impaired maximal respiration in three patients' fibroblast cell lines. Via lentiviral transduction of patients' fibroblasts with the wild-type *FBXL4* allele, I rescued the impaired respiration as I showed via microoxygraphy experiments. Western Blots were generated in collaboration with Matteo Gorza. I performed their analysis, quantification and interpretation.

Section II: Generation of a mouse model (*Wdr45* KO) resembling the human disease BPAN. For a complete spectrum of the human phenotype I summarized all available clinical reports (n = 48). In order to generate a *Wdr45* KO mouse model, I planned and designed the genome editing tool TALEN, specifically. Under supervision of Svenja-Viola Hensler from the Institute of Developmental Genetics, I cloned the corresponding TALENs into different vectors and performed cell culture tests to evaluate their efficiency. I developed a genotyping strategy for the resulting mutant mouse offspring and genotyped them. I performed the breeding and all neurobehavioral characterization experiments of the first three generations. For the characterisation of the following mouse generations I trained and supervised Michael Faerberboeck to perform the experiments. All data analysis was performed by me, as well as dissections and organ withdrawals. Tissue preparations for neuropathology as well as corresponding stainings were performed at the Institute of Pathology at the Helmholtz Zentrum Muenchen by PD Dr. Frauke Neff and Dr. Dirk Janik. In order to get legal approval from the German Authorities to generate mutant mouse lines, I was the leading author of the application for breeding and characterisation of mutant animals.

Section III: Therapeutic strategy for glutaric aciduria type 1. I planned the *Dhtkd1* KO site and designed and ordered the TALEN pairs. Under supervision of Svenja-Viola Hensler from the Institute of Developmental Genetics at the Helmholtz Zentrum Muenchen, I performed the TALEN in vitro testing. All other results, from development of the mouse genotyping strategy for *Dhtkd1*, to animal breeding, crossing and neurologic and behavioural examinations were performed and analysed by me (or the technician trained by me). For neurologic and behavioural examinations I was trained by Dr. Lore Becker. I developed the experimental design and performed all lysine-diet experiments, mouse monitoring and subsequent organ withdrawal. Biochemical measurements via GC/MS (gas chromatography – mass spectrometry) were performed at the Stoffwechselzentrum in Heidelberg, then I analysed all data obtained. I was the leading author of both legal approvals required for the realization of mouse work performed in this section (see V.2.4.1).

VI. TABLE OF FIGURES

| | |
|---|----|
| Figure 1: Mitochondria and oxidative phosphorylation: the electron transport chain. | 14 |
| Figure 2: Exemplified mitochondrial stress experiment. | 16 |
| Figure 3: Pedigrees of paediatric individuals carrying mutations in <i>FBXL4</i> | 18 |
| Figure 4: <i>FBXL4</i> mutation status and gene structure. | 19 |
| Figure 5: Summary of main clinical features of 21 <i>FBXL4</i> patients at initial disease presentation and during course. | 21 |
| Figure 6: Oxygen consumption rate of <i>FBXL4</i> subject 7. | 22 |
| Figure 7: Maximal respiration of non-transduced and transduced <i>FBXL4</i> patient fibroblast cell lines. | 22 |
| Figure 8: Immunoblot analysis of a <i>FBXL4</i> patient shows reduction of mitochondrial proteins. | 23 |
| Figure 9: Schematic comparison of a healthy versus <i>FBXL4</i> -deficient fibroblast. | 28 |
| Figure 10: Schematic of TALEN genome editing. | 31 |
| Figure 11: Schematic of CRISPR/Cas9 genome editing. | 32 |
| Figure 12: Subgroups of NBIA. | 34 |
| Figure 13: WIPI proteins in autophagy. | 38 |
| Figure 14: Clinical summary of BPAN patients. | 41 |
| Figure 15: Clinical presentation of BPAN patients over time. | 42 |
| Figure 16: TALEN target sequences in <i>Wdr45</i> exon 2 and exon 5. | 43 |
| Figure 17: <i>In vitro</i> testing of TALENs. | 44 |
| Figure 18: Timeline to generate a knockout mouse line via TALEN embryo microinjection. | 45 |
| Figure 19: Genetic analysis of <i>Wdr45</i> -Ex2-TALEN injected founder mice and their offspring. | 46 |
| Figure 20: Preliminary analysis of the <i>Wdr45</i> KO cohort. | 48 |
| Figure 21: Neurology screen of the <i>Wdr45</i> disease progression cohort. | 50 |
| Figure 22 Inverted grid of the disease progression <i>Wdr45</i> cohort. | 51 |
| Figure 23: Balance beam of the disease progression <i>Wdr45</i> cohort. | 52 |
| Figure 24: Modified SHIRPA analysis of the disease progression <i>Wdr45</i> cohort. | 53 |
| Figure 25: Limb grasping and trunk curl assessment in wild-type versus <i>Wdr45</i> KO mice at the age of 18 months. | 54 |
| Figure 26: Neurodegeneration in <i>Wdr45</i> KO cerebral cortex and thalamus resembling BPAN patient's substantia nigra. | 55 |
| Figure 27: Timeline of neurodegeneration in <i>Wdr45</i> KO thalamus. | 55 |
| Figure 28: Neurodegeneration in <i>Wdr45</i> KO medulla oblongata, cerebellum and spinal cord with astrocytosis in medulla. | 56 |
| Figure 29 No accumulation of iron, lipofuscin or polysaccharides in degenerating <i>Wdr45</i> KO brain sections. | 57 |

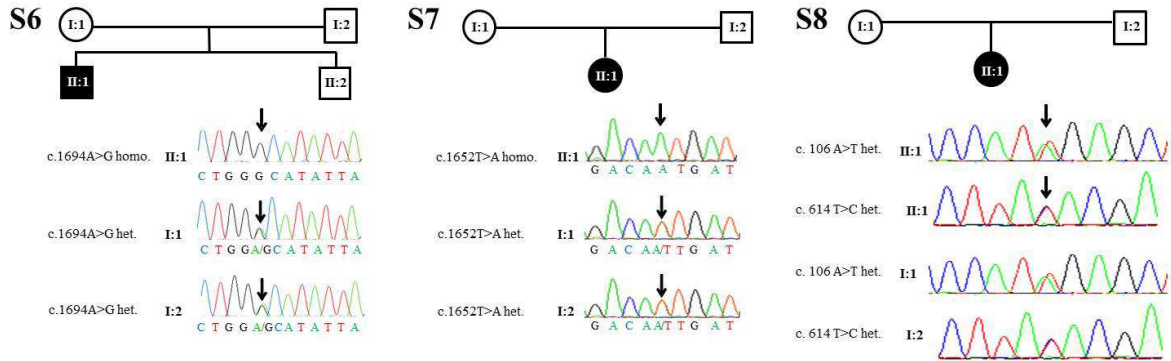
VI. TABLE OF FIGURES

| | |
|---|-----|
| Figure 30: Immunostaining revealed ubiquitin accumulation in medulla oblongata, no SDHA-accumulation in abnormal swollen structures and impaired purkinje cell layer in the cerebellar cortex of <i>Wdr45</i> KO mice. | 57 |
| Figure 31: Weight development of the <i>Wdr45</i> KO GMC cohort. | 58 |
| Figure 32: Overview of identified <i>Wdr45</i> KO phenotypes. | 59 |
| Figure 33: Systematic comparison of BPAN patients' symptoms and <i>Wdr45</i> KO mouse phenotypes. | 60 |
| Figure 34: Schematic of the lysine degradation. | 68 |
| Figure 35: TALEN target sequence in <i>Dhtkd1</i> exon 1 and exon 7. | 73 |
| Figure 36: Murine <i>Dhtkd1</i> gene structure in wild-type and knockout <i>Dhtkd1</i> mice. | 74 |
| Figure 37: <i>In vitro</i> testing of TALENs. | 75 |
| Figure 38: Clinical characterization of <i>Dhtkd1</i> KO mice. | 76 |
| Figure 39: Biochemical characterization of <i>Dhtkd1</i> KO mice. | 77 |
| Figure 40: Mouse backgrounds involved in <i>Gcdh/Dhtkd1</i>-double KO line. | 78 |
| Figure 41: Biochemical characterization of the <i>Gcdh/Dhtkd1</i>-double KO line. | 79 |
| Figure 42: <i>Gcdh-/Dhtkd1</i> double knockout does not rescue weight loss or behavioural decline on high-lysine diet. | 80 |
| Figure 43: Biochemical analysis of the <i>Gcdh-/Dhtkd1</i> double knockout mouse line on normal versus high-lysine diet. | 81 |
| Figure 44: Scheme of a classic research cycle for genetic human diseases. | 85 |
| | |
| Supplementary figure 1: Electropherograms of <i>FBXL4</i> patients and available family members. | 113 |
| Supplementary figure 2: TALEN sequences for murine knockout in <i>Wdr45</i> and <i>Dhtkd1</i>. | 113 |
| Supplementary figure 3: Balance beam of the disease progression <i>Wdr45</i> cohort. | 114 |
| Supplementary figure 4: Modified SHIRPA analysis of the disease progression <i>Wdr45</i> cohort. | 115 |
| Supplementary figure 5: Clinical characterization as weight change per genotype upon normal and high-lysine diet. | 116 |

VII. TABLE OF TABLES

| | |
|--|------------|
| Table 1: Biochemical respiration deficiency in patients' fibroblast cell lines. | 21 |
| Table 2: Summary of findings in CNS-specific <i>Wdr45</i> knockout mouse model (content taken from Zhao et al., 2015). | 37 |
| Table 3: <i>Wdr45</i> KO mouse generation scheme and breeding strategies for different cohorts. | 47 |
| Table 4: Primer table used for <i>FBXL4</i> sequencing in humans and for mouse genotyping of <i>Wdr45</i>, <i>Dhtkd1</i> and <i>Gcdh</i>. | 91 |
| Table 5: List of antibodies. | 100 |
| | |
| Supplementary table 1: Individual clinical symptoms and outcome. | 117 |

VIII. SUPPLEMENTARY MATERIAL



Supplementary figure 1: Electropherograms of *FBXL4* patients and available family members. Arrows depict the mutation site; S6-S8 are the subjects published in 2013 (Gai et al., 2013).

A

| bp in target sequence | RVD: TALEN aa 12/13 | corresponding TALEN prot. repeat sequence |
|-----------------------|---------------------|---|
| A: | NI | LTPEQVVAIASNI GG KQALETVQRLLPVLCQAHG |
| C: | HD | LTPQQVVAIASH DD GKQALETVQRLLPVLCQAHG |
| T: | NG | LTPQQVVAIASN GG GKQALETVQRLLPVLCQAHG |
| G: | NN | LTPQQVVAIASN NG GKQALETVQRLLPVLCQAHG |

B

| gene and exon to be targeted | TALEN 1 target sequence | spacer | TALEN 2 target sequence |
|------------------------------|-------------------------|-----------------|-------------------------|
| <i>Wdr45</i> Ex2 | TGACTCAGCAGCCACT | TCGAGGTGTGACCAG | CCTACATTCAACCAA |
| <i>Wdr45</i> Ex5 | TGCCCGAGAAGGCAAG | GACTCCAAGGACAAA | CTGGTGCTGGAGTTCA |
| <i>Dhtkd1</i> Ex1 | TTCTGCTTCTCCGGCG | CNGTTACCAGACGGA | GAGGGGCGTCTATGGA |
| <i>Dhtkd1</i> Ex7 | TATCAGCGCCAGTTCC | GCAAGGATGTGATTG | TTGATTGTTATGCTA |

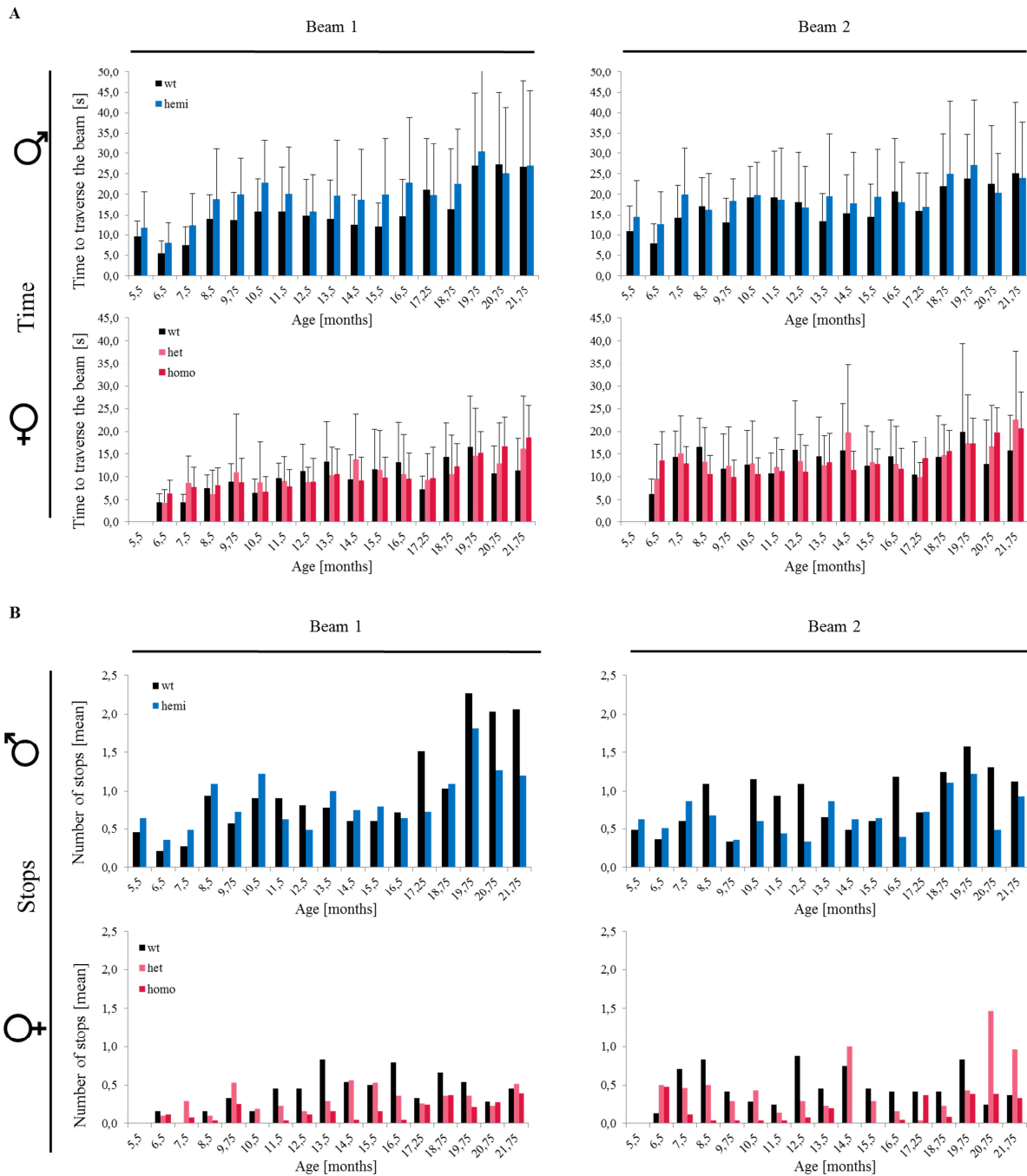
C

TALEN sequence to order as custom designed sequence

| Fixed sequence at TALEN start | first TALEN repeat seq. w/o LT | TALEN repeats 2-15 | last TALEN repeat seq. w/o HG | fixed sequence at TALEN end |
|---------------------------------------|--------------------------------|--------------------|-------------------------------|---|
| GATCGAAGACNNCTTACT | ...NNNNNN... | ...NNNNNNNNN... | ...NNNNN... | CACGGC NG TCITCGATC |
| L T | | | | H G BbsI |

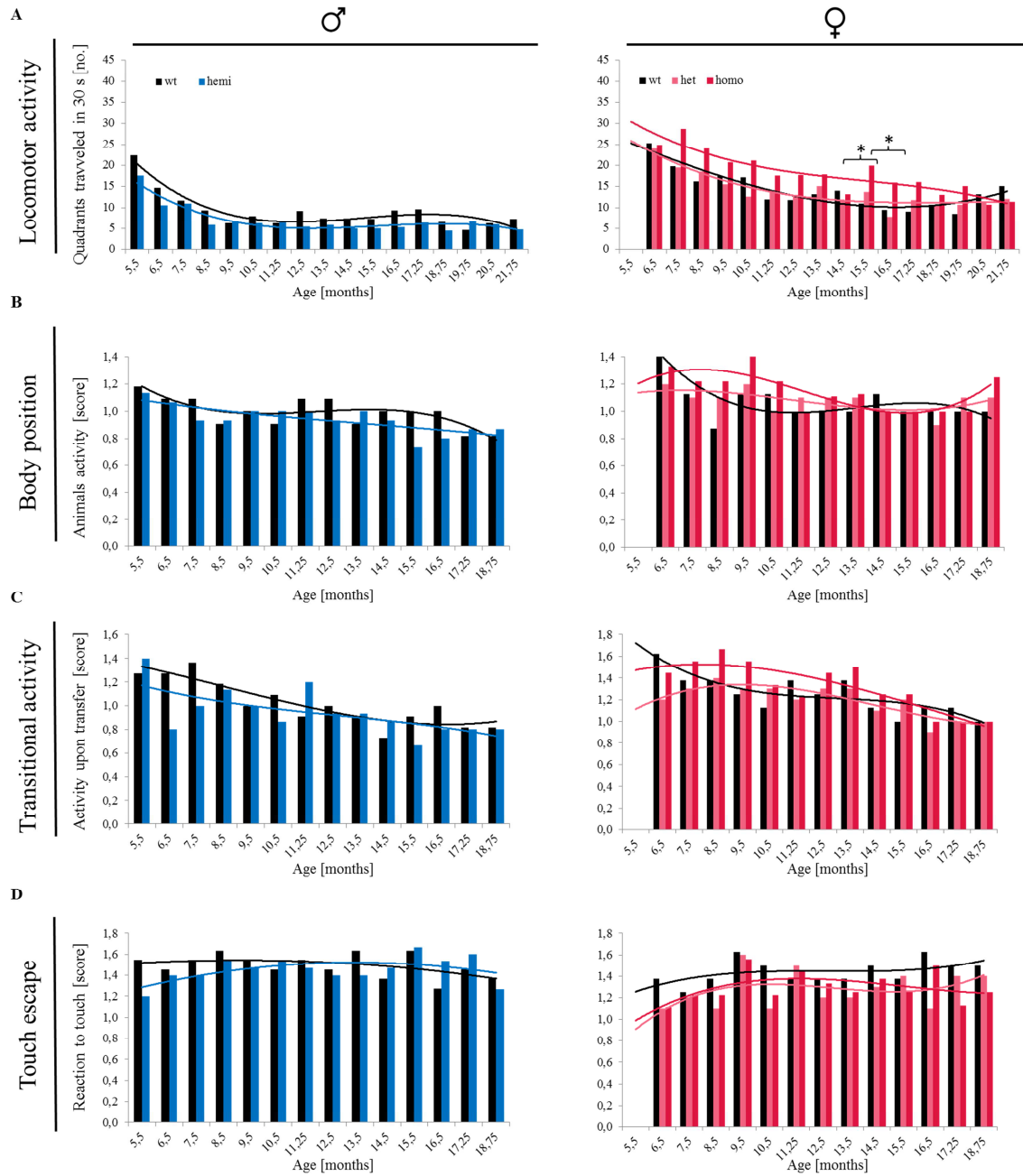
Supplementary figure 2: TALEN sequences for murine knockout in *Wdr45* and *Dhtkd1*. **A)** Description of the specific base pair in the target sequence. This is specifically targeted by two amino acids, the so called repeat variable diresidues (RVD), at position 12 and 13 of the corresponding TALEN sequence. Each of these corresponding TALEN sequence repeats forms a loop structure. **B)** Target sequences for TALEN-pairs separated by a 15 bp spacer, which is not targeted, but instead functions to bring the two fokI nucleases attached to each TALEN into perfect proximity. **C)** Custom designed sequence to be synthesised and ordered for the TALEN cloning strategy developed by Wefers et al., 2013b.

VIII. SUPPLEMENTARY MATERIAL



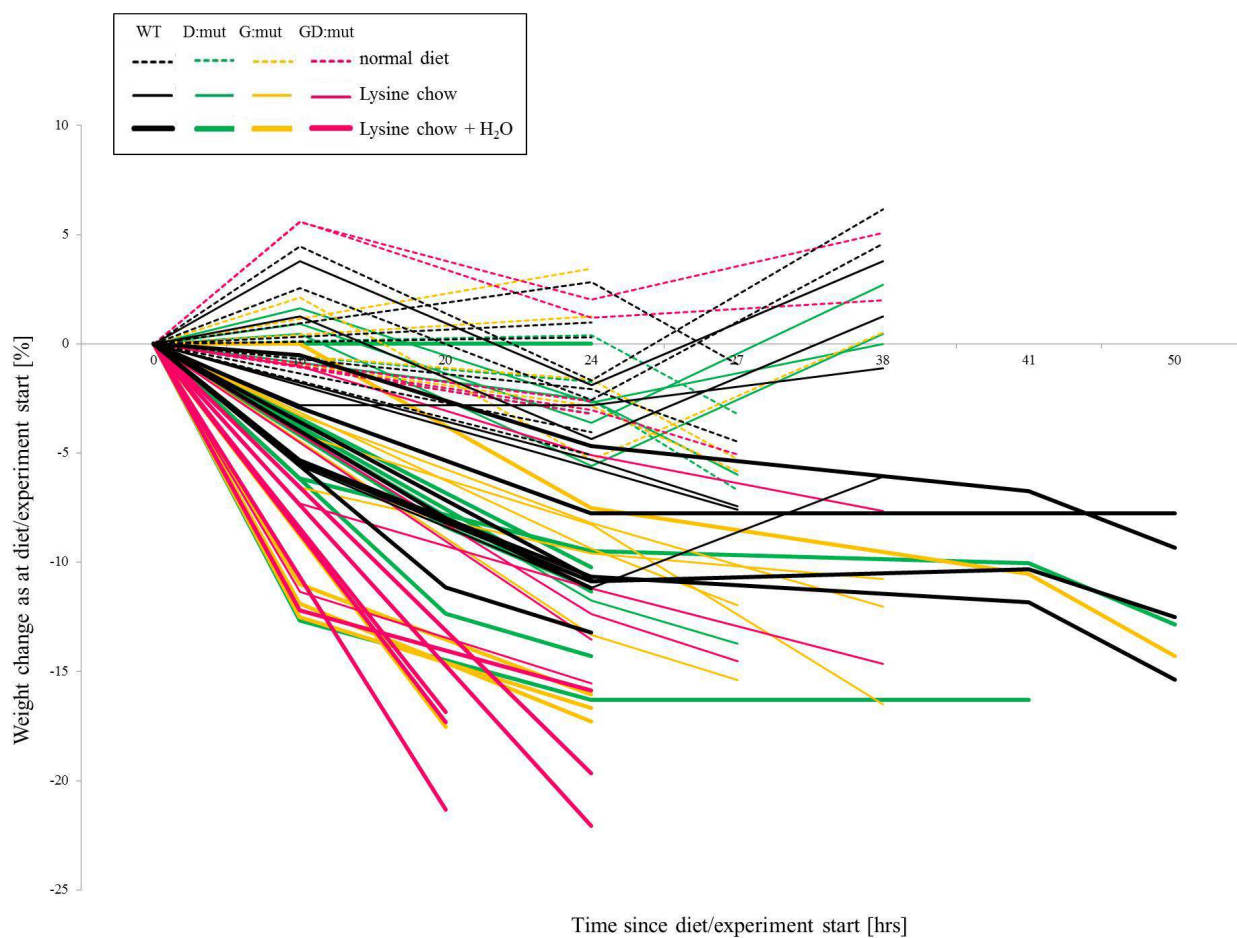
Supplementary figure 3: Balance beam of the disease progression *Wdr45* cohort. Balance beam was performed in triplicate with each mouse. Two different beams were used, with beam 1, round and 22 mm in diameter (left column) and beam 2, rectangular and 7 mm in diameter (right column). **A)** Time to traverse each beam; values are indicated as mean per mouse and per genotype with standard deviations. **B)** Mean number of stops during the traverse of each beam. Wt = wild-type; hemi = hemizygous; het = heterozygous; homo = homozygous; bars indicate standard deviation.

VIII. SUPPLEMENTARY MATERIAL



Supplementary figure 4: Modified SHIRPA analysis of the disease progression *Wdr45* cohort. The analysis included also gait abnormality, tail elevation and urination, but results were not significant and showed no interesting trends (data not shown). **A)** Locomotor activity was assessed by counting quadrants within an arena travelled by an animal within 30 s. **B)** Body position was analysed and scored within a viewing jar with inactive = 0, active = 1 and excessively active behaviour = 2. **C)** Transitional activity was analysed and scored when dropped into an arena with extended freeze = 0, short freeze = 1 and immediate movement = 2. **D)** Touch escape was measured while approaching the animal from the front with no response = 0, reaction to touch = 1 and reaction prior to touch = 2. * t-test: $p < 0.05$ (in females, wt+heterozygote versus homo).

VIII. SUPPLEMENTARY MATERIAL



Supplementary figure 5: Clinical characterization as weight change per genotype upon normal and high-lysine diet. Weight change is measured at several time points a few hours after diet/experiment initiation and is depicted as percentage change since diet/experiment start $n \geq 5$. Diet types are either normal diet, high-lysine chow (235 mg daily intake per mouse) or high-lysine in water and chow (376 mg daily intake per mouse) with an estimated lysine load based on the assumption of 3 ml water and 3.5 mg food daily intake per mouse (Sauer et al., 2015). Wt = wild-type; D:mut = *Dhtkd1* KO; G:mut = *Gcdh* KO; GD:mut = *Gcdh/Dhtkd1*-double KO.

VIII. SUPPLEMENTARY MATERIAL

| Patient ID | Sex | Age at first presentation d=days mo=months | Dysmorphic features (reported by physicians) | Other specific symptoms | Metabolic treatment | Muscular hypotonia | Severely impaired speech | No ambulation | Age (mo) at last follow-up | Deceased at age (mo) |
|-----------------|-----|--|---|--|---|--------------------|--------------------------|---------------|----------------------------|----------------------|
| 1 | F | 1 d | Almond shaped eyes, high arched palate, short forehead, mild <u>synophrys</u> , infraorbital crease, broad nasal bridge, <u>autoverged</u> nostrils and <u>micrognathia</u> | Non-progressive <u>cardiomyopathy</u> | <u>Biotin</u> ; <u>Carnitine</u> ; <u>Coenzyme Q10</u> ; <u>Riboflavin</u> ; <u>Sodumbicarbonate</u> ; <u>Thiamine</u> | + | + | + | | 24 |
| 2 | M | 1 d | Low set ears, broad nasal bridge, almond shaped eyes, mild <u>synophrys</u> | | <u>Coenzyme Q10</u> ; <u>Vit D3</u> ; <u>Riboflavin</u> ; <u>Thiamine</u> | + | + | + | 37 | |
| 4 ^{\$} | M | 1 d | <u>Hypospadia</u> , low set ears, smooth philtrum, pectus excavatum, small hands and feet, short stature | | <u>Carnitine</u> ; <u>Coenzyme Q10</u> ; <u>Riboflavin</u> | + | + | + | 57 | |
| 5 | M | 1 d | Low set ears, long philtrum, curved eyebrows, <u>hypertelorism</u> , high forehead, broad nasal bridge, thickened ear helix | | No treatment | + | + | + | 55 | |
| 7 ^{\$} | F | 1 d | Low set ears, saddle nose, long <u>philtrum</u> , <u>downward</u> slanted eyelids | <u>Hypertrophic</u> <u>cardiomyopathy</u> | <u>Carnitine</u> ; <u>Coenzyme Q10</u> ; <u>Riboflavin</u> ; <u>Sodumbicarbonate</u> | + | + | + | 36 | |
| 9 ^{\$} | M | 1 d | Low set ears, curved, prominent eyebrows, <u>hypertelorism</u> , broad nasal bridge | | <u>Bezafibrate</u> ; <u>Biotin</u> ; <u>Folate</u> ; <u>Carnitine</u> ; <u>Coenzyme Q10</u> ; <u>Riboflavin</u> ; <u>Thiamine</u> ; <u>Vit C</u> ; <u>Vit D</u> | + | + | + | | 26 |
| 10 | F | 1 d | Low set ears, smooth philtrum, small hands and feet | | <u>Coenzyme Q10</u> ; <u>Riboflavin</u> ; <u>Fat rich diet (55%)</u> | + | + | + | | 27 |
| 13 | M | 1 d | none | <u>Hypoplastic</u> <u>cerebellum</u> | No treatment | + | Unknown | Unknown | Unknown | |
| 16 | M | 1 d | none | Borderline left-ventricular hypertrophy and hyperdynamic left ventricular function | <u>Carnitine</u> ; <u>Coenzyme Q10</u> | + | + | + | 37 | |
| 21 | F | 1d | Short stature, microcephaly, facial dysmorphism, <u>synophrys</u> , strabism, hypertrichosis, <u>thyroglossal</u> cyst | Episodic neutropenia, infections, sensorineural hearing loss, optic atrophy, visual impairment, stroke at age 10 years | <u>Coenzyme Q10</u> ; <u>Riboflavin</u> , <u>L-arginine</u> , <u>L-Citrulline</u> ; <u>Sodumbicarbonate</u> | + | + | + | 153 | |
| 17 | M | 2 d | <u>Turricephalus</u> , large anterior fontanelle, blepharophimosis, <u>hypertelorism</u> , epicanthus, broad nasal bridge, low set ears, high-arched palate, broad mouth, short stature, short proximal limbs, cryptorchidism, <u>hypoplastic</u> scrotum, <u>nevus flammeus</u> left arm | <u>Neutropenia</u> , wound healing deficit, recurrent infections. Fatal gastrointestinal bleeding. | No treatment | | unknown | + | | 75 |
| 20 | F | 2d | none | Non-obstructive <u>hypertrophic</u> <u>cardiomyopathy</u> ; <u>hypoplastic</u> <u>cerebellum</u> | <u>Coenzyme Q</u> ; <u>Thiamine</u> ; <u>Propranolol</u> | + | - | n.a. | 2 | |
| 12 | F | 3 d | Craniofacial abnormalities | | No treatment | + | Unknown | Unknown | 24 | |
| 3 | M | 3 mo | none | | No treatment | - | - | + | | 45 |
| 19 | M | 4.5 mo | Long hair line anteriorly, <u>hypertelorism</u> , long smooth philtrum, high arched palate, flat nasal bridge | | <u>Sodumbicarbonate</u> | + | + | | 45 | |
| 14 | M | 5 mo | Frontal bossing, <u>bitemporal</u> narrowing, <u>esotropia</u> | | <u>Carnitine</u> ; <u>Coenzyme Q10</u> | + | + | Assisted | 58 | |
| 6 | M | 6 mo | Craniofacial abnormalities | Bilateral cataracts | No treatment | + | + | + | | 24 |
| 18* | M | 12 mo | none | Small ASD&VSD | <u>Sodumcitrate</u> ; <u>Sodumbicarbonate</u> | + | + | + | Unknown | |
| 15 | F | 17 mo | none | <u>Cardiomyopathy</u> | <u>Sodumcitrate</u> ; <u>Low protein diet</u> | + | + | + | 55 | |
| 11 | M | 24 mo | Craniofacial abnormalities | Bilateral congenital cataracts | No treatment | + | Unknown | Unknown | | 24 |
| 8 | F | Unknown | none | | No treatment | Unknown | + | Unknown | Unknown | |

Supplementary table 1: Individual clinical symptoms and outcome (Huemer et al., 2015). The list is ordered by age at first symptoms. Since elevated lactate, metabolic acidosis, FTT and developmental delay were present in all patients, these symptoms are not listed. (Unfilled fields = no data available). \$\$Published as patients 7, 8 and 9 (Gai et al., 2013); *published as S3 (Bonnen et al., 2013).

IX. ABBREVIATIONS

| | |
|------------------------|--|
| °C | centigrade |
| aa | amino acid |
| Ab | antibody |
| AD | Alzheimer's disease |
| ADP | adenosine diphosphate |
| Approx. | approximately |
| ATP | adenosine triphosphate |
| BSA | bovine serum albumin |
| Bp | base pair |
| BPAN | beta-propeller associated-protein neurodegeneration |
| c. | cDNA sequence position |
| C57Bl/6 | inbred mouse strain created by C. C. Little (1921) substrain 6 |
| Cas | CRISPR associated genes |
| cDNA | complementary DNA |
| chr | chromosome |
| CNS | central nervous system |
| CO ₂ | carbon dioxide |
| CRISPRs | clustered regularly interspaced short palindromic repeats |
| CS | citrate synthase |
| C-terminus | carboxy-terminus |
| Cu | Copper |
| d | day |
| Da | dalton |
| dH ₂ O | deionised water |
| DHPLC-H ₂ O | denaturing high-performance liquid chromatography water |
| DMSO | dimethyl sulfoxide |
| DNA | deoxyribonucleic acid |
| dNTP | deoxynucleotide |
| ds | double-stranded |
| DSB | double-strand break |
| e ⁻ | electron |

IX. ABBREVIATIONS

| | |
|----------------|---|
| <i>E. coli</i> | Escherichia coli |
| EDTA | ethylenediaminetetraacetic acid |
| et al. | et alii |
| FBS | foetal bovine serum |
| FCCP | carbonyl cyanide p-trifluoromethoxyphenylhydrazone |
| FDA | Food and Drug Administration |
| FVB | Friend leukemia virus B mouse strain |
| fs | frame-shift |
| g | gram |
| GA | glutaric acid |
| GA-I | glutaric aciduria type 1 |
| GA-III | glutaric aciduria type 3 |
| GC | gas chromatography |
| GMC | German Mouse Clinic |
| h | hour |
| H ⁺ | Proton, cationic form of atomic hydrogen |
| HEK293 | human embryonic kidney 293 cells |
| hg19 | human genome assembly GRCh38/hg38 (December 2013), UCSC |
| HGMD | Human Gene Mutation Database |
| i.e. | id est |
| IEG | Institute of Experimental Genetics, Helmholtz Zentrum Muenchen |
| IHG | Institute of Human Genetics, Helmholtz Zentrum Muenchen |
| indel | small insertion and deletion variation |
| kb | kilobase |
| kDa | kilodalton |
| KO | knockout |
| l | litre |
| M | molar |
| µg | microgram |
| µl | microlitre |
| µM | micromolar |

IX. ABBREVIATIONS

| | |
|------------------------------|--|
| mA | milliampere |
| MAF | minor allele frequency |
| Mb | megabase |
| mg | milligram |
| MgCl ₂ | magnesium chloride |
| MGI | Mouse Genome Informatics |
| min | minute |
| ml | millilitre |
| mM | millimolar |
| mm9 | mouse genome assembly GRCm38/mm10 (December 2011), UCSC |
| MPAN | mitochondrial-membrane protein-associated neurodegeneration |
| MRC | mitochondrial respiratory chain |
| mRNA | messenger ribonucleic acid |
| MS | mass spectrometry |
| mtDNA | mitochondrial DNA |
| MTS | mitochondrial targeting sequence |
| NA | not available |
| NAD ⁺ /NADH | Nicotinamide adenine dinucleotide (oxidised/reduced) |
| NBIA | neurodegeneration with brain iron accumulation |
| NCBI | National Center for Biotechnology Information |
| ng | nanogram |
| NGS | next-generation sequencing |
| NHDF | normal human dermal fibroblasts |
| NHEJ | non-homologous end joining |
| nm | nanometer |
| nM | nanomolar |
| NM | RefSeq mRNA sequence |
| NP | RefSeq protein sequence |
| NR | nicotinamide riboside |
| N-terminus | amino-terminus |
| O ₂ ^{•-} | superoxide radical anion |

IX. ABBREVIATIONS

| | |
|--------|--|
| OCR | oxygen consumption rate |
| OMIM | Online Mendelian Inheritance in Man |
| OXPHOS | oxidative phosphorylation |
| p. | protein sequence position |
| PAGE | polyacrylamide gel electrophoresis |
| PBS | phosphate buffer saline |
| PCR | polymerase chain reaction |
| pmol | picomol |
| RCC | respiratory chain complex |
| REDOX | reduction oxidation reaction |
| RefSeq | NCBI Reference Sequence Database |
| RNA | ribonucleic acid |
| ROS | reactive oxygen species |
| RT | room temperature |
| RZB | relative Zentrifugalbeschleunigung (relative centrifugal acceleration) |
| s | second |
| SD | standard deviation |
| SDS | sodium dodecyl sulphate |
| SHIRPA | SmithKline Beecham, Harwell, Imperial College, Royal London Hospital, phenotype assessment |
| SN | <i>substantia nigra</i> |
| Suppl. | Supplementary |
| TALEN | transcription activator-like effector nuclease |
| TBE | Tris-borat-EDTA |
| TBST | Tris-buffered saline and Tween 20 |
| UCSC | University of California, Santa Cruz |
| UPS | ubiquitin-proteasome system |
| UV | ultraviolet |
| V | volt |
| WES | whole exome sequencing |
| WT | wild-type |

X. REFERENCES

- ABIDI, A., MIGNON-RAVIX, C., CACCIAGLI, P., GIRARD, N., MILH, M. & VILLARD, L. 2015. Early-onset epileptic encephalopathy as the initial clinical presentation of WDR45 deletion in a male patient. *Eur J Hum Genet*.
- ANTOUN, G., MCBRIDE, S., VANSTONE, J. R., NAAS, T., MICHAUD, J., REDPATH, S., MCMILLAN, H. J., BROPHY, J., DAOUD, H., CHAKRABORTY, P., DYMENT, D., HOLCIK, M., HARPER, M. E. & LINES, M. A. 2015. Detailed Biochemical and Bioenergetic Characterization of FBXL4-Related Encephalomyopathic Mitochondrial DNA Depletion. *JIMD Rep*.
- BECKER, L., KLING, E., SCHILLER, E., ZEH, R., SCHREWE, A., HOLTER, S. M., MOSSBRUGGER, I., CALZADA-WACK, J., STRECKER, V., WITTIG, I., DUMITRU, I., WENZ, T., BENDER, A., AICHLER, M., JANIK, D., NEFF, F., WALCH, A., QUINTANILLA-FEND, L., FLOSS, T., BEKEREDJIAN, R., GAILUS-DURNER, V., FUCHS, H., WURST, W., MEITINGER, T., PROKISCH, H., DE ANGELIS, M. H. & KLOPSTOCK, T. 2014. MTO1-deficient mouse model mirrors the human phenotype showing complex I defect and cardiomyopathy. *PLoS One*, 9, e114918.
- BEHRENDTS, C., SOWA, M. E., GYGI, S. P. & HARPER, J. W. 2010. Network organization of the human autophagy system. *Nature*, 466, 68-76.
- BENNETT, M. J., POLLITT, R. J., GOODMAN, S. I., HALE, D. E. & VAMECQ, J. 1991. Atypical riboflavin-responsive glutaric aciduria, and deficient peroxisomal glutaryl-CoA oxidase activity: a new peroxisomal disorder. *J Inherit Metab Dis*, 14, 165-73.
- BERGER, Z., RAVIKUMAR, B., MENZIES, F. M., OROZ, L. G., UNDERWOOD, B. R., PANGALOS, M. N., SCHMITT, I., WULLNER, U., EVERT, B. O., O'KANE, C. J. & RUBINSZTEIN, D. C. 2006. Rapamycin alleviates toxicity of different aggregate-prone proteins. *Hum Mol Genet*, 15, 433-42.
- BIAGOSCH, C., RAGADEEPHTI, E., HENSLER, S., FAERBERBOECK, M., KUEHN, R., WURST, W., MEITINGER, T., KOELKER, S., SAUER, S., PROKISCH, H. 2016. Dhtkd1 knock-out does not rescue GA-I in a Gcdh- mouse model. Manuscript in preparation.
- BIANCONI, E., PIOVESAN, A., FACCHIN, F., BERAUDI, A., CASADEI, R., FRABETTI, F., VITALE, L., PELLERI, M. C., TASSANI, S., PIVA, F., PEREZ-AMODIO, S., STRIPPOLI, P. & CANAIDER, S. 2013. An estimation of the number of cells in the human body. *Ann Hum Biol*, 40, 463-71.
- BIBIKOVA, M., BEUMER, K., TRAUTMAN, J. K. & CARROLL, D. 2003. Enhancing gene targeting with designed zinc finger nucleases. *Science*, 300, 764.
- BIBIKOVA, M., CARROLL, D., SEGAL, D. J., TRAUTMAN, J. K., SMITH, J., KIM, Y. G. & CHANDRASEGARAN, S. 2001. Stimulation of homologous recombination through targeted cleavage by chimeric nucleases. *Mol Cell Biol*, 21, 289-97.
- BOCH, J., SCHOLZE, H., SCHORNACK, S., LANDGRAF, A., HAHN, S., KAY, S., LAHAYE, T., NICKSTADT, A. & BONAS, U. 2009. Breaking the code of DNA binding specificity of TAL-type III effectors. *Science*, 326, 1509-12.
- BONNEN, P. E., YARHAM, J. W., BESSE, A., WU, P., FAQEIH, E. A., AL-ASMARI, A. M., SALEH, M. A., EYALID, W., HADEEL, A., HE, L., SMITH, F., YAU, S., SIMCOX, E. M., MIWA, S., DONTI, T., ABU-AMERO, K. K., WONG, L. J., CRAIGEN, W. J., GRAHAM, B. H., SCOTT, K. L., MCFARLAND, R. & TAYLOR, R. W.

X. REFERENCES

2013. Mutations in FBXL4 cause mitochondrial encephalopathy and a disorder of mitochondrial DNA maintenance. *Am J Hum Genet*, 93, 471-81.
- BRADFORD, M. M. 1976. A rapid and sensitive method for the quantitation of microgram quantities of protein utilizing the principle of protein-dye binding. *Anal Biochem*, 72, 248-54.
- BRUNETTI, D., DUSI, S., GIORDANO, C., LAMPERTI, C., MORBIN, M., FUGNANESI, V., MARCHET, S., FAGIOLARI, G., SIBON, O., MOGGIO, M., D'AMATI, G. & TIRANTI, V. 2014. Pantethine treatment is effective in recovering the disease phenotype induced by ketogenic diet in a pantothenate kinase-associated neurodegeneration mouse model. *Brain*, 137, 57-68.
- BRUNETTI, D., DUSI, S., MORBIN, M., UGGETTI, A., MODA, F., D'AMATO, I., GIORDANO, C., D'AMATI, G., COZZI, A., LEVI, S., HAYFLICK, S. & TIRANTI, V. 2012. Pantothenate kinase-associated neurodegeneration: altered mitochondria membrane potential and defective respiration in Pank2 knock-out mouse model. *Hum Mol Genet*, 21, 5294-305.
- BUGGE, A., DIB, L. & COLLINS, S. 2014. Measuring respiratory activity of adipocytes and adipose tissues in real time. *Methods Enzymol*, 538, 233-47.
- BUGIANI, M., LAMANTEA, E., INVERNIZZI, F., MORONI, I., BIZZI, A., ZEVIANI, M. & UZIEL, G. 2006. Effects of riboflavin in children with complex II deficiency. *Brain Dev*, 28, 576-81.
- BUNIK, V. I. & DEGTYAREV, D. 2008. Structure-function relationships in the 2-oxo acid dehydrogenase family: substrate-specific signatures and functional predictions for the 2-oxoglutarate dehydrogenase-like proteins. *Proteins*, 71, 874-90.
- BUNIK, V. I., TYLICKI, A. & LUKASHEV, N. V. 2013. Thiamin diphosphate-dependent enzymes: from enzymology to metabolic regulation, drug design and disease models. *Febs j*, 280, 6412-42.
- CALVO, S. E., CLAUSER, K. R. & MOOTHA, V. K. 2016. MitoCarta2.0: an updated inventory of mammalian mitochondrial proteins. *Nucleic Acids Res*, 44, D1251-7.
- CASTETS, P., LIN, S., RION, N., DI FULVIO, S., ROMANINO, K., GURIDI, M., FRANK, S., TINTIGNAC, L. A., SINNREICH, M. & RUEGG, M. A. 2013. Sustained activation of mTORC1 in skeletal muscle inhibits constitutive and starvation-induced autophagy and causes a severe, late-onset myopathy. *Cell Metab*, 17, 731-44.
- CERUTTI, R., PIRINEN, E., LAMPERTI, C., MARCHET, S., SAUVE, A. A., LI, W., LEONI, V., SCHON, E. A., DANTZER, F., AUWERX, J., VISCOMI, C. & ZEVIANI, M. 2014. NAD(+)-dependent activation of Sirt1 corrects the phenotype in a mouse model of mitochondrial disease. *Cell Metab*, 19, 1042-9.
- CHINNERY, P. F. 2010. Defining neurogenetic phenotypes (or how to compare needles in haystacks). *Brain*, 133, 649-51.
- CHRISTENSEN, E., RIBES, A., MERINERO, B. & ZSCHOCKE, J. 2004. Correlation of genotype and phenotype in glutaryl-CoA dehydrogenase deficiency. *J Inherit Metab Dis*, 27, 861-8.
- CHRISTIAN, M., CERMAK, T., DOYLE, E. L., SCHMIDT, C., ZHANG, F., HUMMEL, A., BOGDANOVA, A. J. & VOYTAS, D. F. 2010. Targeting DNA double-strand breaks with TAL effector nucleases. *Genetics*, 186, 757-61.
- CHRISTIAN, P., SACCO, J. & ADELI, K. 2013. Autophagy: Emerging roles in lipid homeostasis and metabolic control. *Biochim Biophys Acta*, 1831, 819-24.

X. REFERENCES

- COSSU, G., ABBRUZZESE, G., MATTA, G., MURGIA, D., MELIS, M., RICCHI, V., GALANELLO, R., BARELLA, S., ORIGA, R., BALOCCO, M., PELOSIN, E., MARCHESE, R., RUFFINENGO, U. & FORNI, G. L. 2014. Efficacy and safety of deferiprone for the treatment of pantothenate kinase-associated neurodegeneration (PKAN) and neurodegeneration with brain iron accumulation (NBIA): results from a four years follow-up. *Parkinsonism Relat Disord*, 20, 651-4.
- DANHAUSER, K., SAUER, S. W., HAACK, T. B., WIELAND, T., STAUFNER, C., GRAF, E., ZSCHOCKE, J., STROM, T. M., TRAUB, T., OKUN, J. G., MEITINGER, T., HOFFMANN, G. F., PROKISCH, H. & KOLKER, S. 2012. DHTKD1 mutations cause 2-aminoadipic and 2-oxoadipic aciduria. *Am J Hum Genet*, 91, 1082-7.
- DURAN, M., BEEMER, F. A., WADMAN, S. K., WENDEL, U. & JANSSEN, B. 1984. A patient with alpha-ketoacidic and alpha-aminoacidic aciduria. *J Inher Metab Dis*, 7, 61.
- EBRAHIMI-FAKHARI, D., SEITZ, A., KOLKER, S. & HOFFMANN, G. F. 2015. Recurrent Stroke-Like Episodes in FBXL4-Associated Early-Onset Mitochondrial Encephalomyopathy. *Pediatr Neurol*, 53, 549-50.
- EBRAHIMKHANI, M. R., NEIMAN, J. A., RAREDON, M. S., HUGHES, D. J. & GRIFFITH, L. G. 2014. Bioreactor technologies to support liver function in vitro. *Adv Drug Deliv Rev*, 69-70, 132-57.
- FLOSS, T. & SCHNUTGEN, F. 2008. Conditional gene trapping using the FLEEx system. *Methods Mol Biol*, 435, 127-38.
- FORNI, G. L., BALOCCO, M., CREMONESI, L., ABBRUZZESE, G., PARODI, R. C. & MARCHESE, R. 2008. Regression of symptoms after selective iron chelation therapy in a case of neurodegeneration with brain iron accumulation. *Mov Disord*, 23, 904-7.
- FUCHS, H., GAILUS-DURNER, V., NESCHEN, S., ADLER, T., AFONSO, L. C., AGUILAR-PIMENTEL, J. A., BECKER, L., BOHLA, A., CALZADA-WACK, J., COHRS, C., DEWERT, A., FRIDRICH, B., GARRETT, L., GLASL, L., GOTZ, A., HANS, W., HOLTER, S. M., HORSCH, M., HURT, A., JANAS, E., JANIK, D., KAHLE, M., KISTLER, M., KLEIN-RODEWALD, T., LENGGER, C., LUDWIG, T., MAIER, H., MARSCHALL, S., MICKLICH, K., MOLLER, G., NATON, B., PREHN, C., PUK, O., RACZ, I., RASS, M., RATHKOLB, B., ROZMAN, J., SCHEERER, M., SCHILLER, E., SCHREWE, A., STEINKAMP, R., STOGER, C., SUN, M., SZYMCAK, W., TREISE, I., VARGAS PANESSO, I. L., VERNALEKEN, A. M., WILLERSHAUSER, M., WOLFF-MUSCATE, A., ZEH, R., ADAMSKI, J., BECKERS, J., BEKEREDJIAN, R., BUSCH, D. H., EICKELBERG, O., FAVOR, J., GRAW, J., HOFER, H., HOSCHEN, C., KATUS, H., KLINGENSPOR, M., KLOPSTOCK, T., NEFF, F., OLLERT, M., SCHULZ, H., STOGER, T., WOLF, E., WURST, W., YILDIRIM, A. O., ZIMMER, A. & HRABE DE ANGELIS, M. 2012. Innovations in phenotyping of mouse models in the German Mouse Clinic. *Mamm Genome*, 23, 611-22.
- GAI, X., GHEZZI, D., JOHNSON, M. A., BIAGOSCH, C. A., SHAMSELDIN, H. E., HAACK, T. B., REYES, A., TSUKIKAWA, M., SHELDON, C. A., SRINIVASAN, S., GORZA, M., KREMER, L. S., WIELAND, T., STROM, T. M., POLYAK, E., PLACE, E., CONSUGAR, M., OSTROVSKY, J., VIDONI, S., ROBINSON, A. J., WONG, L. J., SONDHEIMER, N., SALIH, M. A., AL-JISHI, E., RAAB, C. P., BEAN, C., FURLAN, F., PARINI, R., LAMPERTI, C., MAYR, J. A., KONSTANTOPOULOU, V., HUEMER, M., PIERCE, E. A., MEITINGER, T., FREISINGER, P., SPERL, W., PROKISCH, H., ALKURAYA, F. S., FALK, M. J. & ZEVIANI, M. 2013. Mutations in FBXL4, encoding a mitochondrial protein, cause early-onset mitochondrial encephalomyopathy. *Am J Hum Genet*, 93, 482-95.
- GALLUZZI, L., PIETROCOLA, F., BRAVO-SAN PEDRO, J. M., AMARAVADI, R. K., BAEHRECKE, E. H., CECCONI, F., CODOGNO, P., DEBNATH, J., GEWIRTZ, D. A., KARANTZA, V., KIMMELMAN, A., KUMAR, S., LEVINE, B., MAIURI, M. C., MARTIN, S. J., PENNINGER, J., PIACENTINI, M., RUBINSZTEIN, D. C., SIMON, H. U., SIMONSEN, A., THORBURN, A. M., VELASCO, G., RYAN, K. M. & KROEMER, G. 2015. Autophagy in malignant transformation and cancer progression. *Embo j*, 34, 856-80.

X. REFERENCES

- GONG, B., PAN, Y., VEMPATI, P., ZHAO, W., KNABLE, L., HO, L., WANG, J., SASTRE, M., ONO, K., SAUVE, A. A. & PASINETTI, G. M. 2013. Nicotinamide riboside restores cognition through an upregulation of proliferator-activated receptor-gamma coactivator 1 α regulated beta-secretase 1 degradation and mitochondrial gene expression in Alzheimer's mouse models. *Neurobiol Aging*, 34, 1581-8.
- HAACK, T. B., HOGARTH, P., GREGORY, A., PROKISCH, H. & HAYFLICK, S. J. 2013. BPAN: the only X-linked dominant NBIA disorder. *Int Rev Neurobiol*, 110, 85-90.
- HAACK, T. B., HOGARTH, P., KRUER, M. C., GREGORY, A., WIELAND, T., SCHWARZMAYR, T., GRAF, E., SANFORD, L., MEYER, E., KARA, E., CUNO, S. M., HARIK, S. I., DANDU, V. H., NARDOCCI, N., ZORZI, G., DUNAWAY, T., TARNOPOLSKY, M., SKINNER, S., FRUCHT, S., HANSPAL, E., SCHRANDER-STUMPEL, C., HERON, D., MIGNOT, C., GARAVAGLIA, B., BHATIA, K., HARDY, J., STROM, T. M., BODDAERT, N., HOULDEN, H. H., KURIAN, M. A., MEITINGER, T., PROKISCH, H. & HAYFLICK, S. J. 2012. Exome sequencing reveals de novo WDR45 mutations causing a phenotypically distinct, X-linked dominant form of NBIA. *Am J Hum Genet*, 91, 1144-9.
- HAGEN, J., TE BRINKE, H., WANDERS, R. J., KNEGT, A. C., OUSSOREN, E., HOOGEBOOM, A. J., RUIJTER, G. J., BECKER, D., SCHWAB, K. O., FRANKE, I., DURAN, M., WATERHAM, H. R., SASS, J. O. & HOUTEN, S. M. 2015. Genetic basis of alpha-aminoadipic and alpha-ketoadipic aciduria. *J Inherit Metab Dis*, 38, 873-9.
- HAMDAN, F. F., SROUR, M., CAPO-CHICHI, J. M., DAOUD, H., NASSIF, C., PATRY, L., MASSICOTTE, C., AMBALAVANAN, A., SPIEGELMAN, D., DIALLO, O., HENRION, E., DIONNE-LAPORTE, A., FOUGERAT, A., PSHEZHETSKY, A. V., VENKATESWARAN, S., ROULEAU, G. A. & MICHAUD, J. L. 2014. De novo mutations in moderate or severe intellectual disability. *PLoS Genet*, 10, e1004772.
- HAYFLICK, S. J., KRUER, M. C., GREGORY, A., HAACK, T. B., KURIAN, M. A., HOULDEN, H. H., ANDERSON, J., BODDAERT, N., SANFORD, L., HARIK, S. I., DANDU, V. H., NARDOCCI, N., ZORZI, G., DUNAWAY, T., TARNOPOLSKY, M., SKINNER, S., HOLDEN, K. R., FRUCHT, S., HANSPAL, E., SCHRANDER-STUMPEL, C., MIGNOT, C., HERON, D., SAUNDERS, D. E., KAMINSKA, M., LIN, J. P., LASCELLES, K., CUNO, S. M., MEYER, E., GARAVAGLIA, B., BHATIA, K., DE SILVA, R., CRISP, S., LUNT, P., CAREY, M., HARDY, J., MEITINGER, T., PROKISCH, H. & HOGARTH, P. 2013. beta-Propeller protein-associated neurodegeneration: a new X-linked dominant disorder with brain iron accumulation. *Brain*, 136, 1708-17.
- HERINGER, J., BOY, S. P., ENSENAUER, R., ASSMANN, B., ZSCHOCKE, J., HARTING, I., LUCKE, T., MAIER, E. M., MUHLHAUSEN, C., HAEGE, G., HOFFMANN, G. F., BURGARD, P. & KOLKER, S. 2010. Use of guidelines improves the neurological outcome in glutaric aciduria type I. *Ann Neurol*, 68, 743-52.
- HOLZEROVA, E., DANHAUSER, K., HAACK, T. B., KREMER, L. S., MELCHER, M., INGOLD, I., KOBAYASHI, S., TERRILE, C., WOLF, P., SCHAPER, J., MAYATEPEK, E., BAERTLING, F., FRIEDMANN ANGELI, J. P., CONRAD, M., STROM, T. M., MEITINGER, T., PROKISCH, H. & DISTELMAIER, F. 2015. Human thioredoxin 2 deficiency impairs mitochondrial redox homeostasis and causes early-onset neurodegeneration. *Brain*.
- HRABE DE ANGELIS, M. & BALLING, R. 1998. Large scale ENU screens in the mouse: genetics meets genomics. *Mutat Res*, 400, 25-32.
- HRABE DE ANGELIS, M. H., FLASWINKEL, H., FUCHS, H., RATHKOLB, B., SOEWARTO, D., MARSCHALL, S., HEFFNER, S., PARGENT, W., WUENSCH, K., JUNG, M., REIS, A., RICHTER, T., ALESSANDRINI, F., JAKOB, T., FUCHS, E., KOLB, H., KREMMER, E., SCHAEUBLE, K., ROLLINSKI, B., ROSCHER, A., PETERS, C., MEITINGER, T., STROM, T., STECKLER, T., HOLSBOER, F., KLOPSTOCK, T., GEKELER, F., SCHINDEWOLF, C., JUNG, T., AVRAHAM, K., BEHRENDT, H., RING, J., ZIMMER, A., SCHUGHART, K., PFEFFER, K., WOLF, E. & BALLING, R. 2000. Genome-wide, large-scale production of mutant mice by ENU mutagenesis. *Nat Genet*, 25, 444-7.

X. REFERENCES

- HUANG, J. & BRUMELL, J. H. 2014. Bacteria-autophagy interplay: a battle for survival. *Nat Rev Microbiol*, 12, 101-14.
- HUEMER, M., KARALL, D., SCHOSSIG, A., ABDENUR, J. E., AL JASMI, F., BIAGOSCH, C., DISTELMAIER, F., FREISINGER, P., GRAHAM, B. H., HAACK, T. B., HAUSER, N., HERTECANT, J., EBRAHIMI-FAKHARI, D., KONSTANTOPOULOU, V., LEYDIKER, K., LOURENCO, C. M., SCHOLL-BURGI, S., WILICHOWSKI, E., WOLF, N. I., WORTMANN, S. B., TAYLOR, R. W., MAYR, J. A., BONNEN, P. E., SPERL, W., PROKISCH, H. & MCFARLAND, R. 2015. Clinical, morphological, biochemical, imaging and outcome parameters in 21 individuals with mitochondrial maintenance defect related to FBXL4 mutations. *J Inherit Metab Dis*, 38, 905-14.
- ICHINOSE, Y., MIWA, M., ONOHARA, A., OBI, K., SHINDO, K., SAITSU, H., MATSUMOTO, N. & TAKIYAMA, Y. 2014. Characteristic MRI findings in beta-propeller protein-associated neurodegeneration (BPN). *Neurol Clin Pract*, 4, 175-177.
- JIANG, T., YU, J. T., ZHU, X. C., ZHANG, Q. Q., CAO, L., WANG, H. F., TAN, M. S., GAO, Q., QIN, H., ZHANG, Y. D. & TAN, L. 2014. Temsirolimus attenuates tauopathy in vitro and in vivo by targeting tau hyperphosphorylation and autophagic clearance. *Neuropharmacology*, 85, 121-30.
- JINEK, M., CHYLINSKI, K., FONFARA, I., HAUER, M., DOUDNA, J. A. & CHARPENTIER, E. 2012. A programmable dual-RNA-guided DNA endonuclease in adaptive bacterial immunity. *Science*, 337, 816-21.
- KALMAN, B., LAUTENSCHLAEGER, R., KOHLMAYER, F., BUCHNER, B., KMIEC, T., KLOPSTOCK, T. & KUHN, K. A. 2012. An international registry for neurodegeneration with brain iron accumulation. *Orphanet J Rare Dis*, 7, 66.
- KIM, J., LEE, H., SELIMOVIC, S., GAUVIN, R. & BAE, H. 2015. Organ-on-a-chip: development and clinical prospects toward toxicity assessment with an emphasis on bone marrow. *Drug Saf*, 38, 409-18.
- KLIONSKY, D. J., ABDELMOHSEN, K., ABE, A., ABEDIN, M. J., ABELIOVICH, H., ACEVEDO AROZENA, A., ADACHI, H., ADAMS, C. M., ADAMS, P. D., ADELI, K., ADHIHETTY, P. J., ADLER, S. G., AGAM, G., AGARWAL, R., AGHI, M. K., AGNELLO, M., AGOSTINIS, P., AGUILAR, P. V., AGUIRRE-GHISO, J., AIROLDI, E. M., AIT-SI-ALI, S., AKEMATSU, T., AKPORIAYE, E. T., AL-RUBEAI, M., ALBAICETA, G. M., ALBANESE, C., ALBANI, D., ALBERT, M. L., ALDUDO, J., ALGUL, H., ALIREZAEI, M., ALLOZA, I., ALMASAN, A., ALMONTE-BECERIL, M., ALNEMRI, E. S., ALONSO, C., ALTAN-BONNET, N., ALTIERI, D. C., ALVAREZ, S., ALVAREZ-ERVITI, L., ALVES, S., AMADORO, G., AMANO, A., AMANTINI, C., AMBROSIO, S., AMELIO, I., AMER, A. O., AMESSOU, M., AMON, A., AN, Z., ANANIA, F. A., ANDERSEN, S. U., ANDLEY, U. P., ANDREADI, C. K., ANDRIEU-ABADIE, N., ANEL, A., ANN, D. K., ANOOPKUMAR-DUKIE, S., ANTONIOLI, M., AOKI, H., APOSTOLOVA, N., AQUILA, S., AQUILANO, K., ARAKI, K., ARAMA, E., ARANDA, A., ARAYA, J., ARCARO, A., ARIAS, E., ARIMOTO, H., ARIOSIA, A. R., ARMSTRONG, J. L., ARNOULD, T., ARSOV, I., ASANUMA, K., ASKANAS, V., ASSELIN, E., ATARASHI, R., ATHERTON, S. S., ATKIN, J. D., ATTARDI, L. D., AUBERGER, P., AUBURGER, G., AURELIAN, L., AUTELLI, R., AVAGLIANO, L., AVANTAGGIATI, M. L., AVRAHAMI, L., AWALE, S., AZAD, N., BACHETTI, T., BACKER, J. M., BAE, D. H., BAE, J. S., BAE, O. N., BAE, S. H., BAEHRECKE, E. H., BAEK, S. H., BAGHDIGUIAN, S., BAGNIEWSKA-ZADWORNA, A., et al. 2016. Guidelines for the use and interpretation of assays for monitoring autophagy (3rd edition). *Autophagy*, 12, 1-222.
- KNERR, I., ZSCHOCKE, J., TRAUTMANN, U., DORLAND, L., DE KONING, T. J., MULLER, P., CHRISTENSEN, E., TREFZ, F. K., WUNDISCH, G. F., RASCHER, W. & HOFFMANN, G. F. 2002. Glutaric aciduria type III: a distinctive non-disease? *J Inherit Metab Dis*, 25, 483-90.
- KOELLER, D. M., WOONTNER, M., CRNIC, L. S., KLEINSCHMIDT-DEMASTERS, B., STEPHENS, J., HUNT, E. L. & GOODMAN, S. I. 2002. Biochemical, pathologic and behavioral analysis of a mouse model of glutaric acidemia type I. *Hum Mol Genet*, 11, 347-57.

X. REFERENCES

- KOLKER, S., CHRISTENSEN, E., LEONARD, J. V., GREENBERG, C. R., BURLINA, A. B., BURLINA, A. P., DIXON, M., DURAN, M., GOODMAN, S. I., KOELLER, D. M., MULLER, E., NAUGHTEN, E. R., NEUMAIER-PROBST, E., OKUN, J. G., KYLLERMAN, M., SURTEES, R. A., WILCKEN, B., HOFFMANN, G. F. & BURGARD, P. 2007. Guideline for the diagnosis and management of glutaryl-CoA dehydrogenase deficiency (glutaric aciduria type I). *J Inherit Metab Dis*, 30, 5-22.
- KOLKER, S., GARBADE, S. F., GREENBERG, C. R., LEONARD, J. V., SAUDUBRAY, J. M., RIBES, A., KALKANOGLU, H. S., LUND, A. M., MERINERO, B., WAJNER, M., TRONCOSO, M., WILLIAMS, M., WALTER, J. H., CAMPISTOL, J., MARTI-HERRERO, M., CASWILL, M., BURLINA, A. B., LAGLER, F., MAIER, E. M., SCHWAHN, B., TOKATLI, A., DURSUN, A., COSKUN, T., CHALMERS, R. A., KOELLER, D. M., ZSCHOCKE, J., CHRISTENSEN, E., BURGARD, P. & HOFFMANN, G. F. 2006. Natural history, outcome, and treatment efficacy in children and adults with glutaryl-CoA dehydrogenase deficiency. *Pediatr Res*, 59, 840-7.
- KOMATSU, M., WAGURI, S., CHIBA, T., MURATA, S., IWATA, J., TANIDA, I., UENO, T., KOIKE, M., UCHIYAMA, Y., KOMINAMI, E. & TANAKA, K. 2006. Loss of autophagy in the central nervous system causes neurodegeneration in mice. *Nature*, 441, 880-4.
- KRUEER, M. C. & BODDAERT, N. 2012. Neurodegeneration with brain iron accumulation: a diagnostic algorithm. *Semin Pediatr Neurol*, 19, 67-74.
- KUMA, A., HATANO, M., MATSUI, M., YAMAMOTO, A., NAKAYA, H., YOSHIMORI, T., OHSUMI, Y., TOKUHISA, T. & MIZUSHIMA, N. 2004. The role of autophagy during the early neonatal starvation period. *Nature*, 432, 1032-6.
- KUO, Y. M., DUNCAN, J. L., WESTAWAY, S. K., YANG, H., NUNE, G., XU, E. Y., HAYFLICK, S. J. & GITSCHIER, J. 2005. Deficiency of pantothenate kinase 2 (Pank2) in mice leads to retinal degeneration and azoospermia. *Hum Mol Genet*, 14, 49-57.
- KWIATKOWSKI, A., RYCKEWAERT, G., JISSENDI TCHOFO, P., MOREAU, C., VUILLAUME, I., CHINNERY, P. F., DESTEE, A., DEFEBVRE, L. & DEVOS, D. 2012. Long-term improvement under deferiprone in a case of neurodegeneration with brain iron accumulation. *Parkinsonism Relat Disord*, 18, 110-2.
- LANDER, E. S. 2016. The Heroes of CRISPR. *Cell*, 164, 18-28.
- LAVANDERO, S., TRONCOSO, R., ROTHERMEL, B. A., MARTINET, W., SADOSHIMA, J. & HILL, J. A. 2013. Cardiovascular autophagy: concepts, controversies, and perspectives. *Autophagy*, 9, 1455-66.
- LEMASTERS, J. J. 2005. Selective mitochondrial autophagy, or mitophagy, as a targeted defense against oxidative stress, mitochondrial dysfunction, and aging. *Rejuvenation Res*, 8, 3-5.
- LINDNER, M., KOLKER, S., SCHULZE, A., CHRISTENSEN, E., GREENBERG, C. R. & HOFFMANN, G. F. 2004. Neonatal screening for glutaryl-CoA dehydrogenase deficiency. *J Inherit Metab Dis*, 27, 851-9.
- LU, Q., YANG, P., HUANG, X., HU, W., GUO, B., WU, F., LIN, L., KOVACS, A. L., YU, L. & ZHANG, H. 2011. The WD40 repeat PtdIns(3)P-binding protein EPG-6 regulates progression of omegasomes to autophagosomes. *Dev Cell*, 21, 343-57.
- MASIERO, E., AGATEA, L., MAMMUCARI, C., BLAAUW, B., LORO, E., KOMATSU, M., METZGER, D., REGGIANI, C., SCHIAFFINO, S. & SANDRI, M. 2009. Autophagy is required to maintain muscle mass. *Cell Metab*, 10, 507-15.

X. REFERENCES

- MASIERO, E. & SANDRI, M. 2010. Autophagy inhibition induces atrophy and myopathy in adult skeletal muscles. *Autophagy*, 6, 307-9.
- MASUYA, H., INOUE, M., WADA, Y., SHIMIZU, A., NAGANO, J., KAWAI, A., INOUE, A., KAGAMI, T., HIRAYAMA, T., YAMAGA, A., KANEDA, H., KOBAYASHI, K., MINOWA, O., MIURA, I., GONDO, Y., NODA, T., WAKANA, S. & SHIROISHI, T. 2005. Implementation of the modified-SHIRPA protocol for screening of dominant phenotypes in a large-scale ENU mutagenesis program. *Mamm Genome*, 16, 829-37.
- MAYR, J. A., HAACK, T. B., FREISINGER, P., KARALL, D., MAKOWSKI, C., KOCH, J., FEICHTINGER, R. G., ZIMMERMANN, F. A., ROLINSKI, B., AHTING, U., MEITINGER, T., PROKISCH, H. & SPERL, W. 2015. Spectrum of combined respiratory chain defects. *J Inherit Metab Dis*, 38, 629-40.
- MCMULLEN, C. A., FERRY, A. L., GAMBOA, J. L., ANDRADE, F. H. & DUPONT-VERSTEEGDEN, E. E. 2009. Age-related changes of cell death pathways in rat extraocular muscle. *Exp Gerontol*, 44, 420-5.
- MEYER, M., DE ANGELIS, M. H., WURST, W. & KUHN, R. 2010. Gene targeting by homologous recombination in mouse zygotes mediated by zinc-finger nucleases. *Proc Natl Acad Sci U S A*, 107, 15022-6.
- MEYER, M., ORTIZ, O., HRABE DE ANGELIS, M., WURST, W. & KUHN, R. 2012. Modeling disease mutations by gene targeting in one-cell mouse embryos. *Proc Natl Acad Sci U S A*, 109, 9354-9.
- MOSCOU, M. J. & BOGDANOVA, A. J. 2009. A simple cipher governs DNA recognition by TAL effectors. *Science*, 326, 1501.
- MUHLHAUSEN, C., CHRISTENSEN, E., SCHWARTZ, M., MUSCHOL, N., ULLRICH, K. & LUKACS, Z. 2003. Severe phenotype despite high residual glutaryl-CoA dehydrogenase activity: a novel mutation in a Turkish patient with glutaric aciduria type I. *J Inherit Metab Dis*, 26, 713-4.
- NAKAI, A., YAMAGUCHI, O., TAKEDA, T., HIGUCHI, Y., HIKOSO, S., TANIKE, M., OMIYA, S., MIZOTE, I., MATSUMURA, Y., ASAHI, M., NISHIDA, K., HORI, M., MIZUSHIMA, N. & OTSU, K. 2007. The role of autophagy in cardiomyocytes in the basal state and in response to hemodynamic stress. *Nat Med*, 13, 619-24.
- NARENDRA, D., TANAKA, A., SUEN, D. F. & YOULE, R. J. 2008. Parkin is recruited selectively to impaired mitochondria and promotes their autophagy. *J Cell Biol*, 183, 795-803.
- NARENDRA, D. P., JIN, S. M., TANAKA, A., SUEN, D. F., GAUTIER, C. A., SHEN, J., COOKSON, M. R. & YOULE, R. J. 2010. PINK1 is selectively stabilized on impaired mitochondria to activate Parkin. *PLoS Biol*, 8, e1000298.
- NECHIPORUK, T., MCGANN, J., MULLENDORFF, K., HSIEH, J., WURST, W., FLOSS, T. & MANDEL, G. 2016. The REST remodeling complex protects genomic integrity during embryonic neurogenesis. *Elife*, 5.
- NISHIOKA, K., OYAMA, G., YOSHINO, H., LI, Y., MATSUSHIMA, T., TAKEUCHI, C., MOCHIZUKI, Y., MORI-YOSHIMURA, M., MURATA, M., YAMASITA, C., NAKAMURA, N., KONISHI, Y., OHI, K., ICHIKAWA, K., TERADA, T., OBI, T., FUNAYAMA, M., SAIKI, S. & HATTORI, N. 2015. High frequency of beta-propeller protein-associated neurodegeneration (BPAN) among patients with intellectual disability and young-onset parkinsonism. *Neurobiol Aging*, 36, 2004.e9-2004.e15.
- OHBA, C., NABATAME, S., IJIMA, Y., NISHIYAMA, K., TSURUSAKI, Y., NAKASHIMA, M., MIYAKE, N., TANAKA, F., OZONO, K., SAITSU, H. & MATSUMOTO, N. 2014. De novo WDR45 mutation in a patient showing clinically Rett syndrome with childhood iron deposition in brain. *J Hum Genet*, 59, 292-5.

X. REFERENCES

- OKAMOTO, N., IKEDA, T., HASEGAWA, T., YAMAMOTO, Y., KAWATO, K., KOMOTO, T. & IMOTO, I. 2014. Early manifestations of BPAN in a pediatric patient. *Am J Med Genet A*, 164a, 3095-9.
- OZAWA, T., KOIDE, R., NAKATA, Y., SAITSU, H., MATSUMOTO, N., TAKAHASHI, K., NAKANO, I. & ORIMO, S. 2014. A novel WDR45 mutation in a patient with static encephalopathy of childhood with neurodegeneration in adulthood (SENDA). *Am J Med Genet A*, 164a, 2388-90.
- PANDA, S. K., WEFERS, B., ORTIZ, O., FLOSS, T., SCHMID, B., HAASS, C., WURST, W. & KUHN, R. 2013. Highly efficient targeted mutagenesis in mice using TALENs. *Genetics*, 195, 703-13.
- PENG, J., ZHOU, Y., ZHU, S. & WEI, W. 2015. High-throughput screens in mammalian cells using the CRISPR-Cas9 system. *Febs j*, 282, 2089-96.
- POLSON, H. E., DE LARTIGUE, J., RIGDEN, D. J., REEDIJK, M., URBE, S., CLAGUE, M. J. & TOOZE, S. A. 2010. Mammalian Atg18 (WIPI2) localizes to omegasome-anchored phagophores and positively regulates LC3 lipidation. *Autophagy*, 6, 506-22.
- PORTEUS, M. H. & CARROLL, D. 2005. Gene targeting using zinc finger nucleases. *Nat Biotechnol*, 23, 967-73.
- POWELL, C. A., KOPAJTICH, R., D'SOUZA, A. R., RORBACH, J., KREMER, L. S., HUSAIN, R. A., DALLABONA, C., DONNINI, C., ALSTON, C. L., GRIFFIN, H., PYLE, A., CHINNERY, P. F., STROM, T. M., MEITINGER, T., RODENBURG, R. J., SCHOTTMANN, G., SCHUELKE, M., ROMAIN, N., HALLER, R. G., FERRERO, I., HAACK, T. B., TAYLOR, R. W., PROKISCH, H. & MINCZUK, M. 2015. TRMT5 Mutations Cause a Defect in Post-transcriptional Modification of Mitochondrial tRNA Associated with Multiple Respiratory-Chain Deficiencies. *Am J Hum Genet*, 97, 319-28.
- PROIKAS-CEZANNE, T., TAKACS, Z., DONNES, P. & KOHLBACHER, O. 2015. WIPI proteins: essential PtdIns3P effectors at the nascent autophagosome. *J Cell Sci*, 128, 207-17.
- PROIKAS-CEZANNE, T., WADDELL, S., GAUGEL, A., FRICKEY, T., LUPAS, A. & NORDHEIM, A. 2004. WIPI-1alpha (WIPI49), a member of the novel 7-bladed WIPI protein family, is aberrantly expressed in human cancer and is linked to starvation-induced autophagy. *Oncogene*, 23, 9314-25.
- RAI, P. K., RUSSELL, O. M., LIGHTOWLERS, R. N. & TURNBULL, D. M. 2015. Potential compounds for the treatment of mitochondrial disease. *Br Med Bull*.
- RATHORE, G. S., SCHAAF, C. P. & STOCCO, A. J. 2014. Novel mutation of the WDR45 gene causing beta-propeller protein-associated neurodegeneration. *Mov Disord*, 29, 574-5.
- RAVENSCROFT, G., LAING, N. G. & BONNEMANN, C. G. 2015. Pathophysiological concepts in the congenital myopathies: blurring the boundaries, sharpening the focus. *Brain*, 138, 246-68.
- RAVIKUMAR, B., DUDEN, R. & RUBINSZTEIN, D. C. 2002. Aggregate-prone proteins with polyglutamine and polyalanine expansions are degraded by autophagy. *Hum Mol Genet*, 11, 1107-17.
- REARDON, S. 2015. 'Organs-on-chips' go mainstream. *Nature*, 523, 266.
- ROGERS, D. C., FISHER, E. M., BROWN, S. D., PETERS, J., HUNTER, A. J. & MARTIN, J. E. 1997. Behavioral and functional analysis of mouse phenotype: SHIRPA, a proposed protocol for comprehensive phenotype assessment. *Mamm Genome*, 8, 711-3.

X. REFERENCES

- ROGERS, D. C., PETERS, J., MARTIN, J. E., BALL, S., NICHOLSON, S. J., WITHERDEN, A. S., HAFEZPARAST, M., LATCHAM, J., ROBINSON, T. L., QUILTER, C. A. & FISHER, E. M. 2001. SHIRPA, a protocol for behavioral assessment: validation for longitudinal study of neurological dysfunction in mice. *Neurosci Lett*, 306, 89-92.
- RUBINSZTEIN, D. C., MARINO, G. & KROEMER, G. 2011. Autophagy and aging. *Cell*, 146, 682-95.
- RYU, S. W., KIM, J. S. & LEE, S. H. 2015. Beta-Propeller-Protein-Associated Neurodegeneration: A Case of Mutation in WDR45. *J Clin Neurol*, 11, 289-91.
- SAAYMAN, S., ALI, S. A., MORRIS, K. V. & WEINBERG, M. S. 2015. The therapeutic application of CRISPR/Cas9 technologies for HIV. *Expert Opin Biol Ther*, 15, 819-30.
- SAITSU, H., NISHIMURA, T., MURAMATSU, K., KODERA, H., KUMADA, S., SUGAI, K., KASAI-YOSHIDA, E., SAWAURA, N., NISHIDA, H., HOSHINO, A., RYUJIN, F., YOSHIOKA, S., NISHIYAMA, K., KONDO, Y., TSURUSAKI, Y., NAKASHIMA, M., MIYAKE, N., ARAKAWA, H., KATO, M., MIZUSHIMA, N. & MATSUMOTO, N. 2013. De novo mutations in the autophagy gene WDR45 cause static encephalopathy of childhood with neurodegeneration in adulthood. *Nat Genet*, 45, 445-9, 449e1.
- SAUER, S. W., OKUN, J. G., FRICKER, G., MAHRINGER, A., MULLER, I., CRNIC, L. R., MUHLHAUSEN, C., HOFFMANN, G. F., HORSTER, F., GOODMAN, S. I., HARDING, C. O., KOELLER, D. M. & KOLKER, S. 2006. Intracerebral accumulation of glutaric and 3-hydroxyglutaric acids secondary to limited flux across the blood-brain barrier constitute a biochemical risk factor for neurodegeneration in glutaryl-CoA dehydrogenase deficiency. *J Neurochem*, 97, 899-910.
- SAUER, S. W., OPP, S., HOFFMANN, G. F., KOELLER, D. M., OKUN, J. G. & KOLKER, S. 2011. Therapeutic modulation of cerebral L-lysine metabolism in a mouse model for glutaric aciduria type I. *Brain*, 134, 157-70.
- SAUER, S. W., OPP, S., KOMATSUZAKI, S., BLANK, A. E., MITTELBRONN, M., BURGARD, P., KOELLER, D. M., OKUN, J. G. & KOLKER, S. 2015. Multifactorial modulation of susceptibility to l-lysine in an animal model of glutaric aciduria type I. *Biochim Biophys Acta*, 1852, 768-77.
- SCHWARZ, J. M., RODELSPERGER, C., SCHUELKE, M. & SEELow, D. 2010. MutationTaster evaluates disease-causing potential of sequence alterations. *Nat Methods*, 7, 575-6.
- SHERMAN, E. A., STRAUSS, K. A., TORTORELLI, S., BENNETT, M. J., KNERR, I., MORTON, D. H. & PUFFENBERGER, E. G. 2008. Genetic mapping of glutaric aciduria, type 3, to chromosome 7 and identification of mutations in c7orf10. *Am J Hum Genet*, 83, 604-9.
- SHIM DA, J., NEMERIA, N. S., BALAKRISHNAN, A., PATEL, H., SONG, J., WANG, J., JORDAN, F. & FARINAS, E. T. 2011. Assignment of function to histidines 260 and 298 by engineering the E1 component of the Escherichia coli 2-oxoglutarate dehydrogenase complex; substitutions that lead to acceptance of substrates lacking the 5-carboxyl group. *Biochemistry*, 50, 7705-9.
- SHU, X. H., WANG, L. L., LI, H., SONG, X., SHI, S., GU, J. Y., WU, M. L., CHEN, X. Y., KONG, Q. Y. & LIU, J. 2015. Diffusion Efficiency and Bioavailability of Resveratrol Administered to Rat Brain by Different Routes: Therapeutic Implications. *Neurotherapeutics*, 12, 491-501.
- STILES, A. R., VENTURONI, L., MUCCI, G., ELBALALESY, N., WOONTNER, M., GOODMAN, S. & ABDENUR, J. E. 2015. New Cases of DHTKD1 Mutations in Patients with 2-Ketoadipic Aciduria. *JIMD Rep*.

X. REFERENCES

- STRANNEHEIM, H. & WEDELL, A. 2016. Exome and genome sequencing: a revolution for the discovery and diagnosis of monogenic disorders. *J Intern Med*, 279, 3-15.
- STRAUSS, K. A. & MORTON, D. H. 2003. Type I glutaric aciduria, part 2: a model of acute striatal necrosis. *Am J Med Genet C Semin Med Genet*, 121c, 53-70.
- SUMI-AKAMARU, H., BECK, G., KATO, S. & MOCHIZUKI, H. 2015. Neuroaxonal dystrophy in PLA2G6 knockout mice. *Neuropathology*, 35, 289-302.
- TAKANO, K., SHIBA, N., WAKUI, K., YAMAGUCHI, T., AIDA, N., INABA, Y., FUKUSHIMA, Y. & KOSHO, T. 2015. Elevation of neuron specific enolase and brain iron deposition on susceptibility-weighted imaging as diagnostic clues for beta-propeller protein-associated neurodegeneration in early childhood: Additional case report and review of the literature. *Am J Med Genet A*.
- TROFIMOVA, L., LOVAT, M., GROZNAYA, A., EFIMOVA, E., DUNAEVA, T., MASLOVA, M., GRAF, A. & BUNIK, V. 2010. Behavioral impact of the regulation of the brain 2-oxoglutarate dehydrogenase complex by synthetic phosphonate analog of 2-oxoglutarate: implications into the role of the complex in neurodegenerative diseases. *Int J Alzheimers Dis*, 2010, 749061.
- TSCHECHTSCHER, A., DEKOMIEN, G., ROSS, S., CREMER, K., KUKUK, G. M., EPPLER, J. T. & HOFFJAN, S. 2015. Analysis of the C19orf12 and WDR45 genes in patients with neurodegeneration with brain iron accumulation. *J Neurol Sci*, 349, 105-9.
- UDDIN, S., BHAT, A. A., KRISHNANKUTTY, R., MIR, F., KULINSKI, M. & MOHAMMAD, R. M. 2015. Involvement of F-BOX proteins in progression and development of human malignancies. *Semin Cancer Biol*.
- VAN RECHEM, C., BLACK, J. C., ABBAS, T., ALLEN, A., RINEHART, C. A., YUAN, G. C., DUTTA, A. & WHETSTINE, J. R. 2011. The SKP1-Cul1-F-box and leucine-rich repeat protein 4 (SCF-FbxL4) ubiquitin ligase regulates lysine demethylase 4A (KDM4A)/Jumonji domain-containing 2A (JMJD2A) protein. *J Biol Chem*, 286, 30462-70.
- VERHOEVEN, W. M., EGGER, J. I., KOOLEN, D. A., YNTEMA, H., OLGATI, S., BREEDVELD, G. J., BONIFATI, V. & VAN DE WARRENBURG, B. P. 2014. Beta-propeller protein-associated neurodegeneration (BPAN), a rare form of NBIA: novel mutations and neuropsychiatric phenotype in three adult patients. *Parkinsonism Relat Disord*, 20, 332-6.
- VISCOMI, C., BOTTANI, E. & ZEVIANI, M. 2015. Emerging concepts in the therapy of mitochondrial disease. *Biochim Biophys Acta*, 1847, 544-57.
- WEBB, J. L., RAVIKUMAR, B., ATKINS, J., SKEPPER, J. N. & RUBINSZTEIN, D. C. 2003. Alpha-Synuclein is degraded by both autophagy and the proteasome. *J Biol Chem*, 278, 25009-13.
- WEFERS, B., MEYER, M., ORTIZ, O., HRABE DE ANGELIS, M., HANSEN, J., WURST, W. & KUHN, R. 2013a. Direct production of mouse disease models by embryo microinjection of TALENs and oligodeoxynucleotides. *Proc Natl Acad Sci U S A*, 110, 3782-7.
- WEFERS, B., ORTIZ, O., WURST, W. & KUHN, R. 2014. Generation of targeted mouse mutants by embryo microinjection of TALENs. *Methods*, 69, 94-101.
- WEFERS, B., PANDA, S. K., ORTIZ, O., BRANDL, C., HENSLER, S., HANSEN, J., WURST, W. & KUHN, R. 2013b. Generation of targeted mouse mutants by embryo microinjection of TALEN mRNA. *Nat Protoc*, 8, 2355-79.

X. REFERENCES

- WORTMANN, S. B., KOOLEN, D. A., SMEITINK, J. A., VAN DEN HEUVEL, L. & RODENBURG, R. J. 2015. Whole exome sequencing of suspected mitochondrial patients in clinical practice. *J Inherit Metab Dis*, 38, 437-43.
- XU, W., ZHU, H., GU, M., LUO, Q., DING, J., YAO, Y., CHEN, F. & WANG, Z. 2013. DHTKD1 is essential for mitochondrial biogenesis and function maintenance. *FEBS Lett*, 587, 3587-92.
- XU, W. Y., GU, M. M., SUN, L. H., GUO, W. T., ZHU, H. B., MA, J. F., YUAN, W. T., KUANG, Y., JI, B. J., WU, X. L., CHEN, Y., ZHANG, H. X., SUN, F. T., HUANG, W., HUANG, L., CHEN, S. D. & WANG, Z. G. 2012. A nonsense mutation in DHTKD1 causes Charcot-Marie-Tooth disease type 2 in a large Chinese pedigree. *Am J Hum Genet*, 91, 1088-94.
- ZHANG, D., CONTU, R., LATRONICO, M. V., ZHANG, J., RIZZI, R., CATALUCCI, D., MIYAMOTO, S., HUANG, K., CECI, M., GU, Y., DALTON, N. D., PETERSON, K. L., GUAN, K. L., BROWN, J. H., CHEN, J., SONENBERG, N. & CONDORELLI, G. 2010. MTORC1 regulates cardiac function and myocyte survival through 4E-BP1 inhibition in mice. *J Clin Invest*, 120, 2805-16.
- ZHANG, F., CONG, L., LODATO, S., KOSURI, S., CHURCH, G. M. & ARLOTTA, P. 2011. Efficient construction of sequence-specific TAL effectors for modulating mammalian transcription. *Nat Biotechnol*, 29, 149-53.
- ZHAO, Y. G., SUN, L., MIAO, G., JI, C., ZHAO, H., SUN, H., MIAO, L., YOSHII, S. R., MIZUSHIMA, N., WANG, X. & ZHANG, H. 2015. The autophagy gene Wdr45/Wipi4 regulates learning and memory function and axonal homeostasis. *Autophagy*, 11, 881-90.
- ZSCHOCKE, J., QUAK, E., GULDBERG, P. & HOFFMANN, G. F. 2000. Mutation analysis in glutaric aciduria type I. *J Med Genet*, 37, 177-81.

XI. ACKNOWLEDGEMENTS

This work would not have been possible without the invaluable support of many.

Firstly, I would like to thank the Institute of Human Genetics for providing the frame conditions and giving me the opportunity to work in this group. I am grateful to Dr. Holger Prokisch for his constant support and inspiring discussions throughout the development of this thesis. I want to thank Prof. Dr. med. Thomas Meitinger for taking me to numerous stimulating conferences and for taking the time to provide important comments on this thesis.

I would like to thank the thesis committee PD Dr. Thomas Floss, Prof. Dr. Martin Hrabě de Angelis and Prof. Dr. Angelika Schniecke for their support.

I am grateful for having worked in the AG Prokisch research group with many inspiring people, who were a constant source of motivation and encouragement to me. They have readily exchanged experiences and have created an exceptionally friendly working atmosphere. With any informatics related challenges I was greatly supported by the AG Strom.

I would like to express my thanks to collaborators from the Universitaet Heidelberg as well as the German Mouse Clinic. This work was supported by the seventh framework EU-project, TIRCON (treat iron-related childhood onset neurodegeneration) as well as the DFG (Deutsche Forschungsgemeinschaft) and the NBIA (neurodegeneration with brain iron accumulation) Disorders Association.

A very special thanks goes to my friends in Munich, Regensburg and London, who have constantly supported me in joyful as well as difficult moments. They accepted my limited time especially during the last months and showed their warm support.

My deepest gratitude I would like to express to my family. This work is dedicated to my parents and my sister, who constantly supported me my entire life and especially throughout this thesis.

Diese Arbeit ist meinen Eltern und meiner Schwester gewidmet. Ich bin euch unendlich dankbar dafür, dass ihr immer für mich da seid. Ihr schenkt mir ein außergewöhnliches Gefühl der Geborgenheit und Liebe. Mit euch habe ich es geschafft meine Träume und Vorstellungen zu verwirklichen. Mami, du hast zu jeder Zeit ein offenes Ohr für mich. Die emotionale Sicherheit, die du mir damit gibst ist unbezahlbar. Papi, obwohl bei dir Zeit schon immer ein sehr knappes Gut ist, nimmst du sie dir immer für mich. Du hast mir geholfen herauszufinden in welche Richtung ich gehen möchte und mich unterstützt diese Ziele zu erreichen. Juli, du stehst mir mit Rat und Tat zur Seite und das sogar in deinen Flitterwochen (ein großes Dankeschön hierfür auch an meinen Schwager Christian). Du bist für mich eine Schwester und beste Freundin in jeder Lebenssituation.

Ich danke euch für alles!

XII. CURRICULUM VITAE

21.01.1987 born in Munich

Education

- Since 2012 **Technische Universitaet Muenchen, Germany**
PhD student at the Institut für Humangenetik, Helmholtz Zentrum Muenchen
In collaboration with the Klinikum rechts der Isar
PhD Title: "From novel disease genes to new mouse models - a complementary approach"
- 2014-2015 **Pharmaakademie Muenchen**
Clinical Research Associate degree during a one-year weekend course
- 2012 University College London, UK
Post-graduate in Systems Biology at the department of Genetics, Evolution and Environment
- 2010-2011 **University College London, UK**
MSc Genetics of Human Disease, Grade: Distinction
Master's thesis title: „Transposon mediated saturating mutagenesis to identify functional elements in the genome of *S. pombe*”
- 2006-2009 **Universitaet Regensburg, Germany**
BSc Biologie, Grade: gut (top 30%)
Bachelor's thesis title: „Fluoreszenzproteinfusionen zur Visualisierung von Zellkompartimenten der Hefe“
- 2004-2006 **Nymphenburger Gymnasium, Munich**
Abitur, Grade 1.9
- 2003-2004 **Collège International Brillantmont, Switzerland**
Cambridge International Examinations (Advanced Subsidiary Level)
Listed at the Honour Role for excellent academic achievements
- 1996-2003 **Gymnasium Pullach, Munich**

Work experience

- Laboratory work – several weeks to months
- 2010 **Wacker Chemie AG, Munich**
Internship at the Department for Biotechnology
- 2009 **International Centre for Genetic Engineering and Biotechnology,
Cape Town, South Africa**
Internship at Cancer Science

XII. CURRICULUM VITAE

2009 **Harvard University, Boston, USA**

Internship in Biophysics

2008 **Universitaet Regensburg**

Internship in Biophysics

2007 **Universitaet Regensburg**

Internship in Molecular Genetics

Other skills

IT Experienced with MS Office (Powerpoint, Excel etc.)

Languages German (mother tongue), English (fluent), French (advanced)

Leisure activities

Sport Badminton, running, skiing, tennis, windsurfing, beach volleyball

Travel Travel experiences in Australia, Africa, USA and several European countries

Publications

X. Gai, D. Ghezzi, M. A. Johnson, C. A. Biagosch et. al., Mutations in FBXL4, encoding a mitochondrial protein, cause early-onset mitochondrial encephalomyopathy. *Am J Hum Genet.* 2013 Sep

Huemer M, Karall D, Schossig A, Abdenur JE, Al Jasmi F, Biagosch C, et. al. Clinical, morphological, biochemical, imaging and outcome parameters in 21 individuals with mitochondrial maintenance defect related to FBXL4 mutations. *J Inherit Metab Dis.* 2015 Sep;38(5):905-14. doi: 10.1007/s10545-015-9836-6. Epub 2015

Klionsky DJ et al., Guidelines for the use and interpretation of assays for monitoring autophagy g(3rdedition). *Autophagy.* 2016 Jan 2;12(1):1-222.

Posters

ESHG 2013 Paris, ICIEM 2013 Barcelona, ASHG 2013 Boston, GfH 2014 Essen, ESHG 2014 Milan, Euromit 2014 Tampere, ESHG 2015 Glasgow

Award

ESHG Poster Award "Best Basic Research" for a presentation judged outstanding at the ESHG Conference 2015, Glasgow